Universität Rostock Traditio et Innovatio
HelmholtzZentrum münchen
Deutsches Forschungszentrum für Gesundheit und Umwelt
JOINT MASS SPECTROMETRY CENTRE

Spatio-temporal variability, driving factors, and the health risk assessment of inhalable particulate matter in Germany

Kumulative Dissertation

zur Erlangung des akademischen Grades eines doctor rerum naturalium (Dr. rer. nat.)

vorgelegt der

Mathematisch-Naturwissenschaftlichen Fakultät

der Universität Rostock

von

Xiansheng Liu

geboren am 25. September 1990 in Shandong

München und Rostock, November 2021

https://doi.org/10.18453/rosdok_id00003551

Gutachter:

1. Gutachter:

Prof. Dr. Ralf Zimmermann

Institut für Chemie, Universität Rostock, Germany

2. Gutachter

Prof. Dr. Jan Hovorka

Institute for Environmental Studies, Charles University, Czech Republic

Datum der Einreichung: 15. November 2021

Datum der Antwort: 25. Januar 2022

Doktorandinnen/Doktoranden-Erklärung gemäß § 4 Absatz 1 Buchstaben g und h der Promotionsordnung der Mathematisch-Naturwissenschaftlichen Fakultät der Universität

Name : Xiansheng Liu **Martikelnummer:** 217205910

Address: Aidenbachstr. 68, 81379, München

Ich habe eine Dissertation zum Thema:

"Spatio-temporal variability, driving factors, and the health risk assessment of inhalable particulate matter in Germany"

an der Mathematisch-Naturwissenschaftlichen Fakultät der Universität Rostock angefertigt. Dabei wurde ich von Herrn **Professor Ralf Zimmermann** betreut.

Ich gebe folgende Erklärung ab:

a. Die Gelegenheit zum vorliegenden Promotionsvorhaben ist mir nicht kommerziell vermittelt worden. Insbesondere habe ich keine Organisation eingeschaltet, die gegen Entgelt Betreuerinnen/Betreuer für die Anfertigung von Dissertationen sucht oder die mir obliegenden Pflichten hinsichtlich der Prüfungsleistungen für mich ganz oder teilweise erledigt.

b. Ich versichere hiermit an Eides statt, dass ich die vorliegende Arbeit selbstständig angefertigt und ohne fremde Hilfe verfasst habe. Dazu habe ich keine außer den von mir angegebenen Hilfsmitteln und Quellen verwendet und die den benutzten Werken inhaltlich und wörtlich entnommenen Stellen habe ich als solche kenntlich gemacht.

München, October, 2021 _____

Xiansheng Liu

Contribution of the Author to Published Papers

The contribution of the author to each publication is briefly summarized as following:

Publication I: Liu, X., et al. (2020). Assessment of German population exposure levels to PM_{10} based on multiple spatial-temporal data. Environmental Science and Pollution Research, 27(6), 6637-6648.

For the 1st publication, Xiansheng Liu did all the practical work of obtaining the data, including collecting PM_{10} data from 379 air pollution monitoring stations in Germany, population distribution data. and using population-weighted PM_{10} concentrations to calculate population exposure levels. He carried out all the data processing. He also undertook the writing, submission and revising of the manuscript.

Publication II: Liu, X., et al. (2021). Air pollution in Germany: spatio-temporal variations and their driving factors based on continuous data from 2008 to 2018. Environmental Pollution, 116732.

For the 2nd publication, Xiansheng Liu analysed long-term observational data of particulate matter ($PM_{2.5}$, PM_{10}) variability, gaseous pollutants (CO, NO_2, NO_X, SO_2, and O_3), and meteorological factors in 412 fixed monitoring stations from January 2008 to December 2018 in Germany. He undertook the writing, submission and revising of the paper.

Publication III: Liu, X., et al. (2021). Spatiotemporal characteristics and driving factors of black carbon in Augsburg, Germany: Combination of mobile monitoring and street view images. Environmental Science & Technology, 1,55, 160-168.

For the 3rd publication, Xiansheng Liu carried out a sampling campaign in Augsburg for nearly 2 year and did most of the sampling. He integrated all the data and build a black carbon prediction model based on street view imagery. He undertook the writing, submission and revising of the paper.

Publication IV: Liu, X., et al. (2020). Integration of air pollution data collected by mobile measurement to derive a preliminary spatiotemporal air pollution profile from two neighboring German-Czech border villages. Science of The Total Environment, 722, 137632.

For the 4th publication, Xiansheng Liu carried out a sampling campaign in two neighboring German-Czech border villages. He integrate all the data and analysed the average concentration and variation of each region and to discuss the influencing factors. He undertook the writing, submission and revising of the paper.

Publication V: Liu, X., et al. (2021). Analysis of mobile monitoring data from the microAeth® MA200 for measuring changes in black carbon on the roadside in Augsburg. Atmospheric Measurement Techniques, 14, 5139–5151.

For the 5th publication, Xiansheng Liu assessed the mobile real-time performance of the MA200 to determine a suitable noise reduction algorithm in an urban area, Augsburg, Germany. He integrated all the data and analysed the average concentration and variation of each region and to discuss the influencing factors. He undertook the writing, submission and revising of the paper.

Publication VI: Liu, X., et al. (2021). Combined land-use and street view image model for estimating black carbon concentrations in urban areas. Atmospheric Environment, 118719.

For the 6th publication, Xiansheng Liu developed a novel land-use street view image random forest (LUSRF) model to estimate the equivalent black carbon (eBC) concentration in the urban city of Augsburg, Germany. He integrated all the data, built the model and discussed the influencing factors. He undertook the writing, submission and revising of the paper.

Publication VII: Khedr, M., and Liu, X., et al. (2022). Influence of New Year's fireworks on air quality – A case study from 2010 - 2021 in Augsburg, Germany. Atmospheric Pollution Research 101341.*

For the 7th publication, This paper presented a source apportionment-based approach to estimate the quantitative contributions of fireworks on New Year's days in Augsburg. The contributions of New Year's fireworks to PAH concentrations were estimated based on PMF. Xiansheng Liu undertook the statistic analysis and data evaluation.

München, November, 2021

_____

Xiansheng Liu

All outstanding work, in art as well as in science, results from immense zeal applied to a great idea.

-------Santiago Ramón y Cajal

It always seems impossible until it's done.

------Nelson Mandela

DANKSAGUNG / ACKNOWLEDGEMENTS

The project is funded by the German Federal Ministry of Traffic and Digital Infrastructure as a part of "Smart Air Quality Network". I was all the time working in the Comprehensive Molecular Analysis (CMA) group of Joint Mass Spectrometry Center (JMSC) of Helmholtz Zentrum München and University Rostock. I would like to express my many thanks to their collaboration and help.

First and foremost, I would like to express my sincere gratitude to my supervisor Prof. Dr. Ralf Zimmermann, for giving me the great opportunity to do scientific research in his group and for his continuously support during this period.

I would also like to give my special thanks to my advisor Dr. Jürgen Schnelle-Kreis. He already guided me for almost four years. Without his patience and counsel, I would never have taken on this project and would never have been able to pass it through to completion. He always encourages me to think and work as a good scientist and provided me with the freedom to design the project independently. Last but not least, He always tried his best to shape my attitude to be a great scientist. Thanks a lot !

I would also like to Hadiatullah Hadiatullah thank for his help with work, life, and cooperation in paper writing. His assistance, advice and feedback make me a more energetic student.

My appreciation also goes to Prof. Dr. Xun Zhang for his help with the method and ideas.

I would also like to thank Mohamed Khedr, Jürgen Orasche, Gülcin Abbaszade, and Gert Jakobi for their help with laboratory work and cooperation with field sampling.

I would also like to thank Brigitte Schloter-Hai for her help in revising the language of my article.

Special thank goes to Chinese Scholarship Council’s financial support to my PhD work.

I would also like to thank all of my friends (Xiangyun Cheng, Lingxi Ye, Yanling Xu, Yanning Xu, Xin He and Pengfei, Huang etc.). Thank you for your continued support and help.

Finally, I am extremely grateful to my families (Xiuxiu Lin, Xiuhua Zheng, and Changjiang, Liu), thank them for their hard work and support for my education even it is not easy for them. I am also thankful to them for being patient and not giving me extra pressure during my PhD work.

ZUSAMMENFASSUNG

Die Luftverschmutzung hat in den letzten Jahren zunehmend an Bedeutung gewonnen, und die damit verbundenen Gesundheitsrisiken sind zu einem wichtigen Thema geworden. Nach Angaben der Weltgesundheitsorganisation (WHO, 2016) ist die Luftverschmutzung das größte einzelne Umweltrisiko für die Gesundheit und verantwortlich für schätzungsweise 7 Millionen vorzeitige Todesfälle pro Jahr weltweit und mehr als 550.000 in der Europäischen Region der WHO. Epidemiologische und toxikologische Studien haben gezeigt, dass eine langfristige Exposition gegenüber Luftverschmutzung im Freien mit einer hohen Sterblichkeit in großen europäischen Kohorten verbunden ist, insbesondere in Bezug auf Feinstaub. Luftschadstoffkonzentrationen können sich über kurze Entfernungen und in kurzen Zeiträumen verändern. Daher ist das Verständnis der räumlich-zeitlichen Verteilung von Feinstaub (PM) in der Luft und die genaue Abschätzung der räumlichen Muster der Luftverschmutzung von entscheidender Bedeutung für die Bewertung der Exposition der Bevölkerung und der Gesundheitsrisiken sowie für den Schutz der menschlichen Gesundheit und die Festlegung von Maßnahmen zur Bekämpfung der Verschmutzung. In dieser Studie wurden die räumlich-zeitliche Variabilität und die treibenden Faktoren der Luftverschmutzung auf der Grundlage kontinuierlicher Daten von Messstationen in Deutschland (Meso-Skala) und verschiedener Mikroumgebungen in städtischen und kleinstädtischen Gebieten (Mikro-Skala) untersucht, um die Auswirkungen von Luftschadstoffen (d. h. polyzyklische aromatische Kohlenwasserstoffe (PAK), Metallelemente und Feinstaub (PM)) auf die menschliche Gesundheit zu bewerten.

Der Forschungsprozess umfasste zwei Arten von Analysen: Bewertungen von Daten, die an festen Standorten gesammelt wurden, und mobile Messungen. Für die Bewertung der ortsfesten Überwachung wurde zunächst eine Erhebung der Luftschadstoffbelastung in ganz Deutschland durchgeführt. In diesem Abschnitt wurden langfristige Beobachtungsdaten von 412 ortsfesten Messstationen in Deutschland zu Feinstaub ($PM_{2,5}$, PM_{10}), gasförmigen Schadstoffen (CO, NO_2, NO_X, SO_2 und O_3) und meteorologischen Faktoren untersucht. In städtischen Straßen wurden mobile Messungen durchgeführt, um die Luftschadstoffbelastung in verschiedenen Mikroumgebungen zu untersuchen. Die Belastung durch die Luftschadstoffe PM_X (PM_1, $PM_{2,5}$, PM_{10}), ultraviolett absorbierende Partikel (UVPM), schwarzen Kohlenstoff (BC), braunen Kohlenstoff (BrC), die Partikelanzahlkonzentration (PNC) und die lungendeponierte Oberfläche (LDSA) zu untersuchen. Anschließend wurde die Belastung durch PAH (PAH) und Metallelemente aus Feuerwerkskörpern untersucht, um die Auswirkungen von Feuerwerkskörpern auf die Luftverschmutzung am Neujahrstag abzuschätzen.

Auf der Mesoskala war der Trend der Luftschadstoffe in Deutschland im Untersuchungszeitraum (01. 2008 - 12. 2018) weitgehend stabil. Entsprechend der relativen Korrelationen von gasförmigen Schadstoffen und meteorologischen Faktoren korrelierten CO und Temperatur am stärksten mit den $PM_{2.5}$- und PM_{10}-Konzentrationen. Die Bevölkerungsverteilung nach Expositionsniveau zeigt, dass die Mehrheit der Menschen in Deutschland in verschmutzten Gebieten lebt. Andererseits wiesen die Luftschadstoffkonzentrationen in städtischen Gebieten eine erhebliche räumliche Heterogenität und zeitliche Schwankungen auf der Mikroebene auf

(Augsburger Stadtzentrum). Die höchsten Luftschadstoffkonzentrationen im innerstädtischen Umfeld wurden in verkehrsreichen Gebieten festgestellt. Darüber hinaus wurden signifikante Unterschiede in den PNC- und PM-Konzentrationen zwischen den beiden Kleinstädten (Bayerisch Eisenstein, Deutschland, und Zelezna Ruda, Tschechische Republik) festgestellt, was darauf hindeutet, dass die Luftschadstoffkonzentrationen durch unterschiedliche lokale Quellen beeinflusst werden können. Der Einfluss einzelner Ereignisse auf die Luftqualität wurde anhand von Silvesterfeuerwerken in Augsburg untersucht. B[a]P-Konzentrationen während der Periode um die Neujahrstage (24.Dez.-7.Jan.) überschritten den Zielwert von 1 ng/m^3. Dies deutet darauf hin, dass mehr toxische Verbindungen die menschliche Gesundheit bedrohen und dass Feuerwerkskörper einen erheblichen Einfluss auf die Luftschadstoffbelastung während der Neujahrstage haben. Der Beitrag von Feuerwerkskörpern zur Luftverschmutzung mit PAK, BC und Metallen an den einzelnen Neujahrstagen kann durch PMF-Analysen abgeschätzt werden.

ABSTRACT

Air pollution has become increasingly serious in recent years, and the health risks associated with it have become a hot topic of concern. According to the World Health Organization (WHO, 2016) “Air pollution is the largest single environmental risk to health, responsible for an estimated 7 million premature deaths every year globally and about 550,000 in the WHO European Region”. Long-term exposure to outdoor air pollution was linked to high mortality in large European cohorts, according to epidemiological and toxicological studies, particularly with regard to fine particulate matter. Because air pollutant concentrations can change over short distances and in short time periods understanding the spatio-temporal distribution of ambient particulate matter (PM) and accurate estimation of spatial patterns of air pollution are critical for assessing population exposure and health risks, as well as protecting human health and establishing pollution control policies. In this study, the spatio-temporal variability and driving factors of air pollution were investigated based on continuous data from monitoring stations in Germany (meso-scale), and different micro-environments across urban and small-town areas (micro-scale), to assess the impact of air pollutants (i.e., polycyclic aromatic hydrocarbons (PAHs), metal elements, and PM) on human health.

The research process included two types of analysis: assessments of data collected at fixed sites and mobile measurements. A survey of air pollution exposure levels across Germany was initially conducted for a fixed monitoring assessment. This section examined long-term observational data from 412 fixed monitoring stations in Germany on particulate matter ($PM_{2.5}$, PM_{10}), gaseous pollutants (CO, NO_2, NO_X, SO_2, and O_3), and meteorological factors. For mobile monitoring assessment, surveys of air pollution exposure levels in different micro-environments were conducted in urban and small town streets to investigate the exposure of the air pollutants, PM_X (PM_1, $PM_{2.5}$, PM_{10}), ultraviolet-absorbing particulate matter (UVPM), black carbon (BC), brown carbon (BrC), particle number concentration (PNC), and lung deposited surface area (LDSA), in different micro-environments. Following that, PAH and metal element exposure from fireworks was examined in order to estimate the effect of fireworks on air pollution exposure during New Year's Day.

At the meso-scale, the trend of atmospheric pollutants in Germany was stable during the investigated period (01. 2008 - 12. 2018). CO and temperature had the strongest correlations with $PM_{2.5}$ and PM_{10} concentrations, according to the relative correlations of gaseous pollutants and meteorological factors. The population distribution according to exposure level reveals that the majority of people in Germany lived in polluted areas. On the other hand, air pollutant concentrations in urban areas showed significant spatial heterogeneity and temporal variations at the micro-scale (Augsburg city centre). The highest concentrations of air pollutants were found in areas with a lot of traffic, which may influence the high exposure of air pollutants in these areas. Significant differences in PNC and PM concentrations were discovered between the two small towns (Bayerisch Eisenstein, Germany, and Zelezna Ruda, Czech Republic), indicating that air pollutants concentrations may be influenced by different local sources. These results were comparable with the B[a]P concentrations that exceeded the target value of 1 ng/m^3 during the investigated Augsburg New Year's Days periods (24th.Dec.-7th.Jan.^{2nd}). This indicated that more compounds that are toxic are threatening human health, and fireworks have a significant impact on air pollution exposure during the New Year's Days periods. The contribution of fireworks to the air pollution with PAHs, BC and metals on the individual New Year's days was estimated by PMF analysis.

Contents

ZUSAMMENFASSUNG..... XIII
ABSTRACT..... XIV
1 Introduction..... 1
1.1 Scope of the study..... 1
1.2 Aims of the study..... 3
2 Methodology..... 5
2.1 Sampling campaign..... 5
2.1.1 Study areas..... 5
2.1.2 Fixed site monitoring data..... 5
2.1.3 Mobile monitoring measurement..... 5
2.2 Meteorological monitoring data..... 6
2.3 Chemical analysis of organic species..... 7
2.4 Spatio-temporal analysis..... 9
2.5 The prediction model of air pollutants in urban micro-scale..... 9
2.5.1 Street view images (SVI) model..... 9
2.5.2 Evaluation of model accuracy..... 10
2.6 Evaluation of the PM_{10} effect on human health in meso-scale..... 10
2.6.1 Estimation of the population exposure to PM_{10}..... 10
2.6.2 Spatial distribution of PM_{10} exposure..... 10
2.7 Positive matrix factorization (PMF) analysis..... 11
2.8 Health assessment of PAHs and metal elements..... 11
3 Results and Discussion..... 13
3.1 The current status of atmospheric pollutants in Germany (meso-scale)..... 13
3.1.1 Spatio-temporal variability of air pollutants in Germany..... 13
3.1.2 Spatialisation of demographic data and estimation of the population exposure to PM_{10}..... 17
3.1.3 Correlations between air pollutants..... 18
3.2 The current status of atmospheric pollutant in Augsburg (micro-scale)..... 20
3.2.1 Spatio-temporal variability of air pollutants in different micro-environment..... 20
3.2.2 Correlation of eUVPM, eBC, and eBrC concentrations and its driving factors..... 23
3.2.3 The estimation of eUVPM, eBC, and eBrC concentrations and their model evaluation..... 25
3.2.4 The trend of air pollutants and its health assessment around New Year's Days..... 26
3.3 The characteristics of atmospheric pollutants in small towns (micro-scale)..... 31
3.3.1 Spatio-temporal variability of air pollutants in two neighboring German-Czech border villages..... 32
3.3.2 Hotspots parsing of air pollutants in BE and ZR..... 35
4 Conclusions..... 37
References..... 39
Appendix..... 49

1 Introduction

1.1 Scope of the study

Air pollution, both outdoor and indoor, is a major global health problem [1], which responsible for considerable morbidity and an enormous number of premature deaths annually [2]. According to World Health Origination (WHO), almost 92 % of the world's population lives in places where air quality levels exceed WHO limits [3]. Cities tend to be densely populated and bear the major brunt of ambient air pollution, as more than half the world's population resides in cities [4]. However, the causes of environmental problems in different countries and regions are becoming increasingly complex due to the complex sources of particulate matter (PM) (**Figure 1.1**). Even in areas where annual average pollutant concentrations are met the WHO standards, the celebration of specific events (e.g., fireworks on New Year's Day) can cause a very high increase of air pollutants (e.g., heavy metals, polycyclic aromatic hydrocarbons (PAHs)) in the short term [5, 6], which affects the human health. According to a current calculation by the German Environment Agency (Umweltbundesamt, UBA), around 1,500 tons of particulate matter (PM_{10}) are emitted within a few hours throughout Germany due to of New Year's Eve fireworks [7]. Evaluations of the measurement data from the German air quality measurement networks regularly show peak values of the fine dust concentration for New Year's Day with maximum hourly values around 1,000 µg/m³ PM_{10}. Therefore, knowledge of the present state and the spatio-temporal distribution of air pollutants, exposure of the population and evaluation of the adverse health effects caused by air pollution, are important for understanding the air pollution problem and protecting human health and establishing pollution control policies.

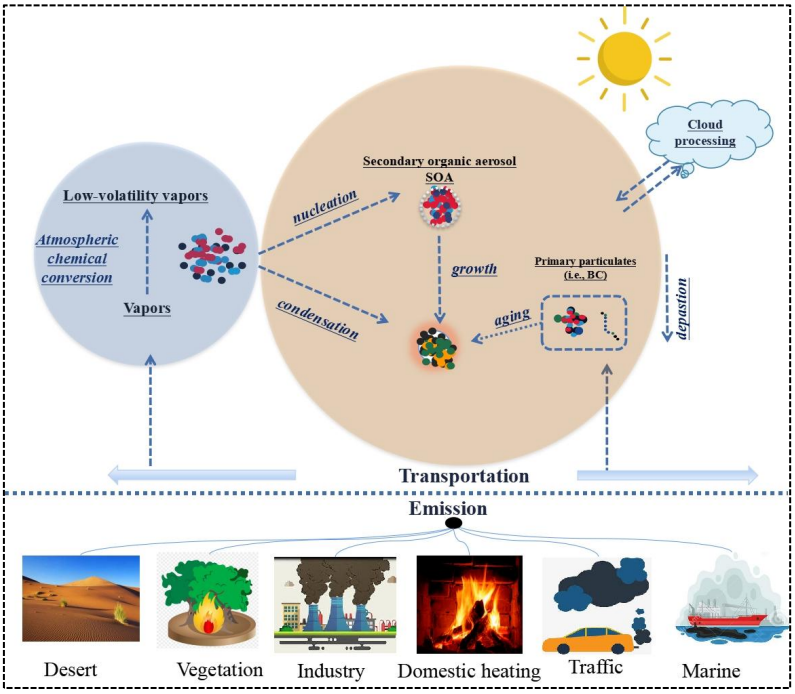


Figure 1.1: *Schematic image of the formation, growth and processing of atmospheric aerosol. Adapted from Zhang et. al [8]. Atmospheric particulate matter (PM) can be generated either directly from primary emissions (i.e., incomplete combustion can emit large amounts of PM directly) or secondarily from primary emissions of gaseous pollutants (sulfur dioxide, nitrogen oxides, and gaseous organic compounds) through chemical reactions with components in the atmosphere.*

In transportation of atmospheric aerosol, secondary organic aerosol (SOA) also accounts for a substantial proportion of the ambient organic aerosol (OA) [9, 10]. The chemical complexity of

SOA is poorly understood and contributes to the uncertainty of atmospheric aerosol studies [11, 12], due to dynamic formation and evolution reactions occurring in the atmosphere (**Figure 1.1**). A widely studied and likely most important mechanism of atmospheric SOA formation is the oxidation of volatile organic compounds (VOCs) to generate products of lower volatility followed by their partitioning into a condensed phase [11]. The gas phase oxidation of VOCs is initiated by atmospheric oxidants, like OH· radical, O_3 or nitrate radical (NO_3·), or through photolysis. The oxidants can participate in further reactions, as well. The initial attack of OH· or NO_3· can either abstract a hydrogen atom or add to a carbon-carbon double bond (C=C) [11]. The simplified reaction mechanism is described in **Figure 1.2.**

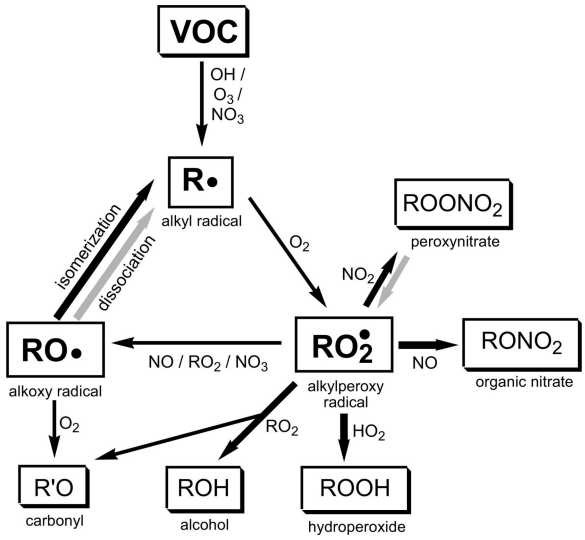


Figure 1.2 *Simplified mechanism for the atmospheric oxidation of a generic VOC. Thick black arrows denote reactions that can lead to a substantial decrease in volatility; gray arrows denote reactions that can lead to a substantial volatility increase [11].*

The spatio-temporal variability of $PM_{2.5}$ and PM_{10} concentrations in the atmosphere and its driving factors are hotspots in the study of air pollution problems [13, 14]. However, the process affecting air pollution is very complex and is not only directly affected by the source of pollutants, but also meteorological conditions [15] and various complex chemical reactions [16]. Therefore, it is essential to study air pollutants, especially particulate matter (PM) combined with gaseous pollutants and meteorological factors. Moreover, a strong non-linear relationship was found between PM concentration changes, meteorological conditions (e.g., temperature, wind speed, etc) , and gaseous pollutants (e.g., O_3, CO, NO_X, etc) [17]. The use of traditional multiple linear regression models for predicting PM mass concentration has significant limitations, such as, lack ability to capture PM mass concentration and driving factors [18, 19]. Therefore, it is imperative to investigate long-term air pollution study, spatio-temporal variations, and their driving factors in Germany.

In addition, the assumption that exposure is uniform within each region may have resulted in errors in the estimation of exposure, especially for pollutants with important local sources [20]. Thus, combination of the exposure study of air pollution and spatial variability is essential to investigate. However, the fixed monitoring of air quality by high-quality stationary measurements, as usually performed in official monitoring networks, has limitations when investigating the spatial variability of human exposure. For instance, the fixed stations are expensive and inefficiently distributed, resulting in undetected hotspots and poor air quality characteristics in the micro-environment, thus limiting the investigation of spatial variability in population pollution exposure [21]. Moreover, many studies have concentrated on urban air pollution in cities [22-27] rather than rural areas due to a few fixed stations installed in rural areas. A preliminary survey of air pollution exposure levels across Germany (meso-scale) was initially performed using fixed site data. Therefore, to further observe the spatial variability on the micro-scale, then survey of air pollution exposure levels on different micro-environments was performed in urban and small towns areas.

Currently, mobile monitoring has been widely applied for air pollution assessments to assess local air quality and air pollutant exposures [28, 29]. Mobile monitoring techniques can be applied not only to the monitoring of atmospheric pollutants and the study of the spatial distribution of atmospheric pollutants, but are also widely used for epidemiological studies, usually to assess

individual human exposure against air pollutants [26], and exposure levels under different traffic patterns [30]. This method can improve the spatial resolution of measurement data in the urban environment and collect the data such as the traffic-related air pollutants concentrations and their driving factors in micro-scale road sections [31]. Therefore, mobile measurements are favorably used in human exposure studies to quantify individual exposures and to demonstrate the importance of exposure differences in different micro-environments [32-34]. Taken together, analysing air pollution from different scales (country, city, and village) is urgently required to fully understand the characteristics of air pollution.

Nowadays, the air quality changes in the urban city and villages are not only related to the distribution of vehicle emissions, but also to the urban and villages development, street characteristics, street location, and land use types [35-39]. Several models have been previously developed to estimate the air pollutant concentration, such as remote sensing (RS) inversion [40], atmospheric dispersion models (DMs) [41], chemistry transport models (CTMs) [42], hybrid DM-CTM (DCTM) [42], land-use regression (LUR) [43], and a feature extraction based model from Google street view imagery (GSV) [44]. For instance, Hankey and Marshall (2015) used bicycle-based, mobile measurements during rush hour in Minneapolis, USA, to build LUR models for estimating particulate concentrations [45]. Apte et al. (2017) equipped Google Street View vehicles with a fast-response pollution measurement platform and repeatedly sampled every street in a 30 km^2 area of Oakland, CA, to obtain urban air pollution patterns [46]. Liang et al. (2017) used remote sensing images to obtain urban sky, trees, and architectural landscape factors to study the correlation between urban environment and air quality [47]. Therefore, the use of images to assess air pollution is potentially feasible and desirable. However, the previous models, such as Google Street View and remote sensing images [46, 47], have certain limitations (e.g., the detailed information may not be obtained in small scales). Nowadays, the street view images provide an excellent option to estimate air pollutants concentrations within urban street canyons and provide a human-centred view of the built environment.

1.2 Aims of the study

In this study, to further elaborate the spatio-temporal distribution of air pollutants, accurate estimation of air pollution concentrations, and assessing population exposure and health risks, we divided our study areas as meso-scale (country) and micro-scale (city and villages). For meso-scale, the spatio-temporal variations of $PM_{2.5}$ and PM_{10} were identified, and their relationships with gaseous pollutants and meteorological factors were quantified, and the population exposure to PM_{10} distribution in Germany were evaluated. For micro-scale, the spatio-temporal variability of air pollutants in urban street environments with a high spatial and temporal resolution were investigated, and a novel street-air pollution model for estimating spatial exposure to air pollutants in urban city was developed. In addition, given that fireworks events on New Year's Day can cause a dramatic rise in air pollutants for a short term period and give serious impact to human health, we investigated the contribution of fireworks to air pollution with selected pollutants, in particular PAHs, black carbon (BC) and (heavy) metals, and evaluated the health assessment of PAHs and metal elements during New Year’s Days periods in Augsburg, Germany. Following that, the application of mobile monitoring equipment in two small towns were also evaluated and analysed.

2 Methodology

2.1 Sampling campaign

2.1.1 Study areas

The studies were conducted in Germany for meso-scale (**Figure 2.1 a**), urban areas in Augsburg and two neighboring German-Czech border (Bayerisch Eisenstein (BE), Germany and Železná Ruda (ZR), Czech Republic) for micro-scale (**Figure 2.1 b, c**).

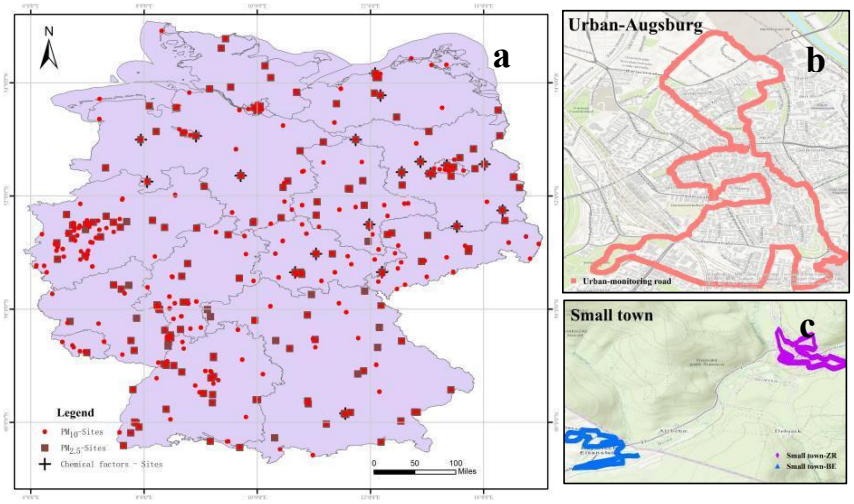


***Figure 2.1**: Sampling site and monitoring stations of air pollutants: a,"•" represents the fixed station of PM_{10}, "■" represents the fixed station of $PM_{2.5}$, "✛" represents the fixed station of gaseous pollutants (CO, SO_2, NO_2, and NO_X and O_3_ 8 h) in Germany [48]; b, urban mobile monitoring road [21]; and c, two small towns mobile monitoring road, the blue line represents Bayerisch Eisenstein, the purple line represents Železná Ruda [49].*

2.1.2 Fixed site monitoring data

The 24 h average data for $PM_{2.5}$, PM_{10}, CO, SO_2, NO_2, NO_X, and 8 h averages data for O_3 were obtained from the German Federal Environment Agency (https://www.umweltbundesamt.de/en/) and employed to analyse monthly and annual averages for each measurement location. The observations data were obtained from 412 fixed sites in Germany from 2008 to 2018 (**Figure 2.1 a**), then characterized the spatio-temporal variations of the air pollutants concentrations.

2.1.3 Mobile monitoring measurement

Mobile platforms were developed on a trolley, and air-monitoring devices were installed in a box attached to the trolley (**Figure 2.2**). The platform consisted of a trolley and a large aluminum box, which protected the instruments and positions the inlets at breathing height (approx. 1.5 m above ground). The detection frequency for PM_X and PNC was 1 Hz. Data on PM_X (PM_1, $PM_{2.5}$, PM_{10}) mass were recorded by a laser nephelometer - DustTrak DT (DRX 8532, TSI Inc, USA / Aerocet 531S, Met One Instruments, USA). The particle size distribution (PSD) was monitored using optical particle sizer (OPS) (3330, TSI, USA) and Grimm (Optical spectrometer 11-E, Grimm Aerosol Technik, DE), to convert $PM_{2.5}$, PM_1, and PM_{10} from number to mass concentrations. PNC, within the size range of 20-1000 nm, was measured by condensation particle counters (P-Trak 8525, TSI Inc, USA / testo DiSCmini, testo, DE). LDSA (lung deposited surface area), which enabled to measure the lung deposited surface area concentrations for both alveolar

and tracheobronchial regions of lungs [50], was measured using a handheld measuring instrument for nanoparticle counting (testo DiSCmini, testo, DE) with a time resolution of 1 s. BC was measured by aethalometers (microAethalometer, MA200, AethLabs, USA) with a time resolution of 10 s to avoid too much noise of the BC signal. The aethalometer measures the light attenuation through a filter tape at 5 wavelengths while the filter is continuously collecting the aerosol [51]. A common black carbon metric called "equivalent black carbon" (eBC) is assessed via the 880 nm channel [52, 53]. Because there is a lot of noise in other wavelengths, the research is mainly concentrating on BC. Besides the PM_X and BC measurements the platforms were equipped with a GPS (Garmin GPSMAP 64 s, recording resolution 1 s) to register measurement location and a POV camera (Olympus Tough TG Tracker, 5 s) to capture local and mobile pollution sources such as smoking chimneys, trucks or smokers.

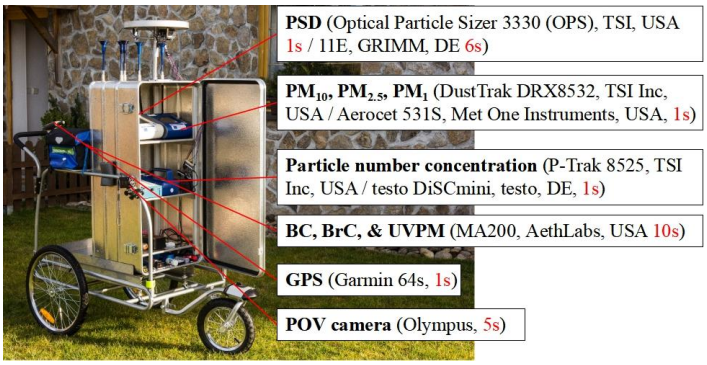


Figure 2.2: *Mobile monitoring platform. The platform consists of a trolley and a large aluminum box, which protects the instruments and positions the inlets at breathing height (approx. 1.5 m above ground). All monitoring instruments were installed in the stroller.*

In urban micro-scale, the route started from Augsburg University of Applied Sciences (UAS), passes through different types of land use to ensure that the selected path runs across different micro-environments and may be representative for the entire city. It was approximately 14 km long each walk (**Figure 2.1 b**), with an average walking time of approximately 3 h. 62 walks were performed, totaling about 248 h (835 km) of monitoring to assess the air pollution concentrations in different periods and different times of day. The routes in BE and ZR were approximately 5 km and 4 km, respectively (**Figure 2.1 c**). The average walking time for the both routes was approximately 1 h. The routes were mostly distributed in residential areas with few traffic. The parallel walks were conducted at both routes to compare their air pollution level every 2-3 h from 5 am to 10 pm. A total of 20 and 21 walks data were successfully collected on 4 days during November 22 to 25, 2018 in BE and ZR, respectively.

2.2 Meteorological monitoring data

In the meso-scale study, the daily meteorological data were collected from 222 fixed sites in Germany from January 2008 to December 2018 by the German Weather Service (Deutscher Wetterdienst) and used to analyse their correlation to air pollution. The meteorological observations include the form of precipitation (only rain, only snow, rain and snow, FP), daily precipitation height (PH), daily average wind speed (WS), daily sunshine duration (SD), daily value snow depth (SnD), daily average of cloud coverage (C), daily average of vapor pressure (VP), daily mean air pressure (AP), daily average relative humidity (RH), and daily average temperature (T).

In micro-scale (Augsburg, BE, and ZR), the meteorological parameters (T, RH, WS, and WD (wind direction)) were measured by a fixed station in Augsburg, located in the urban background of the UAS (the starting point of the walks), and a meteorological station, set up between the two small cities.

2.3 Chemical analysis of organic species

The chemical compounds were analysed by using subsamples of the original quartz fibre filter (QFF) utilizing an Derivatisation Thermal Desorption Gas Chromatography Time-of-Flight Mass Spectrometry (DTD-GC-TOF-MS) method [54]. A schematic representation of the method is shown in **Figure 2.3.** Briefly, an aliquot is punched out from filter samples spiked with internal standard mixtures containing isotope-labeled compounds and placed in a clean and deactivated glass-liner for analysis. The liner was immediately inserted into the GC-injector (Optic 3, GL Sciences, Eindhoven, The Netherlands). Next, the thermal extraction *in situ* derivatisation process of organic species was done in the GC-injector at a temperature of 300 °C, during which the carrier gas was enriched and the temperature in GC oven was kept at 70 °C. After this process, the temperature was increased when the GC system started. The temperature was first heated up to 130 °C, at a rapid 80 °C/min and then increased to 330 °C, at 8 °C, min^{-1} and held for 30 min. The capillary column used was the BPX5 (25 m, 0.22 mm ID, 0.25 µm film, SGE, Australia). The flow rate of column was 4 ml/min and 0.7 ml/min during and after desorption, respectively. The TOF-MS record masses ranged from 35- 500 m/z with an acquisition frequency of 25/s.

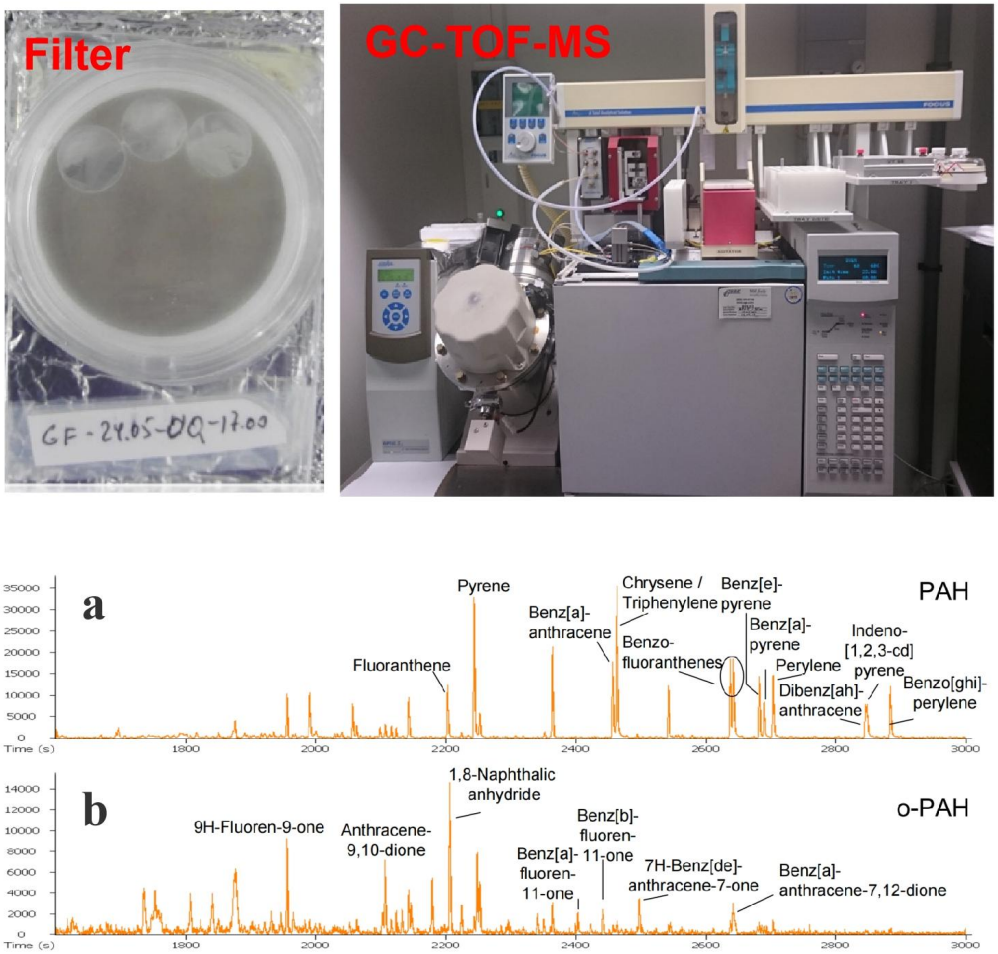


Figure 2.3: *Analysis procedures and in situ derivatisation thermal desorption unit (figure at the top left side indicted the filter, while the top right side indicated the instrument of GC-TOF-MS). (a) polycyclic aromatic hydrocarbons (PAH) (m/z 178+202+228+252+276+278), (b) oxidized PAH (o-PAH) (m/z 126+158+180+196+230+258). This figure was adapted from Orasche et al. (2011) [54].*

In this study, the PAHs, including Ret, Flu, Pyr, B[a]A, Chr, B[b,j,k]F, B[a]P, I[cd]P, D[ah]A, B[ghi]P, and Cor were analysed (for abbreviations see **Table 2.1**). In addition, the concentrations of two oxidized aromatic compounds, including 1,8-Naphthalic anhydride (NA) and 4-H-Cyclopenta[def]phenanthren-4-one (CPO), and 6 Hopanes (17ß(H),21a(H)-30-Norhopane (29aß), 17ß(H),21a(H)-30-Norhopane (29ßa), 17a(H),21ß(H)-Hopane (30aß), 17ß(H),21a(H)-Hopane (30ßa), 22S-17a(H),21ß(H)-Homohopane (31aßS), and 22R-17a(H),21ß(H)-Homohopane (31aßR)), were also analysed using their internal standards (**Table 2.1**). The structures of some predominantly PAHs and multiple ion chromatograms reflecting a sample collected at the aerosol characterisation site at the UAS (urban background) were shown in **Figure 2.3 and Figure 2.4.** Subsequently, 27 elements (Al, As, B, Ba, Be, Ca, Cd, Co, Cr, Cu, Fe, K, Li, Mg, Mo, Na, Ni, P, Pb, S, Sb, Se, Sn, Sr, Ti, V, and Zn) were analysed using inductively coupled plasma-mass spectrometry (ICP-MS), with rhodium and lutetium used as internal standards [55]. The physicochemical and toxicological properties of PAH were shown in **Table 2.2**.

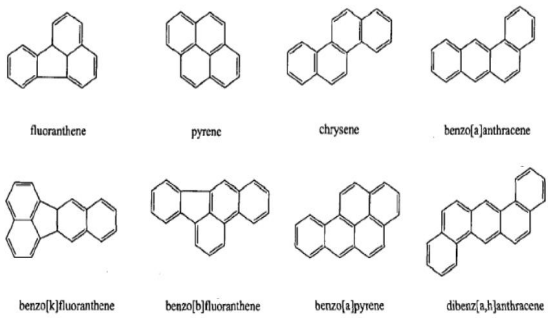


Figure 2.4: *Molecular structure of eight representative PAHs.*

Table 2.1: *Targeted analytes and the analytical parameters used for calculating reported concentrations.*

Analyte	Internal Standard	m/z used for quantification
Retene (Ret)	Phenanthrene-D10	219±500ppm
Fluoranthene (Flu)	Fluoranthene-D10	202±500ppm
Pyrene (Pyr)	Pyrene-D10	202±500ppm
Benzo[a]anthrancene (B[a]A)	Benzo[a]anthracene-D12	228±500ppm
Chrysene (Chr)	Chrysene-D12	228±500ppm
sum Benzo[b, j, k]-fluoranthene (B[b,j,k]F)	Benzo[b]fluoranthene-D12	252±500ppm
Benzo[a]pyrene (B[a]P)	Benzo[a]pyrene-D12	252±500ppm
Indeno[1,2,3-cd]pyrene (I[cd]P)	Indeno[1,2,3-cd]pyrene-D12	276±500ppm
Dibenz[a,h]anthracene (D[ah]A)	Dibenz[a,h]anthracene-D14	278±500ppm
Benzo[ghi]perylene (B[ghi]P)	Benzo[ghi]perylene-D12	276±500ppm
Coronene (Cor)	Coronene-D12	300±500ppm
Cyclopenta[def]phenanthrenone (CPO)	Benzo[a]anthracene-D12	204±500ppm
1,8-Naphthalic anhydride (NA)	9,10-Anthracenedione-D8	126±500ppm
17α(H)21β(H)-30-Norhopane (29αβ)	n-Tetracosane-D50	191±500ppm
17β(H)21α(H)-30-Norhopane (29βα)	n-Tetracosane-D50	191±500ppm
17α(H)21β(H)-Hopane (30αβ)	n-Tetracosane-D50	191±500ppm
17β(H)-21α(H)-Hopane (30βα)	n-Tetracosane-D50	191±500ppm
22S-17α(H)21β(H)-Homohopane (31αβS)	n-Tetracosane-D50	191±500ppm
22R-17α(H)21β(H)-Homohopane (31αβR)	n-Tetracosane-D50	191±500ppm

Table 2.2: *The parameters of physical-chemical and toxicological properties for PAHs .*

PAH	Ring number	IARC class	TEF	MEF
Ret	3	/	/	/
Flu	3	3	0.001	/
Pyr	4	3	0.001	/
B[a]A	4	2B	0.1	0.082
Chr	4	2B	0.01	0.017
B[b]F	4	2B	0.1	0.25
B[k]F	4	2B	0.1	0.11
B[a]P	4	1	1	1
I[cd]P	5	2B	0.1	0.31
D[ah]A	5	3	1	0.29
B[ghi]P	6	2A	0.01	0.19
Cor	7	/	/	/

a Agents Classified by the IARC Monographs, Volumes 1e100 [56]: 1, carcinogenic to humans; 2A, probably carcinogenic to humans; 2B, possibly carcinogenic to humans; 3, not classifiable as to its carcinogenicity to humans. TEF, (toxic equivalency factor) MEF (mutagenic equivalency factor) [57, 58].

2.4 Spatio-temporal analysis

In meso-scale, the ordinary Kriging were used to simulate the spatial distributions of the average atmospheric pollutant concentrations [59]. Then Moran's I was used for spatial autocorrelation to identify the correlation of atmospheric pollutant profiles [60, 61]. Positive and significant Moran's I values indicate that nearby areas have similar spatial patterns, whereas negative values indicate the contrary. If the Moran's I is zero, the values are arranged randomly. Following that, the PM_{10} spatial distribution analysis based on the two-dimensional graph theory [62] clustering method combines the spatial analysis of ArcGIS with the tree algorithm of graph theory. In the micro-scale of the urban area, three micro-environments (park, central business district (CBD), and traffic area) were also chosen to quantify exposure and inhaled dose rate of air pollutants. In the micro-scale of two small towns, the pollutant exposure was compared to analyse the differences air pollutants between two neighboring villages, and to identify the pollution hotspots.

Following that, the rescaled range (R/S) analysis was applied to investigate the annual variability of atmospheric pollutant concentration [63]. Then fractal dimension (D) was used to analyse the internal regularity of atmospheric complex phenomena in meso-scale [64]. For the micro-scale of the urban area, the data on air pollutants were divided into three time periods: the entire period, the non-heating period (May-October), and heating period (November-April$^{2nd\ year}$) with different times of the day (morning, afternoon, and evening). For the micro-scale of the small town, the data on air pollutants were analysed by using different walks of the day.

2.5 The prediction model of air pollutants in urban micro-scale

2.5.1 Street view images (SVI) model

To further quantify the surface type configuration that pedestrians experience in the street canyon, the deep learning method was employed [65], providing a unique description of urban form and composition as experienced by a pedestrian on the street, and therefore more relevant to the human experience of cities than planar bird's-eye views from satellite data. In this study, the images were recorded by the camera in daylight, and the street views were mainly divided into five types: buildings, streets (including parked cars), vegetation, cars (cars in traffic only), and sky.

2.5.2 Evaluation of model accuracy

Challenges in regression-based SVI models involve the difficulty of capturing nonlinear relationships and complex interactions. Random Forest (RF) can counteract and conquer these problems [66, 67]. RF was applied to estimate urban air pollutant concentrations for the SVI model. We used the standard adjustment from the package *scikit-learn*. In this study, bivariate correlation analysis was utilized to obtain the targeted factors required for modeling, and the concentrations of eUVPM, eBC, and eBrC in the training set and the corresponding targeted factors were employed as the input data for the RF regression method. The accuracy evaluation of the model can express the fitting effect and error of the model. In this study, we adopted the cross-validation (CV) method, which used 70 % of the monitoring dataset as the training set, and the ten-fold CV method to estimate the accuracy of the model [68]. This method can equalize the deviation and variance of the model. The simulation accuracy of the model is expressed by evaluating the closeness between the simulation result of the verification set and the actual observed value. The evaluation indicators used in this study involve the correlation coefficient (R), root mean square error (RMSE), mean absolute error (MAE), and index of agreement (IA). Here, R represents the model, the fit effect of RMSE and MAE represents the deviation between the predicted value and the actual value, and IA represents the agreement between the predicted value and the actual value.

2.6 Evaluation of the PM_{10} effect on human health in meso-scale

2.6.1 Estimation of the population exposure to PM_{10}

The population was an essential factor for assessing the population-weighted exposure level (PWEL) [69]. The population dataset were analysed, which collected from the Federal Statistical Office of Germany [70]. However, the spatial distribution of residents in space were not comparable with the spatial distribution of atmospheric pollution [71]. Given grid (1.0 km•1.0 km), *i*, the population-weighted exposure was quantified as following equation:

$$\mathrm{PWEL} = \sum (P_i \times C_i) / \sum P_i \quad (1),$$

where P_i is the population in the grid cell, *i*, and C_i is its average PM_{10} concentration in the grid cell.

In our study, 50 μg/m^3 was used as the pollution concentration. PM_{10} limit value was corresponded to the daily average concentration of PM_{10}. According with this value, the number of exposure days exceeding the standard during the research period were calculated.

2.6.2 Spatial distribution of PM_{10} exposure

Population PM_{10} exposure level was comparable with the duration of population exposure per unit area exposed to severe PM_{10} pollution. The PM_{10} exposure level was calculated by the following equations:

$$N_{ij}^{T} = \sum_{t=t_1}^{t_2} 1(C_{\mathrm{ijt}} \geq STD) \quad (2), \quad \mathrm{E}I_{ij} = N_{ij}^{T} \frac{P_{ij}}{A_{ij}} \quad (3),$$

where A_{ij} is the area of the (i,j)th grid cell (1.0 km•1.0 km), P_{ij} is the population of the (i,j)th grid cell, and N_{ij}^{T} is the accumulated pollution days of the (i,j)th grid cell. EI_{ij} is the pollution exposure level of the (i,j)th grid cell at time T, in day·person/km^2. STD = 50 μg/m^3 for the EU standard. As shown in the equation above, the level of pollution exposure was associated with the accumulated days of pollution and population density.

2.7 Positive matrix factorization (PMF) analysis

The EPA-PMF 5.0.14 (USA EPA, https://www.epa.gov/air-research/positive-matrix-factorization-model-environmental-data-analyses) was used to estimate the major source contributions to air pollutants concentrations (i.e., PAHs, eBC, and metal elements) [72]. In addition to the concentrations of the PAHs, 15 metal elements (i.e. Al, B, Ba, Ca, Cr, Cu, Fe, K, Mg, Na, Pb, S, Sr, Ti, and Zn), eBC, and $PM_{2.5}$ (total variable), the concentration of some selected organic substances (NA and CPO, and 6 Hopanes (29aß, 29ßa, 30aß, 30ßa, 31aßS, and 31aßR)) were included for the PMF analysis, which also could be considered as marker substances for the most significant sources of PAHs and BC.

2.8 Health assessment of PAHs and metal elements

An absorption factor of chemicals has been developed by the US EPA to determine the number of a substance that was actually inhaled into the body, considering the route of exposure [73]. However, many studies have been accomplished for soil contamination [74-76], with very limited studies have performed a risk assessment of the inhaled potentially toxic elements (PTEs) of $PM_{2.5}$ [77]. Therefore, the absorption factors of the $PM_{2.5}$-PTEs was used to estimate the non- and cancer risk induced by toxic metals and PAHs exposure [78], which were recently established by the US EPA for ingestion and inhalation of PM [73].

For PAHs, the carcinogenic risk of a PAH mixture was frequently quantified by its B[a]P equivalent concentration ($B[a]P_{TEQ}$) [79]. The toxicity of different PAHs in $PM_{2.5}$ were normalized and quantified by the equivalent mass concentration based on B[a]P and the value of toxic equivalency factors (TEFs) (**Table 2.2**) [80]. Similarly, to replace the TEF with MEF (mutagenic equivalency factor), the mutagenicity related to B[a]P ($B[a]P_{MEQ}$) was quantified as well. The $B[a]P_{TEQ}$ and $B[a]P_{MEQ}$ of PAHs were quantified by following equations (4-5):

$$\Sigma B[a]P_{TEQ} = \sum_{i=1}^{n} C_i \times TEF_i \quad (4), \quad \Sigma B[a]P_{MEQ} = \sum_{i=1}^{n} C_i \times MEF_i \quad (5),$$

where C_i=concentration of PAH analogue i; TEF_i=the toxic equivalency factors (TEFs) of PAH analogue i; MEF_i=the mutagenic equivalency factors (MEFs) of PAH analogue i. The toxicity assessment of PAHs was determined by benzo[a]pyrene, an equivalent for carcinogenicity ($\Sigma B[a]P_{TEF}$) and mutagenicity ($\Sigma B[a]P_{MEF}$).

Daily inhalation exposure level (E) for each population group was quantified by following equation (6):

$$\mathrm{E} = \sum_{i=1}^{n} B[a]P_{TEQi} \times IR_i \times T_i \quad (6)$$

where T_i= daily exposure time span in the i^{th} area (for all groups of the urban area on one day: they spend the whole day in the urban area, thus n=1, i=1 refers to the urban area, T_1=1); $B[a]P_{TEQi}$ = B[a]P equivalent concentration of PAHs in the i^{th} area (ng/m^3) (for all groups of urban area: n=1, i=1 refers to the urban area); IR = inhalation rate (m^3/day) (5.36, 11.41, and 15.73 m^3/day for infants, children, and adults, respectively) [78, 81].

The risk assessment of metal elements involves carcinogenic and non-carcinogenic risks. Of these monitoring metal elements, As, Ni, Cd and Cr were classified as carcinogenic substances based on International Agency for Research on Cancer (IARC) [82], and their health risk assessment was expressed as lifetime average daily dose (LADD), while non-carcinogenic substances are expressed as average daily dose (ADD). The equations were expressed as follows:

$$\mathrm{ADD} = \mathrm{C} \cdot \frac{\mathrm{IR} \cdot \mathrm{EF} \cdot \mathrm{ED}}{\mathrm{BW} \cdot \mathrm{AT}} \quad (7); \quad \mathrm{LADD} = \frac{\mathrm{C_i} \times \mathrm{EF}}{\mathrm{AT}} \times \left(\frac{\mathrm{IR_{child}} \times \mathrm{ED_{child}}}{\mathrm{BW_{child}}} + \frac{\mathrm{IR_{adult}} \times \mathrm{ED_{adult}}}{\mathrm{BW_{adult}}} \right) \quad (8);$$

$$\mathrm{ILCR} = \mathrm{q} \times \mathrm{LADD} \quad (9); \quad \mathrm{HQ} = \frac{\mathrm{ADD}}{\mathrm{RfD}} \quad (10)$$

where LADD = Lifetime Average Daily Doses; Ci = $\Sigma B[a]P_{TEQ}$ / Metal concentration (mg/m^3); EF = the exposure frequency (day/year); ED = exposure duration (year); BW = body weight (kg); AT = average lifespan for carcinogens (day). ILCR = the incremental cancer risk of the inhalation exposure (dimensionless); q = the cancer slope factor for B[a]P inhalation exposure a lognormal distribution with a geometric mean of 3.14 $(mg/kg/day)^{-1}$ and a geometric standard deviation of 1.80] [83]. HQ refers to the risk factor and the higher the value, the higher the risk. RfD (reference dose) was the maximum amount of pollutant per unit body weight per day that will not cause adverse reactions in humans (mg/(kg d)). The Health risks assessment was age–specific. In urban areas, the citizens were classified into three population groups according to the age: infants (< 1 year), children (2-18 years), and adult (19-70 years), as shown in the **Table 2.3** [78].

Table 2.3: *Risk parameters for different age groups used for Augsburg.*

Parameter	Infants	Children	Adults	Units
Ci	/	/	/	mg/m^3
IR	5.36	11.41	15.73	m^3/d
EF	350	350	350	d/a
ED	0-1	0-17	0-52	a
AT	365	6205	25550	d
BW	9.1	29.7	71.05	kg
q	3.14	3.14	3.14	/

3 Results and Discussion

3.1 The current status of atmospheric pollutants in Germany (meso-scale)

In this section, the results of the investigations of meso-scale variability and trends of air pollutants were discussed. For this purpose, measurement data of particulate matter ($PM_{2.5}$, PM_{10}), gaseous pollutants (CO, NO_X, NO_2, SO_2, and O_3), and meteorological factors from 412 fixed monitoring stations in Germany were analysed. The observation period covered the years 2008 to 2018. The aims of the analysis were 1) to characterise the spatio-temporal variations of $PM_{2.5}$ and PM_{10}, 2) to quantify the correlation of gaseous pollutants and meteorological factors on $PM_{2.5}$ and PM_{10} concentrations, and 3) to investigate the population exposure to the distribution of PM_{10} in Germany.

3.1.1 Spatio-temporal variability of air pollutants in Germany

3.1.1.1 Spatial variability of atmospheric pollutant

The distribution of $PM_{2.5}$ and PM_{10} was analysed in rural, suburban, and urban areas of Germany to investigate their spatial variabilities in different types of areas (**Figure 3.1**). As shown in **Figure 3.1**, generally, as the economic centre, Berlin and Brandenburg were commonly found had severe air pollution level.

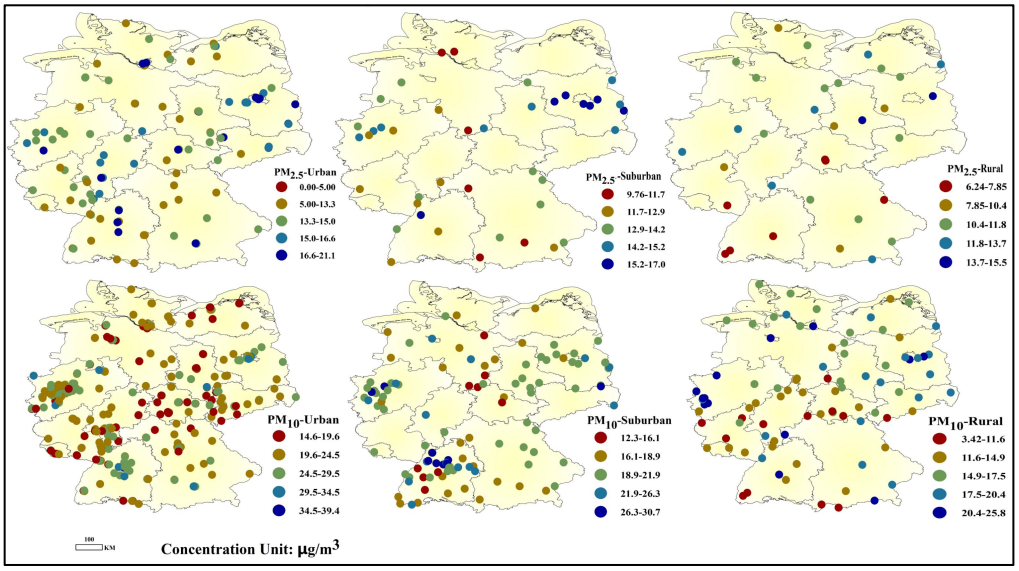


Figure 3.1: *The distribution of $PM_{2.5}$ and PM_{10} in rural, suburban, and urban areas of Germany.*

Then, in order to represent the overall spatial variabilities of air pollutant concentrations ($PM_{2.5}$, PM_{10}, CO, SO_2, O_3, NO_2, and NO_X) in Germany, the daily average mass concentrations of air pollutants at the fixed monitoring stations during eleven years (2008-2018) were investigated using the coefficient of variation (COV). As shown in **Figure 3.2**, SO_2 had the largest spatial variation account of 42.7 %, followed by 12.1 % of $PM_{2.5}$, 10.0 % of PM_{10}, 8.7 % of CO, 7.1 % of NO_2, 5.6 % of NO_X and 2 % of O_3 . The largest spatial variation was found in Berlin for CO account of 20.1 %, Lower Saxony for NO_2 account of 13 %, Mecklenburg-Western Pomerania for NO_X account of 24.3 %, Bavaria for O_3 account of 4.88 %, Bremen for $PM_{2.5}$ account of 19 % and Thuringia for PM_{10} account of 16.5 %. However, the fixed stations were undistributed in some areas of Germany, affecting the spatial distribution of air pollutant concentrations. Therefore, the Kriging interpolation model was chosen to provide the continuous spatial distribution for each factor based on our daily dataset. As a result, the spatial trends and hot spots of gaseous pollutants can be identified in various German regions (**Figure 3.2**).

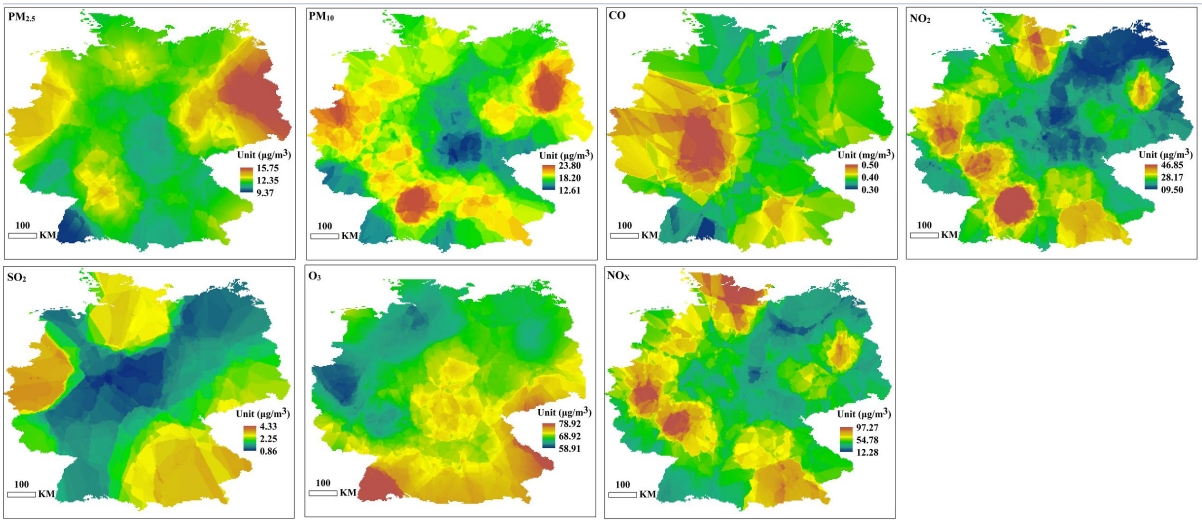


Figure 3.2: *Daily average mass concentrations of seven air pollutants ($PM_{2.5}$, PM_{10}, CO, SO_2, O_3, NO_X, and NO_2) maps obtained by Ordinary Kriging from 2008-2018.*

3.1.1.2 Temporal variability of atmospheric pollutants

The temporal variability of the atmospheric pollutants were analysed using the time series domain rescaling analysis method. The Hurst-index (H) and fractal dimension (D) of $PM_{2.5}$ and PM_{10} in different multi-time scales and different areas were used in this study. When the H value was higher than 0.5, it indicated that the time series of atmospheric pollutants were persistence as a trajectory of the fractional Brownian motion. As a result, the increasing and reducing concentration trend in the past were comparable with the future trend of atmospheric pollution, which can be maintained to some extents. It also implied that the air pollutant statistics showed a certain degree of non-Gaussian (non-random) distribution. These phenomena were further confirmed and validated by the long-term trends of $PM_{2.5}$ and PM_{10} (**Figure 3.3 a**), indicating the stability of air pollutants during the observed period. In addition, the exposure level of air pollutants (15 μg/m^3 for $PM_{2.5}$ and 20 μg/m^3 for PM_{10}) in Germany has been reached the EU standard concentration for $PM_{2.5}$ (25 μg/m^3) and PM_{10} (40 μg/m^3) during 2008 to 2018 (**Figure 3.3 b**).

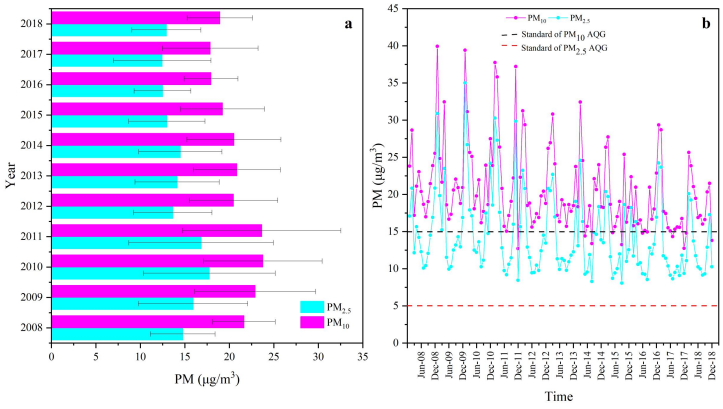


Figure 3.3: *Long-term change trends of $PM_{2.5}$ and PM_{10} from 2008 to 2018 in Germany.(a, The estimation of average $PM_{2.5}$ and PM_{10}; b, The interannual variability of $PM_{2.5}$ and PM_{10}, AQG (air quality guidelines).*

In addition, based on the segmentation analysis **(Figure 3.4)**, the largest of $|H_{i+1} - H_i|$ was found in 2009 for PM_{10} and $PM_{2.5}$. Following that, the high variability of atmospheric pollutants were found in the rural areas (ΔH=0.52 for $PM_{2.5}$; ΔH=0.41 for PM_{10}). Multiple factors, such as building completed area, thermal power generation, gross industrial output value and wind speed, may influence the air pollution trends [84]. In the previous study, the average urban traffic $PM_{2.5}$ concentrations exceeded the WHO standards in the vast majority of European member states in 2009, and the source contribution to ambient $PM_{2.5}$ in Germany was high based the EU Clean Air Policy Package [85]. The main source contribution to rural $PM_{2.5}$ comes from sulfates, residential heating, nitrates, industry, re-suspended dust, sea salt, and long-range dust transport [86]. Moreover, the industrial emissions (SO_2 and NO_X) and traffic emissions (NO_X) mainly interacted with NH_3, which mainly came from rural agriculture [87]. In addition, the house heating in the rural area also gave contribution to the $PM_{2.5}$ concentration [49]. Therefore, both factors may contribute to the high concentration of $PM_{2.5}$ in the rural area. Simultaneously, the high variability of air pollution was also found in 2016 and 2017. It was worth noting that $PM_{2.5}$ variation across many years was found higher in the urban industrial, which was not observed in PM_{10}, indicating that $PM_{2.5}$ and $PM_{2.5\text{-}10}$ might have different source contributions [88].

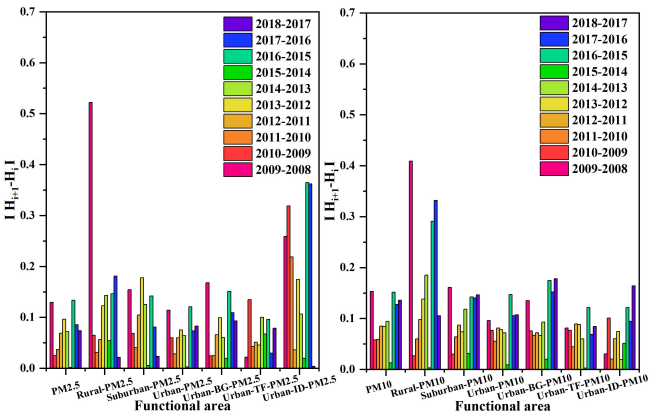


***Figure 3.4**: Segmental analysis of $PM_{2.5}$ and PM_{10} in different functional areas from 2008 to 2018 in Germany (BG, background; TF, traffic; ID, industry).*

3.1.1.3 Spatial autocorrelation of PM_{10} concentration

The Global Moran's I was adopted to observe the spatio-temporal trends of the PM_{10} concentrations in Germany, identifying the spatial autocorrelation of the PM_{10} concentrations. As shown in **Table 3.1**, a significant positive spatial autocorrelation of PM_{10} concentrations was occurred in Germany due to the Moran's I exceeded 0 for monthly average values and ranged from 0.228 to 0.443. When the Moran's I statistically resulted in a random or a nearly normal distribution, the significance test can be changed into a Z value, revealing the statistic normal distribution. At the 5 % significance level, when the Z value was greater than 1.96 or less than -1.96, the spatially significant positive or negative correlation between the observation sites was identified, however, when the Z value ranged from -1.96 to 1.96, the spatial correlation was not significant. When Z value was higher than 2.58, the highly significant correlation was identified [89]. Our result showed that the annual average value of Z(I) was 9.65 (> 2.58), suggesting a significant positive spatial autocorrelation of the PM_{10} concentrations was found in the cities of Germany (High-High or Low-Low agglomeration).

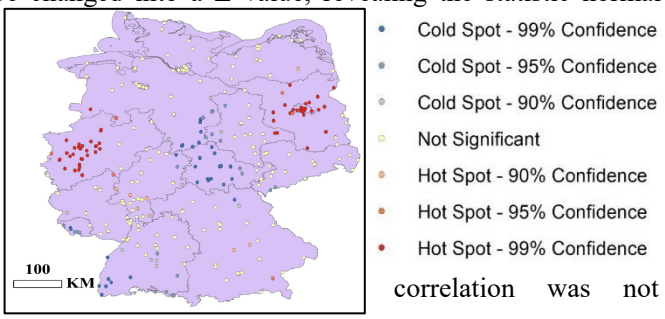


***Figure 3.5:** Spatial agglomeration of annual PM_{10} concentrations in the monitoring sites in Germany.*

In our study, ArcGIS10.2 was used to quantify the spatial autocorrelation model, identifying hot spots, cold spots, and no significant spots area. A confidence level of 99 %, 95 %, and 90 % statistical significance indicated confidence interval of +3 to –3 , +2 to –2, and +1 to -1 elements, respectively. A confidence level was not highly significant when a confidence interval of 0 clustering. As shown in **Figure 3.5**, the hot spots areas were mainly found in North Rhine-Westphalia, Brandenburg, and Berlin based on annual agglomerations analysis. Therefore, air pollution control measures regulation should be considered and developed in these areas. In addition, the cold spots areas were mainly occurred in Thuringia and in the southwest of Baden-Wuerttemberg. While no significant spots areas were occurred in Schleswig-Holstein, Mecklenburg-Vorpommern, Sachsen, and Bavaria.

Table 3.1: *Spatial autocorrelation index of PM_{10} concentrations in Germany.*

Monthly	**Jan.**	**Feb.**	**Mar.**	**Apr.**	**May**	**Jun.**
Moran's I-PM_{10}	0.347	0.443	0.228	0.345	0.342	0.286
P	0.001	0.001	0.001	0.001	0.001	0.001
Z	10.456	13.478	7.181	10.637	10.652	8.747
Monthly	**Jul.**	**Aug.**	**Sep.**	**Oct.**	**Nov.**	**Dec.**
Moran's I-PM_{10}	0.298	0.244	0.369	0.248	0.282	0.296
P	0.001	0.001	0.001	0.001	0.001	0.001
Z	9.386	7.63	11.545	7.864	8.843	9.325

3.1.1.4 Two-dimension graphics cluster in elevated pollution districts

In the following federal states of Germany, Bavaria, North Rhine-Westphalia, Saxony-Anhalt, Brandenburg, and Berlin, the PM_{10} levels were significantly higher than in other federal states. Therefore, only these states were investigated in more detail based on the theory of two-dimension graphics cluster [62].

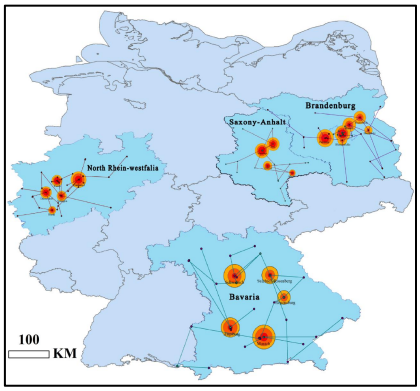


Figure 3.6: *Two-dimension graphics cluster in districts with higher pollution, based on the data of PM_{10} in Germany.*

As shown in **Figure 3.6**, the significance of the fixed sites connections indicated the spatial adjacency and intrinsic similarity between the various fixed monitoring sites. The geographic location information was expressed as spatial adjacency, while similarity of pollution concentrations was expressed as intrinsic similarity. As a result, a relatively large-scale comprehensive consolidation project can be built upon the determination of PM_{10} concentrations and management plans. Meanwhile, combining the GIS spatial method, the mathematical clustering method, the graph theory tree algorithm, and the regional division technology, four functional pollution areas in Germany were obtained (**Figure 3.6**). Briefly, the first group was included the cities of Burg, Bitterfeld, Bernburg, and Magdeburg constituted the Saxony-Anhalt pollution region. The second group was included the cities of Berlin, Potsdam, Hasenholz, Eberswalde, Bernau, and Blankenfelde constituted the Berlin-Brandenburg pollution region. The third group was included the cities of Essen, Hürth, Düsseldorf, Dortmund, and Solingen constituted the North Rhine-Westphalia pollution region. And the fourth group was included the cities of Augsburg, Regensburg, Munich, and Sulzbach-Rosenberg constituted the Bavaria pollution region.

3.1.2 Spatialisation of demographic data and estimation of the population exposure to PM_{10}

According to demographic data and district-county-level boundary data, the population density of the county level in Germany were relatively low, only a few counties had high population density, such as Berlin (**Figure 3.7 a**). To further observe their spatial distribution, the Moran's I index was adopted to analyse the spatial correlation of population distribution across the county. As shown in **Figure 3.7 b**, the Moran's I value was 0.555 for population density, indicating that the area with high population density had a certain aggregation effect.

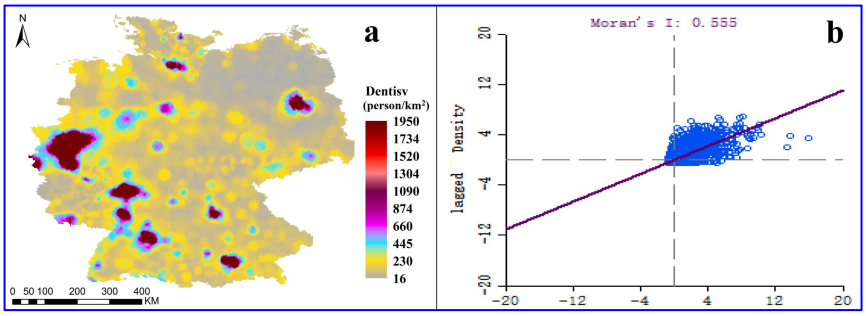


Figure 3.7: *Population density in Germany and the corresponding Moran's I scatter plots (data obtained from the Federal Statistical Office of Germany in 2016 and population density is expressed as inhabitants per km squared) [85].*

Then, to estimate the population exposure, the population-weighted exposure level to PM_{10} (PWEL) and the average of the PM_{10} concentrations (MEAN) in 2017 were further analysed. As shown in **Figure 3.8**, the similar trend of PWEL and PM_{10} average concentration was found in all Germany areas. Meanwhile, to show their monthly trend characteristics, the monthly PWEL and PM_{10} average concentration were also analysed. As shown in **Figure 3.8 b**, the concentrations of PM_{10} were found higher in January (29.14 $\mu g/m^3$) and February (28.93 $\mu g/m^3$) than other months, indicating adverse exposure to PM_{10} was highly exposed to humans in winter. Certainly, it was worth mentioning that the population exposures to PM_{10} in other months were lower than 20 $\mu g/m^3$, suggesting a high ambient air quality in those corresponding months.

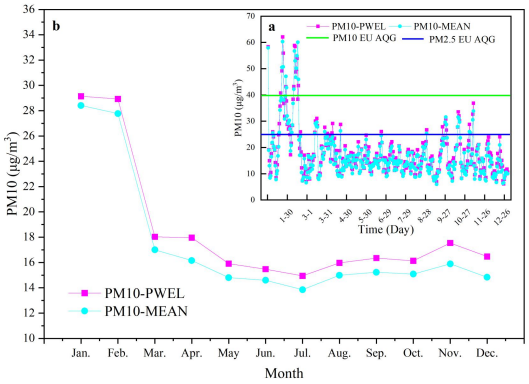


Figure 3.8*: The daily (a) and monthly (b) variations in the total PWEL and MEAN concentration in 2017.*

Base on the daily exposure to PM_{10}, the extremely high exposure was distributed in the south and east of Germany, such as Bavaria, Brandenburg, and Berlin, reached 17 exposure maxima days in 2017. Following that, as shown in **Figure 3.9,** the accumulative distribution of population exposure to PM_{10} was comparable to the accumulative distribution of exposure time. As a result, the highest contaminated areas of PM_{10} concentration were distributed in the following cities, such as Berlin, Dusseldorf, and Munich, but

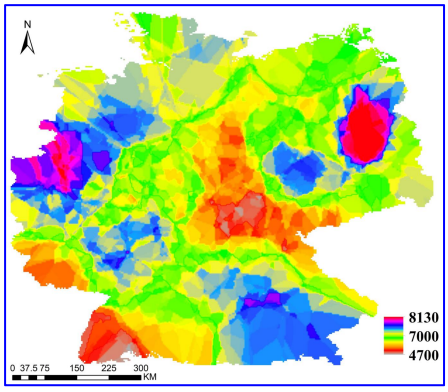


Figure 3.9: *Accumulation population exposure to PM_{10} concentrations (Units: $\mu g/m^3$).*

were not entirely within the city limits. Therefore, based on the population distribution by exposure level in those cities, the majority of people was living in polluted areas, and the exposure level was greatly changing from north to south, and each sub-district retained similar exposure to neighbouring sub-districts.

3.1.3 Correlations between air pollutants

3.1.3.1 Correlations of gaseous pollutants with $PM_{2.5}$ and PM_{10} concentrations

In this section, the correlations of five gaseous pollutants (CO, O_3, SO_2, NO_2, and NO_X) with $PM_{2.5}$ and PM_{10}. were analysed by the back propagation (BP) neural network network algorithm. As shown in **Figure 3.10**, the greater correlations were found between CO *vs.* $PM_{2.5}$ and CO *vs.* PM_{10}, and SO_2 *vs.* $PM_{2.5}$ and SO_2 *vs.* PM_{10}. The combustion of fuel, urban automobile exhaust, and tail gas discharged from industrial plants were found as major contributors, which comparable with the current situation of many industrial and transportation vehicles in Germany. Following that, the NO_X and O_3 had mild correlations with $PM_{2.5}$ and PM_{10}. The high-temperature environment in which the automobile's internal combustion engine operating causes a huge production of NO_X released into the air, though the nitrogen content was less in the car's fuel [90, 91]. Ozone in the atmosphere was mainly derived from the photochemical reaction of nitrogen oxides and volatile organic compounds (VOC) and was the major compound of photochemical smog [92]. The main sources of NO_X and VOC may come from automotive exhaust and chemical production [93]. This phenomenon was comparable with the high ownership of German cars, thus the emission of automobile exhausts and the ozone generated by photochemical reactions was inevitably high, damaging to air quality.

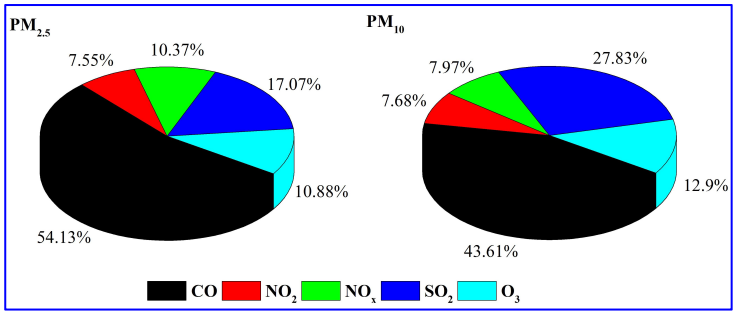


Figure 3.10: *The normalized coefficients of gaseous pollutants with $PM_{2.5}$ and PM_{10}.*

Table 3.2*: The correlations between gaseous pollutants and the $PM_{2.5}$ and PM_{10} (**, $p<0.01$, *, $p<0.05$).*

PM	CO	NO_2	NO_X	O_3	SO_2
$PM_{2.5}$	0.613**	0.417**	0.334**	-0.214**	0.104*
PM_{10}	0.516**	0.368**	0.333**	-0.142**	0.196**

Then, the Spearman analysis was performed to further analyse the positive and negative relationship between $PM_{2.5}$, PM_{10} and gaseous pollutants. As shown in **Table 3.2,** $PM_{2.5}$ and PM_{10} were positively correlated with CO, NO_2, NO_X, and SO_2, but negatively correlated with O_3, which was not comparable with the previous study due to seasonal time [94]. Briefly, these phenomena may be influenced by the different photochemical reactions in different periods [95]. That is, a negative correlation was found in the winter, while positive correlation was found in the summer.

3.1.3.2 Correlation of meteorological factors with $PM_{2.5}$ and PM_{10} concentrations

The BP neural network was also used to analyse the correlation of various meteorological factors with $PM_{2.5}$ and PM_{10} concentrations in Germany. As shown in **Figure 3.11,** the

meteorological factors had similar effects on $PM_{2.5}$ and PM_{10} concentration except daily value snow depth (SnD). The temperature (T) was the most important driving factor based on the weight correlations, reaching 21.1 % for $PM_{2.5}$ and 35.6 % for PM_{10}. Following that snowfall thickness (20.7 %) and wind speed (19.9 %) were the second driving factors for $PM_{2.5}$, while wind speed (17.4 %) was the second driving factor for PM_{10}. In brief, some meteorological factors had a close relationship with air pollutant concentrations, which consistent with previous study [96].

Then, Spearman analysis were also performed to observe the positive and negative relationship of meteorological factors *vs.* $PM_{2.5}$ and PM_{10} concentrations. As shown in **Table 3.3**, $PM_{2.5}$ had negative correlation with meteorological factors (i.e., FP, WS, PH, C, VP, and T). Meanwhile, PM_{10} had also negative correlation with meteorological factors (i.e., FP, WS, PH, C, VP, AP, and T). However, $PM_{2.5}$ and PM_{10} concentrations were positively correlated with RH but had minor impact. This result was comparable with the previous study that RH slightly influenced the PM concentration but its fluctuation change will increase the PM concentration [97]. In addition to RH, T and WS were also important meteorological factors. For instance, low temperature could change the dynamics of air movement, trap air pollutants, and create a build-up of pollution near the ground [98, 99]. Therefore, a change in temperature may affect the PM concentration. Accordingly, the higher the wind speed, the cleaner air involved in pollutants per unit time. However, the effects of air pressure (AP) on $PM_{2.5}$ and PM_{10} were relatively low, which may be influenced by the precipitation effect that played a major role in $PM_{2.5}$ pollution removal [100].

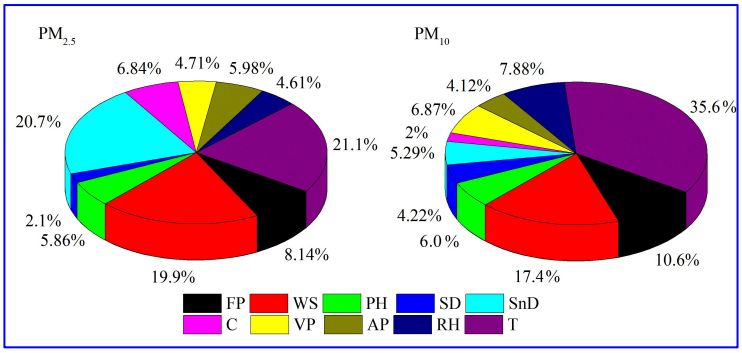


***Figure 3.11**: Impact of meteorological factors on $PM_{2.5}$ and PM_{10} (FP, precipitation form (only rain, only snow, rain and snow); WS, a daily mean wind speed (m/s); PH, a daily precipitation height (mm)； SD, a daily sunshine duration (h); SnD, a daily value snow depth (cm); C, a daily average of coverage (1/8); VP, a daily average of vapor pressure (hPa); AP, a daily mean air pressure (hPa); RH, a daily average relative humidity (%); T, a daily average temperature (°C)).*

***Table 3.3:** The correlation between meteorological factors and the particulate matter (**, $p<0.01$).*

PM	FP	WS	PH	SD	SnD	C	VP	AP	RH	T
$PM_{2.5}$	-0.227**	-0.331**	-0.319**	-0.014	0.288**	-0.016	-0.346**	0.116**	0.173**	-0.353**
PM_{10}	-0.183**	-0.303**	-0.334**	0.131**	0.224**	-0.181**	-0.238**	0.254**	0.080**	-0.363**

***Note**: FP, precipitation form (only rain, only snow, rain and snow); WS, a daily mean wind speed (m/s); PH, a daily precipitation height (mm); SD, a daily sunshine duration (h); SnD, a daily value snow depth (cm); C, a daily average of coverage (1/8); VP, a daily average of vapor pressure (hPa); AP, a daily mean air pressure (hPa); RH, a daily average relative humidity (%); T, a daily average temperature (°C).*

3.1.3.3 Correlations between PM size fractions

The $PM_{2.5}$ concentration had high positive correlation with PM_{10} in Germany, which comparable with several studies performed in California [101], Netherland [102], and China [103]. These results may provide new insight about source characterisation of atmospheric particles, and facilitate to evaluate the $PM_{2.5}$ concentration when the routine monitoring of PM_{10} was available

(since the $PM_{2.5}$ data was less or scarce in Germany). However, fine particles ($PM_{2.5}$) and coarse particles ($PM_{10\text{-}2.5}$) should be considered as separate classes of pollutants due to different sources [104]. In our study, the correlation of $PM_{2.5}$ *vs.* PM_{10} (R=0.96, p<0.01) was higher than $PM_{10\text{-}2.5}$ *vs.* PM_{10} (**R=0.44**, p<0.01) **(Figure 3.12)**, indicating the $PM_{2.5}$ concentrations were the major contributors to the average PM_{10} concentrations at many sites in Germany. However, the correlation of $PM_{2.5}$ *vs.* $PM_{10\text{-}2.5}$ was weak but highly significant (R=0.26, p<0.01), suggesting that $PM_{2.5}$ and $PM_{10\text{-}2.5}$ were derived from different sources, which comparable with previous study in the UK [105]. Taken together, the $PM_{2.5}$ and $PM_{10\text{-}2.5}$ may have obvious different behaviour due to their various sources and properties contribution, suggesting that coarse and fine particles had a different toxic effect in epidemiological studies [106].

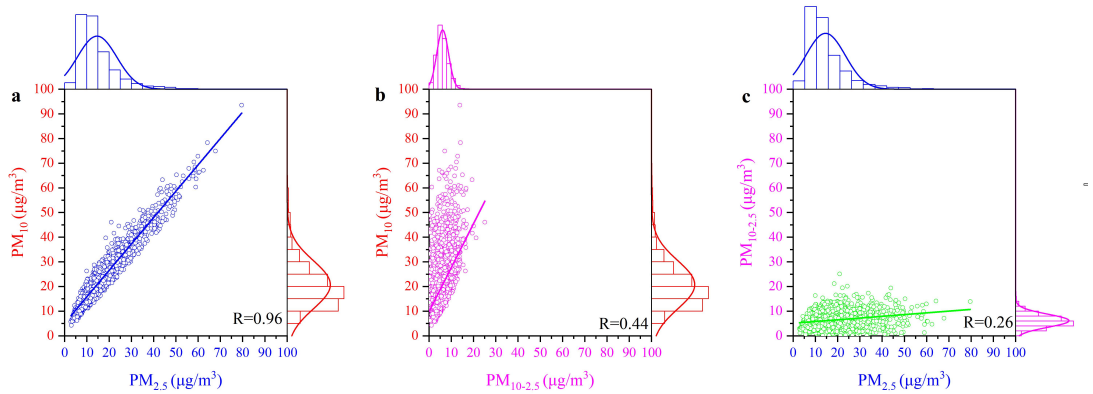


Figure 3.12: *The correlation between annual average concentrations of $PM_{2.5}$ vs. PM_{10} (a), $PM_{10\text{-}2.5}$ vs. PM_{10} (b), and $PM_{2.5}$ vs. $PM_{10\text{-}2.5}$ (c) base on 11 years of data collection all over Germany [48].*

3.2 The current status of atmospheric pollutant in Augsburg (micro-scale)

In the micro-scale, the study was carried out between September 2018 and June 2020. Personal measurements were performed along a defined footpath in the city centre of Augsburg, Germany. The aims of the study were 1) to investigate the spatio-temporal variability of air pollutants (i.e., PM_1, $PM_{2.5}$, PM_{10}, UVPM, BC, BrC, PNC, and LDSA), 2) to develop street-BC models based on street view images for estimating spatial patterns in exposure to BC. In addition, given that fireworks events on New Year's Day can cause a dramatic rise in air pollutants for a short term period and give serious impact to human health, 3) we investigated the contribution of fireworks to air pollution with selected pollutants, in particular PAHs, BC and (heavy) metals, and evaluated the health assessment of PAHs and metal elements during New Year's Days periods from 2010 until 2021 in Augsburg, Germany.

3.2.1 Spatio-temporal variability of air pollutants in different micro-environment

The average air pollution concentration was considered as the concentration for the city centre based on the mobile monitoring data. Assessments of air pollutants exposure were collected in all periods and included walks at all times of day (04:00 - 24:00). As shown in **Figure 3.13**, the averaged concentrations of whole walks for the whole study period, non-heating, and heating

periods were 11.8, 7.5, and 18.3 µg/m^3 for PM_1, 12.1, 7.5, and 18.7 µg/m^3 for $PM_{2.5}$, 13.8, 9.4, 19.9 µg/m^3 for PM_{10}, 9506, 8750, and 10200 #/cm^3 for PNC, 2.03, 1.75, and 2.47 µg/m^3 for eUVPM, 1.84, 1.79, and 1.92 µg/m^3 for eBC, 0.63, 0.55, and 0.74 µg/m^3 for eBrC, and 19.7, 18.5, and 20.1 µm^2/cm^3 for LDSA, respectively. Based on EU concentration standard for $PM_{2.5}$ (25 µg/m^3) and PM_{10} (40 µg/m^3), the air pollutants level in Augsburg reached the requirement standard, indicating that the air quality condition in Augsburg was cleaner than in other cities, such as Athens, Greece [107], Berlin, Germany [108], Helsinki, Finland [50], and Lisbon, Portugal [109]. In general, the air pollution in the downtown of Augsburg was classified under a lower-middle level in Europe [110].

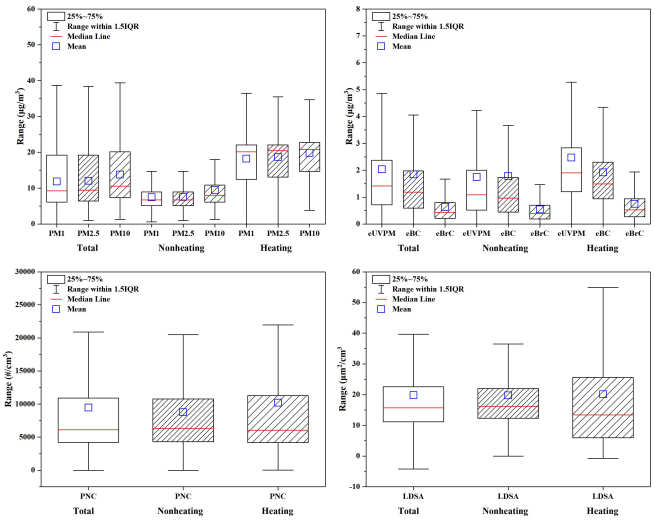


Figure 3.13: *The box diagram of various pollutants in total year, non-heating and heating periods in the Augsburg urban area during 2018-2020.*

3.2.1.1 Spatial variations of air pollution concentrations across street micro-environments

The aggregated median air pollutants concentrations for each meter distance along the route in non-heating and heating periods were shown in **Figure 3.14**. In both periods, the observed median air pollutants concentrations in different micro-environments exhibited substantial spatial heterogeneity, with the lowest exposure values in the park and the highest in the traffic area. The high air pollutants concentrations were frequently found in the highest traffic intensities, particularly on intersections.

Generally, the lowest exposure was commonly found in the park environment, while the highest exposure was found in the traffic area during the non-heating and heating periods. These traffic areas were hotspots for air pollutants, especially for $PM_{1.0}$, $PM_{2.5}$, eBC, and PNC. It was important to mention that in specific condition, PM and PNC levels in Augsburg did not always represent the impact of road traffic emissions, as they were highly influenced by secondary particle formation induced by nucleation processes [25, 111]. In addition, when the spatial exposure of BC in each micro-environment during the heating and non-heating periods was compared, the BC levels were generally higher during the heating than the non-heating period. However, eBC at high traffic intersections remained consistently higher during both periods [112], thus the direct emissions from the traffic could be an important source for BC in Augsburg. In addition to traffic areas, the major transportation in the CBD were trams and natural gas-operated buses. Targino (2016) pointed out that the pollution concentrations, especially eBC concentrations were positively correlated with traffic loads, and specifically observed a strong relationship at intersections [113]. Similarly, the spatial exposure of LDSA had comparable trend to that of BC in all typical micro-environments, i.e. areas with high traffic volumes also had higher LDSA concentrations. The cumulative LDSA may be associated with particle-induced adverse health effects [114].

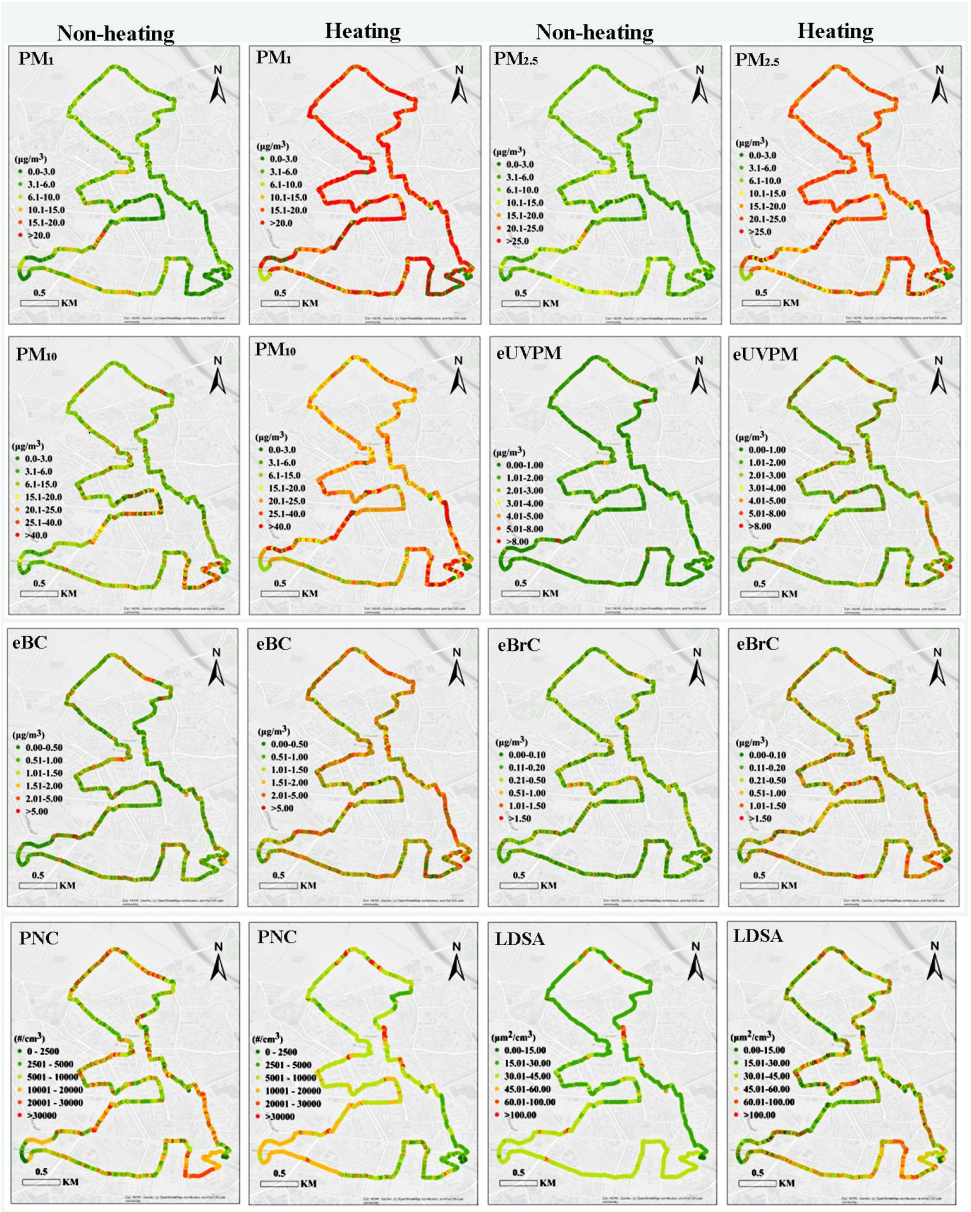


Figure 3.14: *Spatial exposure of the air pollutants (PM_1, $PM_{2.5}$, PM_{10}, UVPM, BC, BrC, PNC, and LDSA) for whole walk during non-heating and heating periods in downtown Augsburg. © OpenStreetMap contributors 2021. Distributed under a Creative Commons BY-SA License.*

3.2.1.2 Temporal variations of air pollution concentrations across street micro-environments

Based on all the sampling data, the air pollution concentrations in heating and non-heating periods were significantly differences (p<0.05). As shown in **Figure 3.13**, the air pollution concentrations were higher during the heating than the non-heating period. In the heating period, the anthropogenic emissions from heating could be largely contributed to air pollution. Moreover, emissions from traffic were higher in winter (heating period), when extended cold start and driving conditions occur [115]. To better quantify the temporal variation of pollutant concentrations in different micro-environments, three typical micro-environments (park, CBD, and traffic) that closely related to people's activities were chosen from our monitoring routes.

The temporal variabilities of air pollutants concentrations were highly heterogeneous both in

non-heating and heating periods. As shown in **Figure 3.15**, the air pollutants concentrations at different typical micro-environments were significantly difference at different times (morning, afternoon, and evening) during the heating and non-heating periods (p<0.01) according to the observed data. For instance, the exposure to PM_1, $PM_{2.5}$ and LDSA was significantly different at different times of day and in the three micro-environments during non-heating period, whereas the temporal exposure of $PM_{2.5}$ and eUVPM was significantly different at different times of day during heating period. These findings suggested that the air pollutants levels during the heating period might be also influenced by increased primary emissions from residential heating beyond traffic emissions [116].

Meanwhile, due to the complexity of pollutant sources and meteorological impacts, some pollutants showed some irregular variation at different time of the day in the typical micro-environments during non-heating and heating periods (**Figure 3.15**). These variations of pollutants may be influenced by interaction of multiple factors such as pollution sources, seasonal differences in meteorological conditions, and geographical location [117, 118]. For instance, most air pollutant exposures were higher at evening in the three typical micro-environment during the non-heating period. The lower wind speeds (< 1 m/s) and eventually lower mixing layer height during the night may result in lower dispersion of air pollutants [119]. The exposure of eUVPM, eBC, eBrC, and LDSA during the heating period showed higher concentrations in the morning and evening, but lower exposure in the afternoon. These results were comparable with the whole walks data, indicating that the lower temperatures in the morning and evening during heating period caused the increased heaters' use of the people.

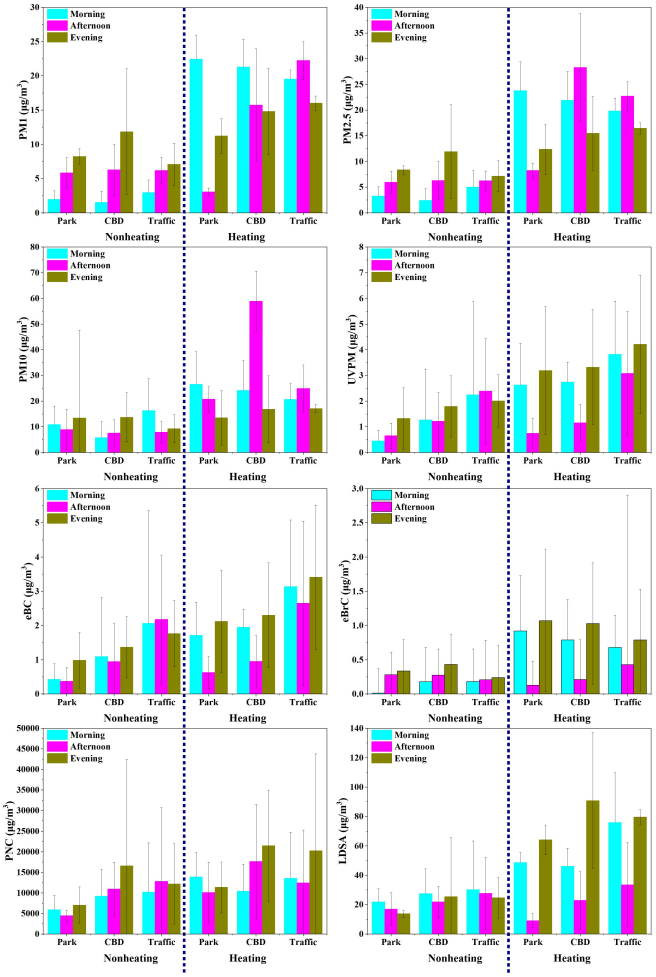


Figure 3.15: *Temporal distribution of the air pollutants exposure concentrations at different micro-environments and different time (morning, 4:00-11:00; afternoon, 14:00-17:00; evening, 18:00-22:00) in Augsburg during non-heating and heating periods.*

3.2.2 Correlation of eUVPM, eBC, and eBrC concentrations and its driving factors

BC can be used as a valuable air quality indicator for assessing the health risks of traffic-related air pollution [120]. Hence, in this study, the correlations of driving factors with BC and its homologous pollutants (UVPM and BrC) were analysed. The specific air pollutants metrics called “equivalent ultraviolet particulate matter (eUVPM) and equivalent black carbon (eBC)” were determined via the 370 nm and 880 nm using aethalometers (microAethalometer, MA200, AethLabs, USA, time resolution, 10s), and equivalent brown carbon (eBrC) = eUVPM (375 nm) –

eBC (880 nm).

The monitoring route were divided into four micro-environment classes to further observe the driving factors effects. The route was classified according to the observed traffic density during the daytime, determined from the traffic flow observed by the street views, including high traffic roads (H_Traffic, average 500-1000 vehicles/h), medium traffic roads (M_Traffic, average 200-500 vehicles/h), low traffic roads (L_Traffic, average 1-200 vehicles/h), and park area (N_Traffic, average 0 vehicles/h).

3.2.2.1 Street scene factors

The correlation of eBC concentration and the street scenes (buildings, roads, cars, vegetation, and sky) was observed. As shown in **Figure 3.16**, the buildings, roads, cars, and vegetation had weak correlations with eUVPM, eBC, and eBrC, but they were highly significant (p<0.01). Similarly, Choi et al. (2016) found that the block-scaled UFP concentrations were highly dependent on the built environment and surface turbulence [39], which comparable with BC. The large dispersion of pollutants may be influenced by open blocks, while the low dispersion of pollution from the upper wind may be influenced by high and narrow buildings. Pan et al. (2013 also found that the dispersion of pollutants in urban canopies was indirectly affected by the shape of the buildings [121]. The impact of automobiles on pollutants was mainly caused by automobile exhaust, which the main source of BC [122]. The relationship between vegetation and BC was inversely related due to the urban forest system can store and capture dust in the air [123], which purified the eBC concentration.

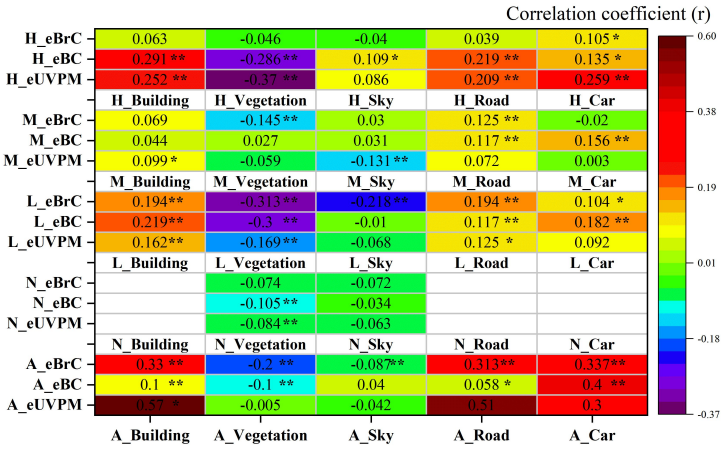


Figure 3.16: *Correlation matrix of measured compounds in different traffic volume (A, all roads; N, no traffic volume (park area); L, low traffic volume; M, middle traffic volume; H, high traffic volume, *p<0.05, **p<0.01, white bands represent nonsense) [21].*

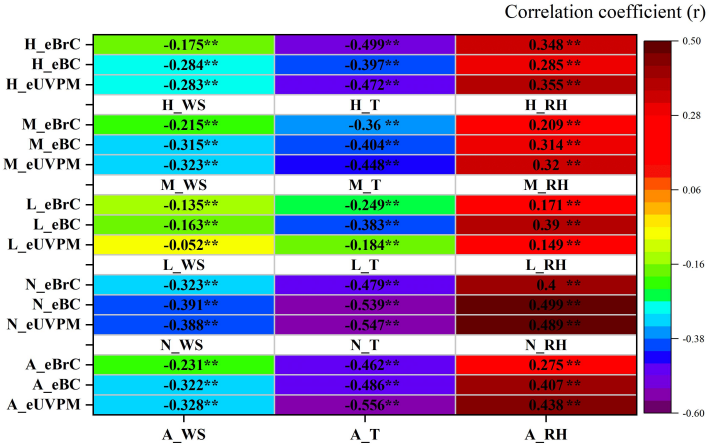


Figure 3.17: *Correlation matrix of measured compounds in different traffic volumes (A, all roads; N, no traffic volume (park area); L, low traffic volume; M, middle traffic volume; H, high traffic volume; WS, wind speed (m/s); T, temperature (°C); RH, relative humidity (°); **p<0.01) [21].*

For different micro-environments the street scenes and the three air pollutants had slightly different correlations, caused by the different proportions of street scenes in different micro-environments (**Figure 3.16**). Most vegetation was found in the park area, resulting in a low concentration of eUVPM, eBC, and eBrC. In the micro-environment containing medium traffic flow, the eUVPM had very weak correlation with the building but still significant. However,

the eBC and eBrC had no significant correlations with the building, which may be affected by a wider range in the proportion of buildings.

3.2.2.2 Meteorological factors

The correlations between air pollutants concentrations (eUVPM, eBC, and eBrC) and meteorological factors (wind speed, temperature, and relative humidity) were calculated using Spearman coefficients analysis within a certain spatial scale of different traffic volumes. The three air pollutant concentrations (eUVPM, eBC, and eBrC) were significantly correlated with all meteorological factors (wind speed, temperature, and relative humidity) (p<0.01) in the four different traffic volumes. As shown in **Figure 3.17**, eUVPM, eBC, and eBrC had negative correlations with wind speed, and temperature, and positive correlations to relative humidity, suggesting that the spatial distributions of eUVPM, eBC, and eBrC were highly influenced by meteorological factors, which was comparable with the previous study [124]. Therefore, this result further showed that the three air pollutants concentrations were mainly affected by the local sources and meteorological conditions. For different micro-environments, the eBC had slightly different correlation with meteorological factors. For instance, the eBC concentration had the strongest correlation with meteorological indicators in the park area (N_traffic).

3.2.3 The estimation of eUVPM, eBC, and eBrC concentrations and their model evaluation

The scatterplots of the estimated and observed values of the eUVPM, eBC, and eBrC for RF based-approach were shown in **Figure 3.18 (a, b, c)**. In the same sampling, we selected 70 % of the monitoring data as the training data, and the ten-fold CV method was applied to estimate the accuracy of the method, where the dataset was randomly separated into ten apportions of equal size. The algorithm was trained using nine-fold and then repeated ten times. We performed the sampling with replacement, suggesting that every fold could be used as the validation set exactly once. Furthermore, the weight of each factor was analysed to determine the dominant factors of the model based on the RF based-approach. Of these, relative humidity was found has a dominant effect on eUVPM, eBC, and eBrC concentrations. In addition, wind speed and temperature for eUVPM, temperature and vegetation for eBC, and vegetation for eBrC were found as other dominant factors influencing their concentrations.

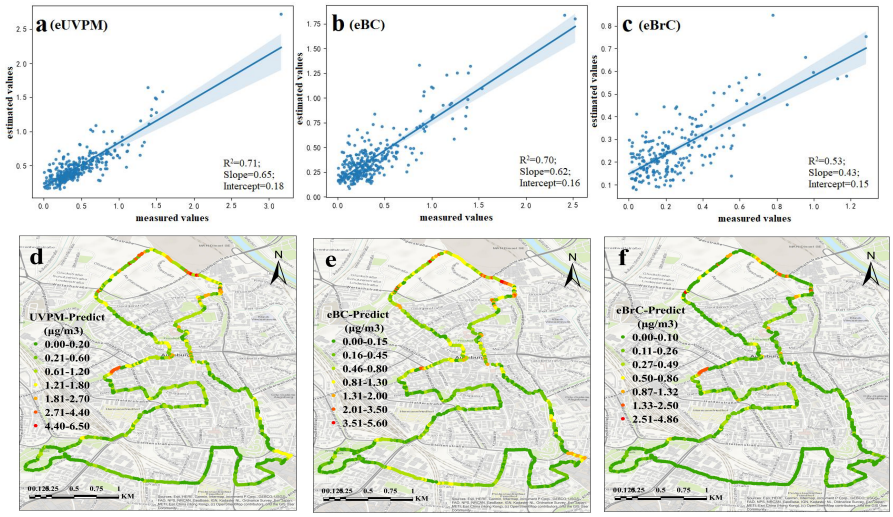


Figure 3.18: *The random forest based-approach and estimation of the spatial distribution of air pollutants (a, b, c: random forest optimization for eUVPM, eBC, and eBrC; d, e, f: Spatial distribution for estimation to eUVPM, eBC, and eBrC exposure) [21].*

It was worth mentioning that the RF based-approach was the most appropriated for eUVPM and eBC concentrations estimation (**Figure 3.18 d, e**), however, it was poor for eBrC concentrations estimation (**Figure 3.18 f**). In the previous study, Brandt et al. (2011) have shown that wood combustion in Germany was frequently used for leisure [125]. Therefore, eBrC should be associated with smoke from the smoldering phase of wood combustion and leisure. However, during the sampling campaign, the camera did not fully capture the appropriated information (e.g., plumes of smoke from wood combustion).

Table 3.4: *The evaluation of the street view image models for eUVPM, eBC, and eBrC concentration estimation.*

Model	Air pollutants	R^2	RMSE	MAE	IA
Street view image	eUVPM	0.71	0.18	0.14	0.90
	eBC	0.70	0.19	0.14	0.89
	eBrC	0.53	0.15	0.11	0.78

In this study, we proposed the street view image (SVI) model, providing an estimation of eUVPM, eBC and eBrC concentration levels with high accuracy and efficiency (**Table 3.4**). This estimation model can effectively overcome some shortcomings of previous models in estimating air pollution, such as, it can be simply applied in the low wind speed condition to identify the hotspot of air pollutants. In addition, this model provided a precise timeliness, which can capture the actual conditions of the daytime air pollution. In the future, the SVI model can be developed in different areas or even areas that were not accessed by fixed air quality monitoring. To improve the accuracy of the model, the eUVPM, eBC and eBrC concentrations can be estimated by using street scenes (buildings, roads, cars, vegetation, and sky) combined with meteorological factors (wind speed, temperature, and relative humidity in the area. Moreover, street scenes were simple and easy to obtain the types of features with highly detailed and precised information. However, the SVI model retained certain shortcomings, for instance, the meteorological data was not measured along the sampling path, thus further improvements are still required in the future.

3.2.4 The trend of air pollutants and its health assessment around New Year's Days

In addition to spatio-temporal variability, some specific issues (e.g., firework celebration) were influenced the specific emission situations (e.g., particulate matter) in the study. For this purpose, we conducted a case study investigating the influence of New Year's Eve fireworks on air quality in downtown of Augsburg. The reduction of air pollutants was significantly reduced when the restrictions of the fireworks activity at the turn of the year 2020 - 2021 was applied due to the Covid-19 pandemic.

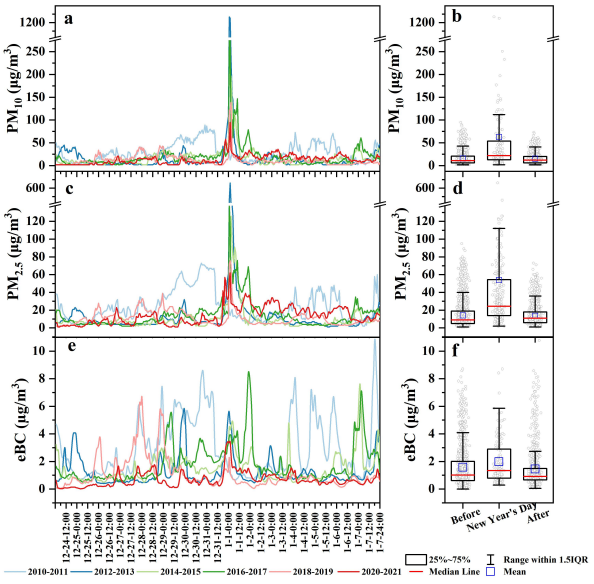


Figure 3.19: *Left panel, Time series of the hourly mean concentrations of PM_{10} (a), $PM_{2.5}$ (c) and eBC (e). Right panel, summarized comparison of the hourly means of the concentrations of PM_{10} (b), $PM_{2.5}$ (d) and eBC (f) on New Year's Day with the reference periods before and after. The significance levels (**, $p<0.01$, *, $p<0.05$) refer to the differences between the respective means.*

3.2.4.1 Air pollutants trends around New Year's Days

(1) $PM_{2.5}$, PM_{10}, and BC

The drastic increase of the PM_{10} and $PM_{2.5}$ concentrations were clearly shown on New Year's Day. As shown in the **Figure 3.19 a-d,** a massive increase in PM concentration was observed at midnight. However, a lighter increase was already found in the several hours earlier. It was worth mentioning that the temporal differences in reaching the maximum concentrations was occurred between 0 and 2 o'clock. However, their maximum concentrations were different, which ranging from about 60 (2020-2021) to > 600 µg/m^3 (2012-2013) for $PM_{2.5}$. The intensity of the fireworks and differences in atmospheric dispersion conditions (especially wind speed) could be the possible causes for this condition. In general, the extremely high particle concentrations decreased within a few hours during firework event, thus concentrations below 25 µg/m^3 were reappeared on January 2. Based on the $PM_{2.5}$ and PM_{10} concentration trends over the entire interval, various concentrations values can be observed and significantly increased in some periods. For instance, $PM_{2.5}$ concentrations was particularly striking (> 70 µg/m^3) between Christmas and New Year's Eve 2010. However, based on the average concentration for the all periods, $PM_{2.5}$ and PM_{10} concentrations were significantly higher on New Year's Day than on the days before or after (**Figure 3.19 b, d**), which was comparable with previous study [74].

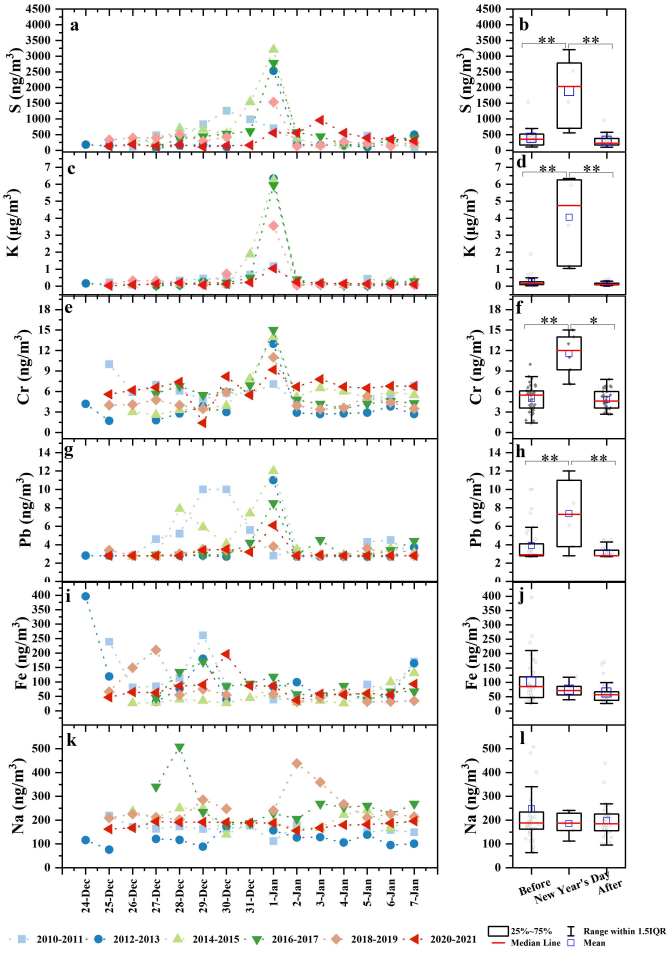


Figure 3.20: *Left panel, Time series of the daily mean concentrations of representative metal elements (S, K, Cr, Pb, Fe, and Na). Right panel, summarized comparison of the daily means of the concentrations of representative metal elements on New Year's Day with the reference periods before and after. The significance levels (**, p<0.01, *, p<0.05) refer to the differences between the respective means.*

A specific influence of the fireworks on the eBC concentration was not clearly detected on New Year's Day. As shown in **Figure 3.19 e**, significant peaks of eBC concentrations were presented at most of the year changes. However, these peaks were much less pronounced than that of PM concentration peaks. It was also worth mentioning that the concentration increase was significantly found before midnight in most years (**Figure 3.19 f**). Furthermore, many short episodes were found with eBC concentrations above those on New Year's Day in almost all years, which were comparable with $PM_{2.5}$ in the period between Christmas and New Year's Eve 2010. However, based on overall average concentration of observed New Years, the average concentration of eBC was significantly or highly significantly larger on New Year's Day than on the days before or after, indicating that the firework contributed to the higher eBC concentrations [126]. Despite the

higher variability, the eBC concentrations had strong correlation with PM concentrations (BC *vs.* $PM_{2.5}$, 0.789; BC *vs.* PM_{10}, 0.843, $p<0.01$) during the observed periods (2010-2021).

(2) Metal elements

A total of 27 metal elements were quantified by ICP-MS. Of these, 15 elements (i.e., Al, B, Ba, Ca, Cr, Cu, Fe, K, Mg, Na, Pb, S, Sr, Ti, and Zn) were identified, while 12 elements (i.e., As, Be, Cd, Co, Li, Mo, Ni, P, Sb, Se, Sn and V) were excluded from further evaluation due to below limit of detection in all $PM_{2.5}$ samples. Following that, the 15 elements were classified into three groups based on different temporal characteristics, which were selected and discussed here as example (**Figure 3.20**). For the first group, the peak concentrations were higher for the elements contributing in the pyrotechnic sets of the fireworks (e.g., K, S, **Figure 3.20 a-d**) or elements contributing in colouring the fireworks (e.g., Al, Ba, Cu, Mg, Sr, Ti) on the New Year's days [6], e.g., S and K were adopted as examples in **Figure 3.20 a, c**. The concentrations were initially increased as early as December 31. Then the low concentration was reached as before the firework on January 2. As shown in **Figure 3.20 b, d** the metal elements levels between the New Year's Day and the comparison periods were significantly different. The second group was included the elements (Cr, Pb, and Z), which exhibited more peaks instead New Year's Day peaks in some cases, for instance, Cr and Pb (**Figure 3.20 e-h**). Lead exhibited elevated concentrations during the episode between Christmas and New Year's Eve 2010, which was comparable with the $PM_{2.5}$ and the eBC trends. However, the concentration trends were significantly higher on New Year's Day (**Figure 3.20 f, h**). This was particularly remarkable, since the mentioned heavy metals were restricted in the fireworks used in Germany. The third group was included the elements (B, Ca, Fe and Na), which showed high variability around the observed period with no recognizable peaks on New Year's Day, for instance, Fe and Na (**Figure 3.20**

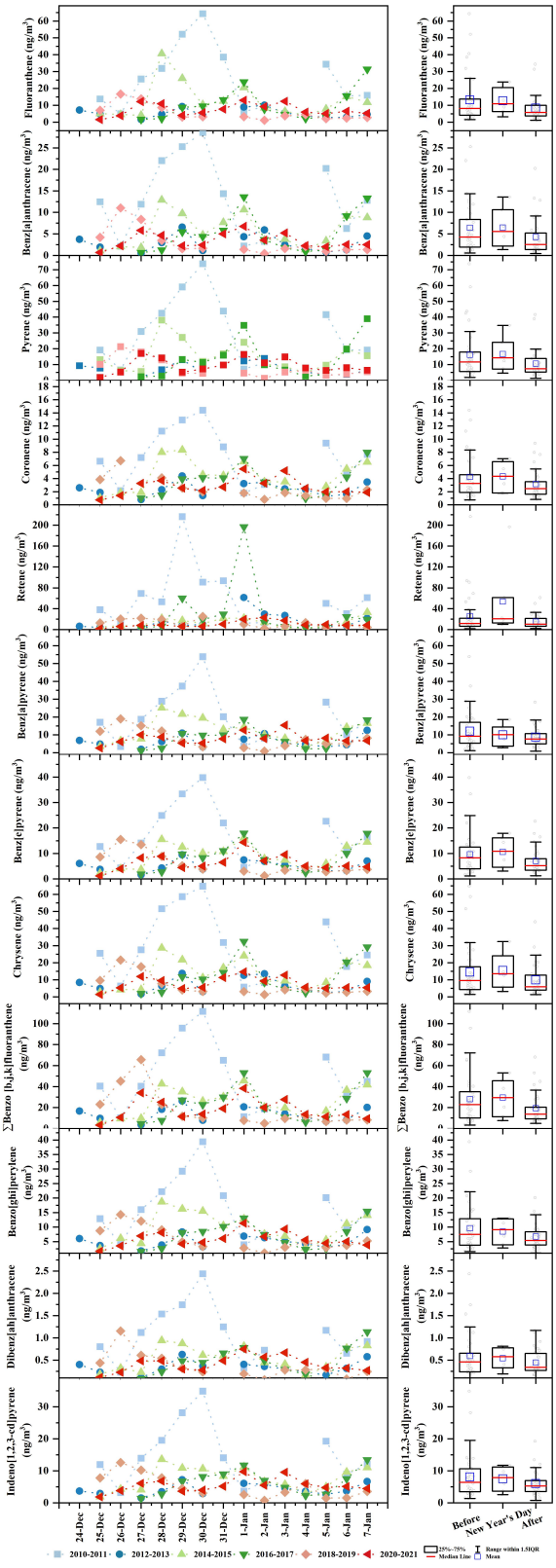


Figure 3.21: *Left panel, Time series of the daily mean concentrations of 11 PAHs. Right panel, summarized comparison of the daily means of the concentrations of 12 PAHs on New Year's Day with the reference periods before and after.*

i-l). Accordingly, there were also no significant differences between fireworks and comparison periods in the concentrations averaged overall periods studied (**Figure 3.20 j, l**).

(3) PAHs

In total, the PAHs concentrations had the similar trends with the some heavy metal elements (Cr, Pb, and Zn). However, the peak concentrations were much less reduced or absent on New Year's Days during some observed periods (**Figure 3.21**). In the comparison periods, more frequent and sometimes higher peak concentrations were found than on January 1. The highest PAHs concentrations were occurred and particularly striking between Christmas and New Year's Eve period 2010. Overall, based on average concentrations during observed periods, the all PAHs were slightly increased on January 1 than in the comparison periods, but they were not significantly different (**Figure 3.21**). In this study, the annual mean concentration for B[a]P was 10.42 ng/m^3, which10 times higher than EU target value (1 ng/m^3) [127]. Therefore, it should be mentioned that the PAHs concentrations were high during the observed periods.

3.2.4.2 Source apportionment of air pollutants by PMF

The PMF 5.0.14 (EPA, US Environmental Protection Agency) was used to determine the most relevant sources of the $PM_{2.5}$, BC, metal elements, and PAHs. Not all sources associated with the $PM_{2.5}$ mass could be identified by PMF due to the limited samples and analysis (including no data on inorganic ions). However, the analytical data were sufficient to identify the major sources of PAHs, BC, and metals and to determine their respective contribution of fireworks to these pollutants. Thus, the objective of PMF analysis was not to determine the all contributors to $PM_{2.5}$, but to determine the major source contributions to the proportions of the above-mentioned pollutants.

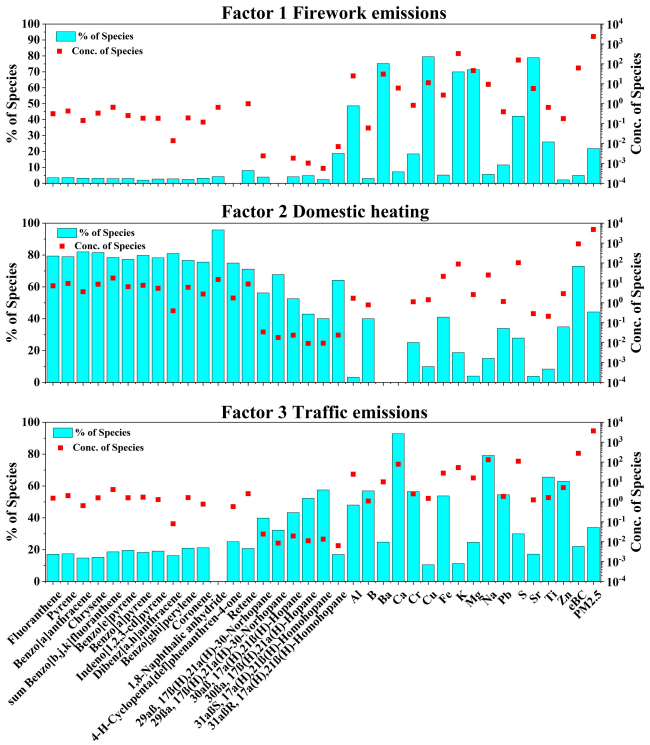


***Figure 3.22**: The profiles of 3 factors separated in the PMF analysis, including firework emissions, domestic heating, and traffic emissions.*

As shown in **Figure 3.22**, 3 factors were classified, including firework emissions, domestic heating, and traffic emissions. Based on the PMF analysis, the contributions of New Year's fireworks to PAH concentrations on January 1 were estimated to be approximately 36 % (20-84 % for individual years) and 45 % to eBC (12-100 % for individual years). Of these PAH species, semivolatile PAH compounds such as Benzo[a]anthracene, Chrysene, Dibenz[a,h]anthracene, Benzo[a]pyrene, Fluoranthene, Pyrene, Benzo[b,j,k]fluoranthene, Indeno[1,2,3-cd]pyrene, Benzo[e]pyrene, and Retene were mainly contributed to exhaust emissions of wood-burning homes. The high metal (Al, Ba, Cu, K, Mg, and Sr) concentrations were attributed on average to more than about 91 % to the fireworks, except Al (about 86 %). The other metals (Ca, Cr, Fe, Na, Pb, Ti, and Zn) showed variable proportions (67 %, 77 %, 44 %, 59 %, 64 %, 75 %, and 33 %) due to fireworks. Therefore, the fireworks have been identified as a strong but short-term source of ambient particulate matter.

3.2.4.3 Health assessment of toxic elements and PAHs

In previous studies it was found that the different firework compounds have significant and different influence in reactive oxygen species (ROS). For example, particulate matter affected the ROS activity response in both airway epithelial and vascular endothelial cell lines [128, 129]. However, a number of fireworks PM had greater impact on ROS responses of cells compared to the typical response of ambient PM [128]. Due to the well-established role of metals in oxidative stress [130, 131], the metal content among the fireworks types were likely responsible for the fireworks type-dependent differences in ROS activity.

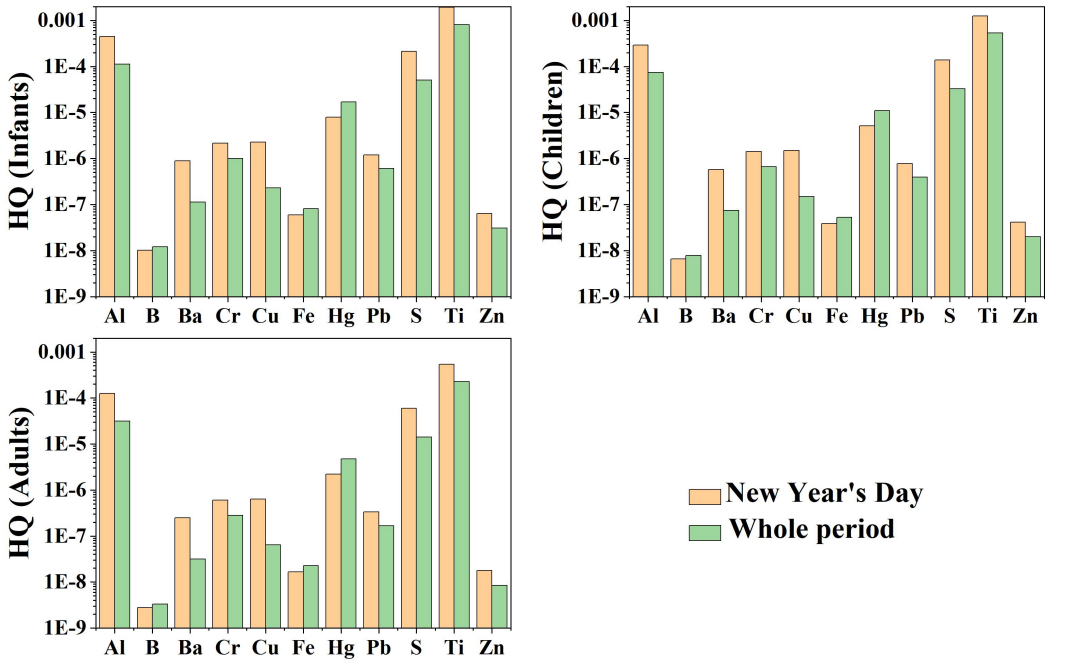


Figure 3.23: *The non-carcinogenic risk factor HQ for heavy metals in the atmosphere at the sampling sites during New Year's Day and whole period.*

As shown in **Figure 3.23** and **Table 3.5**, the values of the non-carcinogenic risk factor (HQ) for metal elements in the atmosphere at the sampling sites during New Year's Day ranged between $1.1 \cdot 10^{-9}$ and $4.3 \cdot 10^{-3}$ based on all age-group, which was below the EPA limit of 1 [132]. However, the higher HQ was found during New Year's Day compared to whole period days. Especially, the Cu element, which was more than 10 times higher than the whole period days, indicating the contribution of fireworks display to high potential risk. In addition, the lifetime

carcinogenic risk (ILCR) values during whole period ranged between 4.4 • 10^{-9} and 1.5 • 10^{-8} for As and Cr in descending order, but their ILCR accumulations were still below the carcinogenic risk threshold range (10^{-4}~10^{-6}) for all age-group [133].

Table 3.5: *Health risk assessment of PAH and metal elements for different groups in Augsburg during the whole period (Dec.24-Jan.07$^{2nd\ year}$).*

Air pollutants	Groups	Infants	Children	Adults
PAH	E (ng)	77.36	164.69	227.04
	ILCR	$2.56 \cdot 10^{-5}$	$1.82 \cdot 10^{-5}$	$1.16 \cdot 10^{-5}$
Metal elements	HQ	$8.29 \cdot 10^{-5}$	$5.41 \cdot 10^{-5}$	$2.32 \cdot 10^{-5}$
	ILCR	$3.73 \cdot 10^{-8}$	$2.65 \cdot 10^{-8}$	$1.68 \cdot 10^{-8}$

Meanwhile, the $B[a]P_{TEQ}$ and $B[a]P_{MEQ}$ values were also computed applying the lists of TEFs and MEFs (**Table 2.1**). The carcinogenic risks of total PAHs ($\Sigma B[a]P_{TEQ}$) in Augsburg New Year's days period was approximately of 14.43 ± 4.67 ng/m^3, which was higher than the target annual mean values of $\Sigma B[a]P_{TEQ}$ range (0.7 - 1.3 ng/m^3) in European countries [134] (**Figure 3.24**). In addition, the mutagenic potencies of total PAHs ($\Sigma B[a]P_{MEQ}$) was approximately of 18.83 ± 6.08 ng/m^3, which was higher than those at the Italian residential zone (4.2 ± 2.7 ng/m^3 for $PM_{2.5}$) [135]. It was worth mentioning that the $B[a]P_{TEQ}$ and $B[a]P_{MEQ}$ values were higher during New Year's Day than whole period days, indicating that many toxic compounds were threatening human health in the New Year's days period. In addition, the ILCR values of PAH ranged from 1.16 • 10^{-5} to 2.56 • 10^{-5} during the whole period, but their ILCR accumulations were also below the carcinogenic risk threshold range (10^{-4}~10^{-6}) for all age-group [133]. However, it was important to note that the average data were only collected over the 15 days (Dec.24-Jan.07) in this study, thus the level of carcinogenic and mutagenic potencies of PAHs cannot fully represent the whole year in some extent.

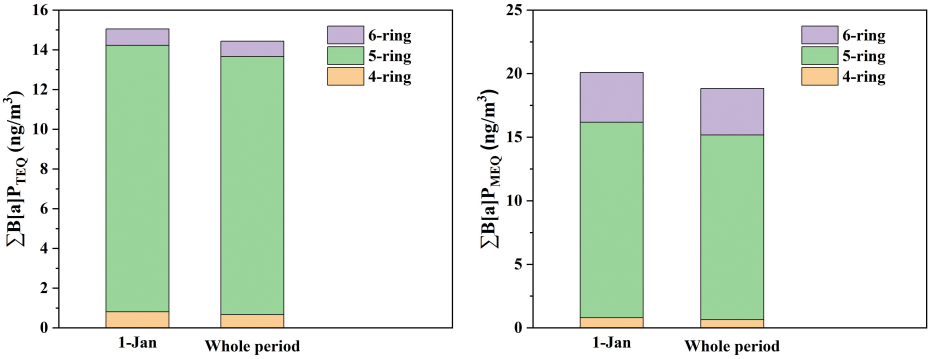


Figure 3.24: *$\Sigma B[a]P_{TEQ}$ (left) and $\Sigma B[a]P_{MEQ}$ (right) concentrations of PAHs in Augsburg during New Year's Day and whole Periods.*

3.3 The characteristics of atmospheric pollutants in small towns (micro-scale)

Generally, limited fixed air quality monitoring stations were installed in villages or rural areas and limited studies on micro-scale variations in air pollution have been described in detail, resulting in difficult to estimate human exposure and related adverse health effects in such environments. Combining of these reasons, in this study, a sampling campaign on rural air pollution was carried out in two small towns on the German-Czech border, 1) to compare the spatio-temporal variability of air pollutants and its differences between two neighboring

German-Czech border cities by mobile monitoring measurement, and 2) to identify air pollution hotspots and their driving factors in villages.

3.3.1 Spatio-temporal variability of air pollutants in two neighboring German-Czech border villages

The observed average of PM_1, $PM_{2.5}$, and PM_{10} concentrations during the study period were 10 ± 11, 11 ± 11, 16 ± 27 μg/m^3 and 19 ± 34, 21 ± 39, 37 ± 108 μg/m^3 in Bayerisch Eisenstein (BE, Germany) and Železná Ruda (ZR; Czechia), respectively, which were similar to some European regions, such as the suburban of Bologna, Italy [136], the urban area in Milan, Italy [137], the urban centre in Austria [138], and the suburban routes in Northampton, UK, during the winter of 1999/2000 [139]. However, the PM_{10} concentrations were much higher than the urban background in Barcelona, Spain and Lugano, Switzerland [25]. For $PM_{2.5}$, they were higher than the urban road way in Newark, US [140].

The average of eBC concentrations were 1.30 ± 1.35 μg/m^3 and 1.70 ± 2.45 μg/m^3 in BE and ZR, respectively, during the observed period, which were similar to those reported and at urban background sites in Barcelona and Lugano [25], Paris [141], and the urban centre of Augsburg [142]. However, the observed average of eBC concentrations was higher than those of the urban industrial area in Huelva [25] and the urban centre in Chicago [27]. Nevertheless, these concentrations were much lower when compared to those reported at the road site of Marylebone [25]. The observed average PNC in BE and ZR during the study period were 4190 ± 1340 #/cm^3 and 5024 ± 2346 #/cm^3, which were similar to those reported from the rural forest and the 100 m high urban tower in Stockholm [143].

3.3.1.1 Spatial variations of air pollution concentrations across street micro-environments

According to the aggregated results, the detected hotspots were combined with on-site photos to verify and confirm their high concentrations, assembling a logically closed loop of the entire mobile monitoring. The spatial variability of air pollution was lower, but they were significant for PNC in BE (p<0.01) and for BC and PNC in ZR (p<0.05). As shown in **Figure 3.25**, the observed PM and PNC were significantly higher on roads between 2250 and 3250 m from the starting point in BE. The observed BC and PNC between 25 m selected road in ZR were significantly different, especially between 1000 m and 2000 m from the starting point. The smoke emitted from residential during heating and the emissions from vehicles were the main causes of this spatial difference identified using the photos during the observed period.

Based on all the sampling data from the two villages over four days, the observed of PM_X (PM_1, $PM_{2.5}$, PM_{10}) and PNC in two villages were significantly different (p<0.05). As shown in **Figure 3.25**, the spatial distribution of air pollution hotspots in ZR was obviously higher than that in BE. Similarly, the abnormally high concentrations in the two villages have become hotspots due to increased of traffic flow. Comparing the concentration of the hotspot area with the background concentration in the city, the concentrations of the hotspot area was 5-10 times higher than that of the background area [138, 144, 145]. However, comparing the observed eBC concentrations in two villages, their concentrations were generally less pronounced than that PM_1 and PNC, and were generally not significant different between them.

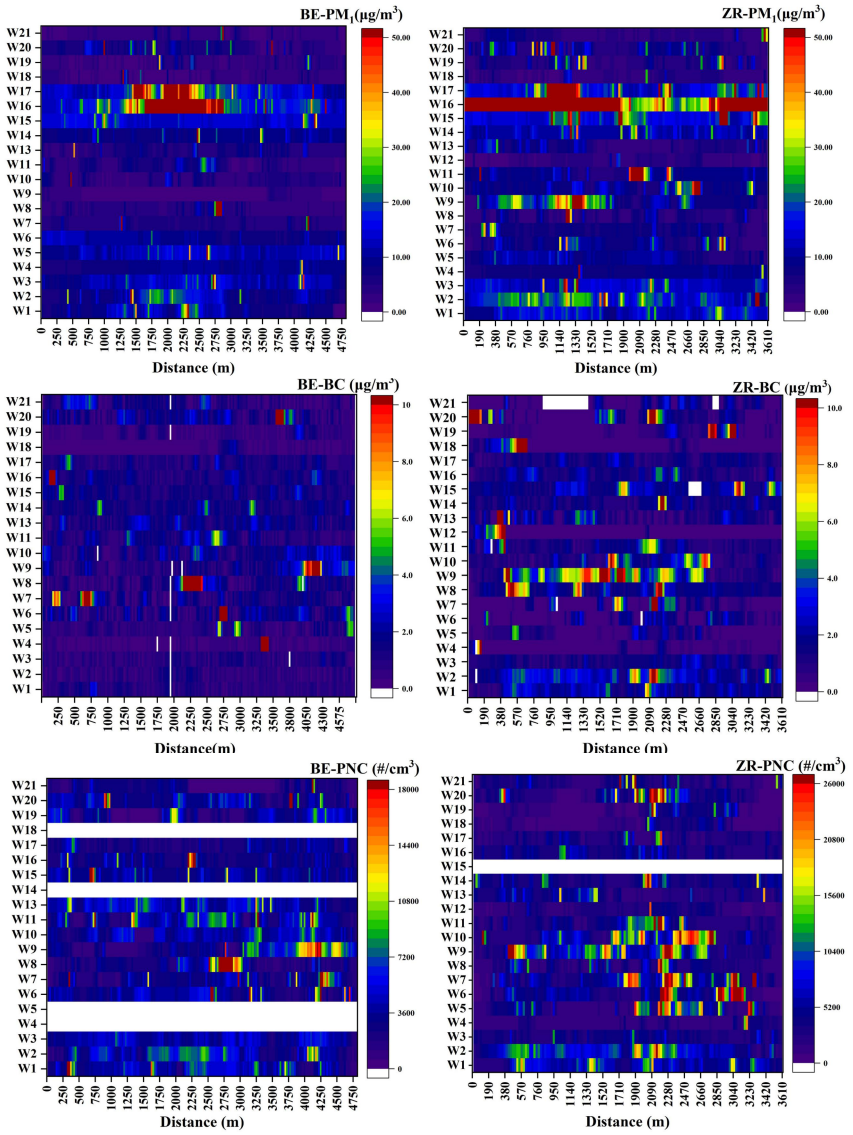


Figure 3.25: *PM_1, BC, and PN concentrations for the different walks (y-axis) at a selection of road (x-axis) in BE and ZR. The colours are scaled between the extremes and differ between the plots. White pixels represent no data due to instrument failures and Black pixels represent abnormal peak samples [49].*

3.3.1.2 Temporal variability of air pollution concentrations in BE and ZR

The average PM_1, eBC and PNC of each walk were analysed based on the hourly averaged stationary measurements. The stationary measurements, carried out in between the walks, and mobile measurements had similar patterns as the average PM_1 and BC in the two villages (**Figure 3.26**). However, the observed values of stationary measurements were generally below the observed concentrations at the previous walks, excluding some walks in ZR. This phenomenon was found because the stationary sites were located in the background while the walks partly occurred closed the source locations. In combination with on-site sampling photos, the concentrations were increasing during stationary measurements due to the passing vehicles.

The observed temporal variabilities of PM_1, PNC and BC were significantly different (p<0.05) between walks carried out within the same measurement day as well as between different measurement days in the same time of day, both in BE and ZR. According to the time distribution, after 16:00 pm, the hotspot area in ZR was found more than that in BE. After analysing the photos

during the observed period, smoke from residential could contribute most probably due to heating increased in ZR,

As shown in **Figure 3.26 a, b**, the average PM_1 concentrations in the 20 walks of BE had the similar patterns with 21 walks of ZR (since PM_1, $PM_{2.5}$ and PM_{10} show the same pattern, only the pattern graph of PM_1 was drawn here). PM_1 concentrations in BE and ZR were lower from 5:00 to 7:00 am local time (LT). Less road traffic and limited heater used influenced the lower concentrations of air pollutants in that period of time, thus reducing the pollutant emissions and improving the air quality. However, the PM_1 concentrations were higher during 18:00-19:00 pm LT in the evening due to the increasing of heater used. Simultaneously, the traffic flows were drastically increased during this period, which can provoke the local air pollution. In addition, as shown in **Figure 3.26 c, d**, the patterns of the average eBC were lower in BE and ZR from 5:00 to 7:00 am, and their temporal variability was comparable to PM_1 (**Figure 3.26 a, b**). The median average concentration of eBC was 1.05 μg/m^3 in BE and 1.16 μg/m^3 in ZR, indicating that the atmospheric concentration of eBC in ZR was slightly higher than that in BE. According to our observation, wood combustion was frequently found in the two villages. The trends of the average PNC in the 20 and 21 walks of BE and ZR were shown in **Figure 3.26 e, f**, respectively (a few of sampled PNC data were missing due to an instrument failure). The result showed that the peaks PNC were generally found in the afternoon (~16:00) due to the rise of traffic flow. Similarly, the PNC had the similar trends as PM_1 and eBC in both villages.

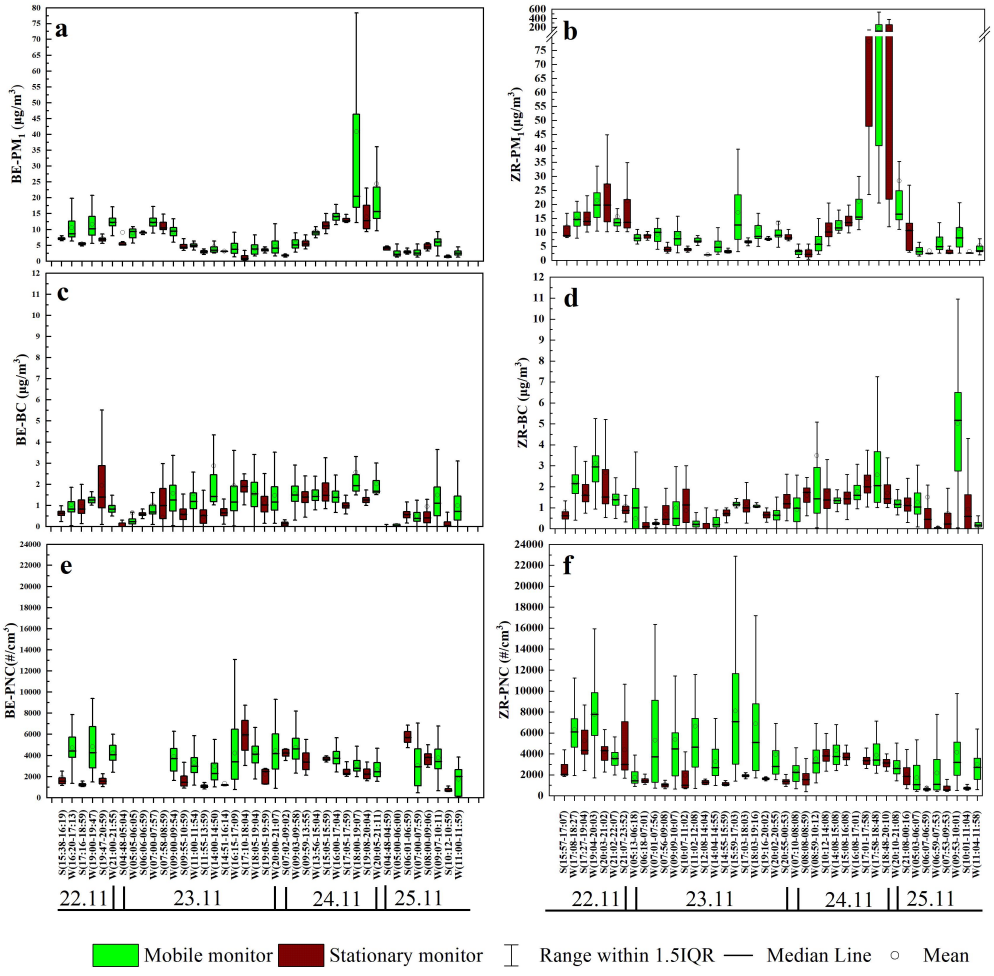


Figure 3.26: *Temporal fluctuations of PM_1, eBC concentrations and PNC from mobile and stationary measurements in BE and ZR on November 22-24, 2018 (S, stationary measurement; W, mobile measurement, there were no PNC data in BE-Walk 4, 5, 12, 13 and ZR-Walk 15).*

3.3.2 Hotspots parsing of air pollutants in BE and ZR

The mobile monitoring data were collected and analysed to observe the spatio-temporal trends of air pollutant. As shown in **Figure 3.27**, the peaks aggregation of multiple mobile patrol periods were found in relatively concentrated regions. It can roughly depict a high concentration of contaminated hotspots with high suspicion in the target area. According to the summary of the hotspot areas, there were no pollution sources such as factories around the two villages. Combining field-specific photos identified during sampling for field verification, the pollution was mainly produced from local pollution, such as wood burning. Therefore, the pollution source in this area was divided into the two following categories. (1) Traffic peaks: peaks of traffic in some sections of the walking path during peak hours due to the surge in traffic volume; (2) Biomass burning: the used of wood in the evening for heating.

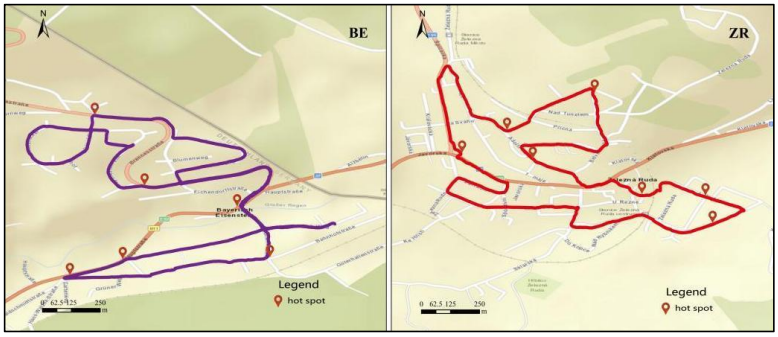


***Figure 3.27**: Schematic diagram of a highly-concentrated contaminated hotspot with high suspicion on the sampling route [49].*

4 Conclusions

In meso-scale, concentration data of particulate matter ($PM_{2.5}$ and PM_{10}), gaseous pollutants (CO, NO_2, NO_X, SO_2, and O_3), and meteorological factors of the monitoring sites of the past 11 years (2008-2018) were analysed to investigate the pollution trends in Germany. In this study, the atmospheric pollutants, especially $PM_{2.5}$ and PM_{10}, revealed a stable trend from 2008 to 2018 in Germany (Hurst index > 0.5) and reached the EU standard. However, the high exposure level to PM_{10} was found in some areas of Germany, which comparable with population density. By analysing the correlations of different gaseous pollutants and meteorological factors on the concentration of $PM_{2.5}$ and PM_{10}, CO and temperature had high correlations with $PM_{2.5}$ and PM_{10} in Germany.

In urban micro-scale, the mobile measurements of the exposure of air pollutants in traffic from the same sampling route covering a total distance of 835 km were conducted during different periods and different times of day in Augsburg. The spatio-temporal distributions of air pollutants concentrations were highly heterogenous, especially in the heating period, with the highest concentrations near traffic areas, especially at traffic intersections. The differences in air pollution concentrations in heating and non-heating periods were generally significant (p<0.05), which can be attributed to seasonal differences in meteorological conditions and emission sources. The relationships between BC and the meteorological parameters, especially temperature, wind speed, and relative humidity, were weak but highly significant (p<0.01). However, the relationships between BC and street view (especially buildings, roads, and vegetation) was significantly strong (p<0.01). Overall, an established street view imagery model in this study based on a random forest algorithm could explain the variability of the measured BC concentrations (71 % for eUVPM; 68 % for eBC, and 57 % for eBrC). In addition, based on the PMF analysis, the contribution of fireworks to the air pollution with PAHs, BC and metals on the individual New Year's days can be estimated. Following this, risk assessed based on elemental levels showed that $PM_{2.5}$-PTEs was below the carcinogenic risk threshold range, indicating no cancer risk was observed during observed periods (24^{th}.Dec.-7^{th}.Jan.$^{2nd\ year}$). However, the $\Sigma B[a]P_{TEQ}$ and $\Sigma B[a]P_{MEQ}$ have the higher values during New Year's days period, indicating that many toxic compounds were threatening human health in the New Year's days period.

In the micro-scale of the small-town area, a mobile monitoring approach was used to capture spatio-temporal trends of air pollutants at small-scale area. Mobile real-time measurement of ambient particle matter (PM_1, $PM_{2.5}$, PM_{10}), BC, and PNC have been carried out using mobile platforms in two neighboring villages, Bayerisch Eisenstein and Zelezna Ruda. The significant differences in PNC and PM concentrations were found in rural air pollutants between the two villages. The spatio-temporal distribution of air pollution hotspots in ZR was higher than that in BE. Overall, our study showed that mobile measurements were suitable for effectively assessing the spatio-temporal trends of air pollutants in the small-scale area.

References

[1]. Organization, W.H., Health and the environment: draft road map for an enhanced global response to the adverse health effects of air pollution: report by the Secretariat. World Health Assembly, 2016(69).

[2]. Stanaway, J.D., et al., Global, regional, and national comparative risk assessment of 84 behavioural, environmental and occupational, and metabolic risks or clusters of risks for 195 countries and territories, 1990–2017: a systematic analysis for the Global Burden of Disease Study 2017. The Lancet, 2018. 10159(392): p. 1923-1994.

[3]. Organization, W.H., WHO releases country estimates on air pollution exposure and health impact. 2016.

[4]. Anenberg, S.C., et al., Particulate matter-attributable mortality and relationships with carbon dioxide in 250 urban areas worldwide. Sci Rep, 2019. 9(1): p. 11552.

[5]. Jia, C., et al., Impacts of Independence Day fireworks on pollution levels of atmospheric polycyclic aromatic hydrocarbons (PAHs) in the U.S. Sci Total Environ, 2020. 743(743): p. 140774.

[6]. Lorenzo, G.R., et al., Measurement report: Firework impacts on air quality in Metro Manila, Philippines, during the 2019 New Year revelry. Atmospheric chemistry and physics, 2021. 21(8): p. 6155-6173.

[7]. Federal Environment Agency., 2020. 2.050 Tonnen Feinstaub durch Feuerwerk pro Jahr Feinstaubbelastung in der Atemluft an Neujahr besonders hoch. https://www.umweltbundesamt.de/presse/pressemitteilungen/2050-tonnen-feinstaub-durch-feuerwerk-pro-jahr (accessed date 11.08.2021).

[8]. Zhang, R., et al., Formation of Urban Fine Particulate Matter. Chemical Reviews, 2015. 115(10): p. 3803-3855.

[9]. Kanakidou, M., et al., Organic aerosol and global climate modelling: a review. Atmospheric Chemistry and Physics, 2005. 5(4): p. 1053-1123.

[10]. Zhang, Q., et al., Ubiquity and dominance of oxygenated species in organic aerosols in anthropogenically‐influenced Northern Hemisphere midlatitudes. Geophysical research letters, 2007. 34(13).

[11]. Kroll, J.H. and J.H. Seinfeld, Chemistry of secondary organic aerosol: Formation and evolution of low-volatility organics in the atmosphere. Atmospheric Environment, 2008. 42(16): p. 3593-3624.

[12]. Pereira, K.L., et al., Insights into the formation and evolution of individual compounds in the particulate phase during aromatic photo-oxidation. Environmental science & technology, 2015. 49(22): p. 13168-13178.

[13]. Song, C., et al., Air pollution in China: Status and spatiotemporal variations. Environmental Pollution, 2017. 227: p. 334-347.

[14]. Chai, F.G.J.C., Spatial and temporal variation of particulate matter and gaseous pollut_x0002_ants in 26 cities in China. J. Environ. Sci, 2014(26): p. 75e82.

[15]. He, J., et al., Air pollution characteristics and their relation to meteorological conditions during 2014–2015 in major Chinese cities. Environmental Pollution, 2017. 223: p. 484-496.

[16]. Xie, Y., et al., Spatiotemporal variations of PM2.5 and PM10 concentrations between 31 Chinese cities and their relationships with SO2, NO2, CO and O3. Particuology, 2015(20): p. 141-149.

[17]. Munir, S. and S. Munir, Modelling the non-linear association of particulate matter (PM10) with meteorological parameters and other air pollutants — a case study in Makkah. Arabian journal of geosciences, 2016. 9(1): p. 1-13.

[18]. Grivas, G. and A. Chaloulakou, Artificial neural network models for prediction of PM10 hourly concentrations, in the Greater Area of Athens, Greece. Atmospheric Environment, 2006. 40(7): p. 1216-1229.

[19]. Chaloulakou, A., M. Saisana and N. Spyrellis, Comparative assessment of neural networks and regression models for forecasting summertime ozone in Athens. Science of The Total Environment, 2003. 313(1-3): p. 1-13.

[20]. Hoek, G., et al., Association between mortality and indicators of traffic-related air pollution in the Netherlands: a cohort study. The Lancet, 2002. 360(9341): p. 1203-1209.

[21]. Liu, X., et al., Spatiotemporal Characteristics and Driving Factors of Black Carbon in Augsburg, Germany: Combination of Mobile Monitoring and Street View Images. Environmental Science & Technology, 2021. 55(1): p. 160-168.

[22]. Alas, H.D., et al., Spatial Characterization of Black Carbon Mass Concentration in the Atmosphere of a Southeast Asian Megacity: An Air Quality Case Study for Metro Manila, Philippines. Aerosol and Air Quality Research, 2018. 18(9): p. 2301-2317.

[23]. Wolf, K., et al., Land use regression modeling of ultrafine particles, ozone, nitrogen oxides and markers of particulate matter pollution in Augsburg, Germany. Science of The Total Environment, 2017. 579: p. 1531-1540.

[24]. Liu, M., et al., Spatial characteristics and determinants of in-traffic black carbon in Shanghai, China: Combination of mobile monitoring and land use regression model. Science of the Total Environment, 2019(658): p. 51-61.

[25]. Reche, C., et al., New considerations for PM, Black Carbon and particle number concentration for air quality monitoring across different European cities. Atmospheric Chemistry and Physics, 2011. 11(13): p. 6207-6227.

[26]. Dons, E., et al., Personal exposure to Black Carbon in transport microenvironments. Atmospheric Environment, 2012. 55: p. 392-398.

[27]. Babich, P., et al., Method comparisons for particulate nitrate, elemental carbon, and PM2.5 mass in seven U.S. cities. J Air Waste Manag Assoc, 2000. 50(7): p. 1095-105.

[28]. Idso, C.D., S.B. Idso and R.C. Balling Jr., THE URBAN CO2 DOME OF PHOENIX, ARIZONA. Physical Geography, 1998. 19(2): p. 95-108.

[29]. Brantley, H.L.H.G., Mobile air monitoring data-processing strategies and effects on spatial air pollution trends. Atmospheric Measurement Techniques, 2014. 7(7): p. 2169-2183.

[30]. Li B, L.X.N.X., Personal exposure to black carbon during commuting in peak and off peak hours in Shanghai. Science of the Total Environment, 2015(s524-525): p. 237-245.

[31]. Kolb, C.E., et al., Mobile Laboratory with Rapid Response Instruments for Real-Time Measurements of Urban and Regional Trace Gas and Particulate Distributions and Emission

Source Characteristics. Environmental Science & Technology, 2004. 38(21): p. 5694-5703.

[32]. Westerdahl, D., et al., Mobile platform measurements of ultrafine particles and associated pollutant concentrations on freeways and residential streets in Los Angeles. Atmospheric Environment, 2005. 20(39): p. 3597-3610.

[33]. Dons, E., et al., Personal exposure to Black Carbon in transport microenvironments. Atmospheric Environment, 2012. 55: p. 392-398.

[34]. Pattinson, W., I. Longley and S. Kingham, Using mobile monitoring to visualise diurnal variation of traffic pollutants across two near-highway neighbourhoods. Atmospheric Environment, 2014(94): p. 782-792.

[35]. Dons, E., et al., Street characteristics and traffic factors determining road users' exposure to black carbon. Science of The Total Environment, 2013. 447: p. 72-79.

[36]. Ragettli, M.S., et al., Commuter exposure to ultrafine particles in different urban locations, transportation modes and routes. Atmospheric Environment, 2013. 77: p. 376-384.

[37]. Ghassoun, Y., et al., Intra-urban variation of ultrafine particles as evaluated by process related land use and pollutant driven regression modelling. Science of The Total Environment, 2015. 536: p. 150-160.

[38]. Klompmaker, J.O., et al., Spatial variation of ultrafine particles and black carbon in two cities: Results from a short-term measurement campaign. Science of The Total Environment, 2015. 508: p. 266-275.

[39]. Choi, W., et al., The effects of the built environment, traffic patterns, and micrometeorology on street level ultrafine particle concentrations at a block scale: Results from multiple urban sites. Science of the Total Environment, 2016(553): p. 474-485.

[40]. Wang, L., et al., Estimate of aerosol absorbing components of black carbon, brown carbon, and dust from ground‐based remote sensing data of sun‐sky radiometers. Journal of Geophysical Research: Atmospheres, 2013. 12(118): p. 6534-6543.

[41]. Chen, X., S. Kang and J. Yang, Investigation of distribution, transportation, and impact factors of atmospheric black carbon in the Arctic region based on a regional climate-chemistry model. Environmental Pollution, 2020. 257(257): p. 113127.

[42]. Hennig, F., et al., Comparison of land-use regression modeling with dispersion and chemistry transport modeling to assign air pollution concentrations within the Ruhr area. Atmosphere, 2016. 3(7): p. 48.

[43]. Van den Hove, A., et al., Development of a land use regression model for black carbon using mobile monitoring data and its application to pollution-avoiding routing. Environmental Research, 2020. 183(183): p. 108619.

[44]. Qi, M. and S. Hankey, Using Street View Imagery to Predict Street-Level Particulate Air Pollution. Environmental Science & Technology, 2021. 55(4): p. 2695-2704.

[45]. Hankey, S. and J.D. Marshall, Land Use Regression Models of On-Road Particulate Air Pollution (Particle Number, Black Carbon, PM2.5, Particle Size) Using Mobile Monitoring. Environmental Science & Technology, 2015. 49(15): p. 9194-9202.

[46]. Apte, J.S., et al., High-Resolution Air Pollution Mapping with Google Street View Cars: Exploiting Big Data. Environmental Science & Technology, 2017. 51(12): p. 6999-7008.

[47]. Liang, J., et al., Automatic sky view factor estimation from street view photographs—a big data approach. Remote Sensing, 2017. 411(9): p. 1-17.

[48]. Liu, X., et al., Air pollution in Germany: Spatio-temporal variations and their driving factors based on continuous data from 2008 to 2018. Environmental Pollution, 2021. 276: p. 116732.

[49]. Liu, X., et al., Integration of air pollution data collected by mobile measurement to derive a preliminary spatiotemporal air pollution profile from two neighboring German-Czech border villages. Science of The Total Environment, 2020. 722: p. 137632.

[50]. Kuuluvainen, H., et al., Lung deposited surface area size distributions of particulate matter in different urban areas. Atmospheric Environment, 2016. 136: p. 105-113.

[51]. Begam, G.R., et al., Measurement and analysis of black carbon aerosols over a tropical semi-arid station in Kadapa, India. Atmospheric Research, 2016. 171: p. 77-91.

[52]. Petzold, A., et al., Recommendations for reporting "black carbon" measurements. Atmospheric Chemistry and Physics, 2013. 13(16): p. 8365-8379.

[53]. Olson, M.R.V.G., Investigation of black and brown carbon multiple-wavelength-dependent light absorption from biomass and fossilfuel combustion source emissions. Journal of Geophysical Research: Atmospheres, 2015. 13(120): p. 6682-6697.

[54]. Orasche, J., et al., In-situ derivatization thermal desorption GC-TOFMS for direct analysis of particle-bound non-polar and polar organic species. Atmospheric Chemistry and Physics, 2011. 17(11): p. 8977-8993.

[55]. Gu, J., et al., Source apportionment of ambient particles: Comparison of positive matrix factorization analysis applied to particle size distribution and chemical composition data. Atmospheric Environment, 2011. 45(10): p. 1849-1857.

[56]. IARC, Agents Classified by the IARC Monographs, Volumes 1 – 120. 2012.

[57]. Nisbet, I.C. and P.K. Lagoy, Toxic equivalency factors (TEFs) for polycyclic aromatic hydrocarbons (PAHs). Regulatory toxicology and pharmacology, 1992. 3(16): p. 290-300.

[58]. Malcolm, H.M. and S. Dobson, The Calculation of an Environmental Assessment Level (EAL) for Atmospheric PAHs Using Relative Potencies. 1994, London: Department of the Environment.

[59]. Jia, T.J.B., Measuring urban sprawl based on massive street nodes and the novel concept of natural cities. arXiv preprint arXiv:1010.0541. 2010.

[60]. Moran, The interpretation of statistical maps. Journal of the Royal Statistical Society B, 1948. 2(10): p. 243 – 251.

[61]. Geary, R.C., The contiguity ratio and statistical mapping. The Incorporated Statistician, 1954. 3(5): p. 115-145.

[62]. Zahn, C.T., Graph-theoretical methods for detecting and describing gestalt clusters. IEEE Trans on Computers, 1971. 1(20): p. 68-86.

[63]. Hurst, H.E., Long term storage. An experimental study, 1965.

[64]. Baillie, R.T., Long memory processes and fractional integration in econometrics. Journal of econometrics, 1996. 1(73): p. 5-59.

[65]. Wang, J., et al., Deep high-resolution representation learning for visual recognition.

IEEE transactions on pattern analysis and machine intelligence, 2020: p. 1-15.

[66]. Breiman, L., Bagging predictors. Machine learning, 1996. 2(24): p. 123-140.

[67]. Ho, T.K., The random subspace method for constructing decision forests. IEEE Transactions on Pattern Analysis and Machine Intelligence, 1998. 20(8): p. 832-844.

[68]. Xu, N., T.C. Fisher and J. Hong, Rademacher upper bounds for cross-validation errors with an application to the lasso. arXiv preprint arXiv:2007.15598., 2020.

[69]. Hao, Y. and F.H. Monti, US census unit population exposures to ambient air pollutants. International journal of health geographics, 2012. 1(11): p. 3.

[70]. Bundesamt, S., "Gemeinden in Deutschland nach Fläche, Bevölkerung und Postleitzahl am 30.09.2016". in German, 2016.

[71]. Diane Ivy, J.A.M.A., Development of Ambient Air Quality Population Weighted Metrics for Use in Time Series Health Studies. Journal of the Air & Waste Management Association, 2008. 5(58): p. 711-720.

[72]. Mohr, C., et al., Spatial Variation of Aerosol Chemical Composition and Organic Components Identified by Positive Matrix Factorization in the Barcelona Region. Environ Sci Technol, 2015. 49(17): p. 10421-30.

[73]. DEP, Characterization of risks due to inhalation of particulates by construction workers. Department of environmental protection, 2008.

[74]. Hamad, S., D. Green and J. Heo, Evaluation of health risk associated with fireworks activity at Central London. Air Quality, Atmosphere & Health, 2016. 7(9): p. 735-741.

[75]. Laidlaw, M.A., et al., Estimates of potential childhood lead exposure from contaminated soil using the US EPA IEUBK Model in Sydney, Australia. Environmental research, 2017. 156: p. 781-790.

[76]. Mills, C.T., et al., Modifications to EPA method 3060A to improve extraction of Cr (VI) from chromium ore processing residue-contaminated soils. Environmental science & technology, 2017. 51(19): p. 11235-11243.

[77]. Fang, W., Y. Yang and Z. Xu, PM10 and PM2. 5 and health risk assessment for heavy metals in a typical factory for cathode ray tube television recycling. Environmental science & technology, 2013. 21(47): p. 12469-12476.

[78]. Moya, J., et al., Exposure Factors Handbook. 2011 Edition. ed. 2011, Washington: US Environmental Protection Agency. Vol. 52.

[79]. Han, Y.M.C.J., Comparison of elemental carbon in lake sediments measured by three different methods and 150-year pollution history in eastern China. Environmental science & technology, 2011. 12(45): p. 5287-5293.

[80]. Liu, X., et al., Analysis of PAHs Associated with PM10 and PM2.5 from Different Districts in Nanjing. Aerosol and Air Quality Research, 2019. 19(10): p. 2294-2307.

[81]. Xia, Z., et al., Pollution level, inhalation exposure and lung cancer risk of ambient atmospheric polycyclic aromatic hydrocarbons (PAHs) in Taiyuan, China. Environmental Pollution, 2013(173): p. 150-156.

[82]. IARC, C., Agents Classified by the IARC Monographs, 2018. Volumes 1 – 123.

[83]. Chen, S.C. and C.M. Liao, Health risk assessment on human exposed to environmental

polycyclic aromatic hydrocarbons pollution sources. Science of the total environment, 2006. 1(366): p. 112-123.

[84]. Yao, W., et al., The factor analysis of fog and haze under the coupling of multiple factors -- taking four Chinese cities as an example. Energy Policy, 2020. 137: p. 111138.

[85]. Kiesewetter, G. and M. Amann, Urban PM2. 5 levels under the EU Clean Air Policy Package. 2014.

[86]. Pokorná, P., et al., Comparison of PM2. 5 chemical composition and sources at a rural background site in Central Europe between 1993/1994/1995 and 2009/2010: Effect of legislative regulations and economic transformation on the air quality. Environmental pollution, 2018(241): p. 841-851.

[87]. Guthrie, S., et al., The impact of ammonia emissions from agriculture on biodiversity. RAND Corporation and The Royal Society, Cambridge, UK, 2018.

[88]. Huang, Y., et al., Quantification of global primary emissions of PM2.5, PM10, and TSP from combustion and industrial process sources. Environ Sci Technol, 2014. 48(23): p. 13834-43.

[89]. Liu, X., et al., Assessment of German population exposure levels to PM10 based on multiple spatial-temporal data. Environmental Science and Pollution Research, 2020. 27(6): p. 6637-6648.

[90]. Cyrys, J., et al., Variation of NO2 and NOx concentrations between and within 36 European study areas: Results from the ESCAPE study. Atmospheric environment (1994), 2012. 62: p. 374-390.

[91]. Mavroidis, I. and M. Ilia, Trends of NOx, NO2 and O3 concentrations at three different types of air quality monitoring stations in Athens, Greece. Atmospheric Environment, 2012. 63: p. 135-147.

[92]. Pusede, S.E., A.L. Steiner and R.C. Cohen, Temperature and recent trends in the chemistry of continental surface ozone. Chem Rev, 2015. 115(10): p. 3898-918.

[93]. Huang, C., et al., Emission inventory of anthropogenic air pollutants and VOC species in the Yangtze River Delta region, China. Atmospheric Chemistry and Physics, 2011. 11(9): p. 4105-4120.

[94]. Jia, M., et al., Inverse relations of PM2. 5 and O3 in air compound pollution between cold and hot seasons over an urban area of east China. Atmosphere, 2017. 3(8): p. 59.

[95]. Khoder, M.I. and M.I. Khoder, Diurnal, seasonal and weekdays – weekends variations of ground level ozone concentrations in an urban area in greater Cairo. Environmental monitoring and assessment, 2009. 149(1): p. 349-362.

[96]. Yoo, J.M., et al., Spatiotemporal variations of air pollutants (O 3 , NO 2 , SO 2 , CO, PM 10 , and VOCs) with land-use types. 2015. 15(18): p. 10857 - 10885.

[97]. Zhang, L., et al., Impact of air humidity fluctuation on the rise of PM mass concentration based on the high-resolution monitoring data. Aerosol and Air Quality Research, 2016. 2(17): p. 543-552.

[98]. Zhang, Z., et al., National scale spatiotemporal land-use regression model for PM2.5, PM10 and NO2 concentration in China. Atmospheric Environment, 2018(192): p. 48-54.

[99]. Wang, J. and S. Ogawa, Effects of Meteorological Conditions on PM2.5 Concentrations

in Nagasaki, Japan. Int J Environ Res Public Health, 2015. 12(8): p. 9089-101.

[100]. Zalakeviciute, R., J. López-Villada and Y. Rybarczyk, Contrasted effects of relative humidity and precipitation on urban PM2.5 pollution in high elevation urban areas. Sustainability, 2018. 6(10): p. 2064.

[101]. Motallebi, N., C.J. Taylor and B.E. Croes, Particulate matter in California: part 2--Spatial, temporal, and compositional patterns of PM2.5, PM10-2.5, and PM10. J Air Waste Manag Assoc, 2003. 53(12): p. 1517-30.

[102]. Janssen, N.A., et al., Short-term effects of PM2.5, PM10 and PM2.5-10 on daily mortality in The Netherlands. Sci Total Environ, 2013. 463-464: p. 20-6.

[103]. Zhou, X., et al., Concentrations, correlations and chemical species of PM2.5/PM10 based on published data in China: Potential implications for the revised particulate standard. Chemosphere, 2016. 144: p. 518-26.

[104]. Pakbin, P., et al., Spatial and Temporal Variability of Coarse (PM10 − 2.5) Particulate Matter Concentrations in the Los Angeles Area. Aerosol Science and Technology, 2010. 44(7): p. 514 – 525.

[105]. Liu, Y.J. and R.M. Harrison, Properties of coarse particles in the atmosphere of the United Kingdom. Atmospheric Environment, 2011. 19(45): p. 3267-3276.

[106]. Wilson, W.E. and H.H. Suh, Fine particles and coarse particles: concentration relationships relevant to epidemiologic studies. J Air Waste Manag Assoc, 1997. 47(12): p. 1238-49.

[107]. Cheristanidis, S., G. Grivas and A. Chaloulakou, Determination of total and lung-deposited particle surface area concentrations, in central Athens, Greece. Environ Monit Assess, 2020. 192(10): p. 627.

[108]. Wagener, S., et al., Source apportionment of organic compounds in Berlin using positive matrix factorization - assessing the impact of biogenic aerosol and biomass burning on urban particulate matter. Sci Total Environ, 2012. 435-436: p. 392-401.

[109]. Gomes, J.F., J.C. Bordado and P.C. Albuquerque, On the assessment of exposure to airborne ultrafine particles in urban environments. J. Toxicol. Environ. health., 2012. 75(Part A): p. 1316-1329.

[110]. Chen, K., et al., Two-way effect modifications of air pollution and air temperature on total natural and cardiovascular mortality in eight European urban areas. Environment international, 2018(116): p. 186-196.

[111]. Pérez, N., et al., Variability of particle number, black carbon, and PM10, PM2. 5, and PM1 levels and speciation: influence of road traffic emissions on urban air quality. Aerosol Science and Technology, 2010. 7(44): p. 487-499.

[112]. Kim, K.H., et al., Carbonaceous and ionic components in ultrafine and fine particles at four sampling sites in the vicinity of roadway intersection. Atmospheric environment (1994), 2013. 74: p. 83-92.

[113]. Targino, A.C., et al., Hotspots of black carbon and PM2. 5 in an urban area and relationships to traffic characteristics. Environmental pollution, 2016(218): p. 475-486.

[114]. Buonanno, G., G.B. Marks and L. Morawska, Health effects of daily airborne particle

dose in children: direct association between personal dose and respiratory health effects. Environ Pollut, 2013. 180: p. 246-50.

[115]. Schnelle-Kreis, J., et al., Semi volatile organic compounds in ambient PM2.5. Seasonal trends and daily resolved source contributions. Environ Sci Technol, 2007. 41(11): p. 3821-8.

[116]. Jung, K.H., et al., Effects of heating season on residential indoor and outdoor polycyclic aromatic hydrocarbons, black carbon, and particulate matter in an urban birth cohort. Atmospheric Environment, 2010. 44(36): p. 4545-4552.

[117]. Merritt, A., et al., Personal exposure to black carbon in Stockholm, using different intra-urban transport modes. Science of the Total Environment, 2019. 674: p. 279-287.

[118]. Kumar, P., et al., New directions: air pollution challenges for developing megacities like Delhi. Atmospheric Environment, 2015. 122: p. 657-661.

[119]. Song, S., et al., Black carbon at a roadside site in Beijing: Temporal variations and relationships with carbon monoxide and particle number size distribution. Atmospheric Environment, 2013. 77: p. 213-221.

[120]. Janssen, N.A., et al., Black carbon as an additional indicator of the adverse health effects of airborne particles compared with PM10 and PM2. 5. Environmental health perspectives, 2011(119): p. 1691-1699.

[121]. Pan, H., et al., Investigation of roadside fine particulate matter concentration surrounding major arterials in five Southern Californian cities. J Air Waste Manag Assoc, 2013. 63(4): p. 482-98.

[122]. Wang, Y., et al., Are emissions of black carbon from gasoline vehicles overestimated? Real-time, in situ measurement of black carbon emission factors. Science of The Total Environment, 2016. 547: p. 422-428.

[123]. Nguyen, T., et al., Relationship between types of urban forest and PM2.5 capture at three growth stages of leaves. Journal of Environmental Sciences, 2015. 27: p. 33-41.

[124]. Farrell, W., et al., Near roadway air pollution across a spatially extensive road and cycling network. Environmental Pollution, 2016. 212: p. 498-507.

[125]. Brandt, C., et al., Ambient PM10 concentrations from wood combustion – Emission modeling and dispersion calculation for the city area of Augsburg, Germany. Atmospheric Environment, 2011. 45(20): p. 3466 - 3474.

[126]. Lin, C.C., L.S. Yang and Y.H. Cheng, Ambient PM2. 5, black carbon, and particle size-resolved number concentrations and the Ångström exponent value of aerosols during the firework display at the lantern festival in southern Taiwan. Aerosol and Air Quality Research, 2016. 2(16): p. 373-387.

[127]. Valerio, F., et al., Air Quality Standard for Benzo (a) pyrene (B[a]P) in Genoa (1994-1995). Polycyclic Aromatic Compounds, 1996. 1-4(9): p. 61-66.

[128]. Hickey, C., et al., Toxicity of particles emitted by fireworks. Particle and fibre toxicology, 2020. 1(17): p. 1-11.

[129]. Yu, H., J.V. Puthussery and V. Verma, A semi-automated multi-endpoint reactive oxygen species activity analyzer (SAMERA) for measuring the oxidative potential of ambient PM2. 5 aqueous extracts. Aerosol Science and Technology, 2020. 54(3): p. 304-320.

[130]. Lippmann, M., et al., National Particle Component Toxicity (NPACT) Initiative: integrated epidemiologic and toxicologic studies of the health effects of particulate matter components. Res Rep Health Eff Inst, 2013. 177(177): p. 5-13.

[131]. Ghio, A.J., Biological effects of Utah Valley ambient air particles in humans: a review. J Aerosol Med, 2004. 17(2): p. 157-64.

[132]. Means, B., Risk-assessment guidance for superfund. Volume 1. Human health evaluation manual. Part A. Interim report (Final) (No. PB-90-155581/XAB; EPA-540/1-89/002). Environmental Protection Agency, Washington, DC (USA). Office of Solid Waste and Emergency Response., 1989.

[133]. EPA, Peer review and peer involvement at the US Environmental Protection Agency. Science Policy Council, Office of the Science Advisor. Environmental Protection Agency, ID 2872, http://epa.gov/osa/spc/htm/perevmem.htm., 1994.

[134]. Ballesta, P.P., E. De Saeger and D. Kotzias, State of the art of the PAHs' analysis in ambient air. Ispra, 22-24 March 1999., 1999: p. 499-505.

[135]. Masiol, M., et al., Carcinogenic and mutagenic risk associated to airborne particle-phase polycyclic aromatic hydrocarbons: a source apportionment. Atmospheric Environment, 2012(60): p. 375-382.

[136]. Sarti, E., et al., The composition of PM1 and PM2. 5 samples, metals and their water soluble fractions in the Bologna area (Italy). Atmospheric Pollution Research, 2015. 4(6): p. 708-718.

[137]. Vecchi, R.M.G.V., The role of atmospheric dispersion in the seasonal variation of PM1and PM2.5 concentration and composition in the urban area of Milan (Italy). Atmospheric Environment, 2004. 27(38): p. 4437-4446.

[138]. Gomišček, B., et al., Spatial and temporal variations of PM1, PM2.5, PM10 and particle number concentration during the AUPHEP—project. Atmospheric Environment, 2004. 24(38): p. 3917-3924.

[139]. Gulliver, J. and D.J. Briggs, Personal exposure to particulate air pollution in transport microenvironments. Atmospheric Environment, 2004. 38(1): p. 1-8.

[140]. Yu, C.H., et al., A novel mobile monitoring approach to characterize spatial and temporal variation in traffic-related air pollutants in an urban community. Atmospheric environment, 2016(141): p. 161-173.

[141]. Healy, R.M., et al., Sources and mixing state of size-resolved elemental carbon particles in a European megacity; Paris. Atmospheric Chemistry and Physics, 2012. 4(12): p. 1681-1700.

[142]. Gu, J., et al., Spatial and temporal variability of PM10 sources in Augsburg, Germany. Atmospheric Environment, 2013(71): p. 131-139.

[143]. Gidhagen, L., et al., Urban scale modeling of particle number concentrationin Stockholm. Atmospheric Environment, 2005(39): p. 1711-1725.

[144]. Kutzner, R.D., et al., Long-term monitoring of black carbon across Germany. Atmospheric Environment, 2018. 185: p. 41-52.

[145]. Peters, J., et al., Monitoring PM10 and Ultrafine Particles in Urban Environments Using Mobile Measurements. Aerosol and Air Quality Research, 2013. 13(2): p. 509-522.

Appendix

1. LIST OF ABBREVIATIONS.....50

2. LIST OF FIGURES.....52

3. LIST OF TABLES.....55

4. PUBLICATION LIST..... 56

5. PUBLICATIONS FOR THE CUMULATIVE DISSERTATION.....57

6. CURRICULUM VITAE.....147

1. LIST OF ABBREVIATIONS

AOD	aerosol optical depth
AP	air pressure
AQG	air quality guidelines
BC	black carbon
BE	Bayerisch Eisenstein
BrC	brown carbon
C	coverage
CBD	central business district
CTM	chemistry Transport Model
COV	coefficient of variation
CV	cross-validation
D	fractal dimension
DM	dispersion model
DCTM	hybrid DM-CTM
EPA	Environmental Protection Agency
FP	form of precipitation (only rain, only snow, rain and snow)
GSV	Google street view imagery
IA	the fitting index (Index of Agreement)
ICP-MS	inductively coupled plasma-mass spectrometry
DTD-GC-TOF-MS	Derivatization Thermal Desorption Gas Chromatography Time-of-Flight Mass Spectrometry
LDSA	lung deposited surface area
Lu-Rh	lutetium and rhodium
LUR	land use regression
MAE	the mean absolute error
MEF	mutagenic equivalency factor
MSTFA	N-methyl-N-trimethylsilyl-trifluoroacetamide
OA	organic aerosol
PAH	polycyclic aromatic hydrocarbon
PH	daily precipitation height,
PM	particulate matter
PM_{10}	inhalable particles, particulate matter with an aerodynamic diameter of less than 10 µm
$PM_{2.5}$	fine particles, particulate matter with an aerodynamic diameter of less than 2.5 µm
PM_X	particulate matter with an aerodynamic diameter of less than x µm
PNC	particle number concentration
PWEL	population-weighted exposure level
QFF	quartz fibre filter
R	correlation coefficient
RF	random forest

RH	relative humidity
RMSE	the root mean squared error
ROS	Reactive Oxygen Species
RS	remote sensing
R/S	rescaled range
SD	sunshine duration
SnD	value snow depth
SOA	secondary organic aerosol
SVI	Street view images
T	temperature
TEF	toxic equivalency factor
VOCs	volatile organic compounds
UAS	University of Applied Sciences
UFP	ultrafine particles
UVPM	ultraviolet particulate matter
VP	vapor pressure
WD	wind direction
WHO	World Health Origination
WS	wind speed
ZR	Zelezna Ruda

2. LIST OF FIGURES

Figure 1.1: Schematic image of the formation, growth and processing of atmospheric aerosol. Adapted from Zhang et. al. Atmospheric particulate matter (PM) can be generated either directly from primary emissions (i.e., incomplete combustion can emit large amounts of PM directly) or secondarily from primary emissions of gaseous pollutants (sulfur dioxide, nitrogen oxides, and gaseous organic compounds) through chemical reactions with components in the atmosphere..... 1
Figure 1.2 Simplified mechanism for the atmospheric oxidation of a generic VOC. Thick black arrows denote reactions that can lead to a substantial decrease in volatility; gray arrows denote reactions that can lead to a substantial volatility increase 2
Figure 2.1: Sampling site and monitoring stations of air pollutants: a,"•" represents the fixed station of PM_{10}, "■" represents the fixed station of $PM_{2.5}$, "✛" represents the fixed station of gaseous pollutants (CO, SO_2, NO_2, and NO_X and O_3_8 h) in Germany; b, urban mobile monitoring road; and c, two small towns mobile monitoring road, the blue line represents Bayerisch Eisenstein, the purple line represents Železná Ruda.....5
Figure 2.2: Mobile monitoring platform. The platform consists of a trolley and a large aluminum box, which protects the instruments and positions the inlets at breathing height (approx. 1.5 m above ground). All monitoring instruments were installed in the stroller..... 6
Figure 2.3: Analysis procedures and in situ derivatization thermal desorption unit (figure at the right side of the bracket). Silylation reaction of polar organic species with MSTFA is shown at the top right corner. And the multiple ion chromatograms reflecting a sample collected at the aerosol characterization site at the UAS (urban background) (a) polycyclic aromatic hydrocarbons (PAH) (m/z 78+202+228+252+276+278), (b) oxidized PAH (o-PAH) (m/z 126+158+180+196+230+258). Adapted from Orasche et al. 2011.....7
Figure 2.4: Molecular structure of eight representative PAHs..... 8
Figure 3.1: The distribution of $PM_{2.5}$ and PM_{10} in rural, suburban, and urban areas of Germany...13
Figure 3.2: Daily average mass concentrations of seven air pollutants ($PM_{2.5}$, PM_{10}, CO, SO_2, O_3, NO_X, and NO_2) maps obtained by Ordinary Kriging from 2008-2018..... 14
Figure 3.3: Long-term change trends of $PM_{2.5}$ and PM_{10} from 2008 to 2018 in Germany.(a, The estimation of average $PM_{2.5}$ and PM_{10}; b,The interannual variability of $PM_{2.5}$ and PM_{10}, AQG (air quality guidelines)..... 14
Figure 3.4: Segmental analysis of $PM_{2.5}$ and PM_{10} in different functional areas from 2008 to 2018 in Germany (BG, background; TF, traffic; ID, industry).....15
Figure 3.5: Spatial agglomeration of annual PM_{10} concentrations in the monitoring sites in Germany..... 15
Figure 3.6: Two-dimension graphics cluster in districts with higher pollution, based on the data of PM_{10} in Germany.....16
Figure 3.7: Population density in Germany and the corresponding Moran's I scatter plots (data obtained from the Federal Statistical Office of Germany in 2016 and population density is expressed as inhabitants per km squared)..... 17
Figure 3.8: The daily (a) and monthly (b) variations in the total PWEL and MEAN concentration

in 2017..... 17
Figure 3.9: Accumulation population exposure to PM_{10} concentrations (Units: μg/m^3)..... 17
Figure 3.10: The normalized coefficients of gaseous pollutants with $PM_{2.5}$ and PM_{10}.....18
Figure 3.11: Impact of meteorological factors on $PM_{2.5}$ and PM_{10} (FP, precipitation form (only rain, only snow, rain and snow); WS, a daily mean wind speed (m/s); PH, a daily precipitation height (mm)； SD, a daily sunshine duration (h); SnD, a daily value snow depth (cm); C, a daily average of coverage (1/8); VP, a daily average of vapor pressure (hPa); AP, a daily mean air pressure (hPa); RH, a daily average relative humidity (%); T, a daily average temperature (°C))..... 19
Figure 3.12: The correlation between annual average concentrations of $PM_{2.5}$ *vs.* PM_{10} (a), $PM_{10-2.5}$ *vs.* PM_{10} (b), and $PM_{2.5}$ vs. $PM_{10-2.5}$ (c) base on 11 years of data collection all over Germany..... 20
Figure 3.13: The box diagram of various pollutants in total year, non-heating and heating periods in the Augsburg urban area during 2018-2020..... 21
Figure 3.14: Spatial exposure of the air pollutants (PM_1, $PM_{2.5}$, PM_{10}, UVPM, BC, BrC, PNC, and LDSA) for whole walk during non-heating and heating periods in downtown Augsburg. © OpenStreetMap contributors 2021. Distributed under a Creative Commons BY-SA License..... 22
Figure 3.15: Temporal distribution of the air pollutants exposure concentrations at different micro-environments and different time (morning, 4:00-11:00; afternoon, 14:00-17:00; evening, 18:00-22:00) in Augsburg during non-heating and heating periods.....23
Figure 3.16: Correlation matrix of measured compounds in different traffic volume (A, all roads; N, no traffic volume (park area); L, low traffic volume; M, middle traffic volume; H, high traffic volume, *p<0.05, **p<0.01, white bands represent nonsense).....24
Figure 3.17: Correlation matrix of measured compounds in different traffic volumes (A, all roads; N, no traffic volume (park area); L, low traffic volume; M, middle traffic volume; H, high traffic volume; WS, wind speed (m/s); T, temperature (°C); RH, relative humidity (°); **p<0.01)..... 24
Figure 3.18: The random forest based-approach and estimation of the spatial distribution of air pollutants (a, b, c: random forest optimization for eUVPM, eBC, and eBrC; d, e, f: Spatial distribution for estimationto eUVPM, eBC, and eBrC exposure).....25
Figure 3.19: Left panel, Time series of the hourly mean concentrations of PM_{10} (a), $PM_{2.5}$ (c) and eBC (e). Right panel, summarized comparison of the hourly means of the concentrations of PM_{10} (b), $PM_{2.5}$ (d) and eBC (f) on New Year's Day with the reference periods before and after. The significance levels (**, p<0.01, *, p<0.05) refer to the differences between the respective means.26
Figure 3.20: Left panel, Time series of the daily mean concentrations of representative metal elements (S, K, Cr, Pb, Fe, and Na). Right panel, summarized comparison of the daily means of the concentrations of representative metal elements on New Year's Day with the reference periods before and after. The significance levels (**, p<0.01, *, p<0.05) refer to the differences between the respective means.....27
Figure 3.21: Left panel, Time series of the daily mean concentrations of 11 PAHs. Right panel, summarized comparison of the daily means of the concentrations of 11 PAHs on New Year's Day with the reference periods before and after.....28
Figure 3.22: The profiles of 3 factors separated in the PMF analysis, including firework emissions, domestic heating, and traffic emissions..... 29

Figure 3.23: The non-carcinogenic risk factor HQ for heavy metals in the atmosphere at the sampling sites during New Year's Day and whole period.....30
Figure 3.24: $\Sigma B[a]P_{TEQ}$ (left) and $\Sigma B[a]P_{MEQ}$ (right) concentrations of PAHs in Augsburg during New Year's Day and whole Periods.....31
Figure 3.25: PM_1, BC, and PN concentrations for the different walks (y-axis) at a selection of road (x-axis) in BE and ZR. The colours are scaled between the extremes and differ between the plots. White pixels represent no data due to instrument failures and Black pixels represent abnormal peak samples 33
Figure 3.26: Temporal fluctuations of PM_1, eBC concentrations and PNC from mobile and stationary measurements in BE and ZR on November 22-24, 2018 (S, stationary measurement; W, mobile measurement, there were no PNC data in BE-Walk 4, 5, 12, 13 and ZR-Walk 15)..... 34
Figure 3.27: Schematic diagram of a highly-concentrated contaminated hotspot with high suspicion on the sampling route.....35

3. LIST OF TABLES

Table 2.1: Targeted analytes and the analytical parameters used for calculating reported concentrations.....8
Table 2.2: The parameters of physical-chemical and toxicological properties for PAHs 8
Table 2.3: Risk parameters for different age groups used for Augsburg..... 12
Table 3.1: Spatial autocorrelation index of PM_{10} concentrations in Germany..... 16
Table 3.2: The correlations between gaseous pollutants and the $PM_{2.5}$ and PM_{10} (**, p<0.01, *, p<0.05)..... 18
Table 3.3: The correlation between meteorological factors and the particulate matter (**, p<0.01).19
Table 3.4: The evaluation of the street view image models for eUVPM, eBC, and eBrC concentration estimation..... 26
Table 3.5: Health risk assessment of PAH and metal elements for different groups in Augsburg during the whole period (Dec.24-Jan.07$^{2nd\ year}$)..... 31

4. PUBLICATION LISTS

[1]**Liu, X.**, Zhang, X., Schnelle-Kreis, J., Jakobi, G., Cao, X., Cyrys, J., ... & Zimmermann, R. (2021). Spatiotemporal Characteristics and Driving Factors of Black Carbon in Augsburg, Germany: Combination of Mobile Monitoring and Street View Images. ***Environmental Science & Technology***, 1, 55, 160-168.

[2]**Liu, X.**, Hadiatullah, H., Zhang, X., Schnelle-Kreis, J., ... & Zimmermann, R. (2021). Combined land-use and street view image model for estimating black carbon concentrations in urban areas. ***Atmospheric Environment,*** 118719.

[3]**Liu, X.**, Hadiatullah, H., Tai, P., Xu, Y., Zhang, X., Schnelle-Kreis, J., ... & Zimmermann, R. (2021). Air pollution in Germany: spatio-temporal variations and their driving factors based on continuous data from 2008 to 2018. ***Environmental Pollution***, 116732.

[4]**Liu, X.**, Hadiatullah, H., Zhang, X., Hill, L. D., White, A. H., Schnelle-Kreis, J., ... & Zimmermann, R. (2021). Analysis of mobile monitoring data from the microAeth® MA200 for measuring changes in black carbon on the roadside in Augsburg. ***Atmospheric Measurement Techniques,*** 14, 5139–5151.

[5]**Liu, X.**, Schnelle-Kreis, J., Zhang, X., Bendl, J., Khedr, M., Jakobi, G., ... & Zimmermann, R. (2020). Integration of air pollution data collected by mobile measurement to derive a preliminary spatiotemporal air pollution profile from two neighboring German-Czech border villages. ***Science of The Total Environment***, 722, 137632.

[6]**Liu, X.**, Huang, H., Jiang, Y., Wang, T., Xu, Y., Abbaszade, G., ... & Zimmermann, R. (2020). Assessment of German population exposure levels to PM10 based on multiple spatial-temporal data. ***Environmental Science and Pollution Research***, 27(6), 6637-6648.

[7]**Liu, X**., Schnelle-Kreis, J., Schloter-Hai, B., Ma, L., Tai, P., Cao, X., ... & Zimmermann, R. (2019). Analysis of PAHs Associated with PM_{10} and $PM_{2.5}$ from Different Districts in Nanjing. ***Aerosol and Air Quality Research***, 19, 2294-2307.

[8]Khedr, M., **Liu, X.***, Hadiatullah, H., Orasche, J., Zhang, X., Cyrys, J., ... & Schnelle-Kreis, J*. (2022). Influence of New Year's fireworks on air quality–A case study from 2010-2021 in Augsburg, Germany. ***Atmospheric Pollution Research***, 101341.

5. PUBLICATIONS FOR THE CUMULATIVE DISSERTATION

Publication I

Liu, X., Huang, H., Jiang, Y., Wang, T., Xu, Y., Abbaszade, G., ... & Zimmermann, R. (2020). Assessment of German population exposure levels to PM10 based on multiple spatial-temporal data. ***Environmental Science and Pollution Research***, 27(6), 6637-6648.

Appendix

Environmental Science and Pollution Research
https://doi.org/10.1007/s11356-019-07071-0

RESEARCH ARTICLE



Assessment of German population exposure levels to PM10 based on multiple spatial-temporal data

Xiansheng Liu[1,2] · Haiying Huang[3,4] · Yiming Jiang[3,4] · Tao Wang[5] · Yanling Xu[6] · Gülcin Abbaszade[1] · Jürgen Schnelle-Kreis[1] · Ralf Zimmermann[1,2]

Received: 21 May 2019 / Accepted: 14 November 2019
© Springer-Verlag GmbH Germany, part of Springer Nature 2019

Abstract
Particulate matter is the key to increasing urban air pollution, and research into pollution exposure assessment is an important part of environmental health. In order to classify PM_{10} air pollution and to investigate the population exposure to the distribution of PM_{10}, daily and monthly PM_{10} concentrations of 379 air pollution monitoring stations were obtained for a period from 01/01/2017 to 31/12/2017. Firstly, PM_{10} concentrations were classified using the head/tail break clustering algorithm to identify locations with elevated PM_{10} levels. Subsequently, population exposure levels were calculated using population-weighted PM_{10} concentrations. Finally, the power-law distribution was used to test the distribution of PM_{10} polluted areas. Our results indicate that the head/tail break algorithm, with an appropriate segmentation threshold, can effectively identify areas with high PM_{10} concentrations. The distribution of the population according to exposure level shows that the majority of people is living in polluted areas. The distribution of heavily PM_{10} polluted areas in Germany follows the power-law distribution well, but their boundaries differ from the boundaries of administrative cities; some even cross several administrative cities. These classification results can guide policymakers in dividing the country into several areas for pollution control.

Keywords PM_{10} air pollution · Spatio-temporal distribution · Head/tail · Power-law distribution · Population exposure · Germany

Introduction

Particulate matter (PM) air pollution can be significantly detrimental to human health (Boldo et al. 2006). The World Health Organization reported that about 0.8 million people are dying each year due to air pollution (WHO 2002). Samet (2000) have found that the relative mortality rate, caused by cardiovascular and respiratory diseases, increases by 0.68 percent per each 10 $\mu g/cm^3$ increase in the PM_{10} level. As PM air pollution events occur frequently, this topic has aroused high social attention and academic interest. Furthermore, PM is currently considered to be the best indicator for health effects by ambient air pollution (Burnett et al. 2014; WHO 2014). Therefore, knowledge of the present state and the spatio-temporal distribution of PM and

Responsible editor: Gerhard Lammel

Electronic supplementary material The online version of this article (https://doi.org/10.1007/s11356-019-07071-0) contains supplementary material, which is available to authorized users.

✉ Jürgen Schnelle-Kreis
juergen.schnelle@helmholtz-muenchen.de

[1] Joint Mass Spectrometry Center, Cooperation Group Comprehensive Molecular Analytics, Helmholtz Zentrum München, German Research Center for Environmental Health, Ingolstädter Landstr. 1, 85764 Neuherberg, Germany

[2] Joint Mass Spectrometry Center, Chair of Analytical Chemistry, University of Rostock, 18059 Rostock, Germany

[3] Institute of Virology, Helmholtz Zentrum München, German Research Center for Environmental Health, Ingolstädter Landstr. 1, 85764 Neuherberg, Germany

[4] Institute of Virology, Technical University of Munich, Trogerstr. 30, 81675 München, Germany

[5] Shanghai Key Laboratory of Atmospheric Particle Pollution and Prevention, Department of Environmental Science & Engineering, Fudan University, Shanghai 200433, China

[6] College of Plant Health and Medicine, Qingdao Agricultural University, Qingdao 266109, China

Published online: 24 December 2019

Appendix

evaluation of the adverse health effects, caused by PM_{10} pollution, are important for understanding this air pollution problem and protecting human health and establishing pollution control policies.

So far, it has been shown that frequent exceedances of the limit for PM_{10} concentrations have been observed widely across Western Europe from the end of the last century to the beginning of this century, particularly in Switzerland, Belgium, Germany, Italy, Norway, and the Czech Republic (Harrison et al. 2008). According to reports, the assumption that exposure is uniform within each region may have resulted in errors in the estimation of exposure, especially for pollutants with important local sources (Hoek et al. 2002). One way to solve this problem is to use spatial interpolation to address the data collected from pollutant detection stations in the study area and to obtain a continuous plane of pollutant concentrations. The Geographic Information System (GIS) has achieved broad application as an interdisciplinary tool, especially in Environmental Science. Johansson et al. (2007) analyzed how differences in emissions, background concentrations, and meteorology affect the temporal and spatial distribution of PM_{10} based on measurements and dispersion modelling in Stockholm, Sweden, and found that up to 90% of the locally emitted PM_{10} may be due to road abrasion. Sampson et al. (2013) successfully predicted $PM_{2.5}$ concentrations at a fine spatial scale across the USA using regionalized universal kriging. Long et al. (2018) estimated sub district-level daily $PM_{2.5}$ concentrations by means of the block cokriging approach.

The population exposure study mainly includes two methods, the sampling method and the mathematical model method. The sampling method can be accurate to the individual exposure in different micro-environments, but the method has limited sampling points and large local environmental differences, resulting in a narrower range of applications. The mathematical model method is an exposure assessment method that combines pollution concentration distribution data and population distribution data and finally obtains a model with strong applicability. Jerrett et al. (2005) reviewed six classes of intraurban exposure models, including (i) proximity-based assessments, (ii) statistical interpolation, (iii) land use regression models, (iv) line dispersion models, (v) integrated emission-meteorological models, and (vi) hybrid models. Anenberg (2010) estimated the global burden of mortality due to O_3 and $PM_{2.5}$ from anthropogenic emissions using global atmospheric chemical transport model simulations of preindustrial and present-day (2000) concentrations to derive exposure estimates. Eeftens (2012) used land use regression (LUR) models for modeling small-scale spatial variation in air pollution concentrations and estimating individual exposure for participants of cohort studies. The more intraurban concentration studies and health studies are described in detail elsewhere (Jerrett et al. 2005).

However, studying human exposure to ambient air pollution, demographic data is also calculated mainly for the total population of the examined city, ignoring the non-uniformity of the spatial distribution of pollutants and populations and their inherent time-varying characteristics. Kousa et al. (2002) presented a mathematical model for the determination of exposure to ambient air pollution in an urban area to evaluate the spatial and temporal variation of the average exposure of an urban population to ambient air pollution in different microenvironments with reasonable accuracy. The model developed has been designed to be utilized by municipal authorities in urban planning. Therefore, in this paper, the total population of the study area was not used as the exposed population. Rather, interpolated spatial data of the population after an investigation was used to obtain a continuous plane of population density. In addition, the spatial distribution of residents is inconsistent with the spatial distribution of air pollution. If air pollution concentrations are simply used to characterize pollution exposures in large spaces, true levels of exposure will not be reflected. Therefore, a population-weighted air pollution exposure model was proposed. The pollutant concentration was superimposed on the population data to obtain a population-weighted concentration. Then the population-weighted exposure level (PWEL) was used to estimate the potential exposure to PM_{10} in Germany in 2017. In this way, different numbers of people in the grid were exposed to different concentrations of atmospheric pollutants.

Based on these knowledge, the objective of this study are to classify PM_{10} air pollution for each month of 2017 based on the head/tail breaks classification method; to explore the population exposure to the distribution of PM_{10} using geospatial statistical tools systematically; to portray the present situation of PM_{10} air pollution with high PM_{10} levels; and to test the distribution of PM_{10} heavily polluted areas using the power-law distribution. These estimates may be useful in assessing health impacts through linkage studies and in communicating with the public and policymakers for potential intervention.

Methods

Monitoring data

Daily PM_{10} concentration data was obtained from the German Federal Environment Agency (UBA) networks (https://www.umweltbundesamt.de/en/) and used to calculate monthly and annual means for each monitoring location. Only data that met the minimum inclusion criteria (within the detection limit) were included. The observations included the daily PM_{10} concentrations at 379 monitoring sites in Germany in 2017 (Fig. 1), which were used to characterize the spatial variability of particle concentrations.

Data analysis was performed with the Data Processing System 9.5 (DPS) (Tang and Zhang 2013). For the spatial autocorrelation and agglomeration analysis, the GeoDA1.4.0

Appendix

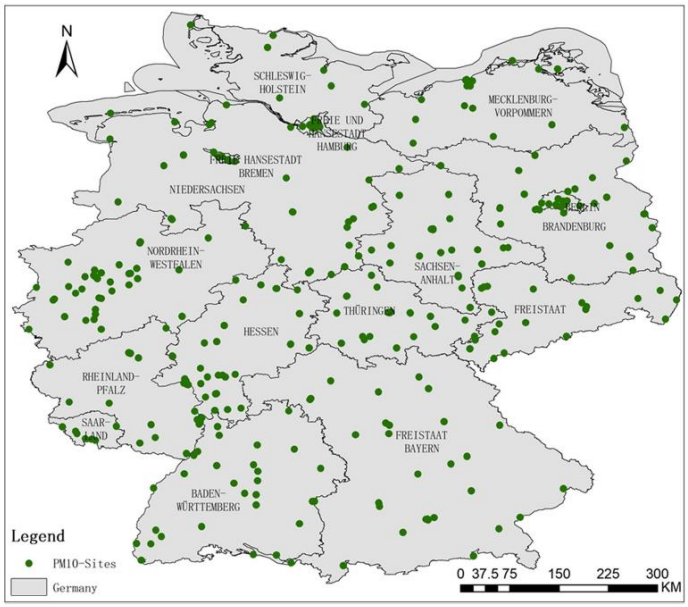


Fig. 1 Locations of surface air pollution PM_{10} monitoring stations in Germany during 2017

and Arc GIS 10.2 were used. Results are displayed with ArcView 4.0.

Spatial analysis

Spatial distributions of the average atmospheric pollutant concentrations for 2017 were simulated using ordinary kriging. Liao et al. (2006) showed that investigation of GIS approaches for estimating daily mean geocoded location-specific air pollutant concentrations supports the use of a spherical model to perform lognormal ordinary kriging on a national scale.

Spatial autocorrelation

Observations made at different locations may not be independent. For example, measurements made at nearby locations may be closer in value than measurements made at locations farther apart. This phenomenon is called spatial autocorrelation, which can be calculated using Moran's I (Moran 1948; Geary 1954).

Spatial autocorrelation measures the correlation of a variable with itself through space. Spatial autocorrelation can be positive or negative. Positive spatial autocorrelation appears when similar values occur near one another, while there is negative spatial autocorrelation when dissimilar values occur near one another.

The spatial autocorrelation method for identifying the correlation of atmospheric pollutant profiles is described in detail elsewhere (Fang et al. 2016; Xu et al. 2016). Fang et al. (2016) covers global spatial autocorrelation (Global Moran's I (GMI)) and local spatial autocorrelation (Local Moran's I (LMI)) (Anselin 1995), which are defined as follows:

$$GMI = \frac{n}{S_0} \frac{\sum_{i=1}^{n} \sum_{j=1}^{n} W_{i,j} Z_i Z_j}{\sum_{i=1}^{n} Z_i^2} \quad (1)$$

where Z_i is the deviation of an attribute for feature i from its mean ($\chi_i - \overline{X}$), $W_{i,j}$ is the spatial weight between features i and j, n is equal to the total number of features, and S_0 is the aggregate of all the spatial weights:

$$S_0 = \sum_{i=1}^{n} \sum_{j=1}^{n} W_{i,j} \quad (2)$$

The local Moran's I statistic is given as

$$LMI_i = \frac{x_i - \overline{X}}{S_i^2} \sum_{j=1, j \neq i}^{n} w_{i,j} \left(x_i - \overline{x} \right) \quad (3)$$

Appendix

where x_i is an attribute for feature j, $\bar{x}$ is the mean of the corresponding attribute, $W_{i,j}$ is the spatial weight between feature i and j, and

$$S_i^2 = \frac{\sum_{j=1, j\neq i}^{n} W_{i,j}}{n-1} \bar{X}^2 \quad (4)$$

In general, Moran's I is similar but not equivalent to a correlation coefficient. Its value varies between −1 and 1 and represents negative and positive spatial autocorrelation, respectively. Positive and significant Moran's I values indicate that nearby areas have similar spatial patterns, whereas negative values indicate the contrary. If the Moran's I is zero, the values are arranged randomly. GMI is used to judge the spatial agglomeration degree of Germany's PM_{10}, and LMI is used to examine the spatial distribution of the "hot spots" and "cold spots."

Since the Moran's I statistic follows a random distribution or a nearly normal distribution, the significance test can be converted into a Z value representing the normal distribution statistic. At the 5% significance level, if the Z value is greater than 1.96 or less than −1.96, there is a spatially significant positive or negative correlation between the observations, while if the Z value is between −1.96 and 1.96, the spatial correlation is not significant. The correlation is extremely significant when Z is greater than 2.58. The standard statistic Z is calculated by following formula:

$$Z = \frac{I - E(I)}{\sqrt{VAR\ (I)}} \quad (5)$$

where E (I) and VAR (I) are expectation and variance of Moran's I, respectively, and E (I) = (−1)/(n−1). When Z is positive and significant, it indicates a positive spatial correlation and the observed values are aggregated. On the contrary, when Z is negative and significant, indicating a negative correlation, the observations tend to be discretely distributed. Z = 0 means that the observations are randomly distributed.

Two-dimension graphics cluster

The graph theory clustering method, also known as the largest (small) support tree clustering algorithm, was first proposed by Zahn (1971). The traditional graph-theoretical clustering methods process the local area's joint characteristics of sample data as the main information. These methods then lead to most joint data in clusters not being settled. Initializing each grid cell as a class makes a large body of processing data. Based on spatial relation, a two-dimension graphics cluster could solve this problem. The method not only considers the relation between grid cells and their neighborhood regions but also makes classes depending on the uniform gray level of grid cells. The PM10 spatial distribution analysis based on the two-dimensional graph theory clustering method combines the spatial analysis of ArcGIS with the tree algorithm of graph theory. The specific methods are as follows: first, the spatial coordinates of the monitoring points are extracted and the spatial autocorrelation analysis is performed. Then, in the DPS software, the minimum spanning tree is divided into n subtrees by using the two-dimensional graph theory minimum tree method, that is, the research area is divided into n regions. A network diagram of the relationship between the partition units is generated by means of the DPS (Data Processing System). Finally, the directly connected places indicate that the adjacency of each unit space and the comprehensive conditional similarity of each aspect are relatively high. When the PM_{10} pollution is controlled, a common control method can be adopted.

Evaluation of the effect of PM_{10} on human health based on GIS

The rule of the head/tail division and power-law distribution

The head/tail breaks classification can be helpful for finding the ht-index of the data, which in turn is helpful for finding the inherent structure of the data. The ht-index based on this kind of classification approach is a special indicator to describe the complexity of the data, and it is an indicator of the underlying hierarchy of the data (Liu 2014). Liu (2014) has used nighttime lighting data and ht-index classification methods to extract the naturally defined urban boundaries constitute that we call natural cities. The method has been described in detail in Jiang and Yin (2014) and Liu (2014). Briefly, the rules for head/tail splitting determine the class or hierarchy of data using a heavy-tailed distribution, which can then be referred to as a scaling, hierarchy, or zoom level. The head of the heavy-tailed distribution contains a small number of large values, while the tail of the heavy-tailed distribution contains the majority of small values. For example, if a given data value is heavy-tailed, the average value of the data value can be divided into all the values to include the head portion of the data value equal to or greater than the average value. Otherwise, the data value should be included in the tail, and then the steps should be repeated until the data values in the head are no longer heavy-tailed. The main focus of the head and tail classification is low-frequency events. These events are more important than high-frequency events because low-frequency events have a larger impact than high-frequency events.

In summary, the head/tail classification ability captures the inherent level of data better than the natural rest classification. The head/tail classification is suitable for discovering the underlying hierarchy and the level of detail inherent in the data. The generalization of the data is now based more efficiently on the captured hierarchy.

Appendix

Also, a heavy-tailed distribution is a common distribution pattern in dynamic and unbalanced nature (Mohajeri 2013). In this case, the data is heavily right skewed, with a minority of large values in the head and a majority of small values in the tail, and is commonly characterized by a power-law, a lognormal, or an exponential function (Jiang 2013). Therefore, to determine if a variable obeys a power-law distribution, it can be judged by plotting the data as a scatter plot on a double logarithmic scale. If the random variable fitting result is a linear function, then the cumulative probability obeys the power-law distribution. For more detail on power-law distribution, see the published literature by Anderson (2005).

Estimation of the population exposure to PM_{10}

Population is an important indicator for measuring the PWEL (Hao et al. 2012). The population data, obtained from the Federal Statistical Office of Germany, was initially analyzed (Bundesamt 2016). However, the spatial distribution of residents in space is inconsistent with the spatial distribution of atmospheric pollution (Ivy et al. 2008). So, if air pollution concentrations are simply used to characterize pollution exposure in a large space, the true level of exposure to residents will not be captured. Therefore, the population-weighted exposure level model is used (Sun et al. 2013). Given grid (1.0 km•1.0 km), i, the population weighted exposure equation is as follows:

$$\mathrm{PWEL} = \sum(P_i \times C_i)/\sum P_i \tag{6}$$

where P_i is the population in the grid cell, i, and Ci is its average PM_{10} concentration in the grid cell.

In our study, we used 50 μg/m^3 as pollution concentration, which is the PM10 limit value corresponding to the mean daily PM_{10} concentration. With this value, we calculated the number of exposure days exceeding the standard during the research period (which can indicate the exposure intensity in different parts of the area).

Spatial distribution of PM_{10} pollution exposure

Population PM_{10} exposure intensity equals the duration of population exposure per unit area exposed to severe PM_{10} pollution. The formula for PM_{10} exposure intensity is as follows:

$$N_{ij}^{T} = \sum_{t=t_1}^{t_2} 1\left(C_{ijt} \geq STD\right) \tag{7}$$

$$\mathrm{EI}_{ij} = N_{ij}^{T}\frac{P_{ij}}{A_{ij}} \tag{8}$$

where A_{ij} is the area of the (i,j)th grid cell (1.0 km•1.0 km), P_{ij} is the population of the (i,j)th grid cell, and N_{ij}^{T} is the accumulated pollution days of the (i,j)th grid cell. EI_{ij} is the pollution exposure intensity of the (i,j)th grid cell at time T, in day·person/km^2. STD = 50 μg/m^3 for the EU standard. As shown in the formula above, the intensity of pollution exposure is directly related to the accumulated days of pollution and population density.

Results and discussion

Pollution area development and changes in Germany

Firstly, in order to reasonably divide the area of high pollution and the area of severely polluted areas reflecting rich urban information, this section used the average of the first and last divisions of PM_{10} pollution concentration in 2017 to extract the high pollution area of the PM_{10} air pollution concentration. The extraction results were compared and analyzed. As shown in Fig. 2, the results of the concentration distribution area were extracted using the first layer to the third layer of the average concentration of PM_{10}. According to the comparison and analysis, when the extraction value was 17.20 μg/m^3, the extraction range was too wide, and many cities were connected. When the extraction value was 18.47 μg/m^3, the extraction effect captured the details of individual cities. However, when the extraction value was 19.38 μg/m^3, the extraction effect was poor, and more details were ignored. Therefore, the average value of 18.47 μg/m^3 was selected as the PM_{10} pollution area division value. In order to better compare the extracted values, this paper also analyzed the values based on the WHO standard (20 μg/m^3 for PM_{10}).

As shown in Fig. 2, higher PM_{10} concentrations occurred in the states of Bavaria, North Rhine-Westphalia, Saxony-Anhalt, and Berlin. In these areas, PM_{10} concentrations exceeded the value of 18.47 μg/m^3.

Secondly, 18.47 μg/m^3 was used as the PM_{10} pollution area division value to extract the PM_{10} pollution area range of all Germany for each month in 2017 (Fig. 3). Among them, the pollution range from January to March was relatively wide, and the pollution distribution range was relatively small in the other months. In June, the PM_{10} concentration was below the value throughout all of Germany. In 2017, PM_{10} pollution was mainly concentrated in North Rhine-Westphalia, Brandenburg, and Berlin; in these areas, the pollution was the most widely distributed and lasted permanently.

Spatial autocorrelation of PM_{10} concentration

To better reflect the spatio-temporal changes of the PM_{10} concentrations in Germany, the Global Moran's I was employed to identify the spatial autocorrelation of the PM_{10} concentrations. Further, the analysis of spatial autocorrelation could help to determine whether sparse ground monitoring sites can meet the requirements.

Appendix

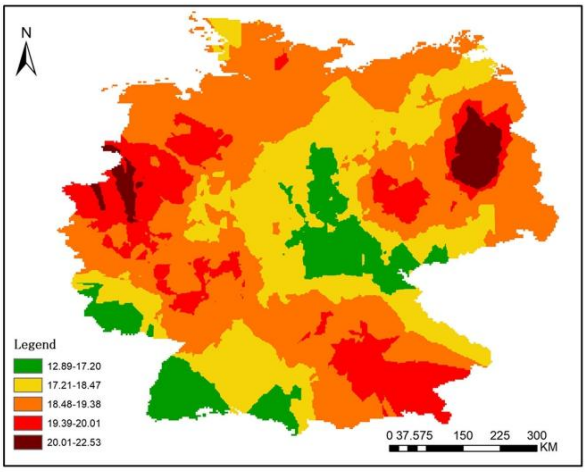


Fig. 2 Distribution of PM_{10} concentrations based on different extraction values

Moran's I scatter plots of the PM_{10} concentrations in Germany using GeoDA are presented in Table 1. Results showed that, for PM_{10}, Moran's I exceeded 0 for monthly values in 2017 and ranged from 0.228 to 0.443, suggesting there was a significant positive spatial autocorrelation of PM_{10} concentrations in Germany. The average Z(I) of 12 months was 9.65, which exceeded 2.58, suggesting that there was a significant positive spatial autocorrelation of the PM_{10} concentrations in the cities of Germany (high-high or low-low agglomeration).

In the analysis of the spatial autocorrelation model based on ArcGIS10.2, the confidence level bin (Gi_Bin) was used to identify statistically significant hot spots and cold spots. A confidence interval of +3 to −3 elements reflected a confidence level of 99% statistical significance; a confidence interval of +2 to −2 elements reflected a confidence level of 95% statistical significance; a confidence interval of −1 to +1 elements reflected a confidence level of 90% statistical significance; and a confidence interval of 0 clustering was not distinctly significant. As shown in Fig. 4, analysis of annual and monthly agglomerations indicated that hot spots occurred mainly in North Rhine-Westphalia, Brandenburg, and Berlin. Therefore, these areas should be considered when formulating air pollution control measures. Cold spots occurred mostly in the south of Bremen Niedersachsen and Thüringen and in the south-west of Baden-Wuerttemberg. No significant spots were found in Schleswig-Holstein, Mecklenburg-Vorpommern, Sachsen, and Bavaria.

Two-dimension graphics cluster in elevated pollution districts

In five states of Germany, Bavaria, North Rhine-Westphalia, Saxony-Anhalt, Brandenburg, and Berlin, the PM_{10} levels were relatively much higher than other states in 2017. Henceforth, this paper analyzed these five states based on the theory of two-dimension graphics cluster.

In Fig. 5, the significance of these connections indicates the spatial adjacency and intrinsic similarity between the various points (monitoring sites). Spatial adjacency represents geographic location information, while intrinsic similarity expresses the degree of similarity of pollution concentrations. With this, a relatively large-scale comprehensive consolidation project can be formed upon the determination of PM_{10} pollution levels and management plans. Meanwhile, using the GIS spatial analysis method, the mathematical clustering analysis method, and the graph theory tree algorithm combined with the regional division analysis technology, four functional pollution areas in Germany were obtained. First, the cities of Burg, Bitterfeld, Bernburg, and Magdeburg constituted the Saxony-Anhalt pollution region; second, the cities of Berlin, Potsdam, Hasenholz, Eberswalde, Bernau, and Blankenfelde constituted the Berlin-Brandenburg pollution region; third, the cities of Essen, Hürth, Düsseldorf, Dortmund, and Solingen Konradas constituted the North Rhine-Westphalia pollution region; and lastly, the cities of Augsburg, Regensburg, Munich and Sulzbach-Rosenberg constituted the Bavaria pollution region.

Appendix

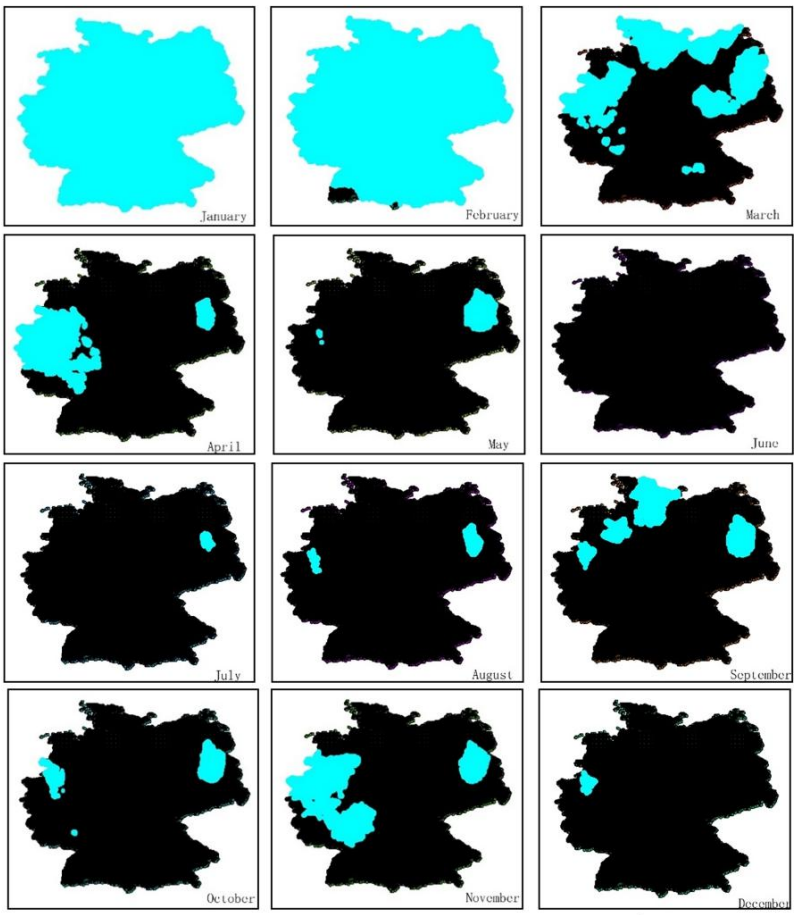


Fig. 3 The PM_{10} contaminated area range for each month of 2017 in Germany, based on the value of 18.47 μg/m^3

Spatialization of demographic data

According to demographic data and district-county-level boundary data, statistics on population density at the county level in Germany show that the population density of most districts and counties in the country are relatively small; only a few counties have high population density. In terms of spatial distribution, the Moran's I index can be

Table 1 Spatial autocorrelation index of PM_{10} concentrations in Germany in 2017

Monthly	Jan.	Feb.	Mar.	Apr.	May	Jun.	Jul.	Aug.	Sep.	Oct.	Nov.	Dec.
Moran's I-PM_{10}	0.347	0.443	0.228	0.345	0.342	0.286	0.298	0.244	0.369	0.248	0.282	0.296
P	0.001	0.001	0.001	0.001	0.001	0.001	0.001	0.001	0.001	0.001	0.001	0.001
Z	10.456	13.478	7.181	10.637	10.652	8.747	9.386	7.630	11.545	7.864	8.843	9.325



Fig. 4 Spatial agglomeration of annual and monthly PM_{10} concentrations in the monitoring sites in Germany, in 2017

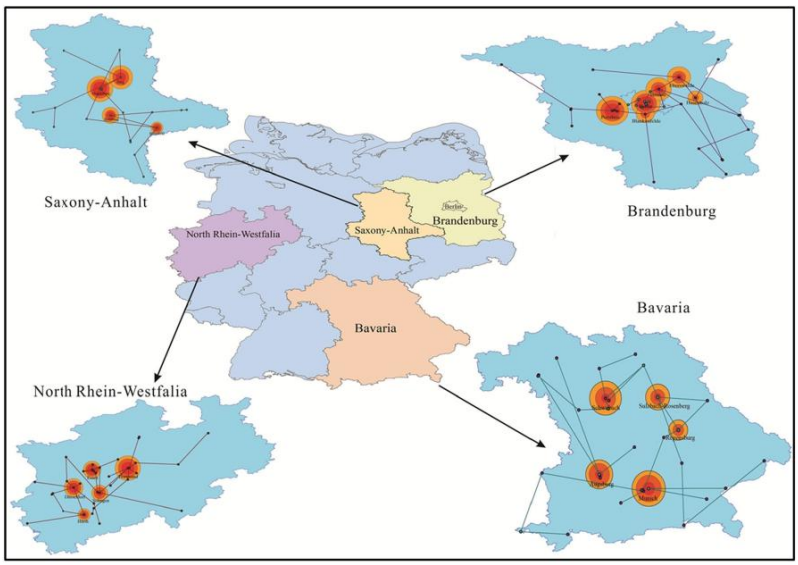


Fig. 5 Two-dimension graphics cluster in districts with higher pollution, based on the data of PM_{10} in Germany in 2017

used to analyze the spatial correlation of population distribution across the county.

Moran's I scatter plots of the population density in Germany using GeoDA are presented following Fig. 6. Results showed that, for population density, Moran's I was 0.555, suggesting that the area with high population density has a certain aggregation effect.

Variation of the total PWEL and MEAN concentration

Combining the PM_{10} concentrations and population spatialization results, the daily total population exposure to PM_{10} (PWEL) and the average of the PM_{10} concentrations were calculated (shown in Fig. 7a). The trend of PWEL was similar to the PM_{10} average in all Germany areas. Meanwhile, the monthly PWEL and PM_{10} average were also calculated to show their monthly trend characteristics more intuitively (Fig. 7b). The concentrations were higher in January and February, reaching average values of 29.14 and 28.93 $\mu g/m^3$, respectively, indicating humans could be adversely affected by exposure to air pollutants in winter. Certainly, it is worth mentioning that the population exposures to PM_{10} in other months were lower than 20 $\mu g/m^3$, suggesting a high ambient air quality in Germany.

Figure 1S shows the cumulative exposure days exceeding the standard value provided by the EU and the cumulative population exposure to PM_{10} concentrations. Figure 1Sa demonstrates days with extremely high exposure in south and east of Germany, mainly belonging to Bavaria, Brandenburg, and Berlin, reaching 17 exposure max days. Figure 1Sb shows that the distribution of cumulative population exposure to PM_{10} was similar to the distribution of cumulative exposure time.

Spatial distribution of PM_{10} pollution exposure in Germany

In Section 3.5, the time evolution of the German PM_{10} pollution exposure level in 2017 was discussed. This section introduces the concept of population pollution exposure intensity to further explore the spatial interaction and distribution of the population PM_{10} pollution distributions.

The results show that long-term exposure to ambient particulate matter air pollution is associated with natural-cause mortality, even in concentration ranges far below the present European annual mean limit value (Beelen et al. 2014) . In addition, the original air pollution concentrations cannot clearly reflect the spatial extent of population exposure to air pollution. The clustered regions extracted by the ht-index method are not affected by human subjective cognition based on legal and administrative factors. Their border ranges differ from the administrative border. In this case, they can show the high concentration ranges of

Appendix

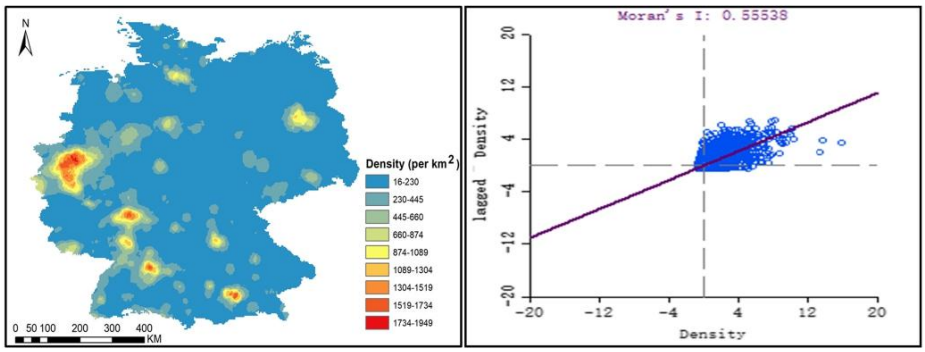


Fig. 6 Population density in Germany and the corresponding Moran's I scatter plots (data obtained from the Federal Statistical Office of Germany in 2016 and population density is expressed as inhabitants per km squared)

human activity and pollution concentration distribution. For this reason, the distribution of exposure intensity was analyzed based on the head/tail breaks classification method.

Firstly, using 50% as threshold, the population distribution of PM_{10} pollution was statistically analyzed with the head/tail breaks classification method. According to the calculations, the ht-index of the PM_{10} pollution exposure of the entire German population is 12. Subsequently, the appropriate aggregation area was determined as the extraction value. According to the mean value of each level, the distribution of the population's PM_{10} pollution exposure was classified, and the above-average range was extracted. In line with the daily standard of WHO and EU, Fig. 8a, b, and c show the effect of clustering regions at means 1912.71 day·person/km^2, 4307.37 day·person/km^2, and 7957.98 day·person/km^2, respectively.

Comparing the extraction results of the three maps, the ranges of the aggregated areas shown in Fig. 8a are quite vague. The urban details shown in Fig. 8c are too few, and the boundaries of the clustered regions are significantly less than the boundaries of the administrative borders.

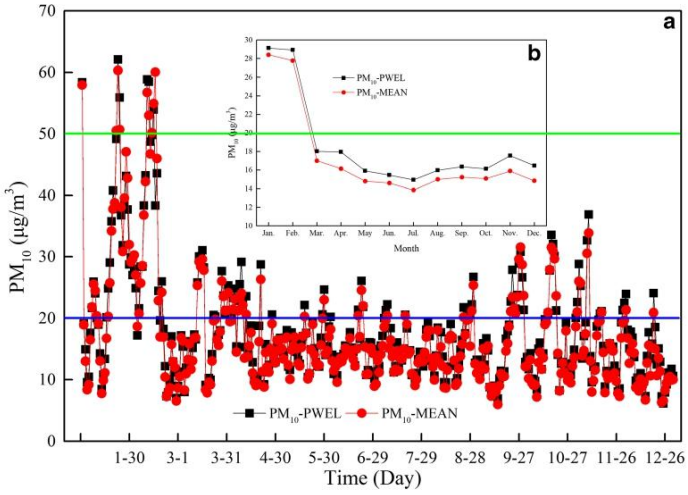


Fig. 7 The daily (a) and monthly (b) variations in the total PWEL and MEAN concentration during 2017

Appendix

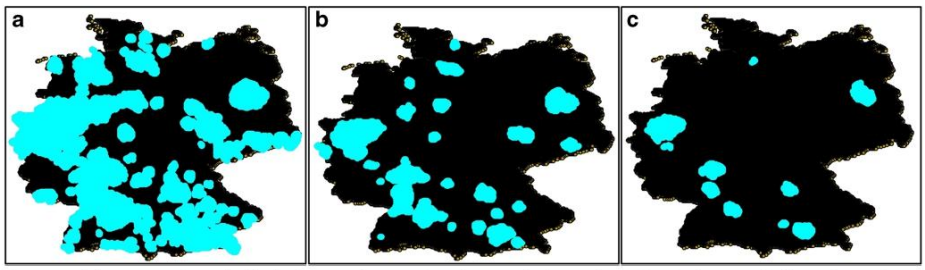


Fig. 8 Population exposure intensity distribution (**a**, value = 1912.71 day·person/km^2; **b**, value = 4307.37 day·person/km^2; **c**, value = 7957.98 day·person/km^2)

The city boundaries in Fig. 8b show a quality extraction effect. Therefore, this section selects 4307.37 (day·person/km^2) for the daily WHO and EU standard as the final aggregation area extraction values. As seen in Fig. 8b, the details are similar. The two largest areas of PM_{10} pollution are located in the surrounding areas of Berlin and Düsseldorf.

Liu (2014) examined the extraction of natural cities based on nightlight data in 2014 and suggested that the scope of natural cities is closely related to the scope of the population's living and activities. Based on the head/tail breaks classification method, the extraction of nocturnal natural cities was realized. Liu (2014) found that in most cities there is some overlap between the natural city boundaries and administrative boundaries. Combining the concepts of natural cities with Fig. 8, the polluted areas in Germany can be used to describe the "PM_{10} pollution exposure and aggregation area of the population."

Power-law distribution test

Various phenomena governed by power-law distributions are ubiquitous in nature and in society; thus, their study carries broad and far-reaching significance. In this section, power-law distribution tests are performed on the area distribution of PM_{10} pollution accumulation. By using Pareto distribution analysis, PM_{10}-gathered area data can be fitted by a power-law distribution in log-log coordinates. The power-law distribution is simulated as $f(x) = 14.25x^{-0.82}$ ($R^2 = 0.7$). From the power-law detection results, it can be concluded that the area distribution of PM_{10} clustering area has a significant heavy-tailed distribution and obeys the power-law distribution.

Conclusions

In summary, this paper investigated the spatio-temporal distribution of PM_{10} air pollution with GIS techniques, analyzed the multi-source spatio-temporal data collected from UBA networks, and obtained additional meaningful discoveries according to PM_{10} spatialization results. The national average PM_{10} amounted 17.20 μg/m^3 in 2017 and was much lower than the annual mean PM_{10} concentration of 40 μg/m^3 as declared by the European Union, and only slightly lower than the standard concentration of the WHO, which amounts for 20 μg/m^3, indicating humans could be adversely affected by exposure to air pollutants in the ambient air. In terms of spatial distribution, PM_{10} pollution was mainly concentrated in North Rhine-Westphalia, Brandenburg, and Berlin. In terms of time distribution, PM_{10} pollution exhibited a distinct seasonal characteristic, i.e., PM_{10} pollution in winter was higher than in summer and lowest in June.

Combined with the concept of a natural city, this paper proposes to use the PM_{10} air pollution accumulation area to describe the current status of PM_{10} air pollution. The German PM_{10} air pollution accumulation area extraction results show that the German PM_{10} pollution accumulation area distribution meets the power-law distribution characteristics; that is, "a small area of pollution agglomeration area is much larger than the number of large areas of pollution agglomeration area." The largest contaminated areas of concentration are in Berlin, Dusseldorf, and Munich but are not entirely within the city limits.

The population distribution by exposure level shows that the majority of people is living in polluted areas. Also, the exposure level changes greatly from North to South, and each sub-district maintains similarity to neighboring sub-districts. In addition, PM_{10} pollution aggregation area boundaries and administrative boundaries do not coincide, even across multiple administrative city boundaries. Therefore, PM_{10} air pollution control is not only the task of a single city but should be a joint effort by multiple cities in order to govern effectively.

Acknowledgments The authors also like to thank Mr. Thomas Himpel from Federal Environment Agency, for providing the data of air pollution in Germany.

Appendix

Funding information Xiansheng Liu's Ph.D. work is funded by the China Scholarship Council (CSC) under the State Scholarship Fund (File No.201706860028).

References

Anderson G, Ge Y (2005) The size distribution of Chinese cities. Reg Sci Urban Econ 35(6):756–776

Anenberg S C, Horowitz L W, Tong D Q, West J J (2010) An estimate of the global burden of anthropogenic ozone and fine particulate matter on premature human mortality using atmospheric modeling. Environ Health Perspect 118(9):1189–1195

Anselin L (1995) Local indicators of spatial association: LISA. Geogr Anal 2(27):93–115

Beelen R, Raaschou-Nielsen O, Stafoggia M, Andersen Z J, Weinmayr G, Hoffmann B, Vineis P (2014) Effects of long-term exposure to air pollution on natural-cause mortality: an analysis of 22 European cohorts within the multicentre ESCAPE project. Lancet 9919(383):785–795

Boldo E, Medina S, LeTertre A, Hurley F, Mücke HG, Ballester F, Aguilera I, Eilstein D, Apheis Group (2006) Apheis: Health impact assessment of long-term exposure to PM(2.5) in 23 European cities. Eur J Epidemiol 21(6):449–458

Bundesamt S (2016) Gemeinden in Deutschland nach Fläche, Bevölkerung und Postleitzahl am 30.09.2016. Erscheinungsmonat: August 2017 (*in German*)

Burnett R T, Pope III C A, Ezzati M, Olives C, Lim S S, Mehta S, Anderson H R (2014) An integrated risk function for estimating the global burden of disease attributable to ambient fine particulate matter exposure. Environ Health Perspect 122(4):397–403

Eeftens M, Beelen R, de Hoogh K, Bellander T, Cesaroni G, Cirach M, Dimakopoulou K (2012) Development of land use regression models for PM2. 5, PM2. 5 absorbance, PM10 and PMcoarse in 20 European study areas; results of the ESCAPE project. Environ Sci Technol 46(20):11195–11205

Fang C, Wang Z and Xu G (2016) Spatial-temporal characteristics of PM2.5 in China: A city-level perspective analysis. J Geogr Sci 26(11):1519–1532

Geary R C (1954) The Contiguity Ratio and Statistical Mapping. The Incorporated Statistician 5 (3):115

Hao Y, Flowers H, Monti M M, Qualters J R (2012) US census unit population exposures to ambient air pollutants. Int J Health Geogr 11(1):3

Harrison RM, Stedman J, Derwent D (2008) New directions: why are PM10 concentrations in Europe not falling? Atmos Environ 42:603–606

Hoek G, Brunekreef B, Goldbohm S, Fischer P, van den Brandt P (2002) Association between mortality and indicators of traffic-related air pollution in the Netherlands: a cohort study. Lancet 360(9341): 1203–1209

Ivy D, Mulholland J A, Russell A G (2008) Development of ambient air quality population-weighted metrics for use in time-series health studies. J Air Waste Manage Assoc 58(5):711–720

Jerrett M, Arain A, Kanaroglou P, Beckerman B, Potoglou D, Sahsuvaroglu T, Morrison J, Giovis C, (2005) A review and evaluation of intraurban air pollution exposure models. J Air Waste Manage Assoc 15(2):185-204

Jiang B (2013) Head/tail breaks: a new classification scheme for data with a heavy-tailed distribution. Prof Geogr 65(3):482–494

Jiang B and Yin J (2014) Ht-Index for quantifying the fractal or scaling structure of geographic features. Ann Assoc Am Geogr 3(104):530–540

Johansson C, Norman M, Gighagen L (2007) Spatial & temporal variations of PM10 and particle number concentrations in urban air. Environ Monit Assess 1-3(127):477–487

Kousa A, Kukkonen J, Karppinen A, Aarnio P, Koskentalo T (2002) A model for evaluating the population exposure to ambient air pollution in an urban area. Atmos Environ 36(13):2109–2119

Liao D, Peuquet DJ, Duan Y, Whitsel EA, Dou J, Smith RL, Lin HM, Chen JC, Heiss G (2006) GIS approaches for the estimation of residential-level ambient PM concentrations. Environ Health Perspect 114(9):1374–1380

Liu Q (2014) A Case Study on the Extraction of the Natural Cities from Nightlight Image of the United States of America. Master thesis, University of Gävle Malevergne Y, Pisaren

Long Y, Wang J, Wu K, Zhang, J (2018) Population exposure to ambient PM2.5 at the subdistrict level in China. International journal of environmental research and public health 15(12):2683

Mohajeri N, French J R, Batty M (2013) Evolution and entropy in the organization of urban street patterns. Ann GIS 19(1):1–16

Moran (1948) The interpretation of statistical maps. J R Stat Soc B 2(10): 243–251

World Health Organiazation (2002) The World Health Report 2002: Reducing Risks, Promoting Healthy Life, WHO, Geneva, Switzerland

Samet J M, Dominici F, Curriero F C, Coursac I, Zeger S L (2000) Fine particulate air pollution and mortality in 20 US cities, 1987–1994. N Engl J Med 343(24):1742–1749

Sampson P D, Richards M, Szpiro A A, Bergen S, Sheppard L, Larson T V, Kaufman J D (2013) A regionalized national universal kriging model using Partial Least Squares regression for estimating annual PM2. 5 concentrations in epidemiology. Atmos Environ 75:383–392

Sun Z, An X, Tao Y, Hou Q (2013) Assessment of population exposure to PM10 for respiratory disease in Lanzhou (China) and its health-related economic costs based on GIS. BMC Public Health 13(1): 891

Tang QY, Zhang CX (2013) Data Processing System (DPS) software with experimental design, statistical analysis and data mining developed for use in entomological research. Insect Sci 2(20):254–260

World Health Organiazation (2014) Burden of disease from ambient air pollution for 2012. Copenhagen: WHO Regional Offiice for Europe

Xu G, Jiao L, Zhao S, Cheng J (2016) Spatial and temporal variability of PM 2.5 concentration in China. Wuhan Univ J Nat Sci 21(4):358–368

Zahn CT (1971) Graph-theoretical methods for detecting and describing gestalt clusters. IEEE Trans Comput 1(20):68–86

Publisher's note Springer Nature remains neutral with regard to jurisdictional claims in published maps and institutional affiliations.

Publication II

Liu, X., Hadiatullah, H., Tai, P., Xu, Y., Zhang, X., Schnelle-Kreis, J., ... & Zimmermann, R. (2021). Air pollution in Germany: spatio-temporal variations and their driving factors based on continuous data from 2008 to 2018. ***Environmental Pollution***, 116732.

Appendix

Environmental Pollution 276 (2021) 116732

Contents lists available at ScienceDirect

Environmental Pollution

journal homepage: www.elsevier.com/locate/envpol

Air pollution in Germany: Spatio-temporal variations and their driving factors based on continuous data from 2008 to 2018☆

Xiansheng Liu [a, b], Hadiatullah Hadiatullah [c], Pengfei Tai [d], Yanling Xu [e], Xun Zhang [f, g, *], Jürgen Schnelle-Kreis [a], Brigitte Schloter-Hai [a], Ralf Zimmermann [a, b]

[a] Joint Mass Spectrometry Center, Cooperation Group Comprehensive Molecular Analytics, Helmholtz Zentrum München, German Research Center for Environmental Health, Ingolstädter Landstr. 1, 85764, Neuherberg, Germany
[b] Joint Mass Spectrometry Center, Chair of Analytical Chemistry, University of Rostock, 18059, Rostock, Germany
[c] School of Pharmaceutical Science and Technology, Tianjin University. 300072, Tianjin, China
[d] School of Geography and Tourism, Qufu Normal University, 276826, Rizhao, China
[e] College of Plant Health and Medicine, Qingdao Agricultural University, 266109, Qingdao, China
[f] Beijing Key Laboratory of Big Data Technology for Food Safety, School of Computer and Information Engineering, Beijing Technology and Business University, 100048, Beijing, China
[g] Key Laboratory of Resources Utilization and Environmental Remediation, Institute of Geographical Sciences and Natural Resources Research, Chinese Academy of Sciences, 100101, Beijing, China

ARTICLE INFO

Article history:
Received 20 November 2020
Received in revised form
2 February 2021
Accepted 10 February 2021
Available online 11 February 2021

Keywords:
Air pollution
Spatio-temporal variation
Gaseous pollutants
Meteorological factors
Natural source contribution

ABSTRACT

This study analyzed long-term observational data of particulate matter ($PM_{2.5}$, PM_{10}) variability, gaseous pollutants (CO, NO_2, NO_X, SO_2, and O_3), and meteorological factors in 412 fixed monitoring stations from January 2008 to December 2018 in Germany. Based on Hurst index analysis, the trend of atmospheric pollutants in Germany was stable during the research period. The relative correlations of gaseous pollutants and meteorological factors on $PM_{2.5}$ and PM_{10} concentrations were analyzed by Back Propagation Neural Network model, showing that CO and temperature had the greater correlations with $PM_{2.5}$ and PM_{10}. Following that, $PM_{2.5}$ and PM_{10} show a strong positive correlation ($R^2 = 0.96$, $p < 0.01$), suggesting that the reduction of $PM_{2.5}$ is essential for reducing PM pollution and enhancing air quality in Germany. Based on typical PM_{10}/CO ratios obtained under ideal weather conditions, it is conducive to roughly estimate the contribution of natural sources. In winter, the earth's crust contributed about 20.1% to PM_{10}. Taken together, exploring the prediction methods and analyzing the characteristic variation of pollutants will contribute an essential implication for air quality control in Germany.

© 2021 Elsevier Ltd. All rights reserved.

1. Introduction

Air pollution has negative impacts on human health, ecological environment, climate, and socio-economic development. The current air pollution situation and driving factors have drawn more attention in recent years (Streets et al., 2007; He et al., 2001; Wang et al., 2001; Gulliver and Briggs, 2004). Epidemiological and toxicological studies showed that long-term exposure to outdoor air pollution in large European cohorts was associated with natural mortality (Strak et al., 2019), especially about fine particulate matter (Wilson and Suh, 1997; Pope et al., 2002; Zanobetti and Schwartz, 2009; Perez et al., 2009; Schwartz, 2000; Samet et al., 2000). At present, some European countries have adopted a monitoring and measures series to control the air pollution problem, which successfully achieved better progress in the field (Waluś et al., 2018).

In the previous studies, researchers used external field detection, laboratory analysis, numerical simulation calculations, and satellite remote sensing to study various physical and chemical characteristics of $PM_{2.5}$ and their temporal and spatial evolution characteristics (Friberg et al., 2018; Xue et al., 2017). Eldred et al. (1997) used observational data from the IMPROVE monitoring network, which revealed the $PM_{2.5}$ concentration was highest in summer, and sulfate performed as main contributor to air pollution. Dawson et al. (2007) investigated the effects of meteorological

☆ This paper has been recommended for acceptance by Pavlos Kassomenos.

* Corresponding author. Beijing Key Laboratory of Big Data Technology for Food Safety, School of Computer and Information Engineering, Beijing Technology and Business University, 100048, Beijing, China.
E-mail address: zhangxun@btbu.edu.cn (X. Zhang).

https://doi.org/10.1016/j.envpol.2021.116732
0269-7491/© 2021 Elsevier Ltd. All rights reserved.

Appendix

factors on PM concentration using a three-dimensional chemical transport model. Querol et al. (2004) studied the spatio-temporal distribution of PM in 7 European cities from 1998 to 2002. In those studies comparison, it was revealed that PM_{10} had the highest concentration in Spain and Germany, and the lowest in Sweden. The highest and lowest concentrations of $PM_{2.5}$ occurred in Austria and Sweden, respectively.

Throughout these studies, the spatio-temporal variation of $PM_{2.5}$ and PM_{10} concentrations in the atmosphere and its driving factors were previously performed by Song et al. (2017) and Chai et al. (2014). The process affecting air pollution is very complex and not only affected by the source of pollutants, but also meteorological conditions (He et al., 2017) and various chemical reactions (Xie et al., 2015). Therefore, it is essential to study PM combined with gaseous pollutants and meteorological factors. However, there is a strong non-linear relationship between PM concentration changes, meteorological conditions, and gaseous pollutants (Munir, 2016). Moreover, traditional multiple linear regression models for predicting PM mass concentration have significant limitations, such as, they are unable to capture PM mass concentration and parameters (Grivas and Chaloulakou, 2006; Chaloulakou et al., 2003). Due to certain conditions, the duration of continuous observations was short, implicating the short-term air pollution concentration change and chemical composition analysis (Kamińska, 2018). Therefore, it is imperative to explore long-term air pollution study, spatio-temporal variations, and their driving factors in Germany.

Based on the above reasons, the annual trend and characteristic variations in the pollutant concentration are necessary to further predict and control air pollution. This study analyzes a dataset of gaseous pollutants (carbon monoxide (CO), nitrogen dioxide (NO_2), nitrogen oxides (NO_X = NO + NO_2), sulfur dioxide (SO_2), ozone (O_3)) and particulate matter ($PM_{2.5}$ and PM_{10}) recorded at 412 monitoring sites in Germany, for 11-years (January 2008 to December 2018). The aims are as follows: 1) to detect the spatio-temporal characteristic variations of $PM_{2.5}$ and PM_{10} in Germany. 2) to quantify the influence of gaseous pollutants and meteorological factors on $PM_{2.5}$ and PM_{10} concentrations based on the artificial BP neural network. To the best of our knowledge, this is the first time large dataset used to systematically probe the variations in characteristics of the seven critical air pollutants and the associated health effects in Germany.

2. Methods

2.1. Monitoring data

The 24-h averages data for $PM_{2.5}$, PM_{10}, CO, SO_2, NO_2, and NO_X and 8 h averages data for O_3 were obtained from the Federal Environment Agency (https://www.umweltbundesamt.de/en/) and utilized to calculate monthly and annual averages at each monitoring location. The observations included daily $PM_{2.5}$, PM_{10}, CO, O_3, SO_2, NO_2, and NO_X concentrations at 412 monitoring sites in Germany from 2008 to 2018, characterizing the spatio-temporal variability of the pollution concentrations. A detailed description of the stations for the different pollutants was listed in Table S1.

2.2. Meteorological data

The routine meteorological data at 222 monitoring sites in Germany from January 2008 to December 2018 were obtained by the German Weather Service (Deutscher Wetterdienst) and used to analyze the relation to air pollution. The observations include a form of precipitation (only rain, only snow, rain and snow, FP), a daily precipitation height (PH), a daily average wind speed (WS), a daily sunshine duration (SD), a daily value snow depth (SnD), a daily average of coverage (C), a daily average of vapor pressure (VP), a daily mean air pressure (AP), a daily average relative humidity (RH), and a daily average temperature (T). To ensure the accuracy of data analysis, the meteorological data were obtained from the close location with fixed monitoring stations (pollutant monitor) and further analyzed to observe the effect of meteorological factors on particulate matter concentrations.

2.3. Time series method

In order to study the annual variation and variation characteristics of atmospheric pollutant concentration time series intuitively and quickly, this study uses rescaled range (R/S) analysis followed by fractal dimension (D) that can analyze the internal regularity of complex atmospheric phenomena.

2.3.1. Rescaled range (R/S) analysis

The formula for R/S analysis (Hurst, 1965) is as follows:

$$\overline{x}(j) = \frac{\sum_{i=1}^{j} x(i)}{j},\ j = 1, 2, 3\ldots \tag{1}$$

$$x(i, j) = \sum_{k=1}^{i} \left(x(k) - \overline{x}(j)\right), 1 \le i \le j \tag{2}$$

$$R(j) = \max_{1\le i\le j} x(i, j) - \min_{1\le i\le j} x(i, j),\ j = 1, 2, 3\ldots \tag{3}$$

$$S(j) = \left[\frac{1}{j}\sum_{i=1}^{j}\left(x(i) - \overline{x}(j)\right)^2\right]^{\frac{1}{2}},\ j = 1, 2, 3\ldots \tag{4}$$

where x_i, x(i, j), R(j) and S(j) are the mean, cumulative dispersion, range and standard deviation of the given time series. So the R/S analysis is the ratio between range and standard deviation.

If x_i is a random sequence that is independent of each other and has a limited variance, ie Brownian motion, then

$$\frac{R(j)}{S(j)} = \left(\frac{\pi j}{2}\right)^{H} \tag{5}$$

where H is the Hurst index of the time series. The magnitude of the H-index can reflect the future atmospheric pollutants of the time series.

(1) If H = 0.5, the time series of air pollution changes are random, and the current air pollution information will not affect the future.
(2) If 0.5 < H < 1, it indicates that the time series has long-term persistence, and the overall change in air pollution in the future will continue the overall trend of the past. The larger H is, the stronger the persistence; the closer H is to 1, the overall change in air pollution in the future continues the overall trend in air pollution in the past.
(3) If 0 < H < 0.5, it indicates that the time series has long-term anti-sustainability. The total change in air pollution in the future will be contrary to the overall trend of the past. The closer H is to 0, the stronger the anti-sustainability.

2.3.2. Fractal dimension (D)

The Hurst index (H) of the one-dimensional Brownian motion

Appendix

has the following relationship to its fractal dimension D:

$$D = 2 - H \quad (6)$$

The Hurst index is closely related to the fractal dimension D of the fractional Brownian motion, reflecting the persistence and anti-persistence of the fractional Brownian motion (Baillie, 1996).

2.4. Statistical analysis

A coefficient of variation (CV) or a coefficient of divergence (CD) was applied to the heterogeneous particle distributions to describe the relative intra-urban concentration heterogeneity (Zhaobin et al., 2013). The CD_{jk} method for identifying the differences in atmospheric pollutant profiles, described in detail by (Pakbin et al., 2010), was defined as follows:

$$CD_{jk} = \sqrt{\frac{1}{p}\sum_{i=1}^{p}\left(\frac{X_{ij} - X_{ik}}{X_{ij} + X_{ik}}\right)^2} \quad (7)$$

where the x_{ij} and x_{ik} represent the observation (concentration of atmospheric pollutants in this case) for variable x in the ith of total p observations at the paired sampling sites j and k (Krudysz et al., 2009). If the value of CD_{jk} approaches zero, the atmospheric pollutant composition in j and k are similar, and if it approaches one, they are significantly different (Pakbin et al., 2010). Thus, the CD_{jk} can provide a relative measure of homogeneity in the concentration fields (Pinto et al., 2004).

The coefficient of variation (CV, i.e., standard deviation (STD) divided by the mean value (x)) was also used to describe the degree of the spatial variation of air pollutant concentration regions, expressed by:

$$CV = \frac{STD}{\overline{X}} \quad (8)$$

2.5. Back propagation (BP) neural network

Artificial neural networks (ANN) (Van Gerven and Bohte, 2017) can be used to forecast short and middle long-term concentration levels for some of the well-known pollutants (Viotti et al., 2002). In this study, back propagation (BP) neural network was chosen, which is used in artificial neural networks to calculate a gradient required for the calculation of the weights to be used in the network (LeCun et al., 2015).

2.6. Natural source contribution to PM_{10}

In a city, gaseous pollutants are mainly derived from urban anthropogenic emissions during a certain period. For example, near-surface gaseous pollutants are mainly derived from the combustion or conversion of fossil fuels and other organic matter, and other sources contribute to their insignificance (Pochanart et al., 2004). However, the particulate matter differs from the gaseous pollutants, including the combustion process (including the secondary conversion of gaseous pollutants) and the natural source contribution of the crustal material (wind and dust).

Depending on the difference between the two factors, it is possible to select the monitoring data of pollutants under ideal meteorological conditions (such as snowfall and low speed wind) whose natural sources contribute a slight impact to the inhalable particulate matter (PM_{10}). At this time, it is challenging to resuspend the crustal material. In the atmosphere, atmospheric particulate matter and gaseous pollutants have the same source of anthropogenic pollution, and there should be a significant positive correlation. At a certain time, the percentage contribution (referred to anthropogenic source) is relatively stable due to a slight change of fuel structure, hence, its ratio emission can be assumed to be a constant. Following the ratio, the contribution rate of natural sources to PM_{10} can be resolved according to the change of ratio.

Data analysis was performed using the SPSS 18.0 software. For the statistical analysis, the one-way analysis of variance (ANOVA) and the correlation analysis with Bivariate Correlations Analysis were completed. The spatial distributions of the average atmospheric pollutant concentrations were simulated using the Kriging interpolation model by Arcgis 10.3.

3. Results and discussion

3.1. Overview of air pollutants

This study analyzed the annual average mass concentrations of the pollutants during the past four years (2015–2018) (Fig. 1) to make a clear comparison. Significant spatial differences in air pollutants concentrations among Germany were observed, and the ranges of annual average values were shown in Table S2. Moreover, the cumulative population distribution of the annual values of $PM_{2.5}$, PM_{10}, $PM_{2.5}/PM_{10}$, CO, O_3, SO_2, NO_2, and NO_X during the past four years (2015–2018) was investigated to make a better understanding of the exposure German population to air pollution. From 2015 to 2018, half of the German population was exposed to annual average values higher than 12.6 μg/m^3 for $PM_{2.5}$, 18.1 μg/m^3 for PM_{10}, 0.32 mg/m^3 for CO, 48.3 μg/m^3 for O_3, 2.03 μg/m^3 for SO_2, 21.9 μg/m^3 for NO_2, and 35.3 μg/m^3 for NO_X, respectively, suggesting during that period only 7.79%, 67.4%, 85.6%, 100% of the population lived in areas that meet the annual standards of the World Health Organization (WHO) air quality guidelines (AQG) of 10, 20, 40, 100 μg/m^3 for $PM_{2.5}$, PM_{10}, NO_2, and O_3, respectively. In addition, when compared with the EU concentration standard for $PM_{2.5}$ and PM_{10} (25 and 40 μg/m^3), the entire German population has been exposed below their standard concentration from 2008 to 2018 (Figure S1).

3.2. Atmospheric pollutant characteristics

The fractal characteristics of the atmospheric pollutant monitoring data were studied by using the time series domain rescaling analysis method. Table S3 showed the Hurst-index (H) and fractal dimension (D) of $PM_{2.5}$ and PM_{10} in different multi-time scales and different areas. Meanwhile, this study also analyzed the H and D of CO, O_3, SO_2, NO_2, and NO_X (Table S4). The results showed that the H was larger than 0.5, indicating the time series of atmospheric pollutants as a trajectory of the fractional Brownian motion shows persistence, that is, a trend of increasing concentration of atmospheric pollution in the past means a future growth trend, and a reduction trend in the past means a future reduction trend, which can be maintained in some extents. It also implied that the air pollutant statistics show a certain degree of non-Gaussian (non-random) distribution. This phenomenon was further confirmed by the long-term change trend of $PM_{2.5}$ and PM_{10} (Figure S1 and S2), showing the air pollutants stability during the study period. Fractal studies are disordered systems with specific characteristics. As fractal constraints change, the fractal dimension will change accordingly (Baillie, 1996). Due to the linear relationship between H and D, the change in H reflects the change in D. Therefore, when the value of H changes greatly, it is the variation of the factors that restrict the system, which is called the variation point. To this end, the study divides the raw data into two parts with the year-end

Appendix

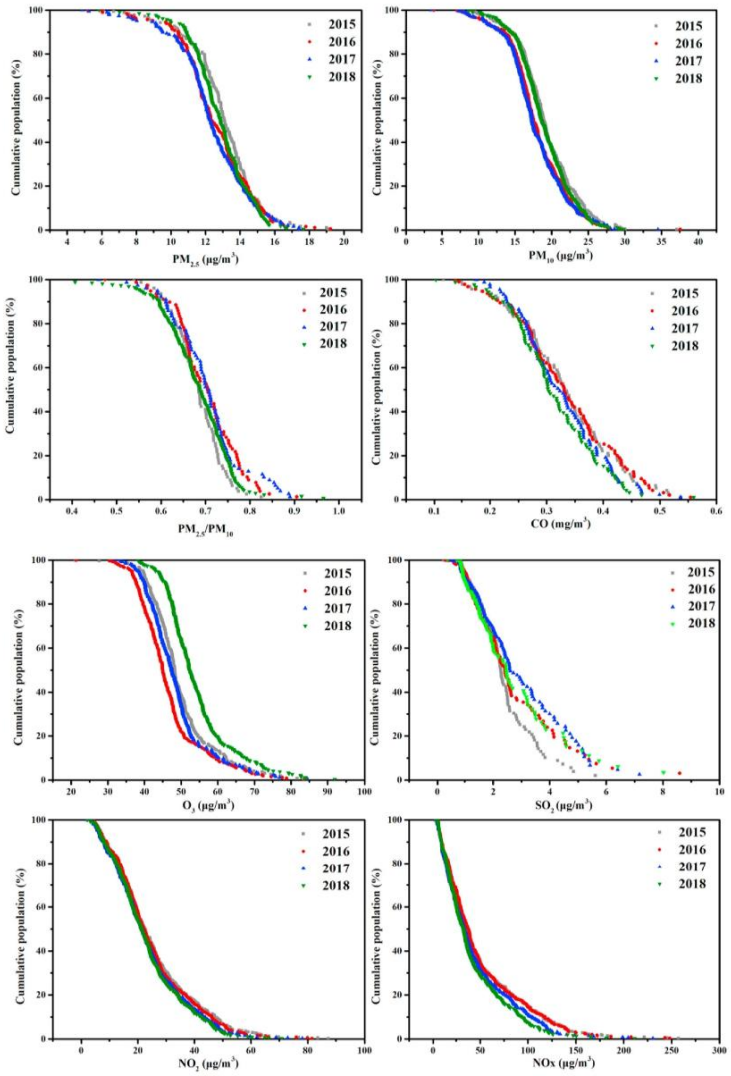


Fig. 1. Cumulative distribution of the annual average of air pollutants in Germany from 2015 to 2018.

date (December 31) as the demarcation point (i.e, the starting point of the previous part and the starting point of the latter part) and performs R/S analysis on the two parts, respectively. The corresponding H index is recorded as H_i and H_{i+1} and then the absolute value $\Delta H = |H_{i+1} - H_i|$ of the difference between H_i and H_{i+1} is obtained, and the ΔH is obtained accordingly. The point with the largest value is regarded as the maximum point of variation, and the variations year can be diagnosed accordingly. Because the maximum point of this variation is compared with the other sample points analyzed, it is relative.

Appendix

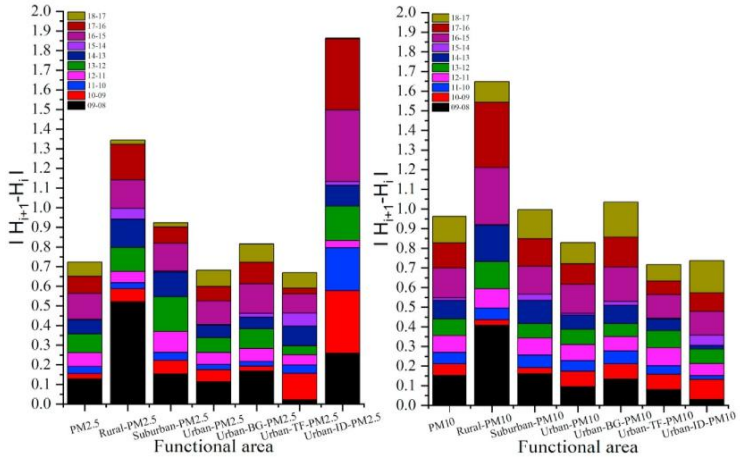


Fig. 2. Segmental analysis of atmospheric pollutants in different functional areas from 2008 to 2018 in Germany (BG, background; TF, traffic; ID, industry).

The results of the segmentation analysis are shown in Fig. 2. As shown in Fig. 2, for PM_{10} and $PM_{2.5}$, the largest of $|H_{i+1} - H_i|$ is found in 2009. Following that, the most variable atmospheric pollutant were found in the rural areas ($\Delta H = 0.52$ for $PM_{2.5}$; $\Delta H = 0.41$ for PM_{10}). The multiple factors may influence the air pollution changes, such as building completed area, thermal power generation, gross industrial output value, and wind speed (Yao et al., 2020). In the previous study, the average urban traffic $PM_{2.5}$ concentrations exceeded the WHO standards in the vast majority of European member states in 2009 (Kiesewetter and Amann, 2014). Moreover, regarding to urban $PM_{2.5}$ levels under the EU Clean Air Policy Package (Kiesewetter and Amann, 2014), the source contribution to ambient $PM_{2.5}$ in Germany is high, influencing the implementation of air pollution policy starting from 2009. The main source contribution to rural $PM_{2.5}$ comes from sulfates, residential heating, nitrates, industry, re-suspended dust, and sea salt and dust-long range transport (Pokorná et al., 2018). Moreover, the industrial emission (SO_2 and NO_X) and traffic emission (NO_X) mainly interacted with Ammonia, which only obtained from rural agriculture, following, the house heating in the rural area also contributed to the $PM_{2.5}$ concentration. Therefore, both factors may influence the high contribution to $PM_{2.5}$ concentration from rural area. Simultaneously, in our study, the variability of air pollution was also large in 2016 and 2017. It is worth noting that $PM_{2.5}$ variation across many years in the urban industrial, which is not observed in PM_{10}, implied that $PM_{2.5}$ and PM_{10} might have different source contributions. These results were consistent with the previous study that these differences were primarily related to different source profiles (Huang et al., 2014).

3.3. Spatial variations

The spatial distribution of the annual average mass concentrations of seven air pollutants ($PM_{2.5}$, PM_{10}, CO, O_3, SO_2, NO_2, and NO_X) at each air quality monitoring station across Germany are shown in Figure S3. In order to observe the spatial distribution in different types of areas, the distribution of $PM_{2.5}$ and PM_{10} was analyzed in rural, suburban, and urban areas (Figure S4). In general, as the center of economic culture, air pollution is commonly more severe in Berlin and Brandenburg, comparable with our previous study in terms of the spatial distribution of PM_{10} (Liu et al., 2020).

In order to represent the overall spatial variations of air pollutant concentrations in Germany, the daily average mass concentrations of air pollutants at over 400 fixed monitoring stations over a period of eleven years was performed, the result showed that SO_2 has the largest spatial variations (42.7%), followed by $PM_{2.5}$ (CV = 12.1%), PM_{10} (CV = 10.0%), CO (CV = 8.7%), NO_2 (CV = 7.1%), NO_X (CV = 5.6%) and O_3 (CV = 2%). The largest spatial variation was located in Berlin for CO (CV = 20.1%), Niedersachsen for NO_2 (CV = 13%), Mecklenburg-Vorpommern for NO_X (CV = 24.3%), Bayern for O_3 (CV = 4.88%), Bremen for $PM_{2.5}$ (CV = 19%) and Thüringen for PM_{10} (CV = 16.5%). However, some areas in Germany cannot be monitored by fixed stations, which may influence the spatial distribution of air pollutant concentrations. Therefore, we selected the Kriging interpolation model to provide the continuous spatial distribution for each factor based on our daily metric data. The results are consistent as described by the cumulative distribution of the annual average of air pollutants in Fig. 1. More than that the spatial changes of pollutants and hot spots in various German regions can be identified (Fig. 3).

3.4. Correlations between air pollutants

3.4.1. Correlations of gaseous pollutants on $PM_{2.5}$ and PM_{10} concentrations

In this section, the BP neural network algorithm was used to select the five common types of pollutants (CO, O_3, SO_2, NO_2, and NO_X) to analyze and compare their correlations on $PM_{2.5}$ and PM_{10}. Fig. 4 showed that the gaseous pollutants with a greater correlation on $PM_{2.5}$ and PM_{10} were CO and SO_2. CO and SO_2 are mainly derived from the combustion of fuel, urban automobile exhaust and tail gas discharged from industrial plants, comparable with the basic situation of many German industrial and transportation vehicles. The second driving gaseous pollutants factors were NO_X and O_3,

Appendix

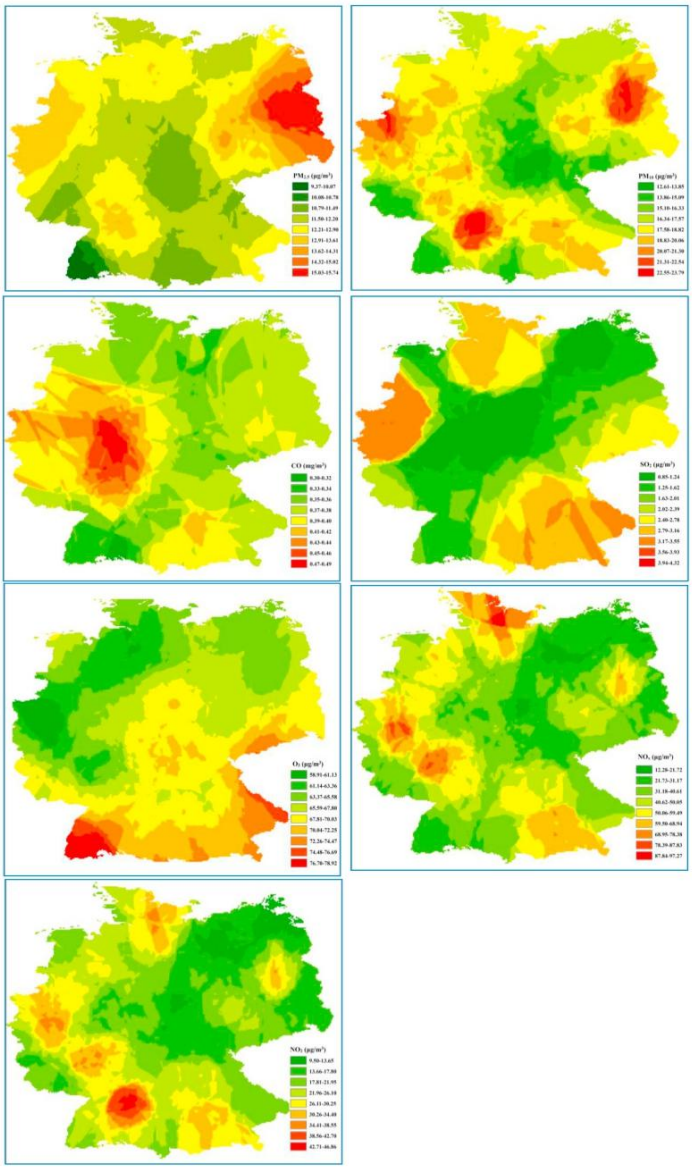


Fig. 3. Annual average mass concentrations of seven air pollutants ($PM_{2.5}$, PM_{10}, CO, SO_2, O_3, NO_X, and NO_2) maps obtained by Ordinary Kriging from 2008 to 2018.

Appendix

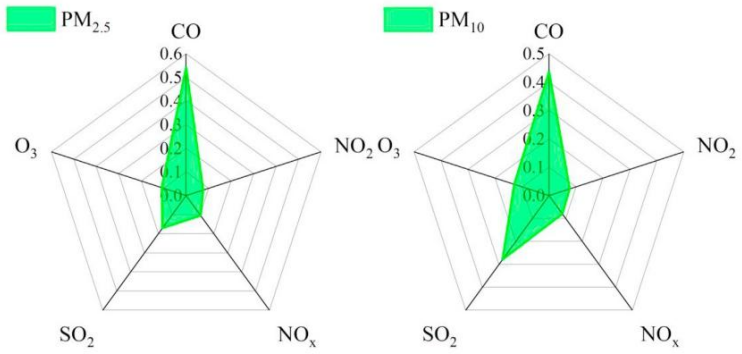


Fig. 4. The normalized coefficients of gaseous pollutants on $PM_{2.5}$ and PM_{10}.

respectively. Although the nitrogen content is minimal in the car's fuel, the high-temperature environment in which the automobile's internal combustion engine operates causes a large production of nitrogen oxides (NO_X) released into the air (Cyrys et al., 2012; Mavroidis and Ilia, 2012). Ozone in the atmosphere is mainly formed by the photochemical reaction of nitrogen oxides and volatile organic compounds and is the main component of photochemical smog (Pusede et al., 2015). The main sources of nitrogen oxides are automotive exhaust and chemical production.

Then, we performed spearman analysis to further analyze the positive and negative relationship between $PM_{2.5}$, PM_{10} and gaseous pollutants (Table S5). The results showed that the $PM_{2.5}$ and PM_{10} were positively correlated with gaseous pollutants, including CO, NO_2, NO_X, and SO_2, and negatively correlated with O_3. The previous study showed the inverse relation between O_3 and PM based on seasonal time (Jia et al., 2017). Briefly, the negative correlation was found in the winter, and positive correlation was found in the summer. These phenomena may be influenced by the different photochemical reactions in different seasons (Khoder, 2009).

3.4.2. *Effect of meteorological factors on $PM_{2.5}$ and PM_{10} concentrations*

Previous studies have shown a close relationship between meteorological conditions and air pollution processes (Yoo et al., 2015). However, the effects of meteorological factors on particulate pollution were typically discussed in qualitative methods (Wang et al., 2010; Chen et al., 2008). Therefore, the quantitative analysis of $PM_{2.5}$ and PM_{10} mass concentrations and meteorological parameters was discussed in this section. The BP neural network was used to calculate the influence of various meteorological elements in Germany on $PM_{2.5}$ and PM_{10}. The results showed that, the effects of meteorological elements on $PM_{2.5}$ and PM_{10} are similar except daily value snow depth (SnD) (Fig. 5). The temperature is the most important driving factor, that reached 21.1% and 35.6% (weight correlation) to $PM_{2.5}$ and PM_{10}, respectively. The second

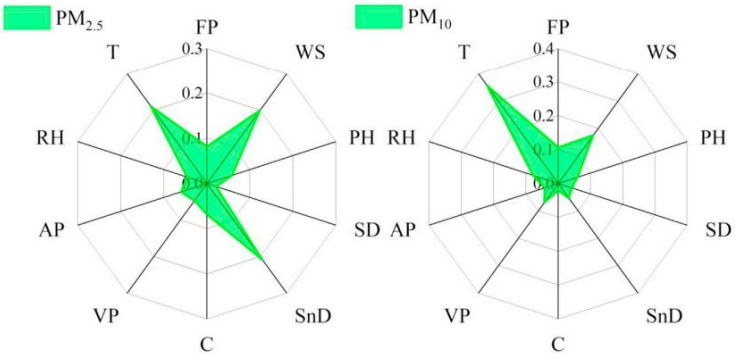


Fig. 5. Impact of meteorological factors on $PM_{2.5}$ and PM_{10} (FP, precipitation form (only rain, only snow, rain and snow); WS, a daily mean wind speed (m/s); PH, a daily precipitation height (mm) ; SD, a daily sunshine duration (h); SnD, a daily value snow depth (cm); C, a daily average of coverage (1/8); VP, a daily average of vapor pressure (hPa); AP, a daily mean air pressure (hPa); RH, a daily average relative humidity (%); T, a daily average temperature (°C)).

Appendix

driving meteorological factors have slightly different effects on $PM_{2.5}$ and PM_{10}. For $PM_{2.5}$, the second driving factors are snowfall thickness (20.7%) and wind speed (19.9%). For PM_{10}, the second driving factor is wind speed (17.4%).

Then, we performed spearman analysis to show the positive and negative relationship between $PM_{2.5}$, PM_{10} and meteorological factors (Table S6). Generally, the $PM_{2.5}$ were negatively correlated with meteorological factors, including FP, WS, PH, C, VP, and T. Following that, the PM_{10} were also negatively correlated with meteorological factors, including FP, WS, PH, C, VP, AP, and T. However, RH was positively correlated both $PM_{2.5}$ and PM_{10} but less impact. This result was similar with previous study that RH has less impact to the PM concentration, but its fluctuation will raise the concentration of PM (Zhang et al., 2016). Moreover, it has already found that temperature (T) and wind speed (WS) were essential meteorological predictors. For example, low temperature could change the dynamics of air movement, trap air pollutants, and create a build-up of pollution near the ground (Zhang et al., 2018). Therefore, a change in temperature may effect on the PM concentration. Accordingly, the higher the wind speed, the cleaner air involved in pollutants per unit time. Moreover, under the control of the strong wind generated by the cold air transit, the particles can hardly accumulate rapidly, so that the concentration of the particulate matter can be maintained at a relatively low level for a long time. The effect of snowfall (SnD) on $PM_{2.5}$ is mainly the removal effect. During the process of snowfall, the aerosol particles can be captured by the Brownian diffusion or inertial wall-impacting processes, thereby removing $PM_{2.5}$ from the air. However, the effects of pressure on $PM_{2.5}$ and PM_{10} are relatively small, contradictory to the previous study (Cheng et al., 2015). This phenomenon may be influenced by the precipitation effect which played a major role in $PM_{2.5}$ pollution removal (Zalakeviciute et al., 2018). Meanwhile, to confirm that meteorological factors also affect particulate matter by affecting gaseous pollutants. Therefore, we also analyzed the gaseous pollutants-meteorological factors correlation (Table S6). The results showed that gaseous pollutants (CO, NO_2, NO_X, and SO_2) have negative relations with wind speed and temperature, and positively correlated with air pressure during yearround, indicating the meteorological factors could affect the variation of the gaseous pollutants as same as PM. In the previous study, the similar trend was found in New York City (Ito et al., 2007). In contrast, O_3 has the opposite correlation with the above meteorological factors compared to the other four gaseous pollutants. These trends may be affected by different photochemical reaction in different season (Khoder, 2009).

3.4.3. Correlations between PM size fractions

The correlation between $PM_{2.5}$ and PM_{10} showed a high positive correlation, which consistent with several studies performed in California (Motallebi et al., 2003), Netherland (Janssen et al., 2013), and China (Zhou et al., 2016). These analyses may provide new knowledge about source characterization of atmospheric particles, and help to evaluate the situation of $PM_{2.5}$ when the routine monitoring of PM_{10} is available (since the $PM_{2.5}$ data is less or scarce in Germany). However, due to different sources, fine particles ($PM_{2.5}$) and coarse particles ($PM_{10\text{-}2.5}$) should be considered as a separate class of pollutant (Payam, 2010). In our study, we found a high correlation between $PM_{2.5}$ *vs.* PM_{10} ($R = 0.96$, $p < 0.01$) than $PM_{10\text{-}2.5}$ *vs.* PM_{10} ($R = 0.44$, $p < 0.01$) (Fig. 6), indicating the $PM_{2.5}$ concentrations are the major contributors to the average PM_{10} concentrations at many sites in Germany. And the relation between $PM_{2.5}$ *vs.* $PM_{10\text{-}2.5}$ is weak but highly significant ($R = 0.26$, $p < 0.01$), suggesting that $PM_{2.5}$ and $PM_{10\text{-}2.5}$ are generally influenced by different sources. The similar report was found in the UK that the relation between $PM_{10\text{-}2.5}$ *vs.* $PM_{2.5}$ is lower than PM_{10} *vs.* $PM_{2.5}$ (Liu and Harrison, 2011). Taken together, the $PM_{2.5}$ and $PM_{10\text{-}2.5}$ may have distinct different behaviour due to their various sources and properties contribution, which further prove that coarse and fine particles have a different toxic effect in epidemiological studies (Wilson and Suh, 1997).

To further confirm the relation between $PM_{2.5}$, $PM_{10\text{-}2.5}$ and PM_{10}, the study has also analyzed the correlations in different types of areas (Figure S5), which showed the strong relations between $PM_{2.5}$ and PM_{10} in all the types of areas, especially in the urban area ($R = 0.97$, $p < 0.01$). In addition, to further reflect this relation in the urban areas, the study was continuously analyzed the relations in the different urban functional areas (Figure S6). Industrial areas have the lowest correlations for $PM_{2.5}$ *vs.* PM_{10} and $PM_{2.5}$ *vs.* $PM_{10\text{-}2.5}$, comparing with others three functional areas, and background area have the lowest correlations for $PM_{10\text{-}2.5}$ vs. PM_{10}, comparing with other three functional areas, suggesting that different source may be found in the different urban functional areas.

Therefore, the source of PM can be analyzed through the ratio of $PM_{2.5}$ - PM_{10}. It is well known that the fine particles primarily originate from combustion processes and gas-to-particle conversion processes in the atmosphere. In terms of mass concentration, the higher the $PM_{2.5}/PM_{10}$, the higher the contribution rate of the secondary particles; the lower the ratio, the higher the contribution rate of the dust source. By analyzing the ratio of $PM_{2.5}$ - PM_{10} in different types of urban areas, it is found that urban background has the highest ratio (0.67), while urban industrial area has the lowest

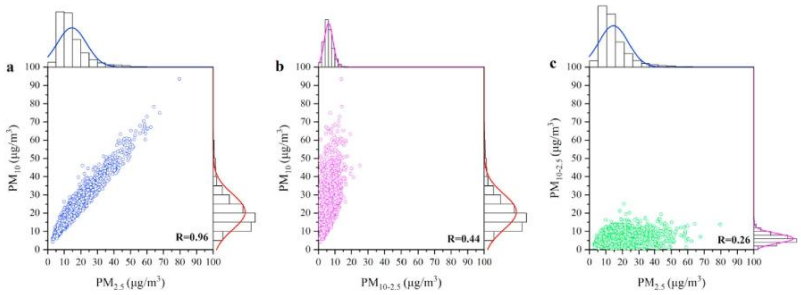


Fig. 6. The correlation between annual average concentrations of $PM_{2.5}$ *vs.* PM_{10} (a), $PM_{10\text{-}2.5}$ *vs.* PM_{10} (b), and $PM_{2.5}$ *vs.* $PM_{10\text{-}2.5}$ (c) base on 11 years of data collection all over Germany.

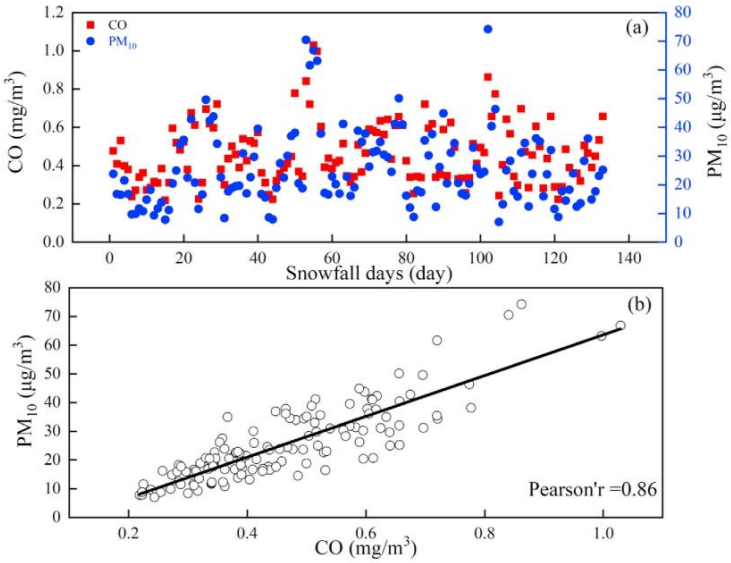


Fig. 7. Daily variations of PM_{10} and CO in snowfall days (a) and the correlation between PM_{10} and CO (b) in winter.

ratio (0.55). The sparse vegetation urban industrial areas may be one reason for the small ratio of $PM_{2.5}$ to PM_{10} (He et al., 2017).

3.4.4. Natural source contribution to PM_{10} in winter

Naturally, after snowing, the ground was covered by snow, which made the particulate matter difficult to reach the atmosphere area, hence, the contribution of air pollutant to atmospheric particulate matter based on natural source is limited (i.e., dust). Thus, in snowfall days, atmospheric particulate matter mainly comes from fossil fuels and the combustion of other organic matter (i.e., urban anthropogenic sources), which has similar pollution source with gaseous pollutants. In this regard, the natural source contribution of PM_{10} in winter can be inferred.

In order to estimate the natural source contribution of PM_{10} in the winter, we selected the monitoring data of pollutants under ideal meteorological conditions (i.e., snowfall days (daily value snow depth $\geq$ 5 cm) and low speed wind). In that condition, it is difficult to obtain the crustal elements and dust. The statistical monitoring data of pollutants after snowing showed that the trend of particulate matter and gaseous pollutants were completely similar, meaning that when PM_{10} concentration was high, the similar trend was also found for CO (Fig. 7a). Considering the relatively stable nature of CO in gaseous pollutants, the concentration of PM_{10} and CO was further analyzed by regression analysis (Fig. 7b), showing the strong relation between them ($R = 0.86$, $p < 0.01$).

The average ratio of PM_{10} to CO concentration is $5.3 \bullet 10^{-2}$ in winter snowfall days, which can be considered as the reference value P. When the ratio of PM_{10} to the anthropogenic CO is greater than this value, it can be assumed that PM_{10} also has other pollution sources, mainly for surface contribution or external transportation, especially if there are many surface sand sources or sand dust. Based on atmospheric pollutant data collected from winter (Dec., Jan., and Feb.) during 2008–2018 in Germany, the ratios of PM_{10} to anthropogenic CO winter are $6.0 \bullet 10^{-2}$ (Dec.), $7.1 \bullet 10^{-2}$ (Jan.), and $7.0 \bullet 10^{-2}$ (Feb.) Based on the value P ($5.3 \bullet 10^{-2}$), it can be estimated that the contribution of German natural sources to atmospheric PM_{10} accounts for about 20.1% (5.58 $\mu g/m^3$) in winter, which is consistent with the previous study, that natural sources contribute with 6 $\mu g/m^3$ of mineral dust to the annual PM_{10} levels in Eastern Spain (Rodrıguez et al., 2004).

4. Conclusions

This paper comprehensively used the particulate matter ($PM_{2.5}$ and PM_{10}), gaseous pollutants (CO, NO_2, NO_X, SO_2, and O_3), and meteorological factors of the monitoring sites in Germany of the past 11 years to analyze the pollution characteristics of particulate pollutants in Germany. In this study, based on the Hurst index, the atmospheric pollutants, specially $PM_{2.5}$ and PM_{10}, revealed a stable trend from 2008 to 2018 in Germany ($H > 0.5$). By analyzing the correlations of different gaseous pollutants and meteorological conditions on the concentration of $PM_{2.5}$ and PM_{10} using Back Propagation Neural Network model, it was found that CO and temperature had greater correlations with $PM_{2.5}$ and PM_{10} in Germany. Regarding on correlations between different PM size fractions, a high correlation between $PM_{2.5}$ *vs.* PM_{10} indicated that the $PM_{2.5}$ concentrations were the major contributors to the average PM_{10} concentrations at many sites in Germany. And the weak correlation between $PM_{2.5}$ *vs.* $PM_{10\text{-}2.5}$ suggested that $PM_{2.5}$ and $PM_{10\text{-}2.5}$ were generally influenced by different sources. Based on typical PM_{10}/CO ratios obtained under ideal weather conditions (i.e., snowfall days (daily value snow depth $\geq$ 5 cm) and low speed wind), it is conducive to roughly estimate the contribution of

Appendix

natural sources. In winter, the earth's crust contributed about 20.1% to PM_{10} (average 5.58 μg/m^3).

Author contributions

Xiansheng Liu: Data curation, Investigation, Methodology, Software, Supervision, Writing – original draft, Writing – review & editing. Hadiatullah Hadiatullah: Methodology, Writing – original draft. Pengfei Tai: Software. Yanling Xu:. Xun Zhang: Funding acquisition, Project administration. Jürgen Schnelle-Kreis: Data curation. Brigitte Schloter-Hai: Writing – review & editing. Ralf Zimmermann: Visualization

Declaration of competing interest

The authors declare that they have no known competing financial interests or personal relationships that could have appeared to influence the work reported in this paper.

Acknowledgements

Xiansheng Liu's PhD work is funded by the China Scholarship Council under the State Scholarship Fund (File No.201706860028) and Support Project of High-level Teachers in Beijing Municipal Universities in the Period of 13th Five-year Plan (CIT&TCD201904037). The authors also like to thank Mr. Thomas Himpel from Federal Environment Agency, for providing the the data of air pollution in Germany.

Appendix A. Supplementary data

Supplementary data to this article can be found online at https://doi.org/10.1016/j.envpol.2021.116732.

References

Baillie, R.T., 1996. Long memory processes and fractional integration in econometrics. J. Econom. 1 (73), 5–59.
Chai, F., Gao, J., Chen, Z., Wang, S., Zhang, Y., Zhang, J., Ren, C., 2014. Spatial and temporal variation of particulate matter and gaseous pollut_x0002_ants in 26 cities in China. J. Environ. Sci. China 26, 75–82.
Chaloulakou, A., Saisana, M., Spyrellis, N., 2003. Comparative assessment of neural networks and regression models for forecasting summertime ozone in Athens. Sci. Total Environ. 313 (1–3), 1–13.
Chen, Z.H., Chen, D.S., Cheng, S.Y., Li, J.B., Guo, X.R., Wang, W.H., 2008. Relationship between atmospheric pollution processes and synoptic pressure patterns in northern China. Atmos. Environ. 42 (24), 6078–6087.
Cheng, Y., He, K.B., Du, Z.Y., Zheng, M., Duan, F.K., Ma, Y.L., 2015. Humidity plays an important role in the PM2. 5 pollution in Beijing. Environ. Pollut. 197, 68–75.
Cyrys, J., Eeftens, M., Heinrich, J., Ampe, C., Armengaud, A., Beelen, R., Cirach, M., 2012. Variation of NO2 and NOx concentrations between and within 36 European study areas: results from the ESCAPE study. Atmos. Environ. 62, 374–390.
Dawson, J.P., Adamas, P.J., Pandis, S.N., 2007. Sensitivity of PM 2.5 to climate in the Eastern US: a modeling case study. Atmos. Chem. Phys. Discuss. Eur. Geosci. Union 3 (7), 6487–6525.
Eldred, R.A., Cahill, T.A., Flocchini, R.G., 1997. Composition of PM2. 5 and PM10 aerosols in the IMPROVE network. J. Air Waste Manag. Assoc. 2 (47), 194–203.
Friberg, M.D., Kahn, R.A., Limbacher, J.A., Appel, K.W., Mulholland, J.A., 2018. Constraining chemical transport PM2.5 modeling outputs using surface monitor measurements and satellite retrievals: application over the San Joaquin Valley. Atmos. Chem. Phys. 18 (17), 12891–12913.
Grivas, G., Chaloulakou, A., 2006. Artificial neural network models for prediction of PM10 hourly concentrations, in the Greater Area of Athens, Greece. Atmos. Environ. 40 (7), 1216–1229.
Gulliver, J., Briggs, D.J., 2004. Personal exposure to particulate air pollution in transport microenvironments. Atmos. Environ. 1 (38), 1–8.
He, J., Gong, S., Yu, Y., Yu, L., Wu, L., Mao, H., Song, C., Zhao, S., Liu, H., Li, X., Li, R., 2017. Air pollution characteristics and their relation to meteorological conditions during 2014-2015 in major Chinese cities. Environ. Pollut. 223, 484–496.
He, K., Yang, F., Ma, Y., Zhang, Q., Yao, X., Chan, C.K., Mulawa, P., 2001. The characteristics of PM2. 5 in Beijing, China. Atmos. Environ. 35 (29), 4959–4970.
Huang, Y., Shen, H., Chen, H., Wang, R., Zhang, Y., Su, S., Tao, S., 2014. Quantification of global primary emissions of PM2.5, PM10, and TSP from combustion and industrial process sources. Environ. Sci. Technol. 48 (23), 13834–13843.
Hurst, H.E., 1965. Long-term storage capacity of reservoirs. Trans. Am. Soc. Civ. Eng. 116, 770–808.
Ito, K., Thurston, G.D., Silverman, R.A., 2007. Characterization of PM2.5, gaseous pollutants, and meteorological interactions in the context of time-series health effects models. J. Expo. Sci. Environ. Epidemiol. 17 (2), S45–S60.
Janssen, N.A.H., Fischer, P., Marra, M., Ameling, C., Cassee, F.R., 2013. Short-term effects of PM2. 5, PM10 and PM2. 5–10 on daily mortality in The Netherlands. Sci. Total Environ. 463, 20–26.
Jia, M., Zhao, T., Cheng, X., Gong, S., Zhang, X., Tang, L., Chen, Y., 2017. Inverse relations of PM2.5 and O3 in air compound pollution between cold and hot seasons over an urban area of east China. Atmosphere 8 (3), 59.
Kamińska, J.A., 2018. The use of random forests in modelling short-term air pollution effects based on traffic and meteorological conditions: a case study in Wrocław. J. Environ. Manag. 217, 164–174.
Khoder, M.I., 2009. Diurnal, seasonal and weekdays–weekends variations of ground level ozone concentrations in an urban area in greater Cairo. Environ. Monit. Assess. 149 (1–4), 349–362.
Kiesewetter, G., Amann, M., 2014. Urban PM2.5 Levels under the EU Clean Air Policy Package.
Krudysz, M., Moore, K., Geller, M., Sioutas, C., Froines, J., 2009. Intra-community spatial variability of particulate matter size distributions in southern California/Los Angeles. Atmos. Chem. Phys. Discuss. 9 (3), 1061–1075.
Liu, X., Huang, H., Jiang, Y., Wang, T., Xu, Y., Abbaszade, G., Zimmermann, R., 2020. Assessment of German population exposure levels to PM10 based on multiple spatial-temporal data. Environ. Sci. Pollut. Control Ser. 27 (6), 6637–6648.
LeCun, Y., Bengio, Y., Hinton, G., 2015. Deep learning. Nature 521, 436–444.
Liu, Y.J., Harrison, R.M., 2011. Properties of coarse particles in the atmosphere of the United Kingdom. Atmos. Environ. 45 (19), 3267–3276.
Mavroidis, I., Ilia, M., 2012. Trends of NOx, NO2 and O3 concentrations at three different types of air quality monitoring stations in Athens, Greece. Atmos. Environ. 63, 135–147.
Motallebi, N., Taylor Jr., C.A., Croes, B.E., 2003. Particulate matter in California: Part 2—spatial, temporal, and compositional patterns of PM2. 5, PM10–2.5, and PM10. J. Air Waste Manag. Assoc. 53 (12), 1517–1530.
Munir, S., 2016. Modelling the non-linear association of particulate matter (PM 10) with meteorological parameters and other air pollutants—a case study in Makkah. Arab. J. Geosci. 9 (1), 1–13.
Pakbin, P., Hudda, N., Cheung, K.L., Moore, K.F., Sioutas, C., 2010. Spatial and temporal variability of coarse (PM10–2.5) particulate matter concentrations in the los angeles area. Aerosol. Sci. Technol. 44, 514–525.
Perez, L., Medina-Ramon, M., Kunzli, N., Alastuey, A., Pey, J., Perez, N., Garcia, R., Tobias, A., Querol, X., Sunyer, J., 2009. Size fractionate particulate matter, vehicle traffic, and case-specific daily mortality in Barcelona, Spain. Environ. Sci. Technol. 43 (13), 4707–4714.
Pinto, J.P., Lefohn, A.S., Shadwick, D.S., 2004. Spatial variability of PM2.5 in urban areas in the United States. J. Air Waste Manag. Assoc. 54 (4), 440–449.
Pochanart, P., Kato, S., Katsuno, T., Akimoto, H., 2004. Eurasian continental background and regionally polluted levels of ozone and CO observed in northeast Asia. Atmos. Environ. 9 (38), 1325–1336.
Pokorná, P., Schwarz, J., Krejci, R., Swietlicki, E., Havránek, V., Ždímal, V., 2018. Comparison of PM2.5 chemical composition and sources at a rural background site in Central Europe between 1993/1994/1995 and 2009/2010: effect of legislative regulations and economic transformation on the air quality. Environ. Pollut. 241, 841–851.
Pope, C.R., Burnett, R.T., Thun, M.J., Calle, E.E., Krewski, D., Ito, K., Thurston, G.D., 2002. Lung cancer, cardiopulmonary mortality, and long-term exposure to fine particulate air pollution. J. Am. Med. Assoc. 287 (9), 1132–1141.
Pusede, S.E., Steiner, A.L., Cohen, R.C., 2015. Temperature and recent trends in the chemistry of continental surface ozone. Chem. Rev. 115 (10), 3898–3918.
Querol, X., Alastuey, A., Ruiz, C.R., Artinano, B., Hansson, H.C., Harrison, R.M., Buringh, E., Ten Brink, H.M., Lutz, M., Bruckmann, P., Straehl, P., Schneider, J., 2004. Speciation and origin of PM10 and PM2.5 in selected European cities. Atmos. Environ. 38 (38), 6547–6555.
Rodrıguez, S., Querol, X., Alastuey, A., Viana, M.M., Alarcon, M., Mantilla, E., Ruiz, C.R., 2004. Comparative PM10–PM2.5 source contribution study at rural, urban and industrial sites during PM episodes in Eastern Spain. Sci. Total Environ. 328 (1–3), 95–113.
Samet, J.M., Dominici, F., Curriero, F.C., Coursac, I., Zeger, S.L., 2000. Fine particulate air pollution and mortality in 20 US cities, 1987–1994. N. Engl. J. Med. 24 (343), 1742–1749.
Schwartz, J., 2000. Assessing confounding, effect modification, and thresholds in the association between ambient particles and daily deaths. Environ. Health Perspect. 108 (6), 563–568.
Song, C., Wu, L., Xie, Y., He, J., Chen, X., Wang, T., Lin, Y., Jin, T., Wang, A., Liu, Y., Dai, Q., Liu, B., Wang, Y.N., Mao, H., 2017. Air pollution in China: status and spatiotemporal variations. Environ. Pollut. 227, 334–347.
Strak, M., Rodopolou, S., Wolf, K., Hvidtfeldt, U., Stafoggia, M., Atkinson, R., Brunekreef, B., 2019. Effects of low-level air pollution: a study in europe. Environ. Epidemiol. 3, 384.
Streets, D.G., Fu, J.S., Jang, C.J., Hao, J., He, K., Tang, X., Zhang, Y., Wang, Z., Li, Z., Zhang, Q., Wang, L., Wang, B., Yu, C., 2007. Air quality during the 2008 beijing olympic games. Atmos. Environ. 3, 480–492.
Van Gerven, M., Bohte, S., 2017. Artificial neural networks as models of neural information processing. Front. Comput. Neurosci. 11, 114.
Viotti, P., Liuti, G., Di Genova, P., 2002. Atmospheric urban pollution: applications of

Appendix

an artificial neural network (ANN) to the city of Perugia. Ecol. Model. 1 (148), 27–46.
Waluś, K.J., Wargula, Ł., Krawiec, P., Adamiec, J.M., 2018. Legal regulations of restrictions of air pollution made by non-road mobile machinery—the case study for Europe: a review. Environ. Sci. Pollut. Control Ser. 25 (4), 3243–3259.
Wang, F., Chen, D.S., Cheng, S.Y., Li, J.B., Li, M.J., Ren, Z.H., 2010. Identification of regional atmospheric PM10 transport pathways using HYSPLIT, MM5-CMAQ and synoptic pressure pattern analysis. Environ. Model. Software 12 (8), 927–934.
Wang, T., Cheung, V.T., Anson, M., Li, Y.S., 2001. Ozone and related gaseous pollutants in the boundary layer of eastern China: overview of the recent measurements at a rural site. Geophys. Res. Lett. 12 (28), 2373–2376.
Wilson, W.E., Suh, H.H., 1997. Fine particles and coarse particles: concentration relationships relevant to epidemiologic studies. J. Air Waste Manag. Assoc. 47 (12), 1238–1249.
Xie, Y., Zhao, B., Zhang, L., Luo, R., 2015. Spatiotemporal variations of PM2.5 and PM10 concentrations between 31 Chinese cities and their relationships with S02, NO2, CO and O3. China Particuol. 3, 141–149.
Xue, T., Zheng, Y., Geng, G., Zheng, B., Jiang, X., Zhang, Q., He, K., 2017. Fusing observational, satellite remote sensing and air quality model simulated data to estimate spatiotemporal variations of PM2. 5 exposure in China. Rem. Sens. 9 (3), 221.
Yao, W., Zheng, Z., Zhao, J., Wang, X., Wang, Y., Li, X., Fu, J., 2020. The factor analysis of fog and haze under the coupling of multiple factors–taking four Chinese cities as an example. Energy Pol. 137, 111–138.
Yoo, J.M., Jeong, M.J., Kim, D., Stockwell, W.R., Yang, J.H., Shin, H.W., Lee, M.I., Song, C.K., Lee, S.D., 2015. Spatiotemporal variations of air pollutants (O 3 , NO 2 , SO 2 , CO, PM 10 , and VOCs) with land-use types. Atmos. Chem. Phys. 15 (18), 10857–10885.
Zalakeviciute, R., López-Villada, J., Rybarczyk, Y., 2018. Contrasted effects of relative humidity and precipitation on urban PM2. 5 pollution in high elevation urban areas. Sustainability 10 (6), 1–21, 2064.
Zanobetti, A., Schwartz, J., 2009. The effect of fine and coarse particulate air pollution on mortality: a national analysis. Environ. Health Perspect. 117 (6), 898–903.
Zhang, L., Cheng, Y., Zhang, Y., He, Y., Gu, Z., Yu, C., 2016. Impact of air humidity fluctuation on the rise of PM mass concentration based on the high-resolution monitoring data. Aerosol. Air Qual. Res. 17 (2), 543–552.
Zhang, Z., Wang, J., Hart, J.E., Laden, F., Zhao, C., Li, T., Chen, K., 2018. National scale spatiotemporal land-use regression model for PM2. 5, PM10 and NO2 concentration in China. Atmos. Environ. 192, 48–54.
Zhaobin, S., Xingqin, A., Yan, T., Hou, Q., 2013. Assessment of population exposure to PM10 for respiratory disease in Lanzhou (China) and its health-related economic costs based on GIS. BMC Publ. Health 1 (13), 891.
Zhou, X., Cao, Z., Ma, Y., Wang, L., Wu, R., Wang, W., 2016. Concentrations, correlations and chemical species of PM2. 5/PM10 based on published data in China: potential implications for the revised particulate standard. Chemosphere 144, 518–526.

Publication III

Liu, X., Zhang, X., Schnelle-Kreis, J., Jakobi, G., Cao, X., Cyrys, J., ... & Zimmermann, R. (2021). Spatiotemporal Characteristics and Driving Factors of Black Carbon in Augsburg, Germany: Combination of Mobile Monitoring and Street View Images. ***Environmental Science & Technology***, 1,55, 160-168.

Environmental Science & Technology

pubs.acs.org/est Article

Spatiotemporal Characteristics and Driving Factors of Black Carbon in Augsburg, Germany: Combination of Mobile Monitoring and Street View Images

Xiansheng Liu, Xun Zhang,* Jürgen Schnelle-Kreis,* Gert Jakobi, Xin Cao, Josef Cyrys, Lanyan Yang, Brigitte Schloter-Hai, Gülcin Abbaszade, Jürgen Orasche, Mohamed Khedr, Michal Kowalski, Marcus Hank, and Ralf Zimmermann

Cite This: *Environ. Sci. Technol.* 2021, 55, 160−168 Read Online

ACCESS | Metrics & More | Article Recommendations | Supporting Information



ABSTRACT: The study investigates the spatial pattern of black carbon (BC) at a high spatial resolution in Augsburg, Germany. Sixty two walks were performed to assess the concentrations of equivalent black carbon (eBC), ultraviolet particulate matter (UVPM), and equivalent brown carbon (eBrC) in different seasons and at different times of the day with a mobile platform (i.e., trolley). Along with BC measurements, images of street microenvironments were recorded. Meteorological parameters, including temperature, relative humidity, and wind speed, were monitored. The BC concentrations showed significant spatial heterogeneity and diurnal variations peaking in the morning and at night. The highest BC concentrations were observed near dense traffic. The correlations between BC and street views (buildings, roads, cars, and vegetation) were weak but highly significant. Moreover, meteorological factors also influenced the BC concentration. A model based on street view images and meteorological data was developed to examine the driving factors of the spatial variability of BC concentrations at a higher spatial resolution as different microenvironments based on traffic density. The best results were obtained for UVPM and eBC (71 and 70% explained variability). eBrC (53%), to which other sources besides road traffic can also make significant contributions, is modeled less well.

Downloaded via HELMHOLTZ ZENTRUM MUENCHEN on September 13, 2021 at 06:40:50 (UTC).
See https://pubs.acs.org/sharingguidelines for options on how to legitimately share published articles.

1. INTRODUCTION

Since the 20th century, air pollution has been one of the major environmental problems in metropolitan areas,[1−3] with black carbon (BC), an optically absorbing substance, contributing less than 5−10% to the total mass concentration of particulate matter ($PM_{2.5}$).[4] Severely, it has different toxicities to sensitive targets in the human body, such as the lungs, the body's main defense cells, and even systemic blood circulation.[5−7] In 2012, the International Agency for Research on Cancer (IARC) classified BC containing diesel soot carcinogenic to humans.[8] Meanwhile, Janssen et al. (2011) found that BC can be used as a valuable air quality indicator for assessing the health risks of traffic-related air pollution.[9] Hence, in this study, the spatial characteristics and driving factors of black carbon were studied.

The monitoring of air quality by high-quality stationary measurements, as usually performed in official monitoring networks, has limitations when investigating the spatial variability of human exposure. Therefore, mobile monitoring[10,11] has been widely applied for the collection of real-time air quality measurements to assess local air quality and air pollutant exposures. This method can improve the temporal and spatial resolution of measurement data of in the urban environment and enables the collection of data such as the traffic-related air pollutant concentrations and driving factors in microscale road sections.[12] Mobile measurements are,

Received: July 20, 2020
Revised: November 26, 2020
Accepted: November 30, 2020
Published: December 8, 2020



ACS Publications © 2020 American Chemical Society

https://dx.doi.org/10.1021/acs.est.0c04776
Environ. Sci. Technol. 2021, 55, 160−168

Appendix

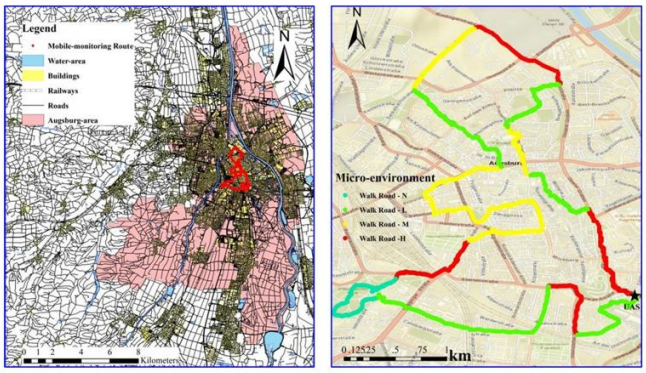


Figure 1. Location and road of the sampling sites in Augsburg, Germany. Left: main urban area of Augsburg (Data/Maps Copyright 2018 Geofabrik GmbH and OpenStreetMap contributors), right: sampling route map, different colors represent different traffic densities in the microenvironments; red, high traffic roads (H_Traffic); yellow, medium traffic roads (M_Traffic); green, low traffic roads (L_Traffic); blue, park area (N_Traffic); start and end point, UAS (University of Applied Sciences).

therefore, favorably used in human exposure studies to quantify individual exposures and to demonstrate the importance of exposure differences in different microenvironments.[13−16] For example, Bassok et al. (2010) used a portable detector to measure the BC concentration of traffic sources in the Seattle International District and discussed the spatial and temporal distributions of the BC concentration on a street scale.[17]

Changes in the air quality in the city are not only related to the distribution of vehicle emissions but also to the urban development, street characteristics, street location, and land use types.[18−22] Hankey et al. (2015) used bicycle-based, mobile measurements during rush hour in Minneapolis, USA to build land-use regression models for particulate concentrations.[16] Apte et al. (2017) equipped Google Street View vehicles with a fast-response pollution measurement platform and repeatedly sampled every street in a 30 km^2 area of Oakland, CA, developing the largest urban air quality data set of its type.[23] Messier et al. (2018) mapped spatial air quality patterns using an unusually rich data set of repeated mobile air quality measurements collected with specially equipped Google Street View cars.[24] Hankey and Marshall (2015) studied the regression models of video-derived traffic counts and particle concentrations.[25] They used the counts of each vehicle type (i.e., passenger cars, trucks, and buses) as independent variables in the regression model to estimate the particulate matter concentration. Liang et al. (2017) used remote sensing images to obtain urban sky, trees, and architectural landscape factors to study the correlation between urban environment and air quality.[26] Therefore, the use of images to assess air pollution is potentially feasible and desirable. However, the previous models, such as Google Street View and remote sensing images, have certain limitations due to the detailed information that may not be obtained in small scales. Nowadays, the street view images provide an excellent option acquired within urban street canyons and provide a human-centered view of the built environment.[27] However, it remains unclear how to develop street view images to predict air pollutants.

In this study, we used portable instrument-based microair pollution monitoring devices to monitor the actual exposure level of black carbon pollution to the population in Augsburg and at the same time to collect the street view images to predict air pollutants. The primary goals of the present study were (1) to provide the spatiotemporal variability of BC in urban street environments with a high spatial and temporal resolution; and (2) to develop street BC models based on street view images for predicting spatial patterns in exposure to BC for Augsburg, Germany. Our approach is innovative because it investigates a street view image model to predict BC exposure as experienced by a pedestrian in an urban environment.

2. MATERIALS AND METHODS

2.1. Study Area. The mobile measurements were carried out in Augsburg, Germany. It is the third largest city in Bavaria (after Munich and Nuremberg) with about 300 000 inhabitants and about 660 000 residents in its metropolitan area. The mean annual temperature and precipitation are 13.2 °C and 767 mm, respectively. It has an oceanic climate that tends to clouds with precipitation.

This investigation was part of the Smart Air Quality Network (https://www.smartaq.net/) project. A fixed walking path within the center of the city was determined. Wherever possible, the walks were carried out on the right side of the road due to people's daily habits (driving and walking on the right side in Germany) and walked repeatedly in the course of the investigations. The route started from Augsburg University of Applied Sciences and passed through different types of land use to ensure that the selected path runs across different microenvironments and may be representative for the entire city. It is approximately 14 km long (Figure 1). The average walking time for the entire route was approximately 3 h.

We divided the monitoring route into four microenvironment classes, high traffic roads (H_Traffic, average 500−1000 vehicles/h), medium traffic roads (M_Traffic, average 200−500 vehicles/h), low traffic roads (L_Traffic, average 1−200 vehicles/h), and park area (N_Traffic, average 0 vehicles/h)

https://dx.doi.org/10.1021/acs.est.0c04776
Environ. Sci. Technol. 2021, 55, 160−168

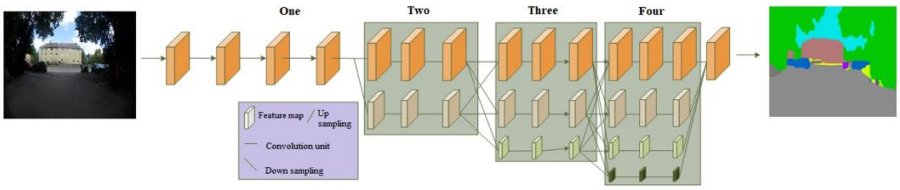


Figure 2. Schematic diagram of sample segmentation image processed by the HRnet model.

according to the actual traffic density examined during the daytime, determined from the traffic flow observed by the street views.

2.2. Sampling Campaign. All walks along the route were conducted on weekdays from August 2018 to June 2020, with clear skies (i.e., nonrainy days) and calm winds. The detailed description for each sampling run is illustrated in Table S1. Mobile platforms were built on a trolley, and air-monitoring devices were installed in a box attached to the trolley. It was equipped with a GPS (GPSMAP 64s, Garmin, USA) to register the measurement location at 1 s resolution, and a point-of-view (POV) camera (TG-Tracker, Olympus, Japan) to record the street view images at 5 s resolution. Comparative measurements of the MicroAeth MA200 to measurements carried out with a stationary instrument (Magee, model AE33, Aerosol Co. Slovenia) were made between the individual walks.

BC concentrations were measured by a multiwavelength Aethalometer (microAethalometer, MA200, AethLabs, USA) with a time resolution of 10 s to avoid excessive noise of the BC signal. The Aethalometer measures the light attenuation through a filter tape at five wavelengths, while the filter is continuously collecting aerosol at a flow rate of 150 mL/min. Measurement at 880 nm is defined as the concentration of BC, while measurement at 375 nm is interpreted as ultraviolet particulate matter (UVPM). The brown carbon (BrC) is the fraction of carbonaceous aerosols, excluding black carbon, which absorbs light primarily at the low visible wavelengths and the near ultraviolet range, expressed as the difference eBrC = UVPM (375 nm) − eBC (880 nm).[28−31]

2.3. Meteorological Data Monitoring. The meteorological parameters including air temperature (T), relative humidity (RH), and wind speed (WS) were measured by a monitoring station in Augsburg located in the urban background on the campus of the University of Applied Sciences (UAS), which is operated jointly since 2004 by the Helmholtz Zentrum München (German Research Center for Environmental Health, Munich) and Environmental Science Center, University Augsburg.[32]

2.4. Postprocessing of BC Data. The Aethalometer measurement in environments with low BC concentrations and/or at high time resolution triggers for negative value detection due to the instrumental noise and changing relative humidity conditions.[33] Negative values frequently contain valid information that is required for postprocessing or smoothing the data over a long interval; hence, the removal of negative values may be detrimental to a dataset.[34]

For postprocessing data, MA200 microAeth users can upload their data file to AethLabs platform (http://www.aethlabs.com) and apply "postprocessing tools" to smoothen their data. Whereas various different algorithms are available in this process. The commonly applied time-adaptive noise reduction method is centered moving average (CMA), which is used to build the underlying trends of a time series.[35] Unlike a simple moving average, there is no shift or group delay in the data using the CMA. Therefore, the CMA was chosen in this study. The comparison between original BC measurements and CMA averaging seven data points is illustrated in Figure S1. The denoising results show that the CMA can reduce negative anomalies that occur in the raw BC data. In our study, comparative measurements of the MicroAeth MA200, which were used in the trolleys to measurements carried out with a stationary instrument (Magee, model AE33, Aerosol Co. Slovenia), were simultaneously made between the individual walks (see details in the Supporting Information, Section 1). The comparison showed very good agreement of the results (Pearson's r = 0.977 and 0.933 and R^2 = 0.955 and 0.871 for UVPM and eBC, respectively, Figure S2) independent on time of day and season.

2.5. BC Modeling Using the Street View Image Model. *2.5.1. Street View Image Model.* In order to quantify the composition of the surface types that pedestrians experience in the street canyon, the method of deep learning was used, which can create a unique description of the urban form and composition as experienced by a pedestrian in the street and is, therefore, more relevant to the human experience of cities compared to planar bird's eye views from satellite data. In this study, the images are captured by a camera in the daylight walking, and the street view images were mainly segmented into five types: buildings, roads (including parking cars), vegetation, cars (only cars in traffic), and sky.

2.5.2. The Semantic Segmentation Algorithm of Street Scenes Based on the HRnet Model. To obtain the surrounding environment elements of the current location, the street view image is segmented into some categories to obtain the proportions area of different elements of the scene in the current image. In this study, the high-resolution network (HRnet) is selected as the main model structure for semantic segmentation.[36] As a standard backbone network, the HRnet network structure has obtained good results in image classification, target detection, and semantic segmentation. Furthermore, the previous studies proved that HRnetV2, one version of HRnet, has a good effect in the cityscape public dataset, and the average intersection ratio (mIoU) obtained by the model in the verification set is higher than that of classic networks such as Unet, PSPNet, and DeepLabv3+.[37−41] Because our street view images are classified into categories and image scenes from the cityscape dataset, they are both very similar to the semantic segmentation of street view images. So this study adopted the HRnetV2 model as the street view image segmentation network.

https://dx.doi.org/10.1021/acs.est.0c04776
Environ. Sci. Technol. 2021, 55, 160−168

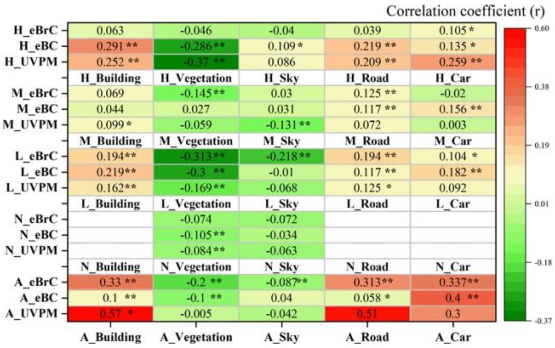


Figure 3. Correlation matrix of measured compounds in different traffic volumes (A, all roads; N, no traffic volume (park area); L, low traffic volume; M, middle traffic volume; H, high traffic volume, $*p < 0.05$, $**p < 0.01$, and white bands represent nonsense).

As shown in Figure 2, the HRnet network structure can be divided into four parts with minor modification.[36] Briefly, the first part is composed of four bottleneck structural blocks, and the second, third, and fourth parts are all composed of structural blocks of residual units. After the transmission of the first part is completed, two branches are generated through two convolutional layers of different sizes and transmitted to the second part in parallel. On the branch, four structural blocks of residual units are serially connected and transmitted. When transmitting to the third part, a new low-resolution branch is generated through the convolutional layer again, and then the feature layers of the three branches are up-sampled and down-sampled. The sampling methods are combined and transmitted to the fourth part. Similarly, in the fourth stage, the data is transmitted in parallel on the four branches, and after the transmission is completed, it is all merged to the original resolution through up-sampling. Finally, the feature layer is output through the convolutional layer. In this study, we used the pytorch1.3 version, with four GTX 1080ti GPUs to pretrain the network, batch size is 12, and training round epochs is 500.

2.5.3. Model Accuracy Evaluation Method. The accuracy evaluation of the model can reflect the fitting effect and the error of the model. In this study, we used the cross-validation (CV) method that used 70% of the monitoring data as the training data, and the 10-fold CV method to estimate the accuracy of the model.[42] This method can balance the deviation and variance of the model. By assessing the closeness between the simulation result of the verification set and the actual observation value, the simulation accuracy of the model is reflected. The evaluation indicators used in this study include the correlation coefficient (R), the root mean square error (RMSE), the mean absolute error (MAE), and the fitting index (index of agreement, IA). Where R represents the model, the fitting effect of RMSE and MAE represent the deviation between the predicted value and the actual value, and IA represents the consistency between the predicted value and the actual value.

2.5.4. Random Forest Algorithm. One of the challenges derived by regression-based street view image models is difficulty to capture nonlinear relationships and complex interactions. Random forest can resist and overcome these problems.[43,44] To predict the urban black carbon concentrations, the random forest was selected for the street view image model. We used the default setting from the package scikit-learn. A bivariate correlation analysis was used in this study to extract the target factors required for modeling, and the concentrations of UVPM, eBC, and eBrC in the training set and the corresponding target factors were used as data for the random forest regression method. In order to express the simulation accuracy of the random forest optimization method, the fitting indices of the support vector machine (SVM) optimization method[45] and the multiple linear regression (MLR) method[46] were also calculated and compared.

3. RESULTS AND DISCUSSION

3.1. Spatiotemporal Variations of Median Black Carbon Concentrations across Street Microenvironments. Because the median is a more representative central tendency measure than the mean,[47] the study preferred to use the median to investigate the spatial variation of BC concentrations. Figure S3 shows the aggregated median UVPM, eBC, and eBrC concentrations for each 15 m distance along the route. The observed median BC concentrations in different microenvironments exhibited substantial spatial heterogeneity, with the lowest values in the park environment (N_traffic) and the highest in the H_traffic environment (see details in the Supporting Information, Section 2.1). For eBC, the averages in the busier roads were obviously higher than those of others ($p < 0.05$ with ANOVA method) (Figure S4). The areas with highest traffic intensities, particularly on crossroads, showed high BC concentrations (Figure S3), e.g., the crossroads of P1 (10.3, 10.0, and 0.34 $\mu g/m^3$), P2 (11.6, 10.4, and 1.20 $\mu g/m^3$), and P3 (10.88, 9.38, and 1.50 $\mu g/m^3$). Meanwhile, based on the Spearman correlation, the three parameters have weak to strong significant correlations, as following UVPM *versus* eBC (0.917, $p < 0.01$); UVPM *versus* eBrC (0.642, $p < 0.01$); and eBC *versus* eBrC (0.361, $p < 0.01$).

Generally, high levels of pollutant concentrations occur in areas with the largest traffic volumes. These regions are hotspots for eBC concentrations. It could be concluded that the direct emissions from the traffic could be an important source for BC in Augsburg. On the other hand, in the central business district, the main means of transportation are trams

https://dx.doi.org/10.1021/acs.est.0c04776
Environ. Sci. Technol. 2021, 55, 160−168

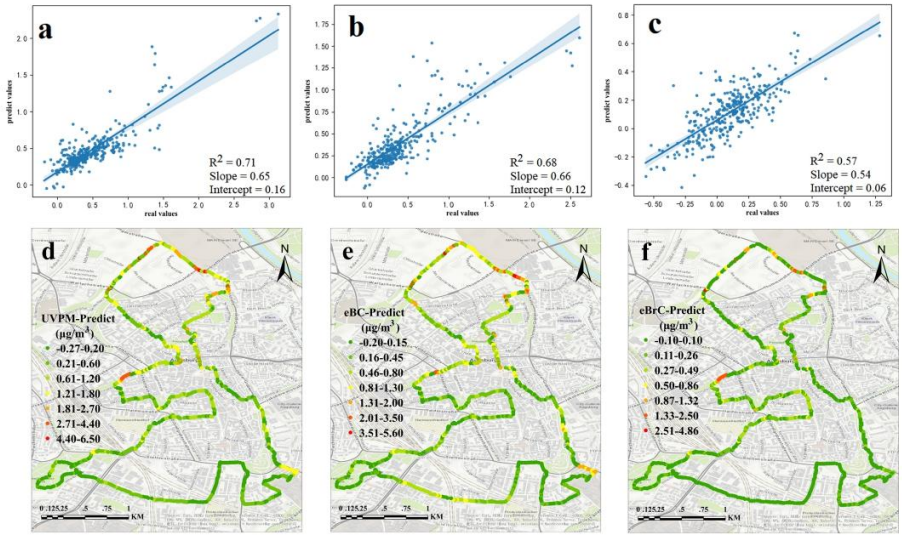


Figure 4. The random forest method and prediction of the spatial distribution of air pollutants (a–c) random forest optimization method for UVPM, eBC, and eBrC; and (d–f) spatial distribution for prediction exposure to UVPM, eBC, and eBrC).

and natural gas-operated buses. In other regions, cars are the mainstay. Especially on some main roads, high-emission vehicles like heavy-duty trucks are common. Targino et al. (2016) pointed out that the pollution concentrations were positively correlated with traffic loads and observed a strong relationship between eBC concentrations at intersections managed by traffic signals and the number of heavy-duty diesel vehicles.[48] Boogaard et al. (2011) averaged the ratio of the pollutant concentration of multiple streets (10 000–18 000 vehicles/day) to the background and found that the street eBC concentration was higher than the background.[49] In summary, the highest eBC concentrations in Augsburg were near traffic roadways, especially at street crossings and traffic lights.

In comparison with temporal variations, the differences in UVPM, eBC, and eBrC concentrations measured in four seasons were generally significant ($p < 0.05$, Figure S5). In spring, summer, autumn, and winter, the variation trends of the three air pollutants were similar. The median concentrations of UVPM, eBC, and eBrC are respectively 3.86, 3.55, and 2.68 times higher in winter than that in spring. This can be attributed to seasonal differences in meteorological conditions and emission sources (Figure S5, details in the Supporting Information, Section 2.2). In addition, the diurnal variation of BC was strikingly sharp in the morning peaks and late afternoon to late night. The maximum concentrations around midnight were 4.2, 3.7, and 6.8 times higher than those observed in the afternoon for UVPM, eBC, and eBrC, respectively (Figure S6, details in the Supporting Information, Section 2.3).

3.2. Association of BC Concentrations and Potential Driving Factors. The correlation analysis between the BC concentration and driving factors and the streetscape images was observed. As shown in Figure 3, the correlations between street scene (buildings, roads, cars, and vegetation) and UVPM, eBC, and eBrC carbon are weak but highly significant. Similarly, Choi et al. (2016) found that the block-scaled ultrafine particle (UFP) concentrations highly depend on the built environment and surface turbulence.[25] Black carbon has a similar character to UFP and is related to the built environment. Open blocks may be one of the reasons and give the benefit to the dispersion of pollutants, while high and narrow buildings reduce the dispersion of pollution from the upper wind. Peters et al. (2013) selected two fixed roads in the cities of Antwerp and Mol in Belgium to test the UFP.[47] The results also showed that the daily concentration of UFP changes closely with the traffic density flow and the structure of the street. Pan et al. (2013) also found that the dispersion of pollutants in urban canopies is indirectly affected by the shape of the buildings.[50] The impact of automobiles on pollutants is mainly caused by automobile exhaust, which is the main source of black carbon.[51] The relationship between vegetation and black carbon is inversely related because the urban forest system can store and capture dust in the air,[52] which purifies the black carbon concentration. More than that, meteorological factors (T, RH, and WS) also influence the BC concentrations in the urban area, which was observed and found in the current and previous studies[34] (see details in Section 3, Supporting Information).

For different microenvironments, the correlation between street scene indicators and the three air pollutants is slightly different, caused by the different proportions of street scenes in different microenvironments (Figure 3).[53] Most of the vegetation is found in the park area, resulting in the low concentrations of UVPM, eBC, and eBrC. In the micro-

https://dx.doi.org/10.1021/acs.est.0c04776
Environ. Sci. Technol. 2021, 55, 160–168

Appendix

environment of medium traffic flow, the correlation between UVPM and the building is very weak but still significant. However, the correlations between eBC, eBrC, and the building are not significant. A wider range in the proportion of buildings may be the reason for this observation.

3.3. Evaluation and Prediction of UVPM, eBC, and eBrC Concentrations. *3.3.1. The Fitting Effects of Random Forest (RF) and Its Application.* The scatterplots of the predicted and observed values of the UVPM, eBC, and eBrC for RF methods are shown in Figure 4a−c), and the relationship between each predictor and the three pollutants are shown in Figure S8. The scatterplots of the predicted and observed values of the UVPM, eBC, and eBrC for SVM and MLR are shown in Figure S9. In the same sampling, 70% of the monitoring data was selected as the training data, and the 10-fold CV method was used to estimate the accuracy of the method, where the data set is randomly separated to 10 partitions with equal-sized folds. The algorithm is trained using ninefolds and repeated 10 times. We performed the sampling with replacement, suggesting that every fold could be used as the validation set exactly once. As a result, the correlation coefficient (R), root mean square error (RMSE), mean absolute error (MAE), and fitting index (IA) of the UVPM (eBC and eBrC) prediction method are shown in Table S2. Based on the R^2 and IA, the RF method is superior to the other two types of methods, and it performs better in the Augsburg black carbon aerosol simulation: concentration space simulation. This is because the main advantage of random forest is that ability to capture the complex and nonlinear relationship between predictor variables and results with small-scale training data.[54] Moreover, the effects of the SVM and the MLR method fitting are not suitable for this study (Table S2), as both applications will lead to an obvious overfitting. If random forests can indeed capture more patterns based on street view images, they may be more accurate predictors of pollutant concentration.[54] Thus, to determine the dominant factors of the model, the weight of each factor was analyzed based on the RF method, and we found that the relative humidity has a greater influence for UVPM, eBC, and eBrC. In addition, other dominant factors are wind speed and temperature for UVPM, temperature and vegetation for eBC, and vegetation for eBrC.

Based on the prediction models of three pollutants established in this study, we have spatialized the model prediction, as shown in Figure 4d−f. The predicted concentrations of the three pollutants (UVPM, eBC, and eBrC) and the actual traffic flow in different microenvironments are mainly consistent (high traffic flow and high pollutant concentration), which further illustrate the applicability of the model built in this study. It is worth noting that the RF method is the best for UVPM and eBC prediction; however, for eBrC, it is poor, which may be caused by the source of eBrC. Previous studies have shown that wood combustion in Germany is frequently used for leisure.[55] We therefore estimated that eBrC can be associated with smoke from the smoldering phase of wood combustion and leisure. However, during the sampling process, the camera did not collect relevant information (e.g., wood combustion).

3.3.2. Street View Image Model and Its Comparison with Other Models. The most widely used models for spatial distribution simulation include spatial interpolation, remote sensing inversion, atmospheric diffusion models, land use regression (LUR), and hybrid models of the latter.[56] Atmospheric diffusion models, LUR, and hybrid models can provide pollution estimates on comparable spatial scale as our model. Hence, we very briefly discuss advantages and disadvantages of these models compared to our street view image-based approach.

If the atmospheric diffusion model (e.g., MISKAM and computational fluid dynamics (CFD) model)[57] is used to simulate black carbon concentration in the microscale environment, the input data required in the model are terrain, meteorological data, pollution source data (point source/area source), and emission factors of relevant sources as well as activity pattern (time-dependent emission strengths). A major advantage is their ability to calculate the pollutant concentration of various sources and integrate simple and complex terrain. Yet their use is improper for the modeling in low wind speeds,[57] where the wind speed inside Augsburg urban area is relatively low, especially in winter and spring (Table S1). Depending on time and spatial resolution of input data, results are comparable in spatiotemporal resolution to our model. However, for the calculation of pollutant concentrations with high spatial resolution (e.g., 10 m grid width),[57] on the one hand, source information in similar resolution is needed, which is usually not available. For the model calculations, therefore, assumptions about the sources (i.e., emission position and intensity and activity pattern) must often be used. On the other hand, the calculations require high computing power or long computing times, especially at high spatial resolution. Regarding LUR, the input data required in this model are representative concentrations of atmospheric pollutants determined at several monitoring sites and land use data, road traffic flow, meteorological data, and other factors potentially influencing concentrations near the monitoring points.[58] Moreover, this model is a cost-effective tool for predicting spatial variability in ambient air pollutant concentrations with high resolution.[16] Usually, input data for LUR modeling is sufficient to achieve similar spatial resolution like our approach for the BC estimation. However, results from LUR modeling are usually time-invariant. In addition, the selection of the number of monitoring sites and how to determine the contribution ability of different elements to pollutants and the distance between them needs to be further explored and discussed.[58] In order to further prove the superiority of our model, we compare LUR with our model more specifically (see details in the Supporting Information, Section 4) in the supporting material, and the results show that the R^2 of LURF (0.33−0.64) in different buffers are lower than that in our street view image model (0.53−0.71).

Hybrid models that combine elements of LUR and dispersion models provide the opportunity to exploit the advantage of the abovementioned techniques while mitigating their shortcomings.[59] When the necessary data support is lacking, advanced dispersion may perform poorly. In this case, the LUR model result can be used as input dispersion modeling.[56] As a result, the hybrid model explained more variance than other compared models in the study. However, it may require more complex analysis than a single model, and the lack in uniformity of the verification model will make it difficult to compare with reviewed models.[60]

The street view image model proposed in this study can provide a prediction of UVPM, eBC, and eBrC concentration levels with high accuracy and efficiency. This model can effectively overcome some shortcomings of other models in predicting air pollution, such as, it is applicable in the low wind

https://dx.doi.org/10.1021/acs.est.0c04776
Environ. Sci. Technol. 2021, 55, 160−168

Appendix

speed level, easily identifying the hotspot and simple analysis. In addition, the model has strong timeliness, which can capture the actual conditions of the daytime environment. In the future, street view image model may prospect to develop in different areas or even areas that cannot be accessed by air quality monitoring equipment. The concentrations of UVPM, eBC, and eBrC can be estimated by using street view images combined with meteorological factors in the area. Moreover, street view images can easily obtain the types of features with highly detailed information. However, the street view image model still has certain limitations, such as meteorological data that is not measured along the path (see in the Supporting Information, Section 5), and further improvements are still needed in the future.

■ ASSOCIATED CONTENT

Supporting Information

The Supporting Information is available free of charge at https://pubs.acs.org/doi/10.1021/acs.est.0c04776.

Comparative measurement of MicroAeth MA200, spatiotemporal variations of median black carbon concentrations in Augsburg, meteorological effects on BC concentrations, comparison LURF and a street view image model, and limitations in BC estimation; descriptions of the meteorological conditions (Table S1); comparison of random forest fitting effects (Table S2); comparison of land use random forest (Table S3); comparison between original BC measurements and corrections (Figure S1); comparative measurements of the MicroAeth MA 200 with AE33 (Figure S2); spatial distribution of the median UVPM, eBC, and eBrC exposure concentrations (Figure S3); box plots of median concentrations of UVPM, eBC, and eBrC in different microenvironments (Figure S4); comparison of UVPM, eBC, and eBrC concentrations among different seasons (Figure S5); diurnal variations of mean UVPM, eBC, and eBrC concentrations in Augsburg (Figure S6); correlation matrix of measured compounds in different traffic volumes (Figure S7); scatter diagrams of relationship between each predictor and the three pollutants (Figure S8); support vector machine optimization and multiple linear regression method (Figure S9); and land use random forest model in different buffers for UVPM, eBC, and eBrC (Figure S10) (PDF)

■ AUTHOR INFORMATION

Corresponding Authors

Xun Zhang − *Beijing Key Laboratory of Big Data Technology for Food Safety, School of Computer Science and Engineering, Beijing Technology and Business University, Beijing 100048, China*; orcid.org/0000-0002-5502-2974; Email: zhangxun@btbu.edu.cn

Jürgen Schnelle-Kreis − *Joint Mass Spectrometry Center, Cooperation Group Comprehensive Molecular Analytics, Helmholtz Zentrum München, German Research Center for Environmental Health, Neuherberg 85764, Germany*; Email: juergen.schnelle@helmholtz-muenchen.de

Authors

Xiansheng Liu − *Joint Mass Spectrometry Center, Cooperation Group Comprehensive Molecular Analytics, Helmholtz Zentrum München, German Research Center for Environmental Health, Neuherberg 85764, Germany; Joint Mass Spectrometry Center, Chair of Analytical Chemistry, University of Rostock, Rostock 18059, Germany;* orcid.org/0000-0002-0228-5551

Gert Jakobi − *Joint Mass Spectrometry Center, Cooperation Group Comprehensive Molecular Analytics, Helmholtz Zentrum München, German Research Center for Environmental Health, Neuherberg 85764, Germany*

Xin Cao − *Joint Mass Spectrometry Center, Cooperation Group Comprehensive Molecular Analytics, Helmholtz Zentrum München, German Research Center for Environmental Health, Neuherberg 85764, Germany; Joint Mass Spectrometry Center, Chair of Analytical Chemistry, University of Rostock, Rostock 18059, Germany*

Josef Cyrys − *Institute of Epidemiology II, Helmholtz Zentrum München, German Research Center for Environmental Health, Neuherberg 85764, Germany; Environmental Science Center (WZU), University of Augsburg, Augsburg 86159, Germany*

Lanyan Yang − *Beijing Key Laboratory of Big Data Technology for Food Safety, School of Computer Science and Engineering, Beijing Technology and Business University, Beijing 100048, China*

Brigitte Schloter-Hai − *Joint Mass Spectrometry Center, Cooperation Group Comprehensive Molecular Analytics, Helmholtz Zentrum München, German Research Center for Environmental Health, Neuherberg 85764, Germany*

Gülcin Abbaszade − *Joint Mass Spectrometry Center, Cooperation Group Comprehensive Molecular Analytics, Helmholtz Zentrum München, German Research Center for Environmental Health, Neuherberg 85764, Germany*

Jürgen Orasche − *Joint Mass Spectrometry Center, Cooperation Group Comprehensive Molecular Analytics, Helmholtz Zentrum München, German Research Center for Environmental Health, Neuherberg 85764, Germany*

Mohamed Khedr − *Joint Mass Spectrometry Center, Cooperation Group Comprehensive Molecular Analytics, Helmholtz Zentrum München, German Research Center for Environmental Health, Neuherberg 85764, Germany; Joint Mass Spectrometry Center, Chair of Analytical Chemistry, University of Rostock, Rostock 18059, Germany*

Michal Kowalski − *Institute of Epidemiology II, Helmholtz Zentrum München, German Research Center for Environmental Health, Neuherberg 85764, Germany*

Marcus Hank − *GRIMM Aerosol Technik Ainring GmbH & Co., Ainring 83404, Germany*

Ralf Zimmermann − *Joint Mass Spectrometry Center, Cooperation Group Comprehensive Molecular Analytics, Helmholtz Zentrum München, German Research Center for Environmental Health, Neuherberg 85764, Germany; Joint Mass Spectrometry Center, Chair of Analytical Chemistry, University of Rostock, Rostock 18059, Germany*

Complete contact information is available at: https://pubs.acs.org/10.1021/acs.est.0c04776

Notes

The authors declare no competing financial interest.

■ ACKNOWLEDGMENTS

The work is funded by the Germany Federal Ministry of Transport and Digital Infrastructure (BMVI) as part of SmartAQnet (grant no.19F2003B), the Research Project of

Appendix

the Ministry of Science and Technology of China (2019YFC0507800), the Support Project of High-Level Teachers in Beijing Municipal Universities in the Period of 13th Five-Year Plan (CIT&TCD201904037), and the China Scholarship Council (CSC) under the State Scholarship Fund (file no. 201706860028). We also gratefully thank Mr. Hadiatullah from Tianjin University for his deep discussion and review editing of our manuscript and Aethlabs (especially Drew Hill and Jeffrey Blair) for providing assistance with troubleshooting the MA200.

■ REFERENCES

(1) World Health Organization *Air quality guidelines: global update 2005: particulate matter, ozone, nitrogen dioxide, and sulfur dioxide*; World Health Organization: 2006.
(2) Qadir, R. M.; Schnelle-Kreis, J.; Abbaszade, G.; Arteaga-Salas, J. M.; Diemer, J.; Zimmermann, R. Spatial and temporal variability of source contributions to ambient PM10 during winter in Augsburg, Germany using organic and inorganic tracers. *Chemosphere* **2014**, *103*, 263−273.
(3) Wei, X.; Gao, B.; Wang, P.; Zhou, H.; Lu, J. Pollution characteristics and health risk assessment of heavy metals in street dusts from different functional areas in Beijing, China. *Ecotoxicol. Environ. Saf.* **2015**, *112*, 186−192.
(4) Putaud, J.-P.; Raes, F.; Van Dingenen, R.; Brüggemann, E.; Facchini, M.-C.; Decesari, S.; Fuzzi, S.; Gehrig, R.; Hüglin, C.; Laj, P.; Lorbeer, G.; Maenhaut, W.; Mihalopoulos, N.; Müller, K.; Querol, X.; Rodriguez, S.; Schneider, J.; Sprindler, G.; Brink, H. t.; Tørseth, K.; Wiedensohler, A. A European aerosol phenomenology—2: chemical characteristics of particulate matter at kerbside, urban, rural and background sites in Europe. *Atmos. Environ.* **2004**, *38*, 2579−2595.
(5) Kampa, M.; Castanas, E. Human health effects of air pollution. *Environ. Pollut.* **2008**, *151*, 362−367.
(6) Ye, B.; Ji, X.; Yang, H.; Yao, X.; Chan, C. K.; Cadle, S. H.; Chan, T.; Mulawa, P. A. Concentration and chemical composition of $PM_{2.5}$ in Shanghai for a 1-year period. *Atmos. Environ.* **2003**, *37*, 499−510.
(7) Cassee, F. R.; Héroux, M.-E.; Gerlofs-Nijland, M. E.; Kelly, F. J. Particulate matter beyond mass: recent health evidence on the role of fractions, chemical constituents and sources of emission. *Inhalation Toxicol.* **2013**, *25*, 802−812.
(8) IARC. Diesel and Gasoline Engine Exhausts and Some Nitroarenes. IARC Monographs on the Evaluation of Carcinogenic Risks to Humans. *IARC Monogr. Eval. Carcinog. Risks Hum.* **2014**, 9−699.
(9) Janssen, N. A. H.; Hoek, G.; Simic-Lawson, M.; Fischer, P.; Van Bree, L.; Brink, H. t.; Keuken, M.; Atkinson, R. W.; Anderson, H. R.; Brunekreef, B.; Cassee, F. R. Black carbon as an additional indicator of the adverse health effects of airborne particles compared with PM10 and PM2. 5. *Environ. Health Perspect.* **2011**, *119*, 1691−1699.
(10) Idso, C. D.; Idso, S. B.; Balling, R. C., Jr. The urban CO_2 dome of Phoenix, Arizona. *Phys. Geogr.* **2013**, *19*, 95−108.
(11) Brantley, H. L.; Hagler, G. S. W.; Kimbrough, E. S.; Williams, R. W.; Mukerjee, S.; Neas, L. M. Mobile air monitoring data-processing strategies and effects on spatial air pollution trends. *Atmos. Meas. Tech.* **2014**, *7*, 2169−2183.
(12) Kolb, C. E.; Herndon, S. C.; McManus, J. B.; Shorter, J. H.; Zahniser, M. S.; Nelson, D. D.; Jayne, J. T.; Canagaratna, M. R.; Worsnop, D. R. Mobile Laboratory with Rapid Response Instruments for Real-Time Measurements of Urban and Regional Trace Gas and Particulate Distributions and Emission Source Characteristics. *Environ. Sci. Technol.* **2004**, *38*, 5694−5703.
(13) Westerdahl, D.; Fruin, S.; Sax, T.; Fine, P. M.; Sioutas, C. Mobile platform measurements of ultrafine particles and associated pollutant concentrations on freeways and residential streets in Los Angeles. *Atmos. Environ.* **2005**, *39*, 3597−3610.
(14) Dons, E.; Panis, L. I.; Van Poppel, M.; Theunis, J.; Wets, G. Personal exposure to Black Carbon in transport microenvironments. *Atmos. Environ.* **2012**, *55*, 392−398.
(15) Pattinson, W.; Longley, I.; Kingham, S. Using mobile monitoring to visualise diurnal variation of traffic pollutants across two near-highway neighbourhoods. *Atmos. Environ.* **2014**, *94*, 782−792.
(16) Hankey, S.; Marshall, J. D. Land Use Regression Models of On-Road Particulate Air Pollution (Particle Number, Black Carbon, $PM_{2.5}$, Particle Size) Using Mobile Monitoring. *Environ. Sci. Technol.* **2015**, *49*, 9194−9202.
(17) Bassok, A.; Hurvitz, P. M.; Bae, C.-H. C.; Larson, T. Measuring neighbourhood air pollution: the case of Seattle's international district. *J. Environ. Plann. Manage.* **2010**, *53*, 23−39.
(18) Dons, E.; Temmerman, P.; Van Poppel, M.; Bellemans, T.; Wets, G.; Panis, L. I. Street characteristics and traffic factors determining road users' exposure to black carbon. *Sci. Total Environ.* **2013**, *447*, 72−79.
(19) Ragettli, M. S.; Corradi, E.; Braun-Fahrländer, C.; Schindler, C.; de Nazelle, A.; Jerrett, M.; Ducret-Stich, R. E.; Künzli, N.; Phuleria, H. C. Commuter exposure to ultrafine particles in different urban locations, transportation modes and routes. *Atmos. Environ.* **2013**, *77*, 376−384.
(20) Ghassoun, Y.; Ruths, M.; Löwner, M.-O.; Weber, S. Intra-urban variation of ultrafine particles as evaluated by process related land use and pollutant driven regression modelling. *Sci. Total Environ.* **2015**, *536*, 150−160.
(21) Klompmaker, J. O.; Montagne, D. R.; Meliefste, K.; Hoek, G.; Brunekreef, B. Spatial variation of ultrafine particles and black carbon in two cities: Results from a short-term measurement campaign. *Sci. Total Environ.* **2015**, *508*, 266−275.
(22) Choi, W.; Ranasinghe, D.; Bunavage, K.; DeShazo, J. R.; Wu, L.; Seguel, R.; Winer, A. M.; Paulson, S. E. The effects of the built environment, traffic patterns, and micrometeorology on street level ultrafine particle concentrations at a block scale: Results from multiple urban sites. *Sci. Total Environ.* **2016**, *553*, 474−485.
(23) Apte, J. S.; Messier, K. P.; Gani, S.; Brauer, M.; Kirchstetter, T. W.; Lunden, M. M.; Marshall, J. D.; Portier, C. J.; Vermeulen, R. C. H.; Hamburg, S. P. High-Resolution Air Pollution Mapping with Google Street View Cars: Exploiting Big Data. *Environ. Sci. Technol.* **2017**, *51*, 6999−7008.
(24) Messier, K. P.; Chambliss, S. E.; Gani, S.; Alvarez, R.; Brauer, M.; Choi, J. J.; Hamburg, S. P.; Kerckhoffs, J.; LaFranchi, B.; Lunden, M. M.; Marshall, J. D.; Portier, C. J.; Roy, A.; Szpiro, A. A.; Vermeulen, R. C. H.; Apte, J. S. Mapping Air Pollution with Google Street View Cars: Efficient Approaches with Mobile Monitoring and Land Use Regression. *Environ. Sci. Technol.* **2018**, *52*, 12563−12572.
(25) Hankey, S.; Marshall, J. D. On-bicycle exposure to particulate air pollution: Particle number, black carbon, PM2. 5, and particle size. *Atmos. Environ.* **2015**, *122*, 65−73.
(26) Liang, J.; Gong, J.; Sun, J.; Zhou, J.; Li, W.; Li, Y.; Liu, J.; Shen, S. Automatic sky view factor estimation from street view photographs—a big data approach. *Remote Sens.* **2017**, *9*, 411.
(27) Middel, A.; Lukasczyk, J.; Zakrzewski, S.; Arnold, M.; Maciejewski, R. Urban form and composition of street canyons: A human-centric big data and deep learning approach. *Landscape Urban. Plann.* **2019**, *183*, 122−132.
(28) Lack, D. A.; Langridge, J. M. On the attribution of black and brown carbon light absorption using the Ångström exponent. *Atmos. Chem. Phys.* **2013**, *13*, 10535−10543.
(29) Petzold, A.; Ogren, J. A.; Fiebig, M.; Laj, P.; Li, S.-M.; Baltensperger, U.; Holzer-Popp, T.; Kinne, S.; Pappalardo, G.; Sugimoto, N.; Wehrli, C.; Wiedensohler, A.; Zhang, X. Recommendations for reporting "black carbon" measurements. *Atmos. Chem. Phys.* **2013**, *13*, 8365−8379.
(30) Olson, M. R.; Victoria Garcia, M.; Robinson, M. A.; Van Rooy, P.; Dietenberger, M. A.; Bergin, M.; Schauer, J. J. Investigation of black and brown carbon multiple-wavelength-dependent light absorption from biomass and fossil fuel combustion source emissions. *J. Geophys. Res.: Atmos.* **2015**, *120*, 6682−6697.

https://dx.doi.org/10.1021/acs.est.0c04776
Environ. Sci. Technol. 2021, 55, 160−168

Appendix

(31) Feng, Y.; Ramanathan, V.; Kotamarthi, V. R. Brown carbon: a significant atmospheric absorber of solar radiation? *Atmos. Chem. Phys.* **2013**, *13*, 2795−2833.
(32) Pitz, M.; Birmili, W.; Schmid, O.; Peters, A.; Wichmann, H. E.; Cyrys, J. Quality control and quality assurance for particle size distribution measurements at an urban monitoring station in Augsburg, Germany. *J. Environ. Monit.* **2008**, *10*, 1017−1024.
(33) Hagler, G. S. W.; Yelverton, T. L. B.; Vedantham, R.; Hansen, A. D. A.; Turner, J. R. Post-processing Method to Reduce Noise while Preserving High Time Resolution in Aethalometer Real-time Black Carbon Data. *Aerosol Air Qual. Res.* **2011**, *11*, 539−546.
(34) Liu, X.; Schnelle-Kreis, J.; Zhang, X.; Bendl, J.; Khedr, M.; Jakobi, G.; Schloter-Hai, B.; Hovorka, J.; Zimmermann, R. Integration of air pollution data collected by mobile measurement to derive a preliminary spatiotemporal air pollution profile from two neighboring German-Czech border villages. *Sci. Total Environ.* **2020**, *722*, 137632.
(35) Popeangă, J.; Lungu, I. Forecasting Final Energy Consumption using the Centered Moving Average Method and Time Series Analysis. *Database Syst. J.* **2014**, *5*, 42−50.
(36) Wang, J.; Sun, K.; Cheng, T.; Jiang, B.; Deng, C.; Zhao, Y.; Liu, D.; Mu, Y.; Tan, M.; Wang, X.; Liu, W.; Xiao, B. Deep high-resolution representation learning for visual recognition. In *IEEE Transaction on Pattern Analysis Machine Intelligence*; IEEE: 2020, 1−15.
(37) Zhou, Z.; Siddiquee, M. M. R.; Tajbakhsh, N.; Liang, J. Unet++: A nested u-net architecture for medical image segmentation. In *Deep Learning in Medical Image Analysis and Multimodal Learning for Clinical Decision Support*; Springer: Cham, 2018, 3−11.
(38) He, K.; Zhang, X.; Ren, S.; Sun, J. Deep residual learning for image recognition. In *Proceedings of the IEEE Conference on Computer Vision and Pattern Recognition*; IEEE: 2016, 770−778.
(39) Chen, L. C.; Papandreou, G.; Schroff, F.; Adam, H. Rethinking atrous convolution for semantic image segmentation. *arXiv* preprint arXiv:1706.05587. **2017**.
(40) Chen, L.-C.; Zhu, Y.; Papandreou, G.; Schroff, F.; Adam, H. Encoder-decoder with atrous separable convolution for semantic image segmentation. In *Proceedings of the European conference on Computer Vision*; ECCV: 2018, 801−818.
(41) Zhao, H.; Zhang, Y.; Liu, S.; Shi, J.; Change Loy, C.; Lin, D.; Jia, J. Psanet: Point-wise spatial attention network for scene parsing. In *Proceedings of the European Conference on Computer Vision*; ECCV: 2018, 267−283.
(42) Xu, N.; Fisher, T. C.; Hong, J. Rademacher upper bounds for cross-validation errors with an application to the lasso. *arXiv* **2020**, 1−17
(43) Breiman, L. Bagging predictors. *Mach. Learn.* **1996**, *2*, 123−140.
(44) Ho, T. K. The random subspace method for constructing decision forests. In *IEEE Transactions on Pattern Analysis and Machine Intelligence*; IEEE: 1998, *20* (8), 832−844.
(45) Vapnik, V. N. An overview of statistical learning theory. In *IEEE Transactions on Neural Networks*; IEEE: 1999, *5* (10), 988−999.
(46) Mnih, V.; Heess, N.; Graves, A. Recurrent models of visual attention. In *Advances in Neural Information Processing Systems*; NIPS: 2014, 2204−2212.
(47) Peters, J.; Theunis, J.; Poppel, M. V.; Berghmans, P. Monitoring PM10 and Ultrafine Particles in Urban Environments Using Mobile Measurements. *Aerosol Air Qual. Res.* **2013**, *13*, 509−522.
(48) Targino, A. C.; Gibson, M. D.; Krecl, P.; Rodrigues, M. V. C.; dos Santos, M. M.; de Paula Corrêa, M. Hotspots of black carbon and $PM_{2.5}$ in an urban area and relationships to traffic characteristics. *Environ. Pollut.* **2016**, *218*, 475−486.
(49) Boogaard, H.; Kos, G. P. A.; Weijers, E. P.; Janssen, N. A. H.; Fischer, P. H.; van der Zee, S. C.; de Hartog, J. J.; Hoek, G. Contrast in air pollution components between major streets and background locations: Particulate matter mass, black carbon, elemental composition, nitrogen oxide and ultrafine particle number. *Atmos. Environ.* **2011**, *45*, 650−658.
(50) Pan, H.; Bartolome, C.; Gutierrez, E.; Princevac, M.; Edwards, R.; Boarnet, M. G.; Houston, D. Investigation of roadside fine particulate matter concentration surrounding major arterials in five Southern Californian cities. *J. Air Waste Manage. Assoc.* **2013**, *63*, 482−498.
(51) Wang, Y.; Xing, Z.; Zhao, S.; Zheng, M.; Mu, C.; Du, K. Are emissions of black carbon from gasoline vehicles overestimated? Real-time, in situ measurement of black carbon emission factors. *Sci. Total Environ.* **2016**, *547*, 422−428.
(52) Nguyen, T.; Yu, X.; Zhang, Z.; Liu, M.; Liu, X. Relationship between types of urban forest and $PM_{2.5}$ capture at three growth stages of leaves. *J. Environ. Sci.* **2015**, *27*, 33−41.
(53) Yassin, M. F. Impact of height and shape of building roof on air quality in urban street canyons. *Atmos. Environ.* **2011**, *45*, 5220−5229.
(54) Brokamp, C.; Jandarov, R.; Rao, M. B.; LeMasters, G.; Ryan, P. Exposure assessment models for elemental components of particulate matter in an urban environment: A comparison of regression and random forest approaches. *Atmos. Environ.* **2017**, *151*, 1−11.
(55) Brandt, C.; Kunde, R.; Dobmeier, B.; Schnelle-Kreis, J.; Orasche, J.; Schmoeckel, G.; Diemer, J.; Zimmermann, R.; Gaderer, M. Ambient PM_{10} concentrations from wood combustion−Emission modeling and dispersion calculation for the city area of Augsburg, Germany. *Atmos. Environ.* **2011**, *45*, 3466−3474.
(56) Jerrett, M.; Arain, A.; Kanaroglou, P.; Beckerman, B.; Potoglou, D.; Sahsuvaroglu, T.; Morrison, J.; Giovis, C. A review and evaluation of intraurban air pollution exposure models. *J. Exposure Sci. Environ. Epidemiol.* **2005**, *15*, 185−204.
(57) Holmes, N. S.; Morawska, L. A review of dispersion modelling and its application to the dispersion of particles: an overview of different dispersion models available. *Atmos. Environ.* **2006**, *40*, 5902−5928.
(58) Wolf, K.; Cyrys, J.; Harciníková, T.; Gu, J.; Kusch, T.; Hampel, R.; Schneider, A.; Peters, A. Land use regression modeling of ultrafine particles, ozone, nitrogen oxides and markers of particulate matter pollution in Augsburg, Germany. *Sci. Total Environ.* **2017**, *579*, 1531−1540.
(59) Tripathy, S.; Tunno, B. J.; Michanowicz, D. R.; Kinnee, E.; Shmool, J. L. C.; Gillooly, S.; Clougherty, J. E. Hybrid land use regression modeling for estimating spatio-temporal exposures to $PM_{2.5}$, BC, and metal components across a metropolitan area of complex terrain and industrial sources. *Sci. Total Environ.* **2019**, *673*, 54−63.
(60) Johnson, A. L.; Abramson, M. J.; Dennekamp, M.; Williamson, G. J.; Guo, Y. Particulate matter modelling techniques for epidemiological studies of open biomass fire smoke exposure: a review. *Air Qual., Atmos. Health* **2020**, *13*, 35−75.

https://dx.doi.org/10.1021/acs.est.0c04776
Environ. Sci. Technol. 2021, 55, 160−168

Publication IV

Liu, X., Schnelle-Kreis, J., Zhang, X., Bendl, J., Khedr, M., Jakobi, G., ... & Zimmermann, R. (2020). Integration of air pollution data collected by mobile measurement to derive a preliminary spatiotemporal air pollution profile from two neighboring German-Czech border villages. ***Science of The Total Environment***, 722, 137632.

Appendix

Science of the Total Environment 722 (2020) 137632

Contents lists available at ScienceDirect

Science of the Total Environment

journal homepage: www.elsevier.com/locate/scitotenv

Integration of air pollution data collected by mobile measurement to derive a preliminary spatiotemporal air pollution profile from two neighboring German-Czech border villages

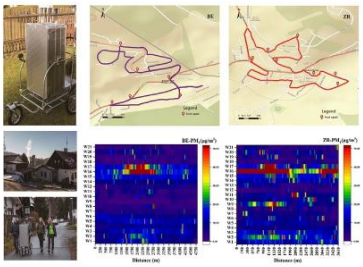
Xiansheng Liu [a,b], Jürgen Schnelle-Kreis [a,*], Xun Zhang [c,*], Jan Bendl [a,d], Mohamed Khedr [a,b], Gert Jakobi [a], Brigitte Schloter-Hai [a], Jan Hovorka [d], Ralf Zimmermann [a,b]

[a] Joint Mass Spectrometry Center, Cooperation Group Comprehensive Molecular Analytics, Helmholtz Zentrum München, German Research Center for Environmental Health, Ingolstädter Landstr. 1, 85764 Neuherberg, Germany
[b] Joint Mass Spectrometry Center, Chair of Analytical Chemistry, University of Rostock, Rostock, Germany
[c] Beijing Key Laboratory of Big Data Technology for Food Safety, School of Computer and Information Engineering, Beijing Technology and Business University, Beijing 100048, China,
[d] Institute for Environment Studies, Faculty of Science, Charles University, Prague, Czech Republic

HIGHLIGHTS

- A novel mobile monitoring approach was used to capture variation in small-scale air.
- The study illustrates the potential of mobile measurement methods in small-scale.
- As an example case study, small-scale air pollution hotspots could be located.

GRAPHICAL ABSTRACT



ARTICLE INFO

Article history:
Received 14 December 2019
Received in revised form 11 February 2020
Accepted 28 February 2020
Available online 11 March 2020

Editor: Jianmin Chen

Keywords:
PM_X
PNC
BC
Mobile monitoring
Small-scale air-pollution

ABSTRACT

Generally, there are only a few fixed air quality monitoring stations installed in villages or rural areas and only a few studies on small-scale variations in air pollution have been described in detail, which make it difficult to estimate human exposure in such environments and related adverse health effects. Moreover, biomass combustion can be an important source of air pollution in rural areas, comparable to vehicle and industrial emissions in urban planning. And their air pollutants are mainly affected by local sources. For this reason, a survey on rural air pollution was carried out in this study. Therefore, portable, battery-powered monitoring devices were used to measure particulate matter (PM_{10}, $PM_{2.5}$, PM_1, particle number concentration, and black carbon) in order to study air quality in rural communities. The focus of the investigations was to explore the application of mobile monitoring equipment in small-scale environments, compare the differences in rural air pollutants between two neighboring villages in two countries, and the identification of pollution hotspots. The measurements were carried out in November 2018 in two villages on the German-Czech border. Over a period of four days, 21 mobile measurements along fixed routes were carried out simultaneously at both locations. The analysis of the data revealed significant differences in PN and PM concentrations in rural air pollutants between the two countries. The spatial and

* Corresponding authors.
E-mail addresses: juergen.schnelle@helmholtz-muenchen.de (J. Schnelle-Kreis), zhangxun@btbu.edu.cn (X. Zhang).

https://doi.org/10.1016/j.scitotenv.2020.137632
0048-9697/© 2018 Elsevier B.V. All rights reserved.

Appendix

temporal distribution of air pollution hotspots in the Czech village was higher than that in the German village. The relationships between the measurement parameters were weak but highly significant and the meteorological parameters can effect air pollution. Overall, the results of this study show that mobile measurements are suitable for effectively recording and distinguishing spatial and temporal characteristics of air quality.
© 2018 Elsevier B.V. All rights reserved.

1. Introduction

In recent years, air pollution research has involved different spatial scales, focusing on different research subjects, including global scales (Van Donkelaar et al., 2010), regional scales (Kutzner et al., 2018), and urban scales (Gong et al., 2015). The research topic is gradually analyzing the characteristics of concentration changes based on observation data, and is gradually investigating optical characteristics and radiation forcing. Accordingly, various European countries have adopted a series of monitoring and control measures in response to the air pollution problem in Europe, and achieved relatively significant phased results. A multi-layered sensor-based monitoring device and a gridded air pollution monitoring system were deployed to monitor the air pollution status of the target area. Air pollution grid monitoring greatly improves the ability to detect small (100 m) hotspots in the target area. So far, many studies have focused on urban air pollution in cities, e.g. Vienna (Dons et al., 2012), Barcelona, Lugano (Reche et al., 2011), Paris (Reche et al., 2011), Chicago (Babich et al., 2000), Augsburg (Wolf et al., 2017), Manila (Alas et al., 2018), Shanghai (Liu et al., 2019), etc. Although the urban air pollution poses a serious health problem for people, the rural air pollution also higher ($PM_{10} \geq 20\ \mu g/m^3$ annual mean, $PM_{2.5} \geq 10\ \mu g/m^3$ annual mean). Braniš and Domasová (2003) found that when comparing PM_{10} data from villages and Prague, the average particle concentration in rural areas was higher in all three seasons (two winter and one summer) studied. Hovorka et al. (2015) also claimed the influence of wood combustion in villages on the air quality near the city. However, there are only a few fixed stations installed in rural areas and only a few studies on small-scale variations of air pollution have been published. PM_1 was studied in rural site of Austria by Gomišček et al. (2004); BC in a rural areas of India by Rehman et al., 2011, and $PM_{2.5}$ in a rural site in Chongqing, southwest China and PM_{10} in Mol, Belgium by Peng and Peters et al. (Peng et al., 2019; Peters et al., 2013).

More importantly, the number of villages is generally much larger than the number of cities. Although the population density in cities is much higher, the number of people living in rural areas has gradually increased during the five-year period from 2010 to 2015 across the EU-28 by 1.7 percentage points (EUROSTAT, 2017).

While in most European cities little solid fuel is used for heating, the use of wood for heating is widespread in rural communities. Therefore, biomass combustion can be an important source of air pollution in rural areas, comparable to vehicle and industrial emissions in urban planning (Begam et al., 2016). Moreover, their air pollutants are mainly affected by local sources. Therefore, field studies on air pollution in villages can help to understand the impact of solid fuel combustion on local air quality and exposure of the rural population to it. For this reason, a survey of rural air pollutants was carried out in this study. In addition, in the Czech countryside firewood is mainly used for home heating, while in Germany it is more frequently used for leisure. To compare differences in rural air pollutants between two countries, two neighboring German-Czech border villages with similar population and structure were selected for this study.

In addition, current gridded air pollution monitoring systems use fixed deployment methods. The monitoring area is usually divided into 500 m to 3 km long grids with each grid containing at least one fixed installation monitoring node (fixed monitoring station). However, based on the fixed sample observation of the atmospheric pollutant concentration, the spatial representation is limited due to the number of sampling points, and the spatial analysis and spatial simulation on the area are relatively few. In order to avoid this case, nowadays, mobile monitoring (Gong et al., 2015) has conducted a collection of real-time air quality measurements to assess in situ emissions, local air quality trends, and air pollutant exposures. This measurement strategy uses the complex, one-second multi-pollution data over time and for each location to drive the limits of traditional data analysis (Brantley et al., 2014). It can solve the central monitoring problem of insufficient description of air pollution exposure. Mobile measurements are used in human exposure studies to quantify individual exposures and demonstrate the importance of exposure differences in different microenvironments (Dons et al., 2012).

Based on the above reasons, this small-scale air pollution monitoring manuscript used a portable instrument-based micro air pollution monitoring devices to investigate the exposure of PM (PM_1, $PM_{2.5}$ and PM_{10}), black carbon (BC) concentration and particulate number concentration (PNC) at two different villages, one in Germany and one in the Czech Republic. The measurements were carried out during November 22–25, 2018. The collected data were used to identify air pollution hotspots, analyze the average concentration and variation of each region and to discuss the influencing factors.

2. Methods

2.1. Study area and monitoring protocol

The mobile measurements were carried out in two neighboring villages at the German-Czech border, Bayerisch Eisenstein (49.12N, 13.20E), Germany and Zelezna Ruda (49.14N, 13.24E), Czech Republic. Both villages are climatic health resorts, which have comparable number of residents (BE: 1045, ZR: 1745), residential houses and geographical structure with one main road following the valley and one main road on the uphill slope northwest. Residential areas are mainly located on the slopes of the valley (Fig. 1). There are no factories in or close to the villages.

In both villages fixed routes were defined using sidewalks or the right hand side of the road which were repeatedly walked in the course of the investigations. The route in Bayerisch Eisenstein was approximately 5 km long, the route in Zelezna Ruda 4 km (Fig. 1). The average walking time for the entire route was approximately 60 min at both sites. Most parts of the routes were located in residential areas with little traffic. From 5 am to 10 pm, parallel walks were carried out at both sites every 2–3 h to compare air pollution in the two villages. 20 and 21 walks were successfully performed on 4 days between November 22 and 25, 2018 in Bayerisch Eisenstein and Zelezna Ruda, respectively (Table 1).

Short-term stationary and mobile monitoring significantly reduces the total measurement time and allows the measurement of a larger number of sites (Begam et al., 2016). Therefore, the mobile platform was placed at the endpoint after every walk, and measurements were continued for 1 h. The results of these measurements were used as short-term stationary measurements and were compared with the mobile monitoring results.

Appendix

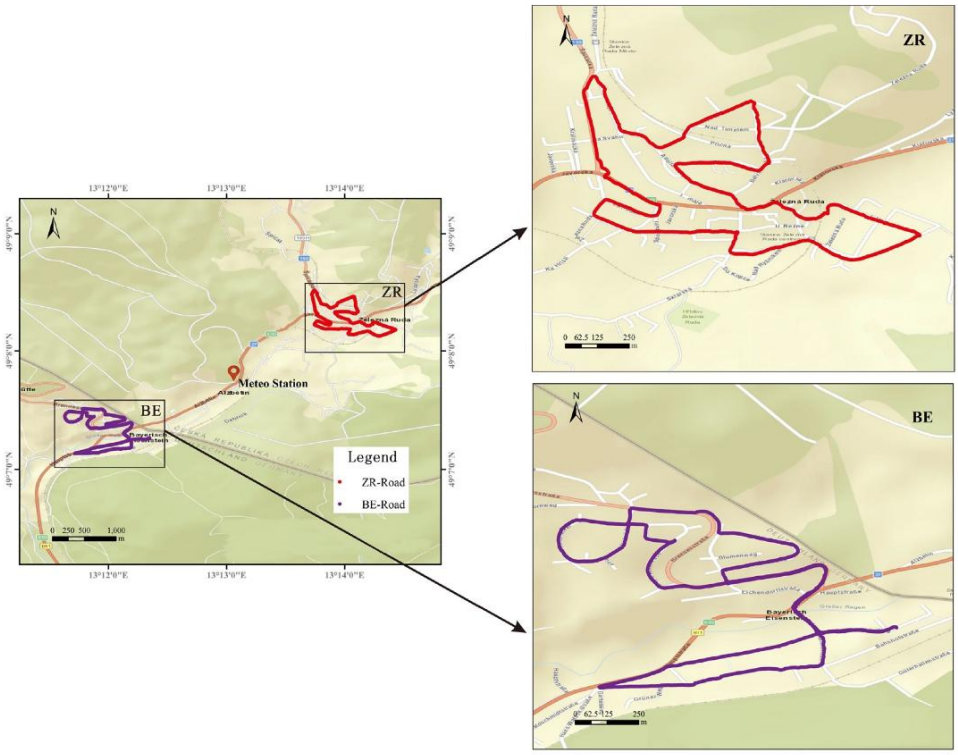


Fig. 1. The monitoring routes in Bayerisch Eisenstein (BE) and Zelezna Ruda (ZR) and Meteo station.

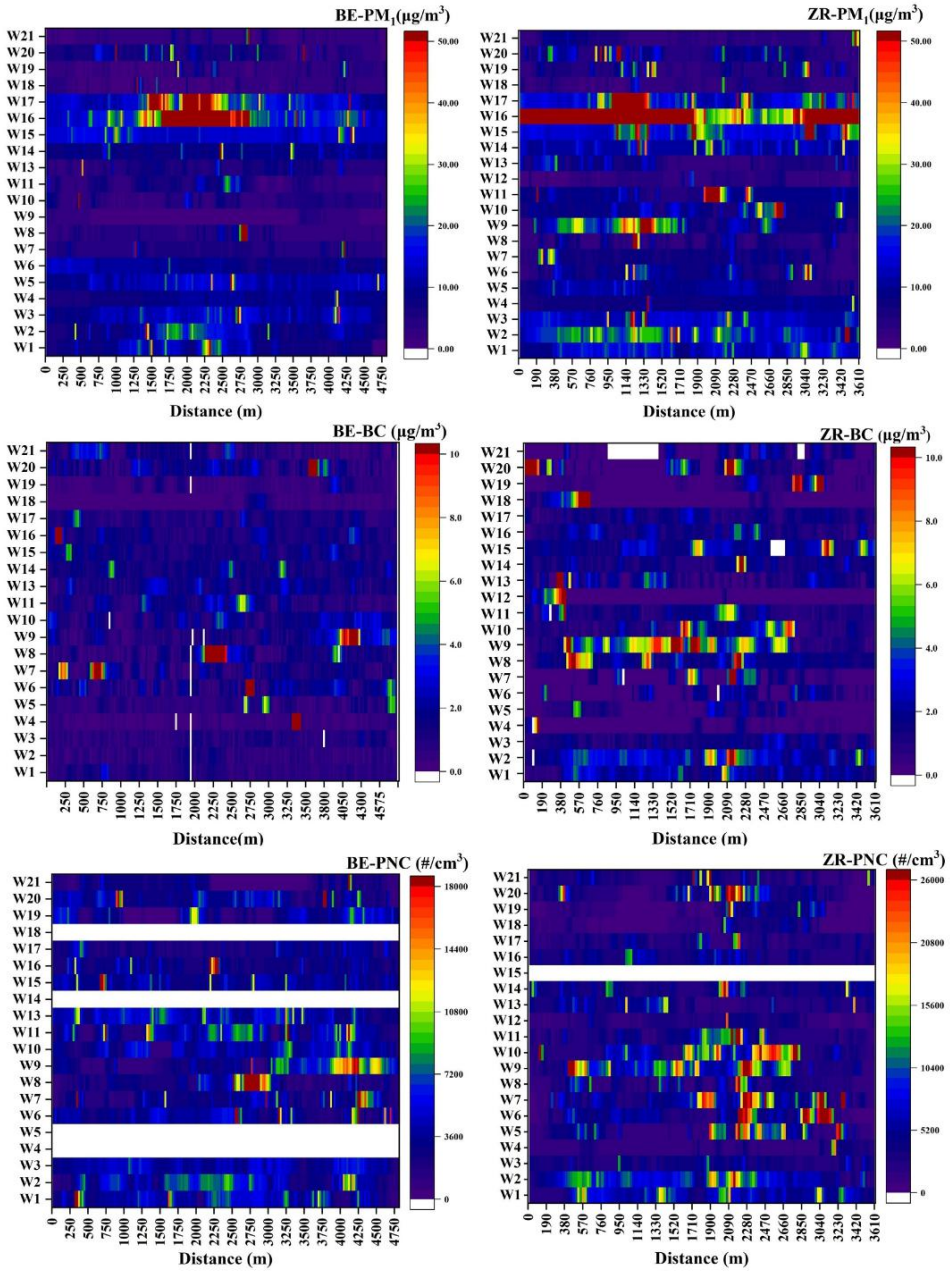
Table 1
Overview of the measurement walks.

Walk	Date	Start time BE	End time BE	Start time ZR	End time ZR
1	2018/11/22	16:20	17:13	17:08	18:27
2		19:00	19:47	19:04	20:03
3		21:00	21:55	21:02	22:07
4	2018/11/23	05:05	06:05	05:13	06:18
5		07:00	07:57	07:02	07:56
6		09:00	09:54	09:09	10:07
7		11:00	11:54	11:02	12:08
8		14:00	14:50	14:04	14:55
9		16:15	17:09	15:59	17:03
10		18:05	19:04	18:03	19:16
11		20:00	21:07	20:02	20:55
12	2018/11/24	Skip	Skip	07:10	08:08
13		09:03	09:58	08:59	10:12
14		13:56	15:04	14:08	15:08
15		16:00	17:04	16:08	17:01
16		18:00	19:07	17:58	18:48
17		20:05	21:11	20:10	21:08
18	2018/11/25	05:00	06:00	05:03	06:07
19		07:00	07:59	06:59	07:53
20		09:07	10:11	09:03	10:01
21		11:00	11:59	11:04	11:58

Meteorological data were measured at a fixed site, Meteo Station (49.13N, 13.23E), between the two villages (Fig. 1).

2.2. Mobile platform

Mobile measurements for PM_x, PNC, and BC, in parallel at both locations, were conducted by two identical mobile platforms. The platform consists of a trolley and a large aluminum box, which protects the instruments and positions the inlets at breathing height (approx. 1.5 m above ground). The detection frequency for PMx and PNC was 1 Hz. Data on PM_x (PM_1, $PM_{2.5}$, PM_{10}) mass were recorded by a laser nephelometer - DustTrak DT (DRX 8532, TSI Inc., USA). Particle number concentrations (PNC), within the size range of 20–1000 nm, were measured by condensation particle counters (P-Trak 8525, TSI Inc., USA). BC concentration was measured by aethalometers (microAethalometer, MA200, AethLabs, USA) with a time resolution of 10 s to avoid too much noise of the BC signal. The aethalometer measures the light attenuation through a filter tape at 5 wavelengths while the filter is continuously collecting the aerosol (Begam et al., 2016). The measurement at 880 nm is defined as the concentration of Black Carbon (BC) (Petzold et al., 2013; Olson et al., 2015). Because there is a lot of noise in other wavelengths, the research is mainly concentrating on BC.


BE-PM1(μg/m3)
ZR-PM1(μg/m3)
BE-BC (μg/m3)
ZR-BC (μg/m3)
BE-PNC (#/cm3)
ZR-PNC (#/cm3)
Distance (m)
Distance(m)

Appendix

Besides the PMx and BC measurements the platforms were equipped with a GPS (Garmin GPSMAP 64s, recording resolution 1s) to register measurement location and a POV camera (Olympus Tough TG Tracker, 5s) to capture local and mobile pollution sources such as smoking chimneys, trucks or smokers.

At the fixed site, air temperature, relative humidity, wind direction WD, wind speed WS, with 1 min integration time, were monitored by the "Ultra-Precision Professional Weather Station System WMR300" from Oregon Scientific.

2.3. Instrumentation preparation and data validation

Instrument preparation took place in our laboratory before each walk and consisted of zero calibration checks, cleaning and greasing of the DustTrak impactor, cleaning of the DustTrak chamber, replacement of the MA200 filter strip, battery and memory checks, and clock synchronization. Flow measurements were performed with a factory calibrated flow meter.

2.4. Data analysis and processing protocols

2.4.1. Kruskal-Wallis test

Firstly, a total data inspection of mobile and stationary measurements was made from Bayerisch Eisenstein and Zelezna Ruda. Pollutant concentrations were statistically compared using a non-parametric Kruskal-Wallis test at a critical value (α) of 0.05 (Kruskal and Wallis, 1952). This is a non-parametric alternative to a one-way ANOVA. The Kruskal-Wallis test investigates whether the sampled populations have the same median. Furthermore, an analysis of the mobile and stationary variability of the air quality measurements was performed by one-way ANOVA. Data analysis was performed using the Data Processing System 9.5 (DPS) (Tang and Zhang, 2013).

2.4.2. Post-processing of BC data

If the aethalometer measures in environments with low BC concentrations and/or at high time resolution negative values can occur. This is caused by using delta ATN to calculate the BC values. Since the aethalometer relies on this delta ATN when calculating eBC values, it does make sense to ensure that delta ATN is above a certain value before doing any calculations. Negative values often contain valid information that is required to post-process or smooth the data over a longer interval, so arbitrary removal of negative values may be detrimental to a dataset.

Data preprocessing must be performed to eliminate these negative values using the BC concentration data measured by the aethalometer. microAeth users can upload their data file to AethLabs and use the post-processing tools to smooth their data (http://www.aethlabs.com). Various different algorithms are available for data smoothing. This study uses a commonly applied time-adaptive noise reduction method centered moving average. The centered moving average is a smoothing technique that is used to make the long term trends of a time series clearer (Easton and McColl, 1997). There is no shift or group delay in the data using the centered moving average, unlike a simple moving average. The comparison between original BC measurements and corrections treated by centered moving average (the averaging period is 70s) is illustrated in Fig. S1 (ZR-Walk monitored on November 24 14:08–14:55 (Walk 14)). The denoising results show that the centered moving average can remove negative anomalies that occur in the original BC.

Table 2
Non-parametric Kruskal-Wallis test of PM_1, BC concentrations and PNCs measured along the routes in BE and ZR.

	BE-PM_1	BE-BC	BE-PNC	ZR-PM_1	ZR-BC	ZR-PNC
Chi-sq.	866.558	366.123	188.448	754.549	413.879	360.662
df	19	19	15	20	20	19
Sig.	0	0	0	0	0	0

3. Results and discussion

3.1. Summary of the mobile measurements

For mobile measurements, the observed average PM_1, $PM_{2.5}$, and PM_{10} concentrations in BE and ZR during the study period were 10 ± 11, 11 ± 11, 16 ± 27 μg/m^3 and 19 ± 34, 21 ± 39, 37 ± 108 μg/m^3, respectively, being similar to those sampled in the suburban of Bologna, Italy (Sarti et al., 2015), the urban area in Milan, Italy (Vecchi et al., 2004), the urban centre in Austria (Gomišček et al., 2004), Chicago, USA (Babich et al., 2000), and the suburban routes in Northampton, UK, during the winter of 1999/2000 (Gulliver and Briggs, 2004). However, for PM_{10}, they are much higher than the urban background in Barcelona, Spain and Lugano, Switzerland (Reche et al., 2011) and for $PM_{2.5}$, they are higher than the urban road way in Newark, US (Yu et al., 2016).

The observed average BC concentrations were 1.30 ± 1.35 μg/m^3 and 1.70 ± 2.45 μg/m^3, which are similar to those reported and at urban background sites in Baden-Württemberg, Barcelona and Lugano (Gidhagen et al., 2005), and Paris (Healy et al., 2012), and the urban center of Augsburg as reported by Gu (2013). However, the observed average BC concentrations were higher than those of the urban industrial area in Huelva (0.7 ± 0.4 μg/m^3) and the urban center in Chicago reported by Reche et al. (2011) and Babich et al. (2000). Nevertheless, these values are much lower when compared to those noticed during the urban traffic investigated in Baden-Württemberg by Reche (Reche et al., 2011). The observed average PNC measured in BE and ZR during the study period were 4190 ± 1340 #/cm^3 and 5024 ± 2346 #/cm^3, being similar to those reported from the rural forest and the 100 m high urban tower in Stockholm (Gidhagen et al., 2005).

When comparing the air pollution in two villages, it can be found that the concentration of air pollution in ZR is generally higher than that in BE villages, and for PM, the concentrations in ZR are twice or more than that of BE.

3.2. Spatio-temporal variation of air pollution across two villages

3.2.1. Spatio-temporal variation

A significant difference between temporal dynamics of PM, PN and BC was observed ($p < 0.05$) by plotting the 25 m average PM, PN and BC concentrations for a selection of roads (Fig. 2).

The temporal variability showed significant differences between walks carried out within the same measurement day as well as between different measurement days comparing data for the same time of day, both in Bayerisch Eisenstein and Zelezna Ruda.

A statistical analysis of the temporal pattern of the factors revealed significant concentrations differences between the measurement walks (Table 2) for both in Bayerisch Eisenstein and Zelezna Ruda, but also between some of the mobile walks on the different days. In Bayerisch Eisenstein, for example, PM_1 concentrations were significantly higher at 18 o'clock (W16 (18:00–19:07)) and 20 o'clock (W17 (20:05–21:11)) on November 24 than in other hours. In Zelezna Ruda, PM_1 concentrations were higher on November 24, 2018, during the fifth (18:00–19:00) walk (W16 (17:58–18:48)) in contrast to the

Fig. 2. PM_1, BC and PN concentrations for the different walks (y-axis) at a selection of road (x-axis) in BE and ZR. The colors are scaled between the extremes and differ between the plots. White pixels represent no data due to instrument failures.

Appendix

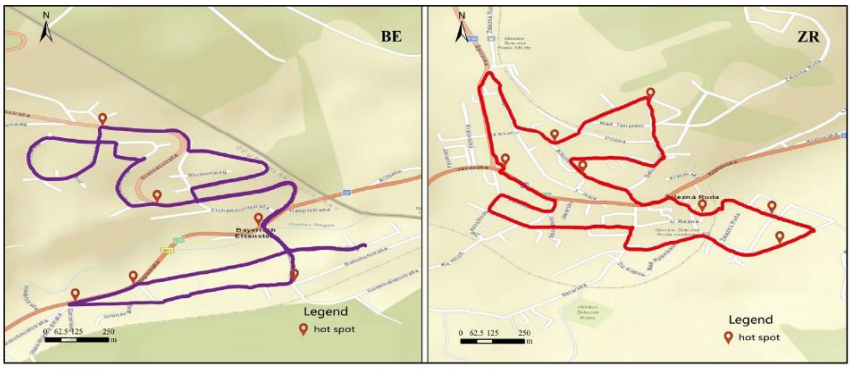


Fig. 3. Schematic diagram of a highly-concentrated contaminated hotspot with high suspicion on the sampling route.

remaining five walks; the same is true for the BC concentrations during the fourth (16:00–17:00) walk (W9 (15:59–17:03)).

The spatial variability of air pollution was lower, but overall significant for PNC in BE ($p < 0.01$) and for BC and PNC in ZR ($p < 0.05$). In BE, measured PM and PN concentrations were significantly higher on roads from 2250 m to 3250 m from the starting point. The differences in BC and PN concentrations between 25 m selected road in ZR were overall significant, especially from 1000 m to 2000 m from the starting

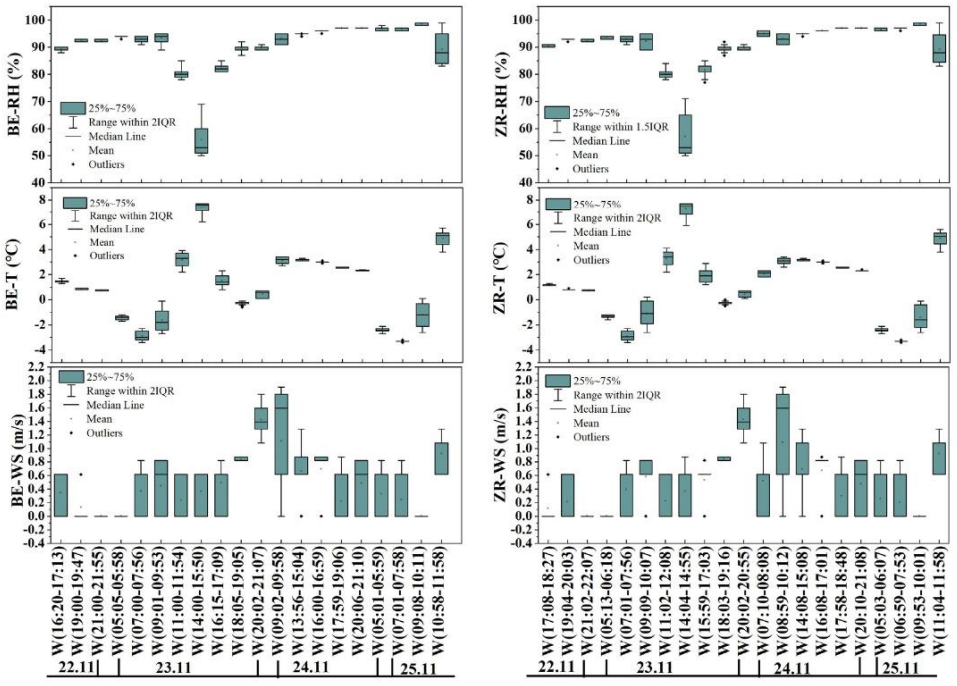


Fig. 4. Meteorology box plots from each mobile sample collection in two villages on November 22–24, 2018 (The meteorological data were monitored at the same place between the two villages and the data were divided according to their respective walking sampling times).

Appendix

point. The main causes of this spatial difference identified using the photos taken during the sampling period are the smoke emitted from homes during heating and the emissions from the vehicles passing by.

When comparing differences in PM (PM_1, $PM_{2.5}$, PM_{10}) concentrations and PN concentrations measured in two villages, these were generally significant ($p < 0.05$), based on all the sampling data from the two villages over four days and using the ANOVA method. From Fig. 2, it is also clear that the spatial and temporal distribution of air pollution hotspots in ZR was higher than that in BE. In the time distribution, after 16 o'clock, the hotspot area of ZR is obviously more than that of BE. After analyzing the photos during the sampling period, it was found that in ZR, smoke from homes due to heating or cooking increased. Similarly, in terms of spatial distribution, most of the abnormally high value points in the two villages have become hotspots due to the increase in traffic flow. When comparing the concentration of the hotspot area with the background concentration of the city, it was found that the value of the hotspot area was 5–10 times that of the background area (Gomišček et al., 2004; Kutzner et al., 2018; Peters et al., 2013).

However, when comparing differences between black carbon concentrations measured in two villages, they are generally less pronounced than for PM_1 concentration and differences in PNC and were often non-significant.

3.2.2. Hotspots parsing of PM_1 and BC in BE and ZR

Starting from the mobile monitoring, the collected data is subjected to peak extraction, position marking, and hotspot area summary. According to the aggregated results, the detected hotspots are combined with on-site photos to verify and analyze the reasons, forming a logical closed loop of the entire mobile monitoring.

Therefore, to capture the fine spatio-temporal patterns required to pinpoint hotspots and periods of the day that are detrimental to human health, multi-angle data display is also important. Based on mobile monitoring data, and combined the Fig. 2, the moving data continuously monitored in different time periods is superimposed and drawn, which can visually display the measured data of the mobile monitoring over a certain period of time. As shown in Fig. S2, the data collected by all the mobile monitoring devices in a period of time is summarized and counted, and the average value is calculated on the walking path segment length and then projected onto the corresponding road segment on the map. By using discrete points of different colors to indicate the concentration of pollutants, the average level of air pollution in the road sections involved can be assessed visually. At same time, PM_1 and black carbon concentration can significantly extract peaks from the environmental background. In addition to feedback of the measured pollution concentration, the data of the mobile monitoring also records the corresponding spatial latitude and longitude coordinates. The location of the extracted peaks is marked on the map (Fig. 3), and this study has also shown that the peak aggregation of multiple mobile patrol periods occurs in relatively concentrated regions. It can roughly depict a high concentration of contaminated hotspots with high suspicion in the target area. According to the summary of the hotspot areas, there are no pollution sources such as factories around the two villages. Combine field-specific photos identified during sampling for field verification. Its pollution mainly comes from local pollution. Therefore, the pollution in this area, was divided into the two following categories.

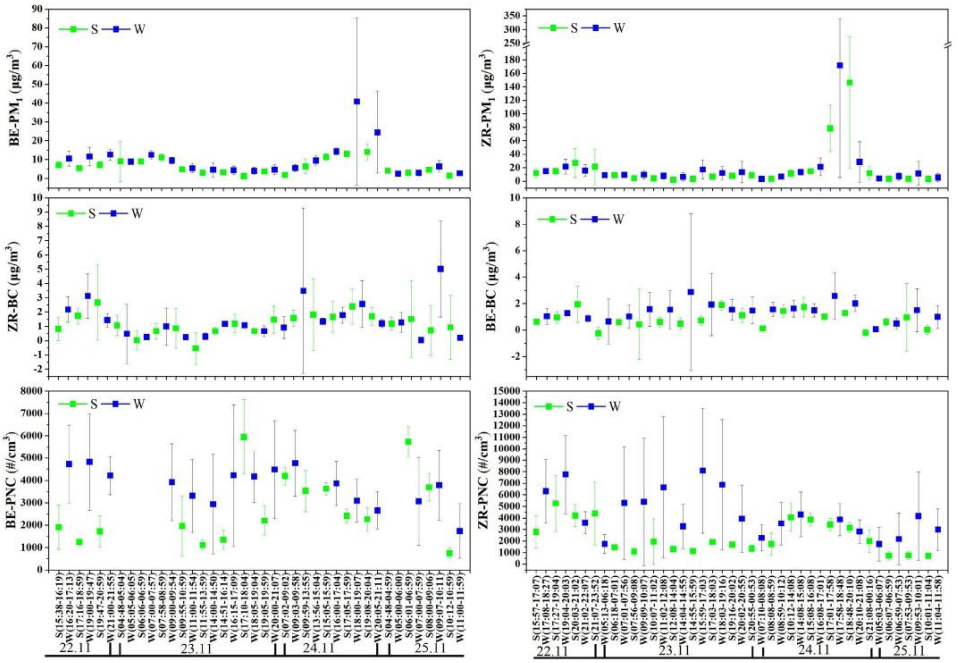


Fig. 5. Temporal fluctuations of PM_1, black carbon concentrations and PNCs from mobile and stationary measurements in BE and ZR (S, stationary measurement; W, mobile measurement).

Appendix

(1) Traffic peaks: Peaks of traffic in some sections of the walking path during peak hours due to the surge in traffic volume.
(2) Biomass burning: Some villagers use wood mainly in the evening for heating.

3.3. Characteristics of meteorology

Studies have shown that elevated temperatures, reduced frequency of precipitation, and low wind speed may adversely affect regional atmospheric conditions (Dawson et al., 2007; Correia et al., 2013). Fig. 4 shows the pattern of the average relative humidity (RH), temperature (T) and wind speed (WS) in the 20 and 21 walks of BE and ZR, respectively. It can be seen, that the RH values are between 75% and 100% except on the 23rd November from 2 pm to 3 pm, where T is between −4 and 8 °C and wind speed is <2 m/s. Tai et al. (2010) used the method of correlation analysis to study the meteorological parameters (such as temperature, relative humidity and wind direction) that affect the concentration of $PM_{2.5}$, and obtained a relationship between the concentration distribution of pollutants and meteorological factors. So the relationship between the pollutants and meteorological factors will be discussed later.

3.4. Characteristics of air pollution concentrations in BE and ZR

3.4.1. Characteristics of PM concentrations in BE and ZR

Fig. S3 represents the pattern of the average PM_1 concentrations in the 20 and 21 walks of BE and ZR (since PM_1, $PM_{2.5}$ and PM_{10} show the same pattern, only the pattern graph of PM_1 was drawn here), respectively. In principle, the PM concentration follows the same pattern in both villages. PM_1 concentrations in BE and ZR are lower all day from 5 to 7 h local time (LT), which may be due to this period of time, there is less road traffic and people have not started house heating. Therefore, the pollutant emissions are less, and the air quality is improved. At around 18:00–19:00 h LT in the evening, however, the PM_1 concentrations are increasing probably due to the heating. At the same time, the traffic flows during this period, which can aggravate local air pollution.

In order to examine the concentration of atmospheric particulate matter in two villages in a more comprehensive way, the frequency distribution of the particles in the two villages is shown in Fig. S4, which used a frequency step size of 1 μg/m^3. PM_1 and $PM_{2.5}$ are approximately normally distributed in monitoring period. It can be seen in Fig. S4 that PM_1 accounts for the vast majority. The ratios of $PM_1/PM_{2.5}$ are generally >90%, which indicates that air pollution mainly comes from submicron particles in the villages. The PM_1 concentration in the two

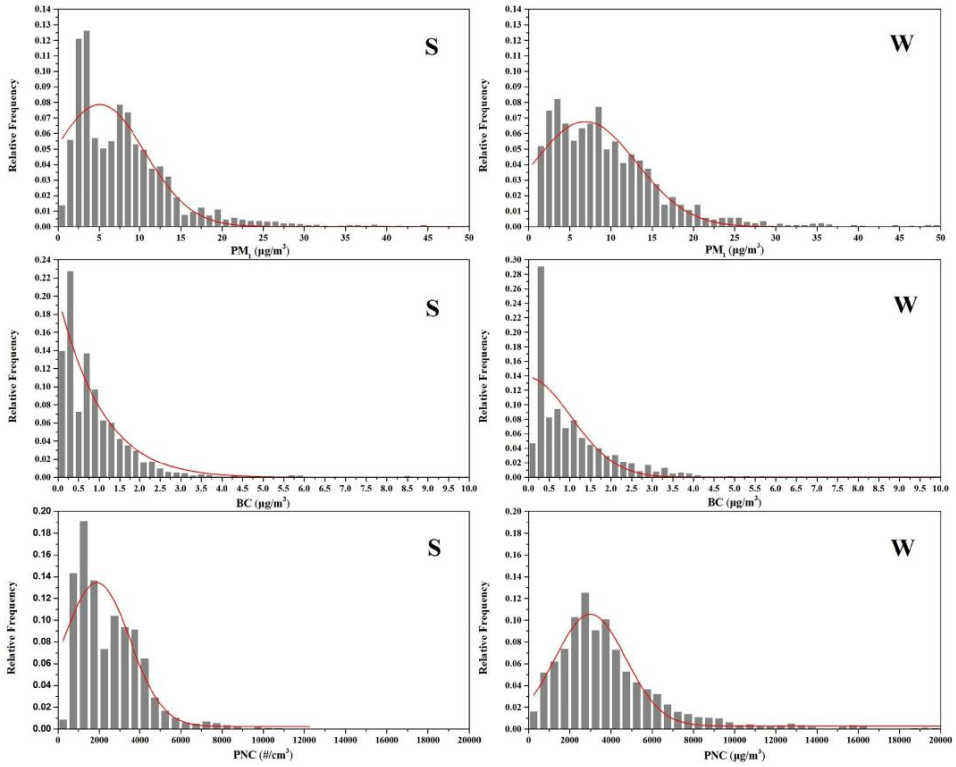


Fig. 6. Comparison of frequency distribution of PM1, BC and PNC for the stationary and mobile monitoring in Bayerisch Eisenstein (BE) and Zelezna Ruda (ZR) (x-axis, PM_1, BC concentrations and PNCs; y-axis, frequency of pollutants concentration, S, stationary measurement, W, mobile measurement).

Appendix

villages of BE and ZR is concentrated between 0 and 30 μg/m^3 and the probability of exceeding 30 μg/m^3 is low for both villages. Comparing the PM_1 of the two villages, the median value of the PM_1 concentration in ZR is close to or even above 9 μg/m^3, which is twice that the value in BE (4 μg/m^3), indicating that the probability of high concentrations of fine particles is higher in the ZR atmosphere. This also determines the characteristic that the total particulate matter concentration in ZR is higher than in BE. This indicates that in the village of ZR more primary pollutants of particulate matter and secondary particulate matter are released.

3.4.2. Characteristics of black carbon concentration in BE and ZR

Fig. S5 is showing the pattern of the average black carbon concentration in the 20 and 21 walks of BE and ZR, respectively. It can be seen that the BC concentrations of BE and ZR are lower all day from 5 to 7 o'clock, and their variation is similar with PM_1. The frequency distribution of the BC concentration was made using a frequency step size of 0.1 μg/m^3 (Fig. S6). The median average concentration of BC was 1.05 μg/m^3 in BE and 1.16 μg/m^3 in ZR, showing that the atmospheric concentration of BC in ZR is slightly higher than that in BE. According to our survey, there is mostly wood combustion in the two villages.

3.4.3. Characteristics of particle number concentration in BE and ZR

Fig. S7 shows the pattern of the average particle number concentration in the 20 and 21 walks of BE and ZR, respectively (a few of sampled PNC data were missing due to an instrument failure). It can be seen that the peak PNC generally occurs in the afternoon, which may be due to the rise of the traffic. Similarly, the PNCs follow the same pattern with PM_1 in both villages. Furthermore, as can be seen from PNC in ZR, they are lower all day from 5 to 7 h local time (LT), showing the same characteristics with PM_1 and BC.

The frequency distribution of the fine mode particles in the mobile monitoring of the two villages is shown in Fig. S8. In general, the frequency distribution of the particulate number concentration in all mobile monitoring periods is approximately normally distributed. The particulate number concentration in the two villages is concentrated between 500 and 10,000 #/cm, and the probability of exceeding 10,000 #/cm^3 is low. Comparing the PNCs of the two villages, both distributions are very similar and in the known background range. The median values of the PNC in two villages are 1154 and 2631 #/cm^3, indicating that there are greater chances of high concentration of ultrafine particles in ZR atmosphere.

3.5. Mobile vs. stationary measurements

The average PM_1, BC concentrations, and PNCs of each walk were compared with the hourly averaged stationary measurements. The stationary measurements followed similar patterns as the average PM_1, BC, and PNC from mobile measurements in the two villages (Fig. 5). However, the stationary measured absolute values were generally below the measured concentrations at the previous walks, except for some walks in ZR. This was the case because the stationary sites were located in the background while the walks partly took place near the sources. Combined with on-site sampling photos, the concentrations became higher during stationary monitoring due to the passing of vehicles.

The frequency distribution of PM, BC, and PN between the mobile and the stationary monitoring of the two villages is shown in Fig. 6. The concentrations from the stationary measurements are concentrated between 0 and 20 μg/m^3 for PM_1, between 0 and 2.5 μg/m^3 for BC, and between 0 and 6000 #/cm^3 for PNC. The mobile measurements revealed concentrations between 0 and 25 μg/m^3 for PM_1, between 0 and 3.5 μg/m^3 for BC, and between 0 and 8000 #/cm^3 for PNC. Obviously, the concentrations range, mode and median of the air pollutants monitored by mobile monitoring are higher than the stationary monitoring. This is due to the fact that the mobile monitoring process will be closer to the source of pollution, which further demonstrates the superiority of mobile monitoring. However, for all mobile and stationary monitored data, the frequency distribution of the BC concentration mean values show a non-normal distribution, while PM_1 and PNC values are nearly normal-distributed.

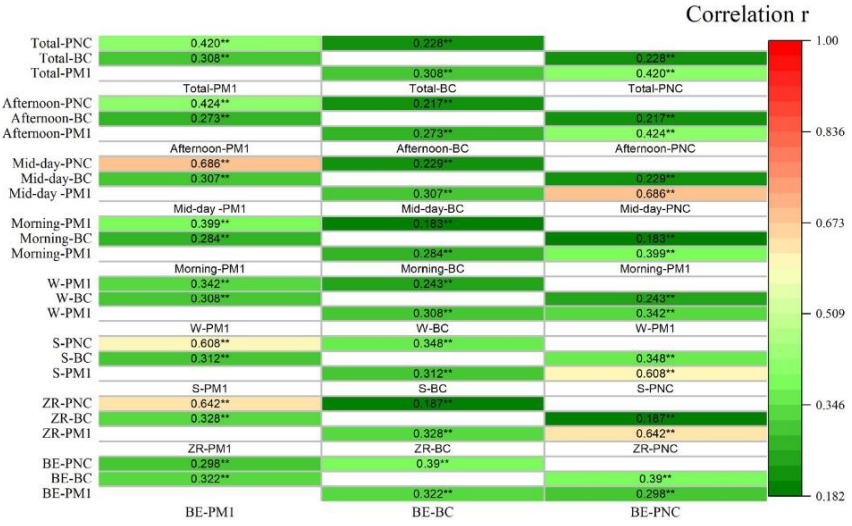


Fig. 7. Spearman correlation coefficient between the three air pollutants ($^{**}p < 0.01$).

Appendix

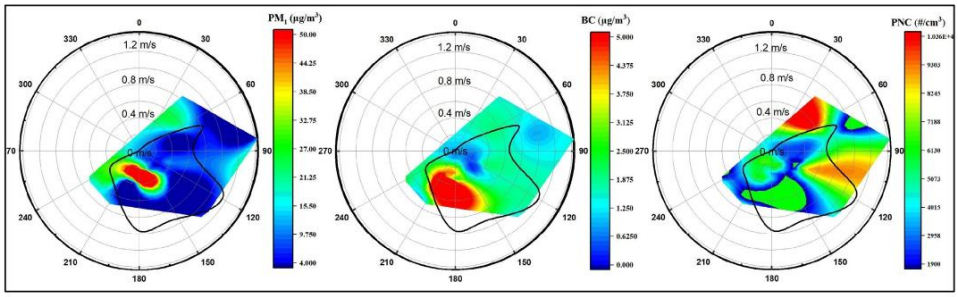


Fig. 8. Relationship of PM_1, BC and PNC with wind direction and speed.

3.6. Relationships between PM_1, BC and PNC

Fig. 7 presents the spearman correlation coefficient between PM_1, BC, and PNC. There were weak but highly significant ($p < 0.01$)correlations between them, which has been also found by Yu et al. (2016). They also found the inter-pollutant correlations varied by the sampling area and sampling time (Yu et al., 2016). Among the three possible pairs (i.e., PM_1-BC, BC-PNC, and PNC-PM_1), the pair of PM_1 and PNC was the strongest, except in BE area. The correlation coefficients of PM_1-BC and PM_1-PNC were stronger in the area of ZR than in BE. Additionally, the three pairs were stronger in the stationary measurement than that in the mobile measurement, which may be due to the stable environment conditions of the air monitoring equipment during fixed monitoring. Authors also reported diurnal correlations being higher during midday (10:00–14:00) than in the morning (5:00–10:00) or in the afternoon (14:00–22:00), which is due to the traffic flow, which was higher during mid-day. Patton et al. (2014) reported different correlation coefficients that were higher in neighborhoods near highways and lower in urban background neighborhoods. This strong correlation also suggests that PM_1, BC and PNC have similar sources. However, it is not possible to quantify the contribution rate of pollutants representing different source to black carbon aerosols.

3.7. Meteorological effects on PM_1, BC concentrations, and PNCs

The analysis revealed that the temperature correlated positively with the black carbon concentration ($r = 0.352$, $p < 0.05$) and the relative humidity was negatively correlated with PNC ($r = -0.428$, $p < 0.05$). Moreover, Zhu et al. (2002) found that wind speed and direction are the determining factors for the concentration of air pollutants. Fig. 8 shows the distributions of PM_1, BC, and PNC with wind speed and direction. The radius in Fig. 8 represents the wind speed (m/s), the color represents mass or number concentrations of contaminants, and the solid black lines show the frequencies of wind from different directions. The figure shows that the wind speed and wind direction are closely related to the pollutant concentration. High PM_1 concentrations rose from the southeast to southwest (150°–210°) and high BC concentrations and PNCs rose from the east (90°–120°). The BC concentrations from the southeast were generally above 5 μg/m^3. It was likely that the pollution in the region of ZR areas was relatively high. Kumar et al. (2011) found that increase in wind speed decreases BC and vice-versa. During the sampling period, the maximum wind speed is <1.6 m/s, which represents the Class 1 wind. Studies have shown that pollution accumulates under low and calm winds (Begam et al., 2016) indicating that the pollution in the study area was highly impacted by local emissions (Shen et al., 2015). Liu et al. (2018) found that the average ratio of $PM_{2.5}$ to PM_{10} significantly increased with the increase of RH during their observation period, which indicated that high RH aggravated the pollution caused by fine particles. During our sampling period, the relative humidity was 91% on average, so high humidity and low wind speed were typical static weather conditions, which aggravated the pollution. In addition, it has been reported that the lifetimes of BC range from 40 h to over 1 week (Ogren and Charlson, 1983). Therefore, BC is also a type of pollutant with long-distance transport. However, the two villages are located in the shallow valley, which has the characteristics of basin topography, small wind speed, high static wind frequency, and the pollutants in the air are not easy to spread, especially in winter. So in this environment case, the extent of regional air pollution influence is mainly limited to the downwind region near the source (Sadiq et al., 2015).

4. Conclusions

In this study, a mobile monitoring approach was used to capture spatial/temporal characteristics at small-scale air pollution. Mobile real-time measurement of ambient particle matter (PM_1, $PM_{2.5}$, PM_{10}), black carbon and particle number concentrations have been carried out using mobile platforms in two neighboring villages.

This study illustrates the potential of mobile measurement methods to map short-term (e.g. winter), small-scale air pollution both for comparison purposes and estimation of absolute aerosol levels. As an example case study, we have completed locating and verifying the pathways of two villages, serving as small-scale PM_1, BC, and PNC hotspots, by several vehicular devices within about 20–21 walks. There are significant differences in PN and PM concentrations in rural air pollutants between the two villages. And the spatial and temporal distribution of air pollution hotspots in ZR was higher than that in BE. The relationships between the measurement parameters were weak but highly significant and the meteorological parameters can effect on the air pollution.

The novel aspect of this mobile monitoring approach was the simultaneous measurement along two pathways at same time to assess and compare spatial gradients at a small-scale air pollution while controlling temporal variations. We also displayed the mobile monitoring data from multiple views and verified the feasibility and values of mobile monitoring for small-scale air pollution.

In the future, this monitoring method can be used for research work. We plan to use this method to study the changes in the four seasons in the countryside to accurately estimate the extent of air pollution exposure and pollution changes on roadsides in rural areas.

CRediT authorship contribution statement

Xiansheng Liu: Resources, Investigation, Data curation, Writing - original draft.**Jürgen Schnelle-Kreis:**Methodology, Supervision.**Xun Zhang:** Data curation.**Jan Bendl:**Resources, Investigation.**Mohamed Khedr:**

Appendix

Resources, Investigation.**Gert Jakobi:**Resources.**Brigitte Schloter-Hai:** Writing - review & editing,**Jan Hovorka:**Conceptualization.**Ralf Zimmermann:**Writing - review & editing.

Acknowledgements

Xiansheng Liu's PhD work is funded by the China Scholarship Council (CSC) under the State Scholarship Fund (File No. 201706860028), and partially by the Germany Federal Ministry of Transport and Digital Infrastructure (BMVI) as part of SmartAQnet (grant No. 19F2003B), and Support Project of High-level Teachers in Beijing Municipal Universities in the Period of 13th Five–year Plan (CIT&TCD201904037). We also thank Pengfei Tai, Xiuxiu Lin and Yanling Xu for providing assistance in data preprocessing and Aethlabs (especially Jeff Blair) for providing assistance with troubleshooting the MA200.

Declaration of competing interest

The authors declare that they have no known competing financial interests or personal relationships that could have appeared to influence the work reported in this paper.

Appendix A. Supplementary data

Supplementary data to this article can be found online at https://doi.org/10.1016/j.scitotenv.2020.137632.

References

Alas, H.D., Müller, T., Birmili, W., Kecorius, S., Cambaliza, M.O., Simpas, J.B.B., ... Wiedensohler, A., 2018. Spatial characterization of black carbon mass concentration in the atmosphere of a Southeast Asian megacity: an air quality case study for Metro Manila, Philippines. Aerosol Air Qual. Res 18, 2301–2317. https://doi.org/10.4209/aaqr.2017.08.0281.

Babich, P., Davey, M., Allen, G., Koutrakis, P., 2000. Method comparisons for particulate nitrate, elemental carbon, and PM2.5 mass in seven US cities. J. Air Waste Manage. Assoc. 50 (7), 1095–1105. https://doi.org/10.1080/10473289.2000.10464152.

Begam, G.R., Vachaspati, C.V., Ahammed, Y.N., Kumar, K.R., Babu, S.S., Reddy, R.R., 2016. Measurement and analysis of black carbon aerosols over a tropical semi-arid station in Kadapa, India. Atmos. Res. 171, 77–91. https://doi.org/10.1016/j.atmosres.2015.12.014.

Braniš, M., Domasová, M., 2003. PM10 and black smoke in a small settlement: case study from the Czech Republic. Atmos. Environ. 37 (1), 83–92. https://doi.org/10.1016/S1352-2310(02)00700-8.

Brantley, H.L., Hagler, G.S.W., Kimbrough, E.S., Williams, R.W., Mukerjee, S., Neas, L.M., 2014. Mobile air monitoring data-processing strategies and effects on spatial air pollution trends. Atmos. Meas. Tech. 7 (7), 2169–2183.

Correia, A.W., Pope III, C.A., Dockery, D.W., Wang, Y., Ezzati, M., Dominici, F., 2013. The effect of air pollution control on life expectancy in the United States: an analysis of 545 US counties for the period 2000 to 2007. Epidimiology 24 (1), 23. https://doi.org/10.1097/EDE.0b013e3182770237.

Dawson, J.P., Adams, P.J., Pandis, S.N., 2007. Sensitivity of PM 2.5 to climate in the Eastern US: a modeling case study. https://hal.archives-ouvertes.fr/hal-00302769.

Dons, E., Panis, L.I., Van Poppel, M., Theunis, J., Wets, G., 2012. Personal exposure to black carbon in transport microenvironments. Atmos. Environ. 55, 392–398. https://doi.org/10.1016/j.atmosenv.2012.03.020.

Easton, V.J., McColl, J.H., 1997. Statistics glossary, time series data. Statistics Glossary-Time Series Data 12, 12. http://www.stats.gla.ac.uk/steps/glossary/.

EUROSTAT, 2017. Statistics on Rural Areas in the EU. https://ec.europa.eu/eurostat/statistics-explained/index.php/Statistics_on_rural_areas_in_the_EU.

Gidhagen, L., Johansson, C., Langner, J., Foltescu, V.L., 2005. Urban scale modeling of particle number concentration in Stockholm. Atmos. Environ. 39 (9), 1711–1725. https://doi.org/10.1016/j.atmosenv.2004.11.042.

Gomišček, B., Hauck, H., Stopper, S., Preining, O., 2004. Spatial and temporal variations of PM1, PM2.5, PM10 and particle number concentration during the AUPHEP—project. Atmos. Environ. 38 (24), 3917–3934. https://doi.org/10.1016/j.atmosenv.2004.03.056.

Gong, W., Zhang, T., Zhu, Z., Ma, Y., Ma, X., Wang, W., 2015. Characteristics of PM1.0, PM2.5, and PM10, and their relation to black carbon in Wuhan, Central China. Atmosphere 6 (9), 1377–1387. https://doi.org/10.3390/atmos6091377.

Gu, J., 2013. Characterizations and Sources of Ambient Particles in Augsburg, Germany. https://opus.bibliothek.uni-augsburg.de/.

Gulliver, J., Briggs, D.J., 2004. Personal exposure to particulate air pollution in transport microenvironments. Atmos. Environ. 38 (1), 1–8. https://doi.org/10.1016/j.atmosenv.2003.09.036.

Healy, R.M., Sciare, J., Poulain, L., Kamili, K., Merkel, M., Müller, T., ... McGillicuddy, E., 2012. Sources and mixing state of size-resolved elemental carbon particles in a European megacity: Paris. Atmospheric Chemistry and Physics 12, 1681–1700. https://doi.org/10.5194/acp-12-1681-2012.

Hovorka, J., Pokorná, P., Hopke, P.K., Křůmal, K., Mikuška, P., Píšová, M., 2015. Wood combustion, a dominant source of winter aerosol in residential district in proximity to a large automobile factory in Central Europe. Atmos. Environ. 113, 98–107. https://doi.org/10.1016/j.atmosenv.2015.04.068.

Kruskal, W.H., Wallis, W.A., 1952. Use of ranks in one-criterion variance analysis. J. Am. Stat. Assoc. 47 (260), 583–621. https://doi.org/10.2307/2280779.

Kumar, K.R., Narasimhulu, K., Balakrishnaiah, G., Reddy, B.S.K., Gopal, K.R., Reddy, R.R., ... Babu, S.S., 2011. Characterization of aerosol black carbon over a tropical semi-arid region of Anantapur, India. Atmospheric Research 100 (1), 12–27. https://doi.org/10.1016/j.atmosres.2010.12.009.

Kutzner, R.D., von Schneidemesser, E., Kuik, F., Quedenau, J., Weatherhead, E.C., Schmale, J., 2018. Long-term monitoring of black carbon across Germany. Atmos. Environ. 185, 41–52. https://doi.org/10.1016/j.atmosenv.2018.04.039.

Liu, F., Tan, Q.W., Jiang, X., Jiang, W.J., Song, D.L., 2018. Effect of relative humidity on particulate matter concentration and visibility during winter in Chengdu. Huan Jing Ke Xue 39 (4), 1466–1472. https://doi.org/10.13227/j.hjkx.201707112.

Liu, M., Peng, X., Meng, Z., Zhou, T., Long, L., She, Q., 2019. Spatial characteristics and determinants of in-traffic black carbon in Shanghai, China: combination of mobile monitoring and land use regression model. Sci. Total Environ. 658, 51–61. https://doi.org/10.1016/j.scitotenv.2018.12.135.

Ogren, J.A., Charlson, R.J., 1983. Elemental carbon in the atmosphere: cycle and lifetime. Tellus Ser. B Chem. Phys. Meteorol. 35 (4), 241–254. https://doi.org/10.1111/j.1600-0889.1983.tb00027.x.

Olson, M.R., Victoria Garcia, M., Robinson, M.A., Van Rooy, P., Dietenberger, M.A., Bergin, M., Schauer, J.J., 2015. Investigation of black and brown carbon multiple-wavelength-dependent light absorption from biomass and fossil fuel combustion source emissions. J. Geophys. Res.-Atmos. 120 (13), 6682–6697. https://doi.org/10.1002/2014JD022970.

Patton, A.P., Perkins, J., Zamore, W., Levy, J.I., Brugge, D., Durant, J.L., 2014. Spatial and temporal differences in traffic-related air pollution in three urban neighborhoods near an interstate highway. Atmos. Environ. 99, 309–321. https://doi.org/10.1016/j.atmosenv.2014.09.072.

Peng, C., Tian, M., Chen, Y., Wang, H., Zhang, L., Shi, G., ... Zhai, C., 2019. Characteristics, Formation Mechanisms and Potential Transport Pathways of PM2.5 at a Rural Background Site in Chongqing, Southwest China. Aerosol and Air Quality Research 19 (9). https://doi.org/10.4209/aaqr.2019.01.0010 (1980-1992+).

Peters, J., Theunis, J., Van Poppel, M., Berghmans, P., 2013. Monitoring PM10 and ultrafine particles in urban environments using mobile measurements. Aerosol Air Qual. Res. 13 (2), 509–522. https://doi.org/10.4209/aaqr.2012.06.0152.

Petzold, A., Ogren, J.A., Fiebig, M., Laj, P., Li, S., Baltensperger, U., ... Wehrli, C., 2013. Recommendations for reporting" black carbon" measurements. https://doi.org/10.5194/acp-13-8365-2013.

Reche, C., Querol, X., Alastuey, A., Viana, M., Pey, J., Moreno, T., ... Rosa, J.D.D.L., 2011. New considerations for PM, Black Carbon and particle number concentration for air quality monitoring across different European cities. https://doi.org/10.5194/acp-11-6207-2011.

Rehman, I.H., Ahmed, T., Praveen, P.S., Kar, A., Ramanathan, V., 2011. Black carbon emissions from biomass and fossil fuels in rural India. Atmos. Chem. Phys. Discuss. 11 (4). https://doi.org/10.5194/acpd-11-10845-2011.

Sadiq, M., Tao, W., Liu, J., Tao, S., 2015. Air quality and climate responses to anthropogenic black carbon emission changes from East Asia, North America and Europe. Atmos. Environ. 120, 262–276. https://doi.org/10.1016/j.atmosenv.2015.07.001.

Sarti, E., Pasti, L., Rossi, M., Ascanelli, M., Pagnoni, A., Trombini, M., Remelli, M., 2015. The composition of PM1 and PM2. 5 samples, metals and their water soluble fractions in the Bologna area (Italy). Atmos. Pollut. Res. 6 (4), 708–718. https://doi.org/10.5094/APR.2015.079.

Shen, L., Li, L., Lü, S., Zhang, X., Liu, J., An, J., Wang, F., 2015. Characteristics of black carbon aerosol in Jiaxing, China during autumn 2013. Particuology 20, 10–15. https://doi.org/10.1016/j.partic.2014.08.002.

Tai, A.P., Mickley, L.J., Jacob, D.J., 2010. Correlations between fine particulate matter (PM2.5) and meteorological variables in the United States: implications for the sensitivity of PM2.5 to climate change. Atmos. Environ. 44 (32), 3976–3984. https://doi.org/10.1016/j.atmosenv.2010.06.060.

Tang, Q.Y., Zhang, C.X., 2013. Data Processing System (DPS) software with experimental design, statistical analysis and data mining developed for use in entomological research. Insect Sci. 20 (2), 254–260. https://doi.org/10.1111/j.1744-7917.2012.01519.x.

Van Donkelaar, A., Martin, R.V., Brauer, M., Kahn, R., Levy, R., Verduzco, C., Villeneuve, P.J., 2010. Global estimates of ambient fine particulate matter concentrations from satellite-based aerosol optical depth: development and application. Environ. Health Perspect. 118 (6), 847–855. https://doi.org/10.1289/ehp.0901623.

Vecchi, R., Marcazzan, G., Valli, G., Ceriani, M., Antoniazzi, C., 2004. The role of atmospheric dispersion in the seasonal variation of PM1 and PM2.5 concentration and composition in the urban area of Milan (Italy). Atmos. Environ. 38 (27), 4437–4446. https://doi.org/10.1016/j.atmosenv.2004.05.029.

Wolf, K., Cyrys, J., Harciníková, T., Gu, J., Kusch, T., Hampel, R., ... Peters, A., 2017. Land use regression modeling of ultrafine particles, ozone, nitrogen oxides and markers of particulate matter pollution in Augsburg, Germany. Science of the Total Environment 579, 1531–1540. https://doi.org/10.1016/j.scitotenv.2016.11.160.

Yu, C.H., Fan, Z., Lioy, P.J., Baptista, A., Greenberg, M., Laumbach, R.J., 2016. A novel mobile monitoring approach to characterize spatial and temporal variation in traffic-related air pollutants in an urban community. Atmos. Environ. 141, 161–173. https://doi.org/10.1016/j.atmosenv.2016.06.044.

Zhu, Y., Hinds, W.C., Kim, S., Sioutas, C., 2002. Concentration and size distribution of ultrafine particles near a major highway. J. Air Waste Manage. Assoc. 52 (9), 1032–1042. https://doi.org/10.1080/10473289.2002.10470842.

Publication V

Liu, X., Hadiatullah, H., Zhang, X., Hill, L. D., White, A. H., Schnelle-Kreis, J., ... & Zimmermann, R. (2021). Analysis of mobile monitoring data from the microAeth® MA200 for measuring changes in black carbon on the roadside in Augsburg. ***Atmospheric Measurement Techniques,*** 14, 5139–5151.

Atmos. Meas. Tech., 14, 5139–5151, 2021
https://doi.org/10.5194/amt-14-5139-2021
© Author(s) 2021. This work is distributed under
the Creative Commons Attribution 4.0 License.

Atmospheric Measurement Techniques
Open Access
EGU

Analysis of mobile monitoring data from the microAeth® MA200 for measuring changes in black carbon on the roadside in Augsburg

Xiansheng Liu[1,2,3], Hadiatullah Hadiatullah[4], Xun Zhang[1,5], L. Drew Hill[6], Andrew H. A. White[6,7], Jürgen Schnelle-Kreis[2], Jan Bendl[2,8], Gert Jakobi[2], Brigitte Schloter-Hai[2], and Ralf Zimmermann[2,3]

[1]Beijing Key Laboratory of Big Data Technology for Food Safety, School of Computer Science and Engineering, Beijing Technology and Business University, 100048 Beijing, China
[2]Joint Mass Spectrometry Centre, Comprehensive Molecular Analytics, Helmholtz Zentrum München, German Research Centre for Environmental Health, Ingolstädter Landstr. 1, 85764 Neuherberg, Germany
[3]Joint Mass Spectrometry Centre, Analytical Chemistry, University of Rostock, 18059 Rostock, Germany
[4]School of Pharmaceutical Science and Technology, Tianjin University, 300072 Tianjin, China
[5]Key Laboratory of Resources Utilization and Environmental Remediation, Institute of Geographical Sciences and Natural Resources Research, Chinese Academy of Sciences, 100101 Beijing, China
[6]AethLabs, San Francisco, CA, USA
[7]Yale School of Medicine, New Haven, CT, USA
[8]Institute for Environment Studies, Faculty of Science, Charles University, Prague, Czech Republic

Correspondence: Xun Zhang (zhangxun@btbu.edu.cn) and Jürgen Schnelle-Kreis (juergen.schnelle@helmholtz-muenchen.de)

Received: 29 December 2020 – Discussion started: 16 February 2021
Revised: 9 June 2021 – Accepted: 30 June 2021 – Published: 28 July 2021

Abstract. The portable microAeth® MA200 (MA200) is widely applied for measuring black carbon in human exposure profiling and mobile air quality monitoring. Due to it being relatively new on the market, the field lacks a refined assessment of the instrument's performance under various settings and data post-processing approaches. This study assessed the mobile real-time performance of the MA200 to determine a suitable noise reduction algorithm in an urban area, Augsburg, Germany. Noise reduction and negative value mitigation were explored via different data post-processing methods (i.e., local polynomial regression (LPR), optimized noise reduction averaging (ONA), and centred moving average (CMA)) under common sampling interval times (i.e., 5, 10, and 30 s). After noise reduction, the treated data were evaluated and compared by (1) the amount of useful information attributed to retention of microenvironmental characteristics, (2) the relative number of negative values remaining, (3) the reduction and retention of peak samples, and (4) the amount of useful signal retained after correction for local background conditions. Our results identify CMA as a useful tool for isolating the central trends of raw black carbon concentration data in real time while reducing nonsensical negative values and the occurrence and magnitudes of peak samples that affect visual assessment of the data without substantially affecting bias. Correction for local background concentrations improved the CMA treatment by bringing nuanced microenvironmental changes into view. This analysis employs a number of different post-processing methods for black carbon data, providing comparative insights for researchers looking for black carbon data smoothing approaches, specifically in a mobile monitoring framework and data collected using the microAeth® series of Aethalometer.

1 Introduction

Black carbon particulate matter with size ranging from 0.01 to 1 µm (Zhou et al., 2020) is a pollutant comprised of a range of carbonaceous materials produced by the incomplete combustion of fossil fuel and biomass containing carbon (Goldberg, 1985), and it is suspected of exerting a significant impact on health (Anenberg et al., 2012; Janssen et al., 2011;

Published by Copernicus Publications on behalf of the European Geosciences Union.

Appendix

Nichols et al., 2013). Black carbon also has an important role in climate systems due to its strong radiative forcing potential (Kutzner et al., 2018; Sadiq et al., 2015). The International Agency for Research on Cancer (IARC) has classified black carbon as a 2B carcinogen, while researchers have linked black carbon exposures to cardiovascular, respiratory, and neurological diseases (e.g., Nichols et al., 2013). However, the high spatial variability of black carbon among small-scale urban blocks is difficult to characterize with existing monitoring networks which typically rely on fixed monitors (Apte et al., 2017), especially for on-road concentrations. Recently, mobile monitoring has been widely applied for the collection of real-time air quality measurements to assess local air quality and air pollutant exposures (Liu et al., 2020, 2021). This method can improve the spatio-temporal resolution of measurement data in the urban environment, and it enables the collection of data such as the traffic-related air pollutant concentrations (Liu et al., 2019). Therefore, mobile measurements are favourably used in human exposure studies to quantify individual exposures and to demonstrate the importance of exposure differences in different microenvironments.

Instrument manufacturers in the USA have recently developed a new instrument for measuring black carbon concentrations in a variety of exposure-related contexts, including personal exposure assessment, ambient and vertical profiling, and indoor emissions concentration measurements, among others. This instrument, the microAeth® MA200 (MA200; AethLabs, San Francisco, CA, USA), continuously collects aerosol particles on a filter and measures the optical attenuation (ATN) at five wavelengths (880, 625, 528, 470, and 375 nm) with a data collection time base as frequent as 1 Hz. This instrument supports the DualSpot® loading compensation method, which corrects the optical loading effect (Virkkula et al., 2007) and provides additional information about aerosol optical properties. However, the raw data recorded by the MA200 at high frequencies (e.g., 1 Hz) can exhibit noise that obscures nuanced signals surrounding the central tendency of the data, increasing the difficulty of analysis in mobile settings or during rapidly changing microenvironmental characteristics. These negative values usually contain valid information required for noise reduction or smoothing, and so simply removing them may result in bias. Noise reduction of the raw data without direct removal of negative values is thereby recommended to enhance data quality and temporal resolution (Liu et al., 2020). In addition, when the sampling equipment traverses from a highly polluted to a marginally polluted area, such as a park, the instrument produces strong negative values due to the measurement principle of the instrument and the strength of the pollution gradient between microenvironments. Therefore, the raw black carbon concentrations collected by MA200 need to be post-processed to ensure that researchers can adequately analyse the spatio-temporal distribution of black carbon.

Some progress has been made in the study of black carbon monitoring (Apte et al., 2011; Dons et al., 2012; Cao et al., 2020); however, noise reduction algorithms have not been fully assessed for the new generation of micro-Aethalometer and for mobile monitoring contexts. In previous studies, Hagler et al. (2011) and Cheng and Lin (2013) evaluated optimized noise reduction averaging (ONA) for post-processing mobile monitoring data. Due to the high spatial heterogeneity of black carbon, the ONA algorithm may ignore important microenvironmental effects and lead researchers to perhaps incorrectly conclude that the resolution of microenvironmental source information cannot be determined from their data.

In this study, we aim to determine a suitable noise reduction algorithm for the MA200 Aethalometer, starting with ONA and moving on to two additional smoothing techniques offered by AethLabs in their suite of free online data post-processing (i.e., noise reduction) tools: the local polynomial regression (LPR) and centred moving average (CMA) algorithms. The interpretation accuracy of data analysed and reported upon in black carbon mobile monitoring studies can be increased by assessing the relative performance of these post-processing methods to each other and to ONA. The quality of each noise reduction approach was assessed on data collected in an urban environment and post-processed with ONA, LPR, and CMA. Assessment criteria included (1) retention of detailed information attributed to microenvironmental characteristics, (2) relative number of negative values remaining, (3) reduction and retention of peak samples, and (4) retention of detailed information on microenvironmental characteristics after background correction.

2 Methods

2.1 Instrumentation

2.1.1 Sampling equipment

The MA200 measures optical ATN from black carbon on a filter across five optical wavelength ranges: infrared, red, green, blue, and ultraviolet (880, 625, 528, 470, and 375 nm, respectively). A common black carbon metric called "equivalent black carbon" (eBC) is assessed via the 880 nm channel, i.e., data from the IR BCc channel. The detection limit of the MA200 is reported at 30 ng/m^3 eBC under a 5 min time base and 150 mL/min flow rate (SingleSpot™ mode) and with a resolution of 1 ng/m^3 (AethLabs, 2018). In mobile monitoring, the MA200 can be used to estimate personal exposure and quantify eBC mass concentrations in different microenvironments. It should be noted that a predecessor instrument to the MA200, the AE51, has demonstrated some sensitivity to mechanical shock during mobile measurements (Cai et al., 2013). When AethLabs took control of manufacturing the AE51, which was originally produced by Magee Scientific (Berkeley, CA, USA), instrument optoelectronics were

Appendix

redesigned to reduce such sensitivity. Researchers using the redesigned AE51 demonstrated only a small effect on data. Supporting this improvement, Cai et al. (2013) found evidence of a substantial improvement in data quality related to vibration-related spikes after an equipment upgrade by AethLabs. In addition, there were no major mechanical shocks to or unique vibrational effects on the instrument and no major differences of accelerometer data in the raw data, precluding these as potential confounders on all instruments.

2.1.2 Preparation of the instruments

In this study, seven MA200 portable black carbon monitors (serial numbers MA200-0051, MA200-0053, MA200-0059, MA200-0060, MA200-0155, MA200-0153, MA200-159) were used simultaneously to measure black carbon levels in the city centre under different interval times (5, 10, and 30 s). To evaluate the relative performance of MA200, this study analysed black carbon data collected from multiple MA200 devices, identified individually by serial numbers. The instruments were prepared and adjusted in our laboratory before each walk, consisting of "zero" calibration checks and the examination of the MA200 filter cassette, battery, GPS, and memory. Flow calibrations were adjusted with a factory-calibrated flowmeter (Alicat Scientific Inc., Tucson, AZ, USA).

Comparative measurements of the MA200 and a stationary Aethalometer (AE33, Magee Scientific, Berkeley, USA) taken approximately 30 to 60 min between walks showed a good agreement (Pearson's $r = 0.933$) (Liu et al., 2021). In addition, it is worth noting that when the AE33 was used for monitoring black carbon at the same time as the MA200, the AE33 was placed in a fixed station, while the MA200 was used outdoors (in the stroller) during the individual walks, which may have presented different relative humidity and temperature values. This condition did not influence the consistency of eBC concentration measured with both instruments. Information about the date, duration, and time resolution (time base) of each MA200 device is summarized in Table 1. To demonstrate the unit-to-unit comparability between the MA200 units, we performed intercomparisons at fixed monitoring stations (Table S1) and during co-located mobile measurements (Fig. S2). No wavelength dependence was observed between different instruments for fixed and mobile monitoring measurements.

2.2 Study design and routes

The MA200 instrument is able to measure black carbon in 1, 5, 10, 30, 60, and 300 s interval times. The 1 s time base exhibits the most challenging interpretation because of low signal-to-noise ratio, especially at low concentrations, which is similar to other optical black carbon monitors (Hagler et al., 2011). Therefore, 1 s measurement resolution may be most useful when sampling in high-concentration environments, performing direct emissions testing and requiring high time resolution for the application. However, the eBC average concentration is low in the city centre of Augsburg, Germany, (measured at 2.62 µg/m^3 in winter by Gu, 2012); thus, we did not use the 1 s time base. Moreover, 60 and 300 s are too long for mobile monitoring, which may affect the accuracy of the spatial variation of pollutants; hence, both time bases were also not selected in this study. In order to better understand at which interval time of sampling might be most useful in this context – mobile measurements at low eBC concentrations – three MA200 devices were used in parallel to measure eBC concentrations with the interval times of 5, 10, and 30 s (measurement numbers 5–7 in Table 1).

To account for the different land-use types of the microenvironments, a fixed walking route within the centre of the city was determined. Wherever possible, the mobile measurements were carried out on the right side of the road, simulating people's common habits (driving and walking on the right side in Germany). All walks along the route were conducted on weekdays, with clear skies and calm winds to avoid misrepresentation of typical urban exposure conditions. The route started from Augsburg University of Applied Sciences (UAS) and continued approximately 14 km for 3 h average walking time, passing through different types of land use to ensure that different microenvironments were represented in the entire area and to ensure the validity of the results (Fig. S1). Meanwhile, as performed in our previous study (Liu et al., 2021), we divided the monitoring route into four microenvironment groups in Augsburg, including high traffic flow (H_Traffic, average 500–1000 vehicles per hour), medium traffic flow (M_Traffic, average 200–500 vehicles per hour), low traffic flow (L_Traffic, average 1–200 vehicles per hour), and park area (N_Traffic, average 0 vehicles per hour), according to the actual traffic density examined during the daytime and determined from the traffic flow observed by street views.

Briefly, the study consisted of the following phases: (1) collecting raw black carbon data using the sampling instruments (MA200); (2) smoothing the acquired raw black carbon data under different post-processing methods (i.e., noise reduction); (3) comparing the noise reduction data based on the detail of microenvironmental characteristic and number of negative values; (4) following the peak samples identification by the coefficient of variation (COV); (5) following the background estimation and correction by thin-plate regression spline (TPRS); and (6), finally, selecting the best noise reduction approach.

2.3 Post-processing methods

In order to reduce the noise of concentration data obtained using high time resolutions, post-processing algorithms can be used. AethLabs offers tools for applying several noise reduction algorithms (ONA, LPR, and CMA) to MA-series device data on its website (https://aethlabs.com, last access:

Appendix

Table 1. Measurements of black carbon by different MA200 devices.

Measurement number	Date (dd/mm/yyyy)	Serial number	Start time (hh:mm:ss)	End time (hh:mm:ss)	Time base (s)	Site
1	27/09/2018	MA200-0051	10:29:10	13:38:20	10	
2	15/11/2018	MA200-0059	11:53:42	16:13:12	10	
3	16/11/2018	MA200-0053	11:34:06	16:33:56	10	
4	26/08/2019	MA200-0060	11:01:56	15:44:46	10	Augsburg, Germany
5	21/02/2020	MA200-0155	10:00:10	13:10:00	5	
6	21/02/2020	MA200-0153	10:00:10	13:10:00	10	
7	21/02/2020	MA200-0159	10:00:10	13:10:00	30	
8	24/11/2020	MA200-0059	09:40:57	11:09:07	10	
9	01/12/2020	MA200-0051	13:29:05	15:19:00	5	Munich, Germany
10	18/12/2020	MA200-0051	14:39:30	15:19:30	30	

26 July 2021; note that a free account is required). The relative utility of the different post-processing methods is determined by (1) the ability to perceive nuanced differences between microenvironmental pollution characteristics after noise reduction, (2) the relative number of negative eBC values remaining, (3) the reduction and retention of peak samples, and (4) the ability to perceive nuanced differences between microenvironmental pollution characteristics with the noise-reduced data after background correction.

2.3.1 ONA (optimized noise reduction averaging)

ONA is based on the time series of three parameters in the original observation data, namely the observation time, the original eBC concentration, and the amount of change in optical ATN over time, as specifically described by Hagler et al. (2011). Briefly, a ΔATN threshold is manually set to prevent the algorithm from recalculating eBC until a certain amount of ATN has been detected (e.g., enough black carbon has deposited on the filter to "confidently" calculate an eBC concentration). The aim is to reduce erroneous and spurious estimation by dynamically extending the effective sample time base; hence, there is sufficient ATN to significantly reduce the error effects of instrument noise. This effective time base will be longer in low concentrations compared to higher concentrations; hence, when operating properly, no negatives and less eBC noise will be reported. When using the ONA algorithm, this ΔATN threshold needs to be manually assigned. Hagler et al. (2011) implemented a ΔATN threshold of 0.05 to post-processed data from a fixed monitoring site by different Aethalometer models (AE21, AE42, and AE51). However, when applied to MA200 data, a ΔATN threshold of 0.05 results in a very smooth curve and may obscure more information than is necessary to provide a usefully smoothed curve. For this reason, a lower ΔATN threshold of 0.01 was selected for the mobile measurement data of our study (Fig. S3).

2.3.2 LPR (local polynomial regression)

The LPR algorithm is a non-parametric tool similar to a moving average, but it operates on polynomial regression rather than simple averaging (Masry, 1996; Breidt and Opsomer, 2000; Kai et al., 2010). In LPR, the number of points to smooth across must be manually identified. This value should be chosen to balance effective smoothing of the measured values and the sensitivity required to provide spatial resolution in mobile measurements (e.g., the distance over which the average was taken). The distance resolution was chosen to be approximately 100 m. Assuming the sampling speed is 1.3 m/s, when the interval time is 5, 10, and 30 s, the smoothing numbers of points are 15, 7, and 3, respectively.

2.3.3 CMA (centred moving average)

The CMA algorithm is a smoothing technique used to make the long-term trends of a time series clearer (Easton and McColl, 1997). Unlike a simple moving average, CMA has no shift or group delay in the data processing, as it incorporates data from both before and after the data point that is being smoothed. The smoothing number of points was determined as previously described in the LPR algorithm, assuming a sampling speed of 1.3 m/s.

2.4 Comparison analysis after noise reduction approach

2.4.1 The nuance of microenvironmental characteristics and the proportion of negative values

After post-processing the data, the characteristic change of the treated data is used as criterion to select the best method. In this regard, when the treated data provide more detailed microenvironmental characteristics, the data reflect the actual situation of air pollutants and facilitate the identification of pollution sources. However, if microenvironmental trends are

Appendix

less pronounced, it may hinder the identification of the pollution source. Therefore, more detailed microenvironmental features result in more accurate information. In addition, the number of remaining negative values is determined as another criterion to propose the best method. Specifically, the method with the smallest proportion of the negative values is selected as the best method. The proportion of negative values (NV) remaining was calculated as the number of negative values divided by the total sample size.

2.4.2 Peak sample identification

An earlier study by Brantley et al. (2014) compared several methods for identifying and eliminating peak samples in mobile air pollution measurements. These include identifying samples outside of a threshold based on a median produced using road segmentation, an α-trimmed arithmetic average (Van den Bossche et al., 2015), a running coefficient of variation (COV) (Hagler et al., 2012), an estimate of background standard deviation (Drewnick et al., 2012), a running low 25 % quantile (Choi et al., 2012), and 3 times the standard deviation (Wang et al., 2015). The formula for the running method used in this analysis was previously described by Hagler et al. (2012) with minor modification (Eq. 1):

$$\mathrm{COV}_t = \frac{\sqrt{\frac{1}{7}\sum_{i=t-3}^{i=t+3}(x_i - \overline{x})^2}}{\overline{x}_{\mathrm{all}}}, \quad (1)$$

where COV_t is the 70 s sliding COV of the tth eBC sample under a 10 s time base (representing 30 s prior to the sample, the sample time, and 30 s after the sample), x_i is the ith eBC sample, $\overline{x}$ is the average of the tth eBC sample and the three samples before and after it, and $\overline{x}_{\mathrm{all}}$ is the average of all eBC data in one experiment. The 99th percentile of the 70 s sliding COV of all eBC data is used as the threshold for determining "peak sample". The eBC samples that are greater than this threshold are flagged as peak samples along with the eBC samples three data points before and after. However, under different time bases (e.g., 5 and 30 s), the sliding COV of the tth black carbon sample is different. Accordingly, the COV equation is required for modification under different time bases.

To calculate the reduction of peak samples (RP), the number of peak samples was calculated before and after post-processing the data, and the difference value was obtained. Then the change in the number of peak samples was divided by the total number of peak samples before post-processing the data. After noise reduction, we compared the reduction and the number of peak samples to further evaluate post-processing methods. In short, if the reduction of peak samples is high, the treated data have a high peak noise reduction without removing the numbers of peak samples. Therefore, the method with high reduction of peak samples and retaining the number of peak samples after post-processing is considered the better method.

2.4.3 Background estimation and correction

The ability of a processing method to adequately remove the estimated background concentration was used to evaluate which method provides the most useful information related to microenvironmental effects. A noise reduction method that appears to better facilitate background estimation and correction (as described below calculated from noise-reduced data via a defined background estimation and evaluation approach) is assessed to select a better post-processing method.

Background correction methods include the single sample standardization method, the sliding minimum method, the linear regression post-processing method, and the spline (of minimum) regression post-processing method. Brantley et al. (2014) suggest that a thin-plate regression spline (TPRS) method can reliably evaluate the background value of mobile measurements and be used to examine the "useful" information in the noise-reduced data (i.e., non-spurious non-background pollution trends). Briefly, the TPRS approach includes three steps: first, the noise reduction data of the pollutant were processed by a 30 s moving average; second, the results of the 30 s moving average were sequentially processed by the specified time window (i.e., 5 and 10 min), and the position of the minimum sample of pollutant concentration was identified in each window; and, finally, thin-plate spline regression was used to fit the sample of minimum pollutant concentration obtained in the previous step, then the background concentration at each time point was obtained.

3 Results and discussion

The average eBC concentrations of raw, ONA-processed, LPR-processed, and CMA-processed data (measurements 1–10) monitored by all instruments were compared in this study (Table S2). The results show that the three post-processing methods accounted of approximately 1 % bias from the average of raw concentrations (except measurement 5, ONA-processed data at 5 s). This indicates that the average concentration under each post-processing method did not affect the average concentration of the raw unprocessed data.

3.1 Post-processing the data under different interval times

As shown in Fig. 1, three MA200 devices were used at the time bases of 5, 10, and 30 s. The proportion of negative values in the raw data collected under different time bases were 42.1 %, 37.6 %, and 30.5 % for 5, 10, and 30 s, respectively (Fig. 1a, Table 2, Fig. S4a). Following this, the raw data were processed using ONA, LPR, and CMA (Fig. 1b, c, and d).

In the 5 s time base, the eBC values changed very rapidly (Fig. 1a), and the ONA processing of the data resulted in only one value (which was negative) (Fig. 1b). Thus, the microenvironmental characteristics of the eBC concentration were not reproduced. We found that all ΔATN ($\mathrm{ATN}_{t\,(0)+\Delta t'}-$

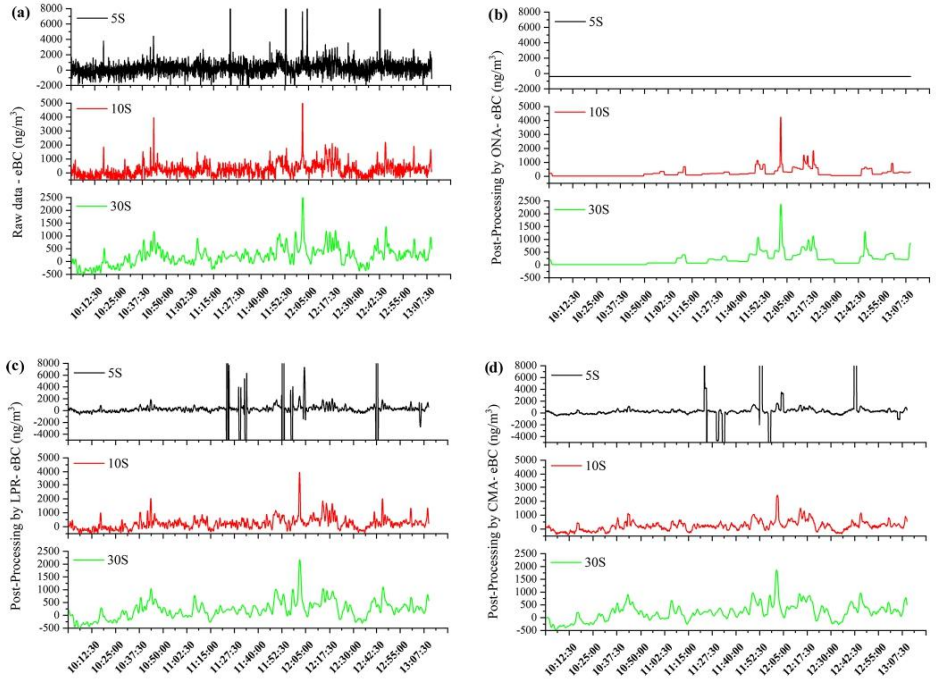


Figure 1. The temporal fluctuations of the black carbon levels measured with the MA200 at sampling time bases of 5, 10, and 30 s during a typical sampling period (about 190 min); **(a)** raw data without noise reduction; **(b)** data treated with optimized noise reduction averaging; **(c)** data treated with local polynomial regression; and **(d)** data treated with centred moving average. The analysis was carried out on data streams from three MA200 devices all collected during a single sampling run (measurements 5, 6, and 7).

Table 2. The proportion of negative value (NV) and average reduction of peak (RP) samples under the different post-processing methods (values are shown in percent; NV [%]: proportion of negative values remaining; RP [%]: average reduction of peak samples. Symbol "–" means no data; measurements 1–10).

Interval time	Factor	Raw	ONA	LPR	CMA
5 s	NV	42.1	–	28.1	22.9
	RP	0	100	72.0	87.4
10 s	NV	37.6	0	30.2	25.3
	RP	0	5.54	22.3	47.7
30 s	NV	30.5	0	25.5	22.4
	RP	0	0.62	6.24	39.1

Appendix

ATN_0) data were negative in the raw data collected at 5 s, which, according to the ONA method described above, resulted in only a single value. In short, after the first measurement, the ΔATN threshold (which is positive) for calculating the next value was never reached. The first value was likely a negative value due to a combination of instrument noise, coincidence, and a low background concentration (i.e., low baseline instrument signal), which is consistent with both the raw data measurements and the typical low eBC concentrations in the city centre of Augsburg, Germany (Gu, 2012). It is unclear why ΔATN remained negative, but, given the long series of low concentration vales at the beginning of the sampling and the initial negative measurement, it is possible that the summed ΔATN became increasingly negative as a result of the initial negative ΔATN measurement. The subsequent measurements at low concentration did not exceed the magnitude of the initial negative ΔATN value. Under these conditions, a cumulative negative sum of ΔATN would prevent the positive ΔATN threshold from being achieved at all. If true, this condition highlights one potential weakness of the ONA algorithm, such as difficulty registering a signal under low concentrations, and requires further investigation of the conditions under which ONA is truly unbiased. The observed event prevented the use of ONA in the 5 s time base (Fig. 1b). Previous studies in which ONA was successfully applied implemented a 1 s time base (Hagler et al., 2011; Van den Bossche et al., 2015). After post-processing with LPR and CMA, the microenvironmental characteristics retained more detailed information on the eBC concentration. Further comparison of their negative values revealed that the remaining negative values comprised 28.1 % and 22.9 % of the dataset for LPR and CMA, respectively, after post-processing.

In the 10 s interval time base, negative values were not found after ONA processing, suggesting that a reasonable smoothing effect is obtained at low black carbon concentration. The microenvironmental characteristics presented strong changes compared to the raw data, leaving less detailed information on air pollution. After post-processing with LPR and CMA, the microenvironmental characteristics revealed more detailed information on air pollution, with 30.2 % of negative values for LPR and 25.3 % for CMA. In the 30 s interval time base, the negative values comprised 0 % of the post-processed data for ONA, 25.5 % for LPR, and 22.4 % for CMA. The 30 s interval dataset presented the lowest proportion of negative values before and after post-processing, due to the longer interval time of sampling. However, the longer 30 s measurement period results in more distance covered during each measurement, given the mobile nature of the sampling device. Thus, 30 s black carbon measurements may be too long to detect local concentration peaks in urban contexts that supported another study (Kerckhoffs et al., 2016).

The ONA algorithm showed a strong tendency to remove negative values and, depending on the ΔATN threshold employed by the user, can remove potentially meaningful low peaks. As a result, the ONA-treated data may present a bias that obscures nuanced microenvironmental trends (Fig. 1b). Interestingly, LPR and CMA post-processing are capable of decreasing negative values while retaining microenvironmental trends. Both methods are promising for the analysis of spatio-temporal changes in pollutant concentrations with sensitivity to local sources. Previous studies have shown that the spatio-temporal variability of black carbon is highly heterogeneous (Liu et al., 2019, 2021); the ability to capture spatio-temporal variability of microenvironments is critical for assessing differential exposures among populations.

3.2 Reduction and number of peak samples after post-processing methods

The processing of peak sample is a pivotal evaluation index for the measurement of time-averaged roadside air quality. Passing vehicles, for example, may bias estimates of typical local concentrations due to their contribution to the dataset of peak concentrations that may substantially relate to arithmetic averages. Therefore, after noise reduction, we compare the reduction and the retained number of peak samples to further evaluate the post-processing methods.

In the interval time 5 s, the average reduction of peak samples (RP) for the LPR and CMA algorithms was 72.0 % and 87.4 %, respectively (as discussed above, the ONA method could not be used). In this interval time, the reduction of peak samples was relatively high, indicating that when monitoring black carbon at low concentrations and high sample frequencies, drastic noise may occur in the raw data, and higher noise reduction may affect the actual values. Therefore, a suitable interval time should be considered when monitoring low eBC concentrations. In the interval time 10 s, the average reduction of peak samples for CMA (47.7 %) is higher than ONA (5.54 %) and LPR (22.7 %). In the interval time 30 s, CMA presented the greatest average reduction of peak samples (39.1 %) compared to ONA (6.24 %) and LPR (0.62 %) (Table 2, Fig. S4b). The retention of peak samples remaining after post-processing was also assessed using the COV method (measurements 1–10). The result showed that all three algorithms retained all peak samples before and after post-processing. In this regard, CMA retained all peak samples despite the highest reduction in their magnitude. Therefore, CMA highlights microenvironmental trends while preserving the identity of peak samples, facilitating the identification of local pollution sources, and may thus be a better post-processing method than ONA or LPR (Table 2, Fig. S4b).

To further characterize the distribution of peak sample concentration under CMA, we performed an intensive graphical analysis on a single data stream (measurement 4; Fig. 2). As shown in Fig. 2, eBC values along the main roads and intersections were higher than other locations, presumably due in large part to stop-and-go traffic and cars in close proximity to the mobile monitor (Fig. 2). It can be seen from Fig. 2a that the peak samples of black carbon were mainly found in

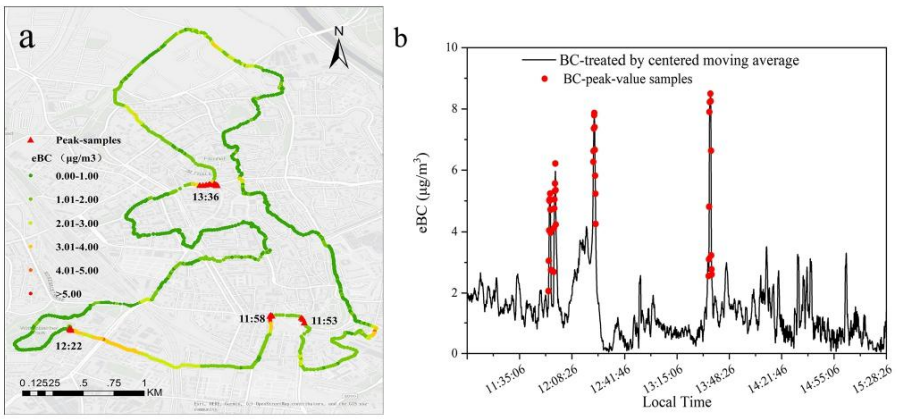


Figure 2. Identification of the spatial **(a)** and temporal **(b)** distribution characteristics of black carbon peak samples based on the coefficient of variation method (the analysis based on measurement 4); © OpenStreetMap contributors 2020. Distributed under the Open Data Commons Open Database License (ODbL) v1.0.

four locations, represented by red triangles. Vehicle counts and traffic in these locations vary depending on the time of measurement. The highest eBC values were repeatedly found in the streets with moderately high traffic volumes and dense coverage with relatively high buildings (street canyon situation), indicating that heterogeneity in air pollution concentrations in Augsburg and similar settings is largely caused by a combination of effects from traffic and topography (Buonanno et al., 2011). To determine whether peak samples are due to local sources or instrumental artefacts and to provide further evidence that traffic and topography effects are primary contributors to spatial heterogeneity in pollution concentrations, we compared the data measurements of the three co-located MA200 units during measurements 5, 6, and 7. The results showed that there were no major differences in the hotspot areas (an indicator of considerable peak samples) identified by the measurements of the three instruments (Fig. S5).

3.3 Comparison of background estimation and correction after noise reduction

Local air pollution can be highly affected by long-range and regional transport. The timing and magnitude of such transport events vary in space and time and are highly dependent upon the stochasticity of meteorology. As a result, local background concentration changes may vary, affecting the comparability of measurements made at the same location at different times (Brantley et al., 2014). For this reason, reliable comparison of time-variable mobile measurements across a city (and thus reliable pinpointing of hotspots and pinpointing of key local sources) requires effective methods to estimate, isolate, and remove the effects of fluctuations in background concentration. Our analysis indicates that the effectiveness of background correction is affected by the noise reduction method chosen during post-processing.

After post-processing, the data were evaluated using the TPRS method. We calculated the 5 and 10 min background concentrations under different post-processing approaches. As shown in Fig. 3a and b, the background concentration after LPR processing has both the largest proportion of negative values and the most negative values (i.e., negative values of the greatest absolute magnitude), resulting in estimates of background-corrected concentrations that are greater than actual monitored concentrations. Background concentrations calculated after ONA and CMA post-processing presented fewer and lower negative values than LPR but were not convincingly different from each other. Therefore, to further compare the ONA and CMA algorithms, we also compared concentrations after background correction (Fig. 3c and d). As shown in Fig. 3c and d, when the concentration is lower than 1 μg/m^3, the background-corrected results after the ONA processing are smoother than after CMA. This result dampens the signal of local pollutant sources, resulting in a lower utility of post-processed data.

In order to verify the CMA applicability and its advantages, this study further analysed the eBC concentrations measured by a fixed background monitoring station at the University of Applied Sciences (UAS) (Fig. S6) (Cyrys et al., 2006). The background value under the 5 min window exhibits wave-like characteristics, and the fitting curve in the 10 min window is relatively smooth. However, the TPRS-

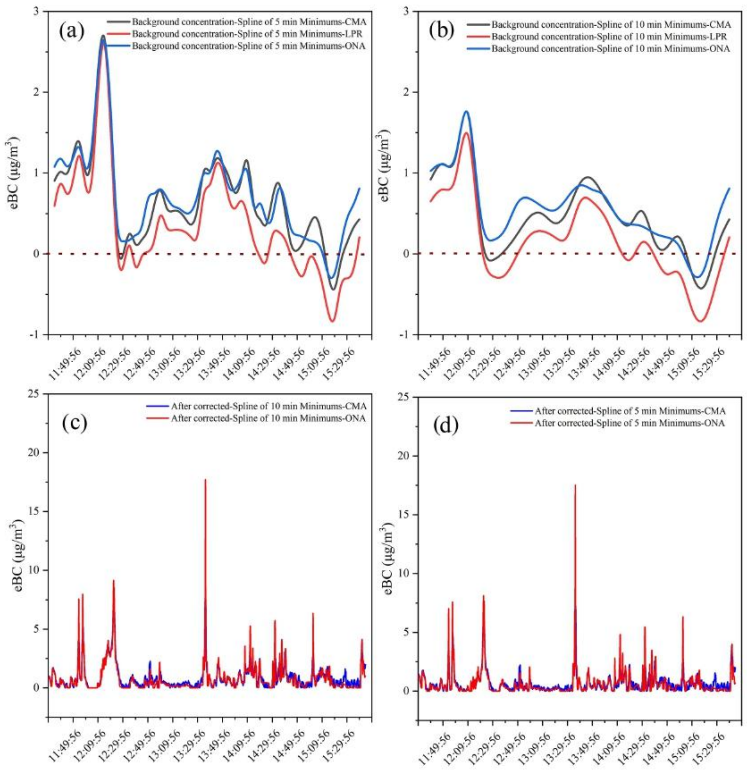
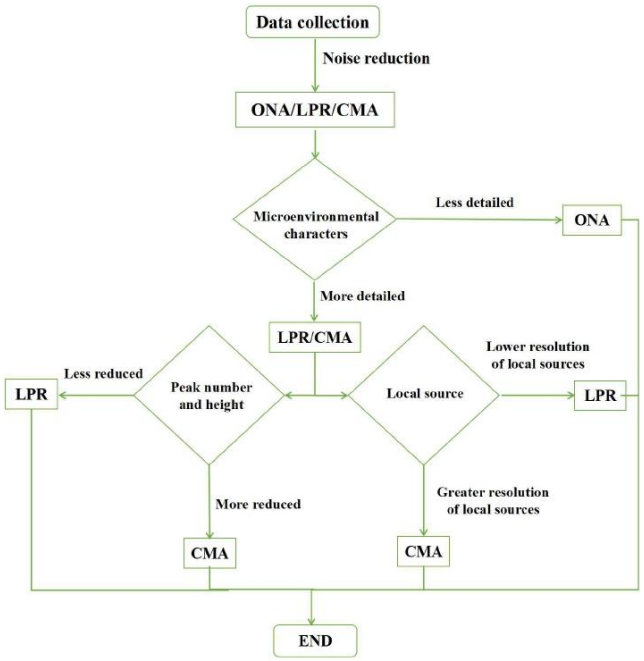


Figure 3. Background concentration of black carbon under different time series for **(a)** spline of 5 min minimums and **(b)** spline of 10 min minimums and after being corrected for **(c)** spline of 5 min minimums and **(d)** spline of 10 min minimums. Analyses are based on measurement 4.

based background value often does not fluctuate greatly over short periods, and the black carbon background value curve under the 5 min window does not conform to the "actual" urban background situation as estimated using the fixed-site monitor data, which are assumed to primarily represent the fluctuations in background concentrations. Moreover, by comparing the curve produced by the spline of 10 min minimums with the eBC background concentration ("Background-UAS", Fig. S6), it can be found that the background correction method based on the time series can well characterize the time-varying characteristics of background pollution in each experiment, suggesting that, of the two options, 10 min showed the better window for fitting the background value curve of black carbon.

Under the TPRS method, the background concentration of eBC can be fitted at any sampling time. The TPRS-estimated background contribution of the observed eBC concentration averaged 37.8 % of the total measured concentration. However, when the contribution of background concentration to a single measurement was examined, a large fluctuation (10.4 %–71.3 %) was observed, which may be closely related to sizable changes in the meteorological conditions, traffic conditions along the road (and over time at the same point in the road), and urban street canyon effects in each measurement. Therefore, based on the comparison of background correction, CMA showed better applications for estimating the background concentration and location source contribution.



Scheme 1. The proposed decision tree for mobile monitoring data from the microAeth® MA200.

3.4 Generalizability

To verify the generalizability of our assessment, we performed another three measurement runs in Munich (measurements 8, 9, and 10). Raw data were post-processed for noise reduction using CMA (Fig. S7). The results showed that the following method is equally applicable in a city like Munich as in our study site in Augsburg, which are two cities that differ in location and environmental characteristics (e.g., population, economy, traffic density, etc.). After treated using CMA, the peak samples can be identified in different interval times (Fig. S8), and the estimated background concentrations showed few negative values (Fig. S9). Further research into the transferability of our results to a more diverse set of contexts is still needed.

3.5 Practical implications

The MA200 is widely used to measure human exposure to black carbon and for mobile air quality monitoring. In this study the MA200 devices were applied in mobile measurements in an urban area (Augsburg), and the sensitivity of the final analysis to various data post-processing methods was investigated. In contrast to our findings, Hagler et al. (2011) suggested the use of the ONA algorithm to post-process Aethalometer data from microAeth AE51, portable AE42, and rack-mounted AE21 Aethalometer instruments (Magee Scientific, Berkeley, CA, USA). In their analysis, ONA demonstrated a strong noise reduction in all datasets and retained spatio-temporal variation. ONA also reduced the occurrence of negative data values in low concentration sampling environments. However, for the microAeth® series of black carbon monitoring instruments, our study showed that ONA under reasonable ΔATN thresholding may lead to a considerable dampening of spatio-temporal resolution in local black carbon signals at street level – an effect that is lower under CMA post-processing.

In addition, our analysis highlights that the selection of an appropriate data post-processing method is crucial to the proper assessment and interpretation of exposure-relevant microenvironmental contributors to pollution concentrations in urban areas. This analysis is important when estimating exposures that occur during transit, where spatio-temporal

Appendix

variability in pollution concentrations is vast, like in commuter traffic (Snyder et al., 2013). Due to the typically low-but-heterogeneous nature of eBC concentrations in many areas like Augsburg, noisy measurement with the MA200 under high-frequency sampling may obscure actual trends in measured values. This study demonstrated that post-processing MA200 data using CMA can reliably extract the actual signals from such noise and, alternatively, that post-processing via ONA and LPR could be less reliable. Future researchers and agencies may find a distillation of our results in the form of the flow diagram in Scheme 1 useful in determining how to reliably assess spatio-temporal variability of MA200 measurements for black carbon in different microenvironments.

4 Conclusion

A mobile monitoring campaign was conducted in the city centre of Augsburg, Germany, to determine a suitable noise reduction algorithm for the MA200 Aethalometer. Our results showed that, at the interval times of 5, 10, and 30 s, CMA post-processing effectively removed spurious negative concentrations without major bias and reliably highlighted effects from local sources, effectively increasing spatio-temporal resolution in mobile measurements. Evaluation of the effects of each method on peak sample reduction and the estimation of background concentrations further support the reliability of CMA. Further analysis is needed to understand how well these findings apply in different seasons; across different diurnal patterns; and in more rural, more urban, and non-German locations.

Data availability. The data are available upon request by contacting the first author of the paper (xiansheng.liu@helmholtz-muenchen.de).

Supplement. The supplement related to this article is available online at: https://doi.org/10.5194/amt-14-5139-2021-supplement.

Author contributions. XL was responsible for data curation, methodology and software analysis, and writing original draft. HH was responsible for methodology, software analysis, and writing original draft. XZ was responsible for funding acquisition and project administration. LDH was responsible for discussion and review and editing. JSK was responsible for investigation and supervision. JB and GJ were responsible for methodology. AHAW and BSH were responsible for writing, review and editing. RZ was responsible for investigation.

Competing interests. L. Drew Hill is an employee of AethLabs (San Francisco, CA, USA) and Andrew H. A. White was, at the time of contribution, an intern at AethLabs. These affiliations did not affect the conclusions of the paper.

Disclaimer. Publisher's note: Copernicus Publications remains neutral with regard to jurisdictional claims in published maps and institutional affiliations.

Acknowledgements. We gratefully thank Erik Hopp (AethLabs, San Francisco, CA, USA) for the implementation and maintenance of the AethLabs data processing web tool.

Financial support. The work is funded by the National Key Research and Development Program of China (grant no. 2020YFB1806500), Support Project of High-level Teachers in Beijing Municipal Universities in the Period of 13th Five-year Plan (grant no. CIT&TCD201904037), the National Natural Science Foundation of China (grant no. 81800854), and the Germany Federal Ministry of Transport and Digital Infrastructure (BMVI) as part of SmartAQnet (grant no. 19F2003B).

Review statement. This paper was edited by Alfred Wiedensohler and reviewed by two anonymous referees.

References

AethLabs: MicroAeth® MA Series MA200, MA300, MA350 Operating Manual, available at: https://aethlabs.com/sites/all/content/microaeth/maX/MA200MA300MA350OperatingManualRev03Dec2018.pdf (last access: 5 April 2021), 2018.

Anenberg, S. C., Schwartz, J., Shindell, D., Amann, M., Faluvegi, G., Klimont, Z., Janssens-Maenhout, G., Pozzoli, L., Dingenen., R. V., Vignati, E., Emberson, L., Muller, N. Z., West, J. J., Williams, M., Demkine, M., Demkine, V., Hicks, W. K., Kuylenstierna, J., Raes, F., and Ramanathan, V.: Global air quality and health co-benefits of mitigating near-term climate change through methane and black carbon emission controls, Environ. Health Persp., 120, 831–839, https://doi.org/10.1289/ehp.1104301, 2012.

Apte, J. S., Kirchstetter, T. W., Reich, A. H., Deshpande, S. J., Kaushik, G. C. A., Marshall, J, D., and Nazaroff, W. W.: Concentrations of fine, ultrafine, and black carbon particles in auto-rickshaws in New Delhi, India, Atmos. Environ., 45, 4470–4480, https://doi.org/10.1016/j.atmosenv.2011.05.028, 2011.

Apte, J. S., Messier, K. P., Gani, S., Brauer, M., Kirchstetter, T. W., Lunden, M. M., Maeshall, J. D., Portier, C. J., Vermeulen, R. C. H., and Hameurg, S. P.: High-Resolution Air Pollution Mapping with Google Street View Cars. Exploiting Big Data, Environ. Sci. Technol., 12, 6999–7008, https://doi.org/10.1021/acs.est.7b00891, 2017.

Brantley, H. L., Hagler, G. S. W., Kimbrough, E. S., Williams, R. W., Mukerjee, S., and Neas, L. M.: Mobile air monitoring data-processing strategies and effects on spatial air pollution trends,

Appendix

Atmos. Meas. Tech., 7, 2169–2183, https://doi.org/10.5194/amt-7-2169-2014, 2014.

Breidt, F. J. and Opsomer. J. D.: Local polynomial regression estimators in survey sampling, Ann. Stat., 28, 1026–1053, available at: https://www.jstor.org/stable/2673953 (last access: 22 November 2020), 2000.

Buonanno, G., Fuoco, F. C., and Stabile, L.: Influential parameters on particle exposure of pedestrians in urban microenvironments, Atmos. Environ., 7, 1434–1443, https://doi.org/10.1016/j.atmosenv.2010.12.015, 2011.

Cai, J., Yan, B., Kinney, P. L., Perzanowski, M. S., Jung, K. H., Li, T., Xiu, G., Zhang, D., Olivo, C., Ross, J., Miller, R. L., and Chillrud, S. N.: Optimization approaches to ameliorate humidity and vibration related issues using the microAeth black carbon monitor for personal exposure measurement, Aerosol Sci. Tech., 47, 1196–1204, https://doi.org/10.1080/02786826.2013.829551, 2013.

Cao, R., Li, B., Wang, H. W., Tao, S., Peng, Z. R., and He, H. D.: Vertical and Horizontal Profiles of Particulate Matter and Black Carbon Near Elevated Highways Based on Unmanned Aerial Vehicle Monitoring, Sustainability, 12, 1204, https://doi.org/10.3390/su12031204, 2020.

Cheng, Y. H. and Lin, M. H.: Real-time performance of the microAeth® AE51 and the effects of aerosol loading on its measurement results at a traffic site. Aerosol Air Qual. Res., 13, 1853–1863, https://doi.org/10.4209/aaqr.2012.12.0371, 2013.

Choi, W., He, M., Barbesant, V., Kozawa, K. H., Mara, S., Winer, A. M., and Paulosn, S. E.: Prevalence of wide area impacts downwind of freeways under pre-sunrise stable atmospheric conditions, Atmos. Environ., 62, 318–327, https://doi.org/10.1016/j.atmosenv.2012.07.084, 2012.

Cyrys, J., Pitz, M., Soentgen, J., Zimmermann, R., Wichmann, H. E., and Peters, A.: New Measurement Site for Physical and Chemical Particle Characterization in Augsburg. Germany, Epidemiology (Cambridge, Mass.), 17, S250–S251, 2006.

Dons, E., Int Panis, L., Van Poppel, M., Theunis, J., and Wets, G.: Personal exposure to Black Carbon in transport microenvironments, Atmos. Environ., 55, 392–398, https://doi.org/10.1016/j.atmosenv.2012.03.020, 2012.

Drewnick, F., Böttger, T., von der Weiden-Reinmüller, S.-L., Zorn, S. R., Klimach, T., Schneider, J., and Borrmann, S.: Design of a mobile aerosol research laboratory and data processing tools for effective stationary and mobile field measurements, Atmos. Meas. Tech., 5, 1443–1457, https://doi.org/10.5194/amt-5-1443-2012, 2012.

Easton, V. J. and McColl, J. H.: Statistics Glossary v1.1, available at: http://www.stats.gla.ac.uk/steps/glossary/index.html, (last access: 22 November 2020), 1997.

Goldberg, E. D.: Black carbon in the environment: properties and distribution, J. Wiley, available at: https://agris.fao.org/agris-search/search.do?recordID=US880866588 (last access: 22 November 2020), ISBN 04-718-19794, 1985.

Gu, J.: Characterizations and sources of ambient particles in Augsburg. Germany, available at: https://opus.bibliothek.uni-augsburg.de/opus4/2103, (last access: 22 November 2020), 2012.

Hagler, G. S., Yelverton, T. L., Vedantham, R., Hansen, A. D., and Turner, J. R.: Post-processing Method to Reduce Noise while Preserving High Time Resolution in Aethalometer Real-time Black Carbon Data, Aerosol Air Qual. Res., 11, 539–546, https://doi.org/10.4209/aaqr.2011.05.0055, 2011.

Hagler, G. S. W., Lin, M., Khlystov, A., Baldauf, R. W., Isakov, V., Faircloth, J., and Jackson, L. E.: Field investigation of roadside vegetative and structural barrier impact on near-road ultrafine particle concentrations under a variety of wind conditions, Sci. Total Environ., 416, 7–15, https://doi.org/10.1016/j.scitotenv.2011.12.002, 2012.

Janssen, N. A., Hoek, G., Simic-Lawson, M., Fischer, P., Van Bree, L., Ten Brink, H., Keuken, M., Atkinson, R. W., Anderson, H. R., Brunekreef, B., and Cassee, F. R.: Black carbon as an additional indicator of the adverse health effects of airborne particles compared with PM_{10} and $PM_{2.5}$, Environ. Health Persp., 119, 1691–1699, https://doi.org/10.1289/ehp.1003369, 2011.

Kai, B., Li, R., and Zou, H.: Local composite quantile regression smoothing: an efficient and safe alternative to local polynomial regression, J. Roy. Stat. Soc. B, 72, 49–69, https://doi.org/10.1111/j.1467-9868.2009.00725.x, 2010.

Kerckhoffs, J., Hoek, G., Messier, K. P., Brunekreef, B., Meliefste, K., Klompmaker, J. O., and Vermeulen, R.: Comparison of ultrafine particle and black carbon concentration predictions from a mobile and short-term stationary land-use regression model, Environ. Sci. Technol., 50, 12894–12902, https://doi.org/10.1021/acs.est.6b03476, 2016.

Kutzner, R. D., von Schneidemesser, E., Kuik, F., Queddenau, J., Weatherhead, E. C., and Schamle, J.: Long-term monitoring of black carbon across Germany, Atmos. Environ., 185, 41–52, https://doi.org/10.1016/j.atmosenv.2018.04.039, 2018.

Liu, M., Peng, X., Meng, Z., Zhou, T., Long, L., and She, Q.: Spatial characteristics and determinants of in-traffic black carbon in Shanghai, China: Combination of mobile monitoring and land use regression model, Sci. Total Environ., 658, 51–61, https://doi.org/10.1016/j.scitotenv.2018.12.135, 2019.

Liu, X., Schnelle-Kreis, J., Zhang, X., Bendl, J., Khedr, M., Jakobi, G., Schloter-Hai, B., Hovorka, J., and Zimmermann, R.: Integration of air pollution data collected by mobile measurement to derive a preliminary spatiotemporal air pollution profile from two neighboring German-Czech border villages, Sci. Total Environ., 722, 137632, https://doi.org/10.1016/j.scitotenv.2020.137632, 2020.

Liu, X., Zhang, X., Schnelle-Kreis, J., Jakobi, G., Cao, X., Cyrys, J., Yang, L., Schloter-Hai, B., Abbaszade, G., Orasche, J., Khedr, M., Kowalski, M., Hank., M., and Ralf Zimmermann, R.: Spatiotemporal Characteristics and Driving Factors of Black Carbon in Augsburg, Germany: Combination of Mobile Monitoring and Street View Images, Environ. Sci. Technol., 55, 160–168, https://doi.org/10.1021/acs.est.0c04776, 2021.

Masry, E.: Multivariate local polynomial regression for time series: uniform strong consistency and rates, J. Time Ser. Anal., 17, 571–599, https://doi.org/10.1111/j.1467-9892.1996.tb00294.x, 1996.

Nichols, J. L., Owens, E. O., Dutton, S. J., and Luben, T. J.: Systematic review of the effects of black carbon on cardiovascular disease among individuals with pre-existing disease, Int. J. Public Health, 58, 707–724, https://doi.org/10.1007/s00038-013-0492-z, 2013.

Sadiq, M., Tao, W., Tao, S., and Liu, J.: Air quality and climate responses to anthropogenic black carbon emission changes from

Appendix

East Asia, North America and Europe, Atmos. Environ., 120, 262–276, https://doi.org/10.1016/j.atmosenv.2015.07.001, 2015.

Snyder, E. G., Watkins, T. H., Solomon, P. A., Thoma, E. D., Williams, R. W., Hagler, G. S., Shelow, D., Hindin, D. A., Kilaru, V. J., and Preuss, P. W.: The changing paradigm of air pollution monitoring, Environ. Sci. Technol., 47, 11369–11377, https://doi.org/10.1021/es4022602, 2013.

Van den Bossche, J., Peters, J., Verwaeren, J., Botteldooren, D., Theunis, J., and De Baets, B.: Mobile monitoring for mapping spatial variation in urban air quality: Development and validation of a methodology based on an extensive dataset, Atmos. Environ., 105, 148–161, https://doi.org/10.1016/j.atmosenv.2015.01.017, 2015.

Virkkula, A., Mäkelä, T., Hillamo, R., Yli-Tuomi, T., Hirsikko, A., Hämeri, K., and Koponen, I. K.: A simple procedure for correcting loading effects of aethalometer data, J. Air. Waste Manage., 57, 1214–1222, https://doi.org/10.3155/1047-3289.57.10.1214, 2007.

Wang, Z., Lu, F., He, H., Lu, Q., Wang, D., and Peng, Z.: Fine-scale estimation of carbon monoxide and fine particulate matter concentrations in proximity to a road intersection by using wavelet neural network with genetic algorithm, Atmos. Environ., 104, 264–272, https://doi.org/10.1016/j.atmosenv.2014.12.058, 2015.

Zhou, H., Lin, J., Shen, Y., Deng, F., Gao, Y., Liu, Y., Dong, H., Zhang, Y., Sun, Q., Fang, J., Tang, S., Wang, Y., Du, Y., Cui, L., Ruan, S., Kong, F., Liu, Z., and Li, T.: Personal black carbon exposure and its determinants among elderly adults in urban China, Environ. Int., 138, 105607, https://doi.org/10.1016/j.envint.2020.105607, 2020.

Publication VI

Liu, X., Hadiatullah, H., Zhang, X., Schnelle-Kreis, J., ... & Zimmermann, R. (2021). Combined land-use and street view image model for estimating black carbon concentrations in urban areas. ***Atmospheric Environment,*** 118719.

Appendix

Atmospheric Environment 265 (2021) 118719

Contents lists available at ScienceDirect

Atmospheric Environment

journal homepage: www.elsevier.com/locate/atmosenv

Combined land-use and street view image model for estimating black carbon concentrations in urban areas

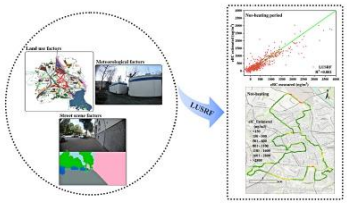
Xiansheng Liu [a,b,c], Hadiatullah Hadiatullah [d,e], Xun Zhang [a,*], Jürgen Schnelle-Kreis [b,**], Xiaohu Zhang [f], Xiuxiu Lin [g], Xin Cao [b,c], Ralf Zimmermann [b,c]

[a] Beijing Key Laboratory of Big Data Technology for Food Safety, School of Computer Science and Engineering, Beijing Technology and Business University, Beijing, 100048, China
[b] Joint Mass Spectrometry Center, Cooperation Group Comprehensive Molecular Analytics, Helmholtz Zentrum München, German Research Center for Environmental Health, Ingolstädter Landstr. 1, Neuherberg, 85764, Germany
[c] Joint Mass Spectrometry Center, Chair of Analytical Chemistry, University of Rostock, Rostock, 18059, Germany
[d] School of Pharmaceutical Science and Technology, Tianjin University, Tianjin, 300072, China
[e] Biology Department, Faculty of Mathematics and Natural Sciences, Brawijaya University, 65145, Indonesia
[f] College of Agriculture, Nanjing Agricultural University, Nanjing, 210095, China
[g] School of Mathematical Sciences, South China Normal University, Guangzhou, 510631, China

HIGHLIGHTS

- Land use street view images random forest (LUSRF) model were developed.
- LUSRF model were exploited for black carbon (BC) estimation.
- LUSRF have superiority compared to other models with average-R^2: 0.73.
- LUSRF model reduced average 10–15% estimation error.
- LUSRF model was verified for different periods and areas.

GRAPHICAL ABSTRACT



ARTICLE INFO

Keywords:
Black carbon
Land-use
Street view images
Random forest

ABSTRACT

In this study, we developed a novel land-use street view image random forest (LUSRF) model to estimate the equivalent black carbon (eBC) concentration based on land-use random forest (LURF) and street view imagery (SVI) models and compared their accuracy and precision in the urban city of Augsburg, Germany. The variables of the LUSRF model were constructed by combining LURF and SVI model variables (i.e., land-use, street scene, and meteorological factors). Stratified cross-validation (CV) was used to validate the model performance. Based on R^2 and IA (Index of Agreement), LUSRF has superiority (average-R^2: 0.73, average-IA: 0.91) compared to the LURF (average-R^2: 0.52, average-IA: 0.81) and SVI model (average-R^2: 0.68, average-IA: 0.89) in the urban city of Augsburg during the observed period. The main driving factors of the LUSRF model for BC estimation were different in heating and non-heating periods (i.e., elevation, the proportion of moving cars, and relative humidity for the non-heating period; and elevation, the proportion of building, and relative humidity for the heating

* Corresponding author. Beijing Key Laboratory of Big Data Technology for Food Safety, School of Computer Science and Engineering, Beijing Technology and Business University, Beijing, 100048, China.
** Corresponding author.
E-mail addresses: zhangxun@btbu.edu.cn (X. Zhang), juergen.schnelle@helmholtz-muenchen.de (J. Schnelle-Kreis).

https://doi.org/10.1016/j.atmosenv.2021.118719
Received 18 June 2021; Received in revised form 27 August 2021; Accepted 9 September 2021
Available online 12 September 2021
1352-2310/© 2021 Elsevier Ltd. All rights reserved.

Appendix

period), which improves the estimation accuracy of eBC concentration and its sources. The model verification in other areas (i.e., suburban and small towns) further proved that the model has certain generalizability. Overall, the LUSRF model will provide insight for epidemiological studies in urban areas as a personal exposure assessment.

1. Introduction

Atmospheric particulate matter (PM) is one of the major contributors to air pollution (Wang et al., 2018). Black carbon (BC), a component of ambient PM, is a product of various combustion processes (Gu et al., 2020) that has different toxicity against sensitive organs in the human body (e.g., lungs) (Jiang et al., 2018). Based on International Agency for Research on Cancer (IARC), diesel exhaust particles (DEP) composed of BC are classified as 2B carcinogens and harm the environment and human health (IARC, 2012). Therefore, studies to measure or model ambient BC and their spatio-temporal variability are urgently necessary. In our study, the equivalent black carbon, eBC, was used when quantitative values were derived from the optical measurement (Liu et al., 2021a,b).

In general, the exposure studies have revealed that the proximity of the pollutant sources significantly affects the exposure concentration (e.g., different types of transportation) (Morales Betancourt et al., 2017; Targino et al., 2020). Vette et al. (2013) used an integrated measurement and modeling approach to estimate the contribution of traffic sources to roadside air pollution and their impact on children's exposure. Ham et al. (2017) found that the train trips have the highest average air pollution levels, while light rail trips have the lowest levels, and that bicyclists can reduce commuting exposures by 15–75%. Although the mode of transport, traffic volume, and meteorological variables have been commonly identified as driving factors of eBC concentrations (Morales Betancourt et al., 2017; Krecl et al., 2020; Şahin et al., 2020), the exposure of eBC concentration in aerosol studies remained partially explained.

So far, several models were previously used for ambient BC estimation, including remote sensing inversion (Bao et al., 2019), atmospheric dispersion models (e.g. Chen et al., 2020), land-use regression (LUR) (Van Den Hove et al., 2020), land-use random forest (LURF) (Wu et al., 2021), Google Street View (GSV) imagery (Qi and Hankey, 2021), hybrid dispersion-LUR models (Tripathy et al., 2019), and feature extraction based model from the imagery of the built environment (Ganji et al., 2020). However, those models remained some limitations, for example, the LURF model requires satellite data with a higher spatio-temporal resolution to improve the estimation accuracy of the model (Araki et al., 2018; Yang et al., 2018). In principle, the land-use model can be improved by the integration of GSV data. However, GSV data are usually temporally invariant and cannot fully capture the current situation at the street level (Qi and Hankey, 2021). In that limitation, we developed the street view images (SVI) based model to estimate urban eBC concentration in our previous study (Liu et al., 2021a,b), which can compensate for the deficiency of higher spatio-temporal resolution. However, albeit our SVI model has shown the superiority of the street level in estimating eBC concentration, it explains only 68% of the variability in eBC concentration. Therefore, due to the high spatio-temporal variability of pollutant concentrations at the local scale (Krecl et al., 2019, 2020), land-use random forest (LURF) and SVI models can be incorporated into future air pollution estimation models, which can provide a more accurate estimation for eBC concentration (Liu et al., 2021a,b; Araki et al., 2018), reducing both previous model limitations.

Combining the above reasons, in this study, we developed a combined land-use street view images random forest (LUSRF) model and compared its accuracy and precision to LURF and SVI models for estimating the eBC concentrations in the urban city of Augsburg, Germany. Finally, the model was verified in different areas (suburban and small-town) to evaluate its generalizability.

2. Material and methods

2.1. Sampling layout and instrument settings

Three different study areas were selected for this study, located in the urban city of Augsburg, in the suburbs of Munich, Germany, and in the two neighbouring small towns of Bayerisch Eisenstein (BE, Germany) and Zelezna Ruda (ZR, Czechia) at the German-Czech border. The main study area was located in the urban city of Augsburg, and the other sites were only used to verify the generalizability of the model, in which the data were collected during the heating period (Fig. 1). Mobile platforms were built on trolleys and equipped with measurement devices, including micro-aethalometer (MA200, AethLabs, USA) to measure eBC concentrations with a time resolution of 10 s, GPS (GPSMAP 64 s, Garmin, USA) to register the measurement location with 1 s resolution, and a POV camera (TG-Tracker, Olympus, Japan) to record street view images with 5 s resolution.

The walks were repeatedly performed by mobile measurement platforms along fixed routes in the sampling areas. During BC sampling, meteorological indicators (temperature, wind speed, and relative humidity) were simultaneously monitored at fixed monitoring stations (Liu et al., 2021a,b). In the urban area of Augsburg, the route was covered over 14 km from the Augsburg University of Applied Sciences with an average walking time of about 4 h. In the suburbs of Munich, the route was covered over 6 km with an average walking time of 1 h. In the two small towns, the routes in BE and ZR have covered over 5 km and 4 km, respectively. The average walking time was about 1 h in both locations. Different types of land-use were traversed in all the fixed routes to ensure that the selected routes represented the entire area through different microenvironments.

2.2. Spatio-temporal smoothing of mobile measurement data

The eBC concentrations in urban areas were highly spatio-temporally variable (Krecl et al., 2019; Targino et al., 2021). Therefore, we investigated the quality of the model for different averaging times (or walked distances). In general, the sampling speed was about 1.5 m/s (i.e., 90 m corresponding to 60 s). Then, we performed 10, 20, 30, 40, 50, and 60 s as the different averaging times for the time series concentration measurement to observe the model performance. Following that, we developed corresponding estimation models for BC using land-use variables combining with SVI variables, and performed the simulation effects of BC estimation.

2.3. Air pollution estimation models

2.3.1. Land-use random forest (LURF) model

The LURF model was adopted as described in the previous study by Brokamp et al. (2017). Briefly, the model estimates the air pollutants using a land-use model applying random forest. In this study, the variables of the LURF model were obtained from OpenStreetMap Data Extracts (https://download.geofabrik.de/), except for elevation, which was recorded by the GPS (Table 1 and S1). All the variables were analyzed at the different buffer sizes (25 m, 50 m, 100 m, 200 m, 500 m, 1000 m, and 2000 m) at the various sampling sites (Fig. S1).

Appendix

2.3.2. Street view images (SVI) model

The SVI model was adopted as described in our previous study, including the corresponding data (Liu et al., 2021a,b). The model quantifies the composition of the surface types perceived by pedestrians on the street and creates a unique description of the urban types and composition. In this model, the images segmented by deep learning (the deep high-resolution network, HRnet) and meteorological variables (Table 1 and S1) were used to estimate the eBC concentration. Briefly, the images are segmented into five street scenes, i.e., buildings, roads, vegetation, moving cars, and the sky, to obtain the proportions area of different variables of the scene in the observed image. All variables are aligned with the timing of air pollutant monitoring (clock synchronization). In this approach, the HRnet is chosen as the main model structure for semantic segmentation (Wang et al., 2020).

2.3.3. Land-use street view images random forest (LUSRF) model

LURF models are usually time-invariant and cannot fully capture street-level pollution. In this regard, the SVI model can compensate for the temporal deficiency to some extent. Therefore, this study attempted to combine the variables of both models (LURF and SVI) with building a new model of LUSRF, integrating the advantages of both models, i.e., high spatio-temporal variability. As a result, to estimate the eBC concentration, the LUSRF model was built based on the implementation of the LURF model (Brokamp et al., 2017) and the SVI model (Liu et al., 2021a,b) (Table S1). All the variables were also analyzed at the different buffer sizes (25 m, 50 m, 100 m, 200 m, 500 m, 1000 m, and 2000 m) at the various sampling sites (Fig. S1).

Table 1
The variables built for the LURF, SVI and LUSRF model.

Model		Factors	Variables	Data source
LUSRF	LURF	Land-use	Construction, cemetery, commercial, farm, forest, grass, health, industrial, meadow, natural, park, points of interest (POIs), recreation, residential, retail, scrub, traffic, transport, water, roads, railway, waterways, and elevation	OpenStreetMap Data Extracts (https://download.geofabrik.de/)
	SVI	Street scene	The proportion of buildings, roads, vegetation, moving cars, and sky	Camera
		Meteorological variables	Temperature, relative humidity, and wind speed	Fixed monitoring station

2.4. LUSRF model validation

The accuracy of the model can reflect the fitting effect and the estimation error of the model. The measured eBC concentrations in different microenvironments exhibited substantial spatial heterogeneity.

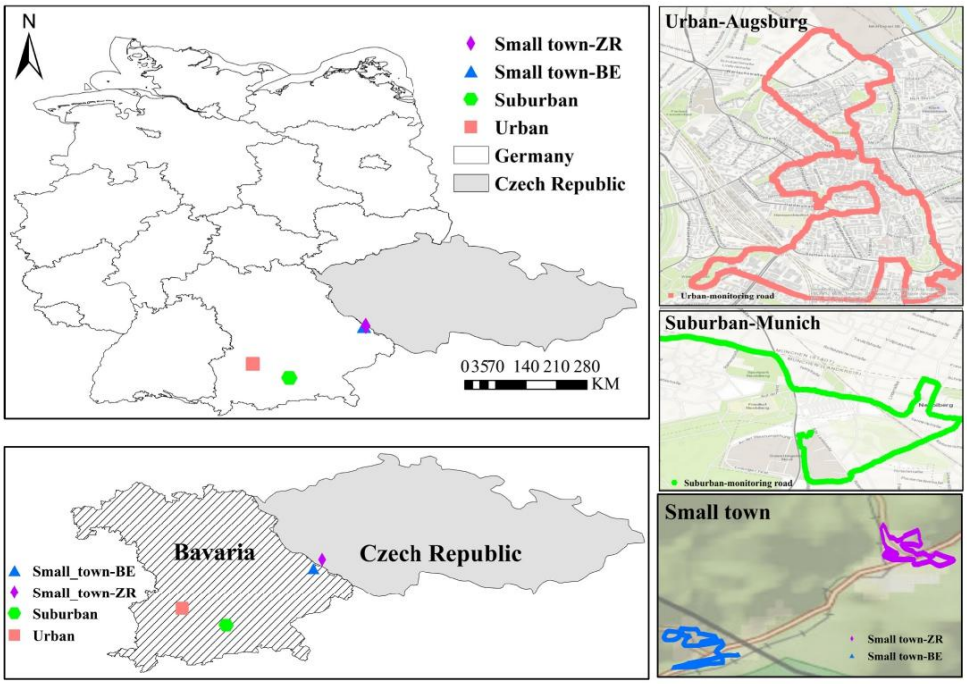


Fig. 1. Locations of sampling sites. © OpenStreetMap contributors 2021. Distributed under a Creative Commons BY-SA License.

Appendix

Therefore, we used the stratified five-folds cross-validation (CV) method in this study, which has a better interpretation than the general cross-validation (Van Den Hove et al., 2020). The stratified five-folds CV method was used to estimate the accuracy of the model. By assessing the proximity between the simulation result of the verification set and the actual measured concentration, the simulation validity of the model is reflected. The evaluation indicators used in this study include the correlation coefficient (R) to represent the model, the root mean squared error (RMSE) and the mean absolute error (MAE) to represent the deviation between the estimated value and the actual value, and the fitting index (Index of Agreement, IA) to represent the consistency between the estimated value and the actual value. Similarly, the verification of stratified five-folds CV was also used to evaluate and validate the generalizability of the model in other areas.

2.5. Data analysis

Pollutant concentrations were statistically analyzed using a non-parametric Kruskal-Wallis test at a critical value (α) of 0.05 (one-way ANOVA) (Kruskal and Wallis, 1952). The random forest was selected for the models to estimate the eBC concentrations (LURF and LUSRF). The default setting from the package scikit-learn (version 3.7, Scikit-learn Version 0.21, http://scikit-learn.org/) was used. In this study, a Bivariate correlation analysis was used to extract the target factors required for modeling, and the eBC concentrations in the training set and the corresponding target factors were used as data for the random forest regression method.

3. Results and discussion

3.1. Overview of black carbon measurements

The eBC concentrations were measured along the fixed-route. The sampling periods were divided into the non-heating (May–Oct.) and heating (Nov.–Apr.) periods (Fig. S2). Due to the limited usability of street view imagery during the darkness, we focused on BC measurement during the daylight. Based on one-way ANOVA analysis, the temporal variability of the eBC concentration revealed significant differences between the non-heating and heating periods. The average daytime eBC concentrations in Augsburg during the heating period was 1.56 μg/m^3, which was significantly higher than in the non-heating period (0.93 μg/m^3). These results suggested that the increase in eBC concentration during the heating period may be influenced by the emissions from residential heating, traffic emissions, and seasonal differences in meteorological conditions. Under different meteorological conditions, the eBC concentration at the ground level from the same source can vary by tens or even hundreds of times, for example, a central role for dilution or accumulation of locally emitted air pollutants is influenced by the dispersion conditions (Cichowicz et al., 2017; Jung et al., 2010). Therefore, we separated the period, including non-heating and heating periods, to better estimate eBC concentrations and evaluated the versatility of the model.

3.2. Temporal smoothing of the LURF model

Due to the high spatio-temporal variability of urban air quality (Van Den Bossche et al., 2015; Liu et al., 2019), spatial and temporal scales can affect the accuracy of the spatio-temporal variability of air pollutants as determined in mobile measurements. Therefore, to investigate the effects of temporal smoothing on model performance, we have varied the averaging time of the mobile measurement data. The results showed that when the average time was increased (10 s–60 s) (Fig. 2 and S3), the adjusted R^2 of the corresponding LURF model gradually decreased, which was inconsistent with the previous study (Hankey and Marshall, 2015). They found that the adjusted R^2 of the model remained almost unchanged with the longer time averages (notably, the absolute error was unchanged). Following that, the adjusted R^2 of the LURF model was analyzed using one-way ANOVA analysis, showing a significant difference ($p < 0.05$, Table S2) between the different time and space scales. This result indicated that the random forest method was more suitable to represent the spatial variability of air pollutants than the regression analysis, because relations between land-use factors and air pollution were primarily non-linear. Overall, our results showed the superiority of the random forest model in capturing complex and non-linear relationships between variables and the eBC concentration, and 10 s resolution showed the best interval time for estimating the eBC concentration at different buffer sizes.

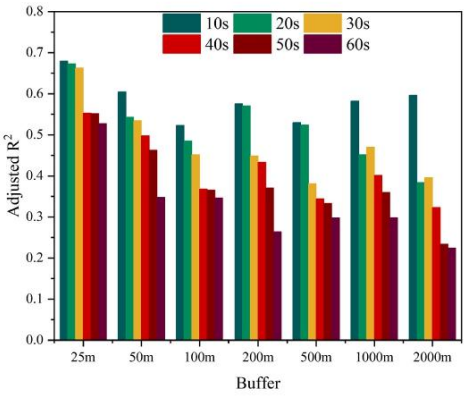


Fig. 2. LURF model performance at different smoothing time (10 s, 20 s, 30 s, 40 s, 50 s, and 60 s) at different buffer sizes (25 m, 50 m, 100 m, 200 m, 500 m, 1000 m, and 2000 m).

3.3. LUSRF model and its validation

3.3.1. LUSRF model

The combination of LURF and SVI variables may provide a more accurate model to estimate the eBC concentration. In this regard, we developed the LUSRF model combining the input variables listed in Table 1. In this model, we applied 10 s resolution to build the model at different buffer sizes (25 m, 50 m, 100 m, 200 m, 500 m, 1000 m, and 2000 m).

To determine the main driving factors of the model, the weight of each factor was analyzed for the three models. For the SVI model, we found that the temperature, relative humidity, and the proportion of moving cars were the main driving factors during the non-heating period. While the temperature, relative humidity, and the proportion of buildings were the main driving factors during the heating period (Table S3). For the LURF model, the elevation, road, and industrial were the main driving factors during the non-heating period. While the elevation, construction, and residential were the main driving factors during the heating period (Table S4). In addition, among the LUSRF variables, elevation (among all land-use variables), the proportion of moving cars (among all street scene variables), and relative humidity (among all meteorological variables) were important driving factors for BC in the non-heating period (Table S5), having the largest weighting in the estimated models. Next, the elevation (among all land-use variables), the proportion of buildings (among all street scene variables), and relative humidity (among all meteorological variables) were important driving factors for BC in the heating period (Table S5). This finding was partially consistent with previous study (Zalakeviciute et al., 2018; Zhang et al., 2016), which indicated that elevation and relative

humidity likely influence air pollution through various influencing mechanisms. Therefore, the result further proved that the LUSRF was a combination of LURF and SVI in the "selection" of the important variables and facilitated the estimation of eBC concentration and its source.

3.3.2. Stratified five-folds CV method

To verify the validity of the LUSRF model, we used stratified CV to compare the performance of the SVI, LURF, and LUSRF models for mobile monitoring in the non-heating and heating periods. The mobile monitoring data were divided into five-folds for BC estimation, and each fold was used to create a model to estimate the eBC concentrations. The average IA, R^2, RMSE, and MAE for the different models in different periods were presented in Table S6, and the different buffer estimations for the LURF and LUSRF models were plotted against the observed concentrations in Fig. 3. Based on R^2 and IA, LUSRF has superiority (average-R^2: 0.76, average-IA: 0.92) as an effective tool for estimation compared to the LURF (average-R^2: 0.61, average-IA: 0.81) and SVI model (average-R^2: 0.68, average-IA: 0.89) (Liu et al., 2021a,b) in the

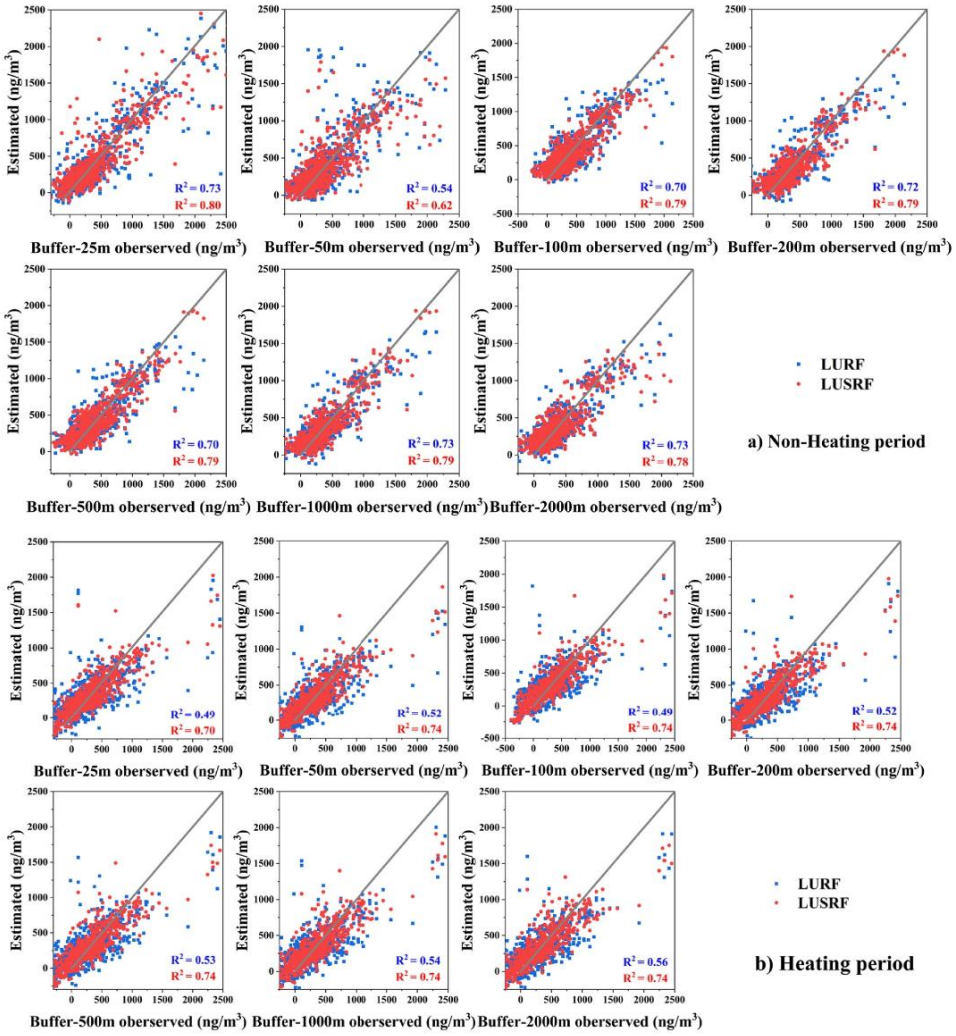


Fig. 3. Stratified cross-validation estimations from the LUSRF and LURF models according to the observed values in the non-heating (a) and heating (b) periods. The 1:1 line represents the perfect agreement between observed and estimated concentration.

Appendix

urban city of Augsburg during the non-heating and heating periods (Table S6), further demonstrating the versatility of the model in the different periods. The addition of SVI elements and real-time meteorological elements as estimated variables can better reflect the eBC concentrations in microenvironments. Hence, the LUSRF model can accurately estimate eBC concentrations in different periods with different buffer sizes.

In summary, although the LURF model provided an accurate tool to estimate the eBC concentrations, however, the variables of the LURF model were limited, hence, the estimated air pollution concentration cannot fully clarify the direction and magnitude of air pollution sources (Brokamp et al., 2017). In comparison, the LUSRF model added meteorological elements and on-site sampling of SVI elements to provide information about pollution sources. As reported in our previous study, the SVI model variables can provide a better estimation of eBC concentration on possible local sources (i.e. buildings and cars) and also sinks (trees), and these advantages were covered by the LURSF model. In addition, the estimation error of LUSRF was reduced by 10–15% on average compared with the LURF and SVI model for BC, suggesting that the LUSRF model has a better prospect to estimate eBC concentration.

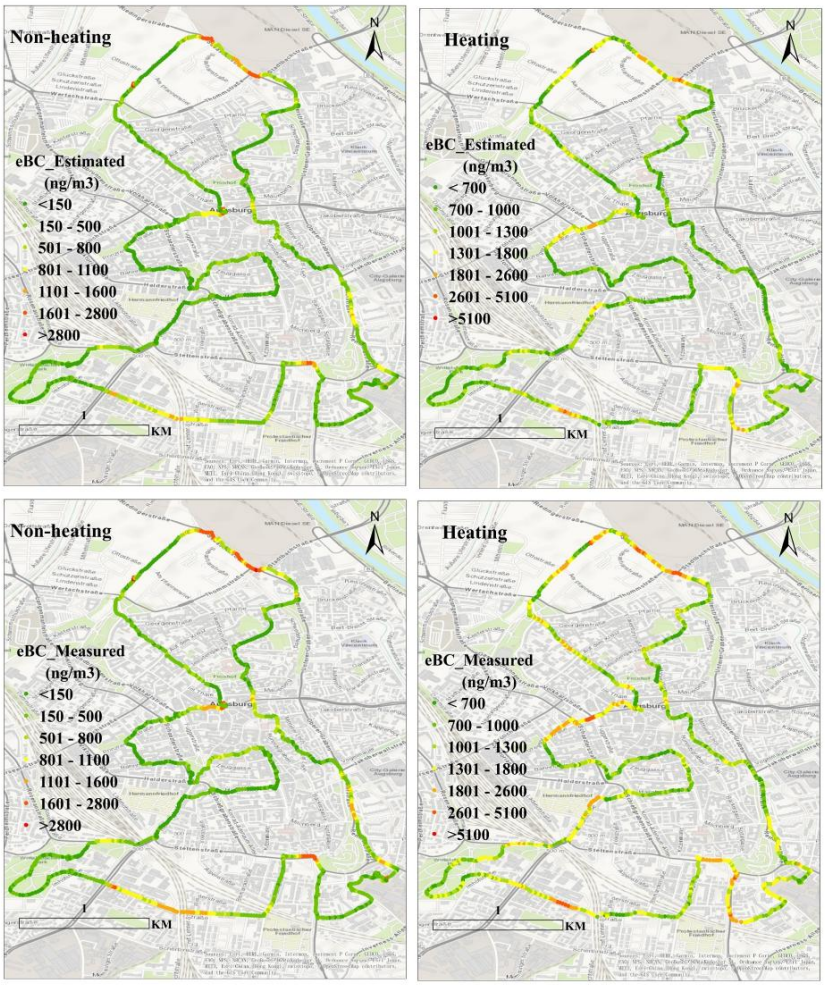


Fig. 4. The estimated (top) and measured (bottom) of eBC concentrations in the non-heating (left) and heating (right) periods based on LUSRF model. © OpenStreetMap contributors 2021. Distributed under a Creative Commons BY-SA License.

Appendix

3.4. LUSRF model visualization

In this study, a model based on land-use and street view image was developed to provide an integrated assesment to estimate the eBC concentrations during the non-heating and heating periods across urban microenvironments. As shown in Fig. 4, comparing the estimated and actual measured of eBC concentrations, the model estimates (LUSRF) are able to capture the hotspots at the appropriate locations and determine between different microenvironmental concentrations. Overall, the change trend of estimated eBC concentrations in different microenvironments is closely similar to the actual measured concentrations in both the non-heating and heating periods, further demonstrating the applicability of the LUSRF model. In brief, the LUSRF model, such a tool for estimating spatio-temporal variation of BC, can complement the fixed-site BC measurements in the health risk assessment and long-term public health improvement.

3.5. LUSRF model generalization

To further verify the generalizability of the LUSRF model, we conducted three additional sampling surveys in the suburb of Munich and two small towns on the German-Czech border. The results showed that the average-R^2 of the LUSRF models were 0.60 for suburb, 0.71 for small-town BE, and 0.58 for small-town ZR at different buffer sizes (Table S7), suggesting the generalizability of the LUSRF model for the estimation of spatio-temporal variation eBC concentrations. Therefore, the LUSRF model can be applied not only in the urban areas, but also in suburban and rural areas.

Comparing the results from the LUSRF models in the two small towns, the models of the Czech town of ZR were less valid than those of the German town of BE (Table S7). In ZR, households heat much more with wood, while wood stoves in Germany are commonly used only for coziness in the evening (Liu et al., 2020). The air pollution in Augsburg is also higher during the heating than the non-heating period. This fact can be attributed to seasonal differences in meteorological conditions, human activities, and emission sources (Gu et al., 2019; He et al., 2017), thus affecting the generalizability of the model to some extent. Taken together, this generalization assessment demonstrated the applicability of the LUSRF model to estimate eBC concentrations in a different type of area and country, reflecting the potential and superiority of the LUSRF model.

The generalizability of the LUSRF models in BC estimation is limited by the characteristics and uncertainties of the input data. The quality of the variables and their representativeness would directly affect the model performance (Van Den Bossche et al., 2018). In our study, the classification of the SVI variables into the five classes was not sufficient to represent all relevant variables at the street-level. Another limitation is monitoring meteorological data at the central site and not along the path, which caused the observed values were not fully represented the respective measurement location along the walking path. For example, the local wind speed and direction at most measurement locations may vary from the centrally measured values. In this regard, a more accurate and more refined classification of street view images and *in situ* meteorological data could reduce the model uncertainty.

4. Conclusions

In the current study, we developed and validated a novel land-use street view images random forest (LUSRF) model to estimate the ambient eBC concentrations combining land-use random forest (LURF) and street view imagery (SVI) approaches. The variables of the LUSRF model were built by combining LURF and SVI model variables (i.e., land-use, street scene, and meteorological factors). Stratified cross-validation was used to validate the model performance. Based on R^2 and IA, LUSRF is superior (average-R^2: 0.73, average-IA: 0.91) to the LURF (average-R^2: 0.52, average-IA: 0.81) and SVI model (average-R^2: 0.68, average-IA: 0.89) in the urban city of Augsburg during the non-heating and heating periods. The main driving factors of the LUSRF model for eBC concentration were different in different periods (i.e., elevation, the proportion of moving cars, and relative humidity in non-heating period; and elevation, the proportion of building, and relative humidity in heating period), which further proved that the LUSRF is a combination of LURF and SVI in the "selection" of the important variables and facilitated the estimation of eBC concentration and its source. In addition, the estimation error of LUSRF is reduced by 10–15% on average compared to the LURF and SVI models for BC estimation in the urban city of Augsburg. Moreover, testing the LUSRF model in other areas (i.e., suburban and small-towns) further proved that the model has generalizability (the average-R^2: 0.60 for suburban, 0.71 for small-town BE, and 0.58 for small-town ZR). In conclusion, the LUSRF model provides another alternative approach to estimate eBC concentration with a high spatio-temporal resolution. And this model may provide new insight into personal exposure assessment for epidemiological studies in different urban areas.

CRediT authorship contribution statement

Xiansheng Liu: Data curation, Methodology, Software, Writing – original draft. **Hadiatullah Hadiatullah:** Methodology, Writing – original draft. **Xun Zhang:** Investigation, Project administration. **Jürgen Schnelle-Kreis:** Data curation, Supervision, Writing – review & editing. **Xiaohu Zhang:** Software. **Xiuxiu Lin:** Software. **Xin Cao:** Writing – review & editing. **Ralf Zimmermann:** Investigation, Supervision.

Declaration of competing interest

The authors declare that they have no known competing financial interests or personal relationships that could have appeared to influence the work reported in this paper.

Acknowledgements

The work is funded by National Natural Science Foundation of China (42101470), the Research Project of the Ministry of Science and Technology of China (2019YFC0507800), the Germany Federal Ministry of Transport and Digital Infrastructure (BMVI) as part of SmartAQnet (19F2003B), the Support Project of High-level Teachers in Beijing Municipal Universities in the Period of 13th Five - year Plan (CIT&TCD201904037), the China Scholarship Council (CSC) under the State Scholarship Fund (201706860028), and Peiyang Future Scholar Scholarship (6120000246).

Appendix A. Supplementary data

Supplementary data to this article can be found online at https://doi.org/10.1016/j.atmosenv.2021.118719.

References

Araki, S., Shima, M., Yamamoto, K., 2018. Spatiotemporal land use random forest model for estimating metropolitan NO2 exposure in Japan. Sci. Total Environ. 634, 1269–1277.

Bao, F., Cheng, T., Li, Y., Gu, X., Guo, H., Wu, Y., Gao, J., 2019. Retrieval of black carbon aerosol surface concentration using satellite remote sensing observations. Remote Sens. Environ. 226, 93–108.

Brokamp, C., Jandarov, R., Rao, M.B., Lemasters, G., Ryan, P., 2017. Exposure assessment models for elemental components of particulate matter in an urban environment: a comparison of regression and random forest approaches. Atmos. Environ. 151, 1–11.

Chen, X., Kang, S., Yang, J., 2020. Investigation of distribution, transportation, and impact factors of atmospheric black carbon in the Arctic region based on a regional climate-chemistry model. Environ. Pollut. 257, 113127.

Cichowicz, R., Wielgosiński, G., Fetter, W., 2017. Dispersion of atmospheric air pollution in summer and winter season. Environ. Monit. Assess. 189 (12), 605.

Appendix

Ganji, A., Minet, L., Weichenthal, S., Hatzopoulou, M., 2020. Predicting traffic-related air pollution using feature extraction from built environment images. Environ. Sci. Technol. 54 (17), 10688–10699.
Gu, Y., Li, Q., Wei, D., Gao, L., Tan, L., Su, G., Wang, Q., 2019. Emission characteristics of 99 NMVOCs in different seasonal days and the relationship with air quality parameters in Beijing, China. Ecotoxicol. Environ. Saf. 169, 797–806.
Gu, Y., Zhang, W., Yang, Y., Wang, C., Streets, D.G., Yim, S.H.L., 2020. Assessing outdoor air quality and public health impact attributable to residential black carbon emissions in rural China. Resour. Conserv. Recycl. 159, 104812.
Ham, W., Vijayan, A., Schulte, N., Herner, J.D., 2017. Commuter exposure to PM2.5, BC, and UFP in six common transport microenvironments in Sacramento, California. Atmos. Environ. 167, 333–345.
Hankey, S., Marshall, J.D., 2015. Land use regression models of on-road particulate air pollution, particle number, black carbon, PM2.5, particle size) using mobile monitoring. Environ. Sci. Technol. 49 (15), 9194–9202.
He, J., Gong, S., Yu, Y., Yu, L., Wu, L., Mao, H., Song, C., Zhao, S., Liu, H., Li, X., Li, R., 2017. Air pollution characteristics and their relation to meteorological conditions during 2014–2015 in major Chinese cities. Environ. Pollut. 223, 484–496.
International Agency for Research on Cancer (Iarc), 2012. Diesel and gasoline engine exhausts and some nitroarenes. IARC (Int. Agency Res. Cancer) Monogr. Eval. Carcinog. Risks Hum. 105. ISBN 978-92-832-1210-2. 2012.
Jiang, S., Shang, M., Mu, K., Jiang, N., Wen, H., Wang, R., Li, W., 2018. In vitro and in vivo toxic effects and inflammatory responses induced by carboxylated black carbon-lead complex exposure. Ecotoxicol. Environ. Saf. 165, 484–494.
Jung, K.H., Patel, M.M., Moors, K., Kinney, P.L., Chillrud, S.N., Whyatt, R., Hoepner, L., Garfinkel, R., Yan, B., Ross, J., 2010. Effects of heating season on residential indoor and outdoor polycyclic aromatic hydrocarbons, black carbon, and particulate matter in an urban birth cohort. Atmos. Environ. 44 (36), 4545–4552.
Krecl, P., Cipoli, Y.A., Targino, A.C., Castro, L.B., Gidhagen, L., Malucelli, F., Wolf, A., 2020. Cyclists' exposure to air pollution under different traffic management strategies. Sci. Total Environ. 723, 138043.
Krecl, P., Cipoli, Y.A., Targino, A.C., Toloto, M.O., Segersson, D., Parra, A., Polezer, G., Godoi, R., Gidhagen, L., 2019. Modelling urban cyclists' exposure to black carbon particles using high spatiotemporal data: a statistical approach. Sci. Total Environ. 679, 115–125.
Kruskal, W.H., Wallis, W.A., 1952. Use of ranks in one-criterion variance analysis. J. Am. Stat. Assoc. 47 (260), 583–621.
Liu, M., Peng, X., Meng, Z., Zhou, T., Long, L., She, Q., 2019. Spatial characteristics and determinants of in-traffic black carbon in Shanghai, China: combination of mobile monitoring and land use regression model. Sci. Total Environ. 658, 51–61.
Liu, X., Hadiatullah, H., Zhang, X., Hill, L.D., White, A.H.A., Schnelle-Kreis, J., Bendl, J., Jakobi, G., Schloter-Hai, B., Zimmermann, R., 2021a. Analysis of mobile monitoring data from the microAeth® MA200 for measuring changes in black carbon on the roadside in Augsburg. Atmos. Meas. Tech. 14, 5139–5151.
Liu, X., Schnelle-Kreis, J., Zhang, X., Bendl, J., Khedr, M., Jakobi, G., Schloter-Hai, B., Hovorka, J., Zimmermann, R., 2020. Integration of air pollution data collected by mobile measurement to derive a preliminary spatiotemporal air pollution profile from two neighboring German-Czech border villages. Sci. Total Environ. 722, 137632-137632.
Liu, X., Zhang, X., Schnelle-Kreis, J., Jakobi, G., Cao, X., Cyrys, J., Yang, L., Schloter-Hai, B., Abbaszade, G., Orasche, J., Khedr, M., Kowalski, M., Hank, M., Zimmermann, R., 2021b. Spatiotemporal characteristics and driving factors of black carbon in Augsburg, Germany: combination of mobile monitoring and street view images. Environ. Sci. Technol. 55 (1), 160–168.
Morales Betancourt, R., Galvis, B., Balachandran, S., Ramos-Bonilla, J.P., Sarmiento, O. L., Gallo-Murcia, S.M., Contreras, Y., 2017. Exposure to fine particulate, black carbon, and particle number concentration in transportation microenvironments. Atmos. Environ. 157, 135–145.
Qi, M., Hankey, S., 2021. Using street view imagery to predict street-level particulate air pollution. Environ. Sci. Technol. 55 (4), 2695–2704.
Sahin, U.A., Onat, B., Akin, O., Ayvaz, C., Uzun, B., Mangır, N., Harrison, R.M., 2020. Temporal variations of atmospheric black carbon and its relation to other pollutants and meteorological factors at an urban traffic site in Istanbul. Atmos. Pollut. Res. 7 (11), 1051–1062.
Targino, A.C., Krecl, P., Brimblecombe, P., Oukawa, G.Y., Danziger Filho, J.E., Moreno, F.L., 2021. Spatio-temporal variability of airborne particulate matter in the São Paulo subway. Build. Environ. 189, 107526.
Targino, A.C., Krecl, P., Cipoli, Y.A., Oukawa, G.Y., Monroy, D.A., 2020. Bus commuter exposure and the impact of switching from diesel to biodiesel for routes of complex urban geometry. Environ. Pollut. 263, 114601.
Tripathy, S., Tunno, B.J., Michanowicz, D.R., Kinnee, E., Shmool, J., Gillooly, S., Clougherty, J.E., 2019. Hybrid land use regression modeling for estimating spatio-temporal exposures to PM2.5, BC, and metal components across a metropolitan area of complex terrain and industrial sources. Sci. Total Environ. 673, 54–63.
Van Den Bossche, J., De Baets, B., Verwaeren, J., Botteldooren, D., Theunis, J., 2018. Development and evaluation of land use regression models for black carbon based on bicycle and pedestrian measurements in the urban environment. Environ. Model. Software 99, 58–69.
Van Den Bossche, J., Peters, J., Verwaeren, J., Botteldooren, D., Theunis, J., De Baets, B., 2015. Mobile monitoring for mapping spatial variation in urban air quality: development and validation of a methodology based on an extensive dataset. Atmos. Environ. 105, 148–161.
Van Den Hove, A., Verwaeren, J., Van Den Bossche, J., Theunis, J., De Baets, B., 2020. Development of a land use regression model for black carbon using mobile monitoring data and its application to pollution-avoiding routing. Environ. Res. 183, 108619.
Vette, A., Burke, J., Norris, G., Landis, M., Batterman, S., Breen, M., Isakov, V., Lewis, T., Gilmour, M.I., Kamal, A., Hammond, D., Vedantham, R., Bereznicki, S., Tian, N., Croghan, C., 2013. The near-road exposures and effects of urban air pollutants study (NEXUS): study design and methods. Sci. Total Environ. 448, 38–47.
Wang, J., Sun, K., Cheng, T., Jiang, B., Deng, C., Zhao, Y., Liu, W., 2020. Deep high-resolution representation learning for visual recognition. IEEE Trans. Pattern Anal. Mach. Intell. 1–15.
Wang, Z., Zhong, S., Peng, Z.R., Cai, M., 2018. Fine-scale variations in PM2. 5 and black carbon concentrations and corresponding influential factors at an urban road intersection. Build. Environ. 141, 215–225.
Wu, X., Yang, D., Gu, J., Wen, Y., Zhang, S., Wu, R., Hao, J., 2021. High-resolution mapping of regional traffic emissions by using land-use machine learning models. Atmos. Chem. Phys. 1–20.
Yang, D., Lu, D., Xu, J., Ye, C., Zhao, J., Tian, G., Zhu, N., 2018. Predicting spatio-temporal concentrations of PM 2.5 using land use and meteorological data in Yangtze River Delta, China. Stoch. Environ. Res. Risk Assess. 8 (32), 2445–2456.
Zalakeviciute, R., López-Villada, J., Rybarczyk, Y., 2018. Contrasted effects of relative humidity and precipitation on urban PM2. 5 pollution in high elevation urban areas. Sustainability 6 (10), 2064.
Zhang, H., Wang, Z., Zhang, W., 2016. Exploring spatiotemporal patterns of PM2.5 in China based on ground-level observations for 190 cities. Environ. Pollut. 216, 559–567.

Publication VII

Khedr, M., and **Liu, X***., et al. (2022). *Influence* of New Year's fireworks on air quality – A case study from 2010 - 2021 in Augsburg, Germany. ***Atmospheric Pollution Research***, 101341.

Appendix

Atmospheric Pollution Research 13 (2022) 101341

Contents lists available at ScienceDirect

Atmospheric Pollution Research

journal homepage: www.elsevier.com/locate/apr

Influence of New Year's fireworks on air quality – A case study from 2010 to 2021 in Augsburg, Germany

Mohamed Khedr [a,b], Xiansheng Liu [a,b,*], Hadiatullah Hadiatullah [c], Jürgen Orasche [a], Xun Zhang [d], Josef Cyrys [e], Bernhard Michalke [f], Ralf Zimmermann [a,b], Jürgen Schnelle-Kreis [a,**]

[a] Joint Mass Spectrometry Center, Cooperation Group Comprehensive Molecular Analytics, Helmholtz Zentrum München, German Research Center for Environmental Health, Ingolstädter Landstr. 1, 85764, Neuherberg, Germany
[b] Joint Mass Spectrometry Center, Chair of Analytical Chemistry, University of Rostock, 18059, Rostock, Germany
[c] Tianjin Key Laboratory for Modern Drug Delivery & High-Efficiency, Collaborative Innovation Center of Chemical Science and Engineering, School of Pharmaceutical Science and Technology, Tianjin University, Tianjin, 300072, China
[d] Beijing Key Laboratory of Big Data Technology for Food Safety, School of Computer Science and Engineering, Beijing Technology and Business University, Beijing, 100048, China
[e] Institute of Epidemiology, Helmholtz Zentrum München, German Research Center for Environmental Health, 85764, Neuherberg, Germany
[f] Research Unit Analytical BioGeoChemistry, German Research Center for Environmental Health, Ingolstädter Landstr. 1, 85764, Neuherberg, Germany

ARTICLE INFO

Keywords:
Fireworks
Source apportionment
PAHs
eBC
Metals

ABSTRACT

Fireworks have been shown to contribute short-term but potent source of ambient particulate matter (PM). Here we present a source apportionment-based approach to estimate the quantitative contributions of fireworks in releasing black carbon (eBC), polycyclic aromatic hydrocarbons (PAHs) and metals into urban ambient air on six New Year's Day fireworks events from the period 2010 to 2021. Simplified PMF analyses were performed to assign PAHs, eBCs, and metals to major contributors (building heating, traffic, and fireworks) of ambient PM. The trends of PM_{10} and $PM_{2.5}$ concentrations clearly showed the drastic increase of the concentrations on New Year's Days. The PMF analyses showed that, on average, about 35% (20–80% for individual years) of the PAHs and about 45% of eBC (10–100%) were associated with the fireworks. Metals presented in high concentrations in pyrotechnic sets, namely Ba, Cu, K, Mg, and Sr were attributed to fireworks about 90%, while Al was attributed to fireworks by 86%. Other metals (Ca, Cr, Fe, Na, Pb, Ti, and Zn) were attributed to fireworks by variable proportions averaging at 67%, 77%, 44%, 59%, 64%, 75%, and 33%, respectively. Overall, these findings complement future monitoring programs and regulations for fireworks emissions.

1. Introduction

New Year's Day is internationally celebrated by releasing large quantities and a wide diversity of fireworks. People in many places simultaneously set off fireworks starting from midnight on December 31. Consequently, large quantities of particulate matter are released within a short period. According to a recent calculation by the German Environment Agency (Umweltbundesamt, UBA), the New Year's Eve fireworks emitted around 1500 tons of particulate matter (PM_{10}) across Germany within a few hours (Federal Environment Agency, 2020). Since the vast majority of the fireworks used are ignited near the ground, this causes a sharp increase in the concentration of particulate matter in the air. Evaluations of the data from the German air quality measurement networks regularly show peak particulate matter concentration during New Year's Day with maximum hourly values around 1000 $\mu g/m^3$ PM_{10}. A recent study on fireworks' emissions concluded that about 80% of the particulate matter emitted by the explosive content of the fireworks is in the $PM_{2.5}$ fraction, i.e., respirable (Keller and Schragen, 2021).

The links between air pollution from fireworks emissions and human health have been poorly studied. A study from the Netherlands examining the associations between PM_{10} concentrations and daily mortality in the period around New Year's celebrations from 1995 to 2012 did not

Peer review under responsibility of Turkish National Committee for Air Pollution Research and Control.
* Corresponding author. Joint Mass Spectrometry Center, Cooperation Group Comprehensive Molecular Analytics, Helmholtz Zentrum München, German Research Center for Environmental Health, Ingolstädter Landstr. 1, 85764, Neuherberg, Germany.
** Corresponding author.
E-mail addresses: xiansheng.liu@helmholtz-muenchen.de (X. Liu), juergen.schnelle@helmholtz-muenchen.de (J. Schnelle-Kreis).

https://doi.org/10.1016/j.apr.2022.101341
Received 5 October 2021; Received in revised form 24 January 2022; Accepted 24 January 2022
Available online 25 January 2022
1309-1042/© 2022 Turkish National Committee for Air Pollution Research and Control. Production and hosting by Elsevier B.V. All rights reserved.

Appendix

reach a clear conclusion. In the study, linear regression models showed no clear association between PM_{10} concentrations and daily mortality, while case-crossover analyses suggested an association (Greven et al., 2019). Saucy et al. (2021) found an increased of cardiovascular mortality risk on fireworks days independent from NO_2 and $PM_{2.5}$ concentrations. A recent study on the toxicity of fireworks particles showed significant increases in reactive oxygen species (ROS) formation as a function of particles composition. They found that the high concentrations of Pb and Cu in some fireworks were responsible for the significantly increased toxicity compared to typical urban fine dust (Hickey et al., 2020).

Depending on the type, 25–40% of the fireworks used consist of pyrotechnic compositions. These are mostly black powder (a mixture of potassium nitrate, charcoal, and sulfur), that give bangs, whistles, and colors. Among other components, the metals used for coloring the fireworks (e.g., red: Sr and Ca, green: Ba and Cu, blue: Cu, white or silver: Mg, Al, and Ti, and gold: Fe) are released in large quantities during firework's set off. The contribution of fireworks in elevating the concentrations of many metals and sulfate on New Year's Day has been confirmed in numerous studies in several countries, such as Auckland, New Zeland, Manila, Philippines, Mexico City, Mexico, and Rotterdam, The Netherlands (Lorenzo et al., 2021; Retama et al., 2019; Rindelaub et al., 2021, ten Brink et al., 2019). The clear data situation is mainly due to the mixture and partly source-specific metals emitted by fireworks (Croteau et al., 2010; Keller and Schragen, 2021). The study situation is different for carbonaceous components and especially polycyclic aromatic hydrocarbons (PAHs). To our knowledge, there is very limited evidence about PAHs emission factors or profiles from fireworks. Betha and Balasubramanian (2014) reported that PAHs profiles for particle-bound PAHs in various sparklers showed high variability in emitted PAHs, making it difficult to determine or quantitatively estimate the contributions of fireworks to air pollution with PAHs. Therefore, different studies arrived at different assessments of the significance of the contribution of fireworks to particulate matter pollution with PAHs.

For example, Pongpiachan et al. (2017) found an increase >150% in total PAHs concentrations during the fireworks period in Bangkok, Thailand. Their analyses using binary PAH ratios, hierarchical cluster, and principal component analyses (PCA) indicated that both road traffic and fireworks were major sources of PAHs. In contrast, Sarkar et al. (2010) reported that fireworks were not major source of PAHs during Diwali fireworks. They indicated that PAHs were either not correlated or negatively correlated with firework metals (Na, K, Mg, Al, Ba, Sr), but positively correlated with industrial and vehicle specific markers (Zn, V, Ni, Cr, Cu; $R > 0.5$), suggesting their common origin. Shi et al. (2014) also found PAHs were not directly influenced by fireworks, but rather affected by biomass combustion (firework is made by paper and cracker). A recent study in the U.S. also showed no significant contribution of fireworks to PAH concentrations, although the diagnostic ratios used in the study indicated their contributions (Jia et al., 2020).

For Germany, however, there have been a few studies to date that have examined in more detail about the contributions of fireworks to pollutant levels beyond particulate matter mass concentrations. In this study, we aimed to investigate the contribution of fireworks to air pollution with selected pollutants, in particular PAHs, black carbon (BC) and metal elements in Augsburg, Germany. For this purpose, measurement and data analysis from six periods around the turn of the year from 2010 to 2021 were evaluated. Simplified positive matrix factorization (PMF) analyses were performed to estimate the contributions of the main pollutants to PAHs, BC, and metals. This approach made it possible to estimate the contributions of fireworks to particulate pollution with an estimated uncertainty of about 50%. Furthermore, the special situation at the New Year 2020/21 allowed investigating the effects of significantly reduced fireworks on air quality. Due to various regulations imposed in the context of the COVID-19 pandemic, including a prohibition on the sale of fireworks, a ban on fireworks in public places, and a nighttime curfew, significantly reduce fireworks were set off in the city, especially in 2020/21.

2. Methods

2.1. Monitoring site location and study period

The sampling site was located on the campus of the University of Applied Sciences Augsburg (UAS, 48.35793 N, 10.91544 E), specifically at the ambient aerosol monitoring station operated jointly by the Helmholtz Zentrum München and the University of Augsburg. The site is characterized as an urban background site with 120 m away from the nearest road and ~250 m far from the nearest residential buildings. A more detailed description of the corresponding location can be found in the previous publication (Gu et al., 2011). In this study, particulate matter measurements are analyzed biennially from December 24 till January 7 at the turn of years 2010–2011, 2012–2013, 2014–2015, 2016–2017, 2018–2019 and 2020–2021.

2.2. Continuous measurements and particle sampling

The Tapered Element Oscillating Microbalances (TEOM, model 1405-F, Thermo Fisher Scientific Inc, U.S.) was used to measure particle mass concentration of PM_{10} and $PM_{2.5}$. Equivalent black carbon (eBC) was determined by aethalometers (Magee, model AE31 until 2019 and AE33 since 2020, Aerosol d. o. o, Slovenia). Measurement values of air pollutants were evaluated based on their hourly averages. In addition, hourly averages of meteorological parameters including wind speed (WS), wind direction (WD), temperature (T), and relative humidity (RH), measured at the UAS site. Moreover, precipitation data collected from the German Weather Service (Deutscher Wetterdienst, DWD), were considered for the interpretation of the results.

$PM_{2.5}$ samples were collected from a sequential filter sampler (Thermo Scientific, USA). Daily $PM_{2.5}$ samples (midnight to midnight) were collected on quartz fibre filters (QFF: T293, Munktell, Grycksbo, Sweden), heated at 500 °C overnight before analysis. Samples were returned to the laboratory on a weekly basis, packed in Petri dishes, and stored at −20 °C until chemical analysis. One blank sample was collected every week as a control. In total, 79 p.m.$_{2.5}$ samples were collected and investigated within this study.

2.3. Chemical analysis of $PM_{2.5}$ samples

The organic components and elements were analyzed using subsamples of the original QFF. The organic composition of the $PM_{2.5}$ samples was determined using *in situ* Derivatization Thermal Desorption Gas Chromatography Time-of-Flight Mass Spectrometry (DTD-GC-TOF-MS) method (Schnelle-Kreis et al., 2011). A total of 13 PAHs, including fluoranthene (Flu), pyrene (Pyr), Benzo [a]anthracene (BaA), Chrysene (Chr), the sum of Benzofluoranthenes (BbjkF), Benz [e]pyrene (BeP), Benz [a]pyrene (BaP), Indeno [1,2,3-cd]pyrene (Ind), Dibenz [ah] anthracen (DahA), Benmzo [ghi]perylene (BghiP), Coronen (Cor), and Retene (Ret) (Table S1), were quantified. In addition, the concentrations of two oxidized aromatic compounds, 1,8-Naphthalic anhydride (NA) and 4-H-Cyclopenta [def]phenanthren-4-one (CPO) and 6 Hopanes (17β (H),21a(H)-30-Norhopane (29aβ), 17β(H),21a(H)-30-Norhopane (29βa), 17a(H),21β(H)-Hopane (30aβ), 17β(H),21a(H)-Hopane (30βa), 17a(H),21β(H)-Homohopane (31aβS), and 17a(H),21β(H)-Homohopane (31aβR)) were evaluated. Subsequently, 27 elements, namely Al, As, B, Ba, Be, Ca, Cd, Co, Cr, Cu, Fe, K, Li, Mg, Mo, Na, Ni, P, Pb, S, Sb, Se, Sn, Sr, Ti, V, and Zn were evaluated by Inductively Coupled Plasma-Mass Spectrometry (ICP-MS) using rhodium and lutetium as internal standards (Gu et al., 2011). The limits of quantification (LOQ) of the methods (GC-MS and ICP-MS) were added in the supporting information (Table S1). For the quality assurance/quality control (QA/QC), the method is based on a internal calibration, which means that an isotopically labelled standard mixture is added to each calibration point as

Appendix

well as to all samples. The quality of the measurements is ensured by frequent measurements of reference samples and weekly replicates of real samples (Orasche et al., 2011).

2.4. PMF analysis

In recent years, positive matrix factorization (PMF) (Paatero and Tapper, 1994) has been widely used in sources apportionment studies. Unlike most source apportionment studies conducted to date, our PMF analysis aims neither to identify all possible sources of $PM_{2.5}$ nor estimate their contributions to the measured $PM_{2.5}$ values. Rather, the goal was to estimate the contributions of fireworks emissions to the PAHs, eBC and metal elements concentrations. Therefore, we focused on the source groups that have already been shown to be the major contributors of PAHs and elemental carbon (EC) in previous studies in Augsburg (Gu et al., 2013). By limiting the analysis to the main contributors to PAHs and BC, the contribution of the sources identified in our study to the $PM_{2.5}$ concentration is certainly overestimated, as important contributions such as secondary inorganic aerosols are not considered. Previous studies have shown that fraction of ammonium nitrate and sulfate in urban background PM in Augsburg can average about 50% of the total particle mass in winter (Gu et al., 2013).

However, from the contributions of PAHs, eBC, and metals to the factors determined by PMF and the proportional contribution of the

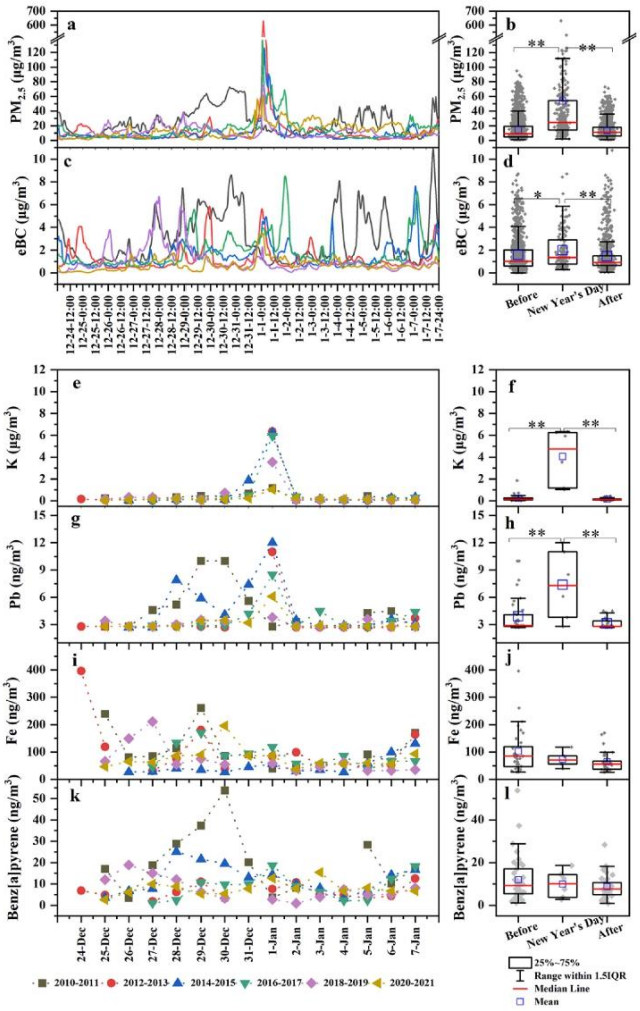


Fig. 1. Left panel, Time series of the hourly mean concentrations of $PM_{2.5}$ (a) and eBC (c), and daily mean concentrations of K (e), Pb (g), Fe (i), and Benz [a]pyrene (BaP) (k) in the periods studied. Right panel, summarized comparison of the hourly means of the concentrations of $PM_{2.5}$ (b), eBC (d) and the daily means of the concentrations of K (f), Pb (h), Fe (j), and BaP (l) on New Year's Day with the reference periods before and after. The significance levels (**, $p < 0.01$, *, $p < 0.05$) refer to the differences between the respective means.

Appendix

fireworks factor to the $PM_{2.5}$ load on New Year's Day, the contribution of fireworks to the total load of PAHs, eBCs, and metals can be estimated with a reasonable degree of accuracy. A detailed description of the PMF analysis can be found in the supporting information (SI, section 1).

2.5. Toxic and mutagenic equivalent factors of PAH

The carcinogenic risk of a PAH mixture is often expressed by its BaP equivalent concentration (BaP_{TEQ}) (Han et al., 2011). To normalize the toxicity of different PAHs in $PM_{2.5}$, it was calculated using the equivalent mass concentration based on BaP and the value of toxic equivalency factors (TEFs) (Table S2), which has been described elsewhere (Liu et al., 2019). Similarly, BaP related mutagenicity (BaP_{MEQ}) was calculated, except that the TEF was replaced by MEF (mutagenic equivalency factor). The BaP_{TEQ} and BaP_{MEQ} were calculated according to following equations (1) and (2):

$$\sum BaP_{TEQ} = \sum_{i=1}^{n} C_i \times TEF_i, \quad (1)$$

$$\sum BaP_{MEQ} = \sum_{i=1}^{n} C_i \times MEF_i, \quad (2)$$

where C_i = concentration of PAH congener i; TEF_i = the toxic equivalency factors (TEFs) of PAH congener i; MEF_i = the mutagenic equivalency factors (MEFs) of PAH congener i. The toxicity assessment of PAHs was determined by benzo(a)pyrene, as an equivalent for carcinogenicity (ΣBaP_{TEF}) and mutagenicity (ΣBaP_{MEF}).

3. Results and discussion

3.1. Air pollutants trends around New Year's days

3.1.1. Particulate matter

The trends of PM_{10} (Figure S1) and $PM_{2.5}$ concentrations (Fig. 1(a)) clearly showed the drastic increase of the concentrations on New Year's Day. The data showed that there was massive increase in PM concentration at midnight. However, a slighter increase was already observed in the hours before midnight. The temporal differences in reaching the maximum concentrations were observed between 0:00 and 2:00, which for $PM_{2.5}$ ranged from about 60 (2020–2021) to > 600 $\mu g/m^3$ (2012–2013). Possible causes underlying this condition were influenced by different intensity of the fireworks and the dispersion conditions, especially wind speed. Normally, the extremely high particle concentrations decline within a few hours, resulting in the concentrations below 25 $\mu g/m^3$ again on January 2. When the concentration trends are considered across the entire interval, numerous periods of different length with sometime significantly elevated $PM_{2.5}$ and PM_{10} concentrations can be identified. The period between Christmas and New Year's Eve 2010 was particularly striking, with $PM_{2.5}$ concentrations exceeding 70 $\mu g/m^3$ in some periods. However, on average, $PM_{2.5}$ and PM_{10} concentrations on New Year's Day were significantly higher than on the days before or after (Fig. 1(b)), which was consistent with previous study (Hamad et al., 2016).

3.1.2. Black carbon

A possible influence of the fireworks on the eBC concentration was not clearly detected on New Year's Day (Fig. 1(c)). However, a significant peak of eBC concentrations was found at most of the year changes, but it was much less pronounced than the peaks of PM concentration. It was also noticeable that the increase in concentration was significant before midnight in most years (Fig. 1(d)). In addition, many short episodes with eBC concentrations above those of New Year's Day were observed in almost all years. As previously observed for $PM_{2.5}$, the period between Christmas and New Year's Eve 2010 was characterized by comparatively high eBC concentrations. However, on average the studied New Years, the average concentration of eBC on New Year's Day was significantly or highly significantly higher than on the days before or after, indicating that eBC concentrations may also be influenced by firework (Lin et al., 2016). Despite the higher variability, the eBC concentration was strongly correlated with PM concentrations during the observation periods (BC *vs.* $PM_{2.5}$, 0.789; BC *vs.* PM_{10}, 0.843, $p < 0.01$).

3.1.3. Elements

A total of 27 metal elements were quantified by ICP-MS. Of these, 15 elements (i.e., Al, B, Ba, Ca, Cr, Cu, Fe, K, Mg, Na, Pb, S, Sr, Ti, and Zn) were quantified, while 12 elements (i.e., As, Be, Cd, Co, Li, Mo, Ni, P, Sb, Se, Sn and V) were excluded from further evaluation because their concentrations were below the limits of detection in all $PM_{2.5}$ samples. Three different temporal characteristics can be considered for the elements (K, Pb, and Fe), which were discussed here as an example (Fig. 1(e–j)), while temporal characteristics for other elements were supplemented in SI (Figure S2). Elements with highly abundant in the pyrotechnic sets of the fireworks (e.g., K, S) or that can be emitted in very high amounts due to their known use in coloring the fireworks (e.g., Al, Ba, Cu, Mg, Sr, Ti) had indeed very high peak concentrations on the New Year's days (Lorenzo et al., 2021), as can be illustrated by K element (Fig. 1(e)). Slightly elevated concentrations were observed as early as December 31. On January 2, the low concentrations were reached again as period before the fireworks. Apart from the pronounced peak around New Year's Day, there were either an absent of concentration peaks or relatively low peaks observed. The differences between the New Year's Day and the comparison periods were highly significant (Fig. 1(f)). The second group of elements (Cr, Pb, and Zn), in addition to pronounced peak concentrations on New Year's Day, also exhibited other concentration peaks before and/or after the fireworks display in some cases (Fig. 1(g)). Similar to the $PM_{2.5}$ and the eBC, lead and zinc (Figure S2) also exhibited elevated concentrations during the episode between Christmas and New Year's Eve 2010, and significantly higher concentrations on New Year's Day (Fig. 1(h)). This is particularly noteworthy since the aboved mentioned heavy metals are not (anymore) allowed to be used for fireworks approved in Germany (Eu Directive, 2013). The third group includes B, Ca, Fe and Na. The course of the concentrations of these elements showed high variability around the studied turn of the year with no noticeable peaks on New Year's Day (Fig. 1(i)). Accordingly, there were also no significant differences between fireworks and comparison periods in the concentrations averaged over all periods studied (Fig. 1(j)).

In total, the temporal trends of PAHs concentrations were comparable to those of some heavy metal group (Cr, Mn, Pb, and Zn) (Figure S3). However, the peak concentrations on New Year's Days were much less pronounced or absent in some of the studied periods (Fig. 1(k)). More frequent and sometimes higher peak concentrations than on January 1 were observed during the comparison periods. When the highest PAHs concentrations occurred, the period between Christmas and New Year's Eve 2010 was particularly striking. Overall, slightly higher concentrations were detected on January 1 for all PAHs than in the comparison periods, but these were not significantly different (Fig. 1(l)). However, it is worth mentioning that the PAHs concentrations were classified as high concentration in the observed periods. For example, the annual average of BaP concentration was 10 times higher than the EU target value of 1 ng/m^3 (Hellén et al., 2017).

3.2. Meteorological impacts on $PM_{2.5}$ and eBC concentrations

Under different meteorological conditions, the concentration of pollutants on the ground from the same source can vary by tens or even hundreds of times due to atmospheric dispersion. Therefore, the Spearman correlation coefficients (r) were calculated between the air pollutants concentrations and meteorological variables in the observed periods. Our analysis revealed that the air pollutants concentrations were negatively correlated with wind speed (WS) and temperature (T)

Appendix

and positively correlated with relative humidity (RH) (Table S3), indicating the temporal variability of PM concentrations were strongly influenced by meteorological variables. However, meteorological conditions alone did not provide a discernible approach to explain the sometimes very large differences in $PM_{2.5}$ and eBC concentrations on New Year's Day.

The period around the turn of 2010–2011 had several notable features. First, there was a multi-day episode with high PM concentrations from the afternoon of December 28 to the morning of New Year's Eve. This period was characterized by low average WS (<1.5 m/s) and relatively constant high RH (Figure S4). During the period between January 3 and 6, comparatively high concentrations were observed at night, each associated with low WS and high RH, which decreased significantly during the respective day simultaneously with increasing WS and decreasing RH. During these two periods, the highest concentrations were associated with circulating winds with a slight north-easterly component (Figure S4e). However, the absence of high concentrations on New Year's Day, which could be attributed to fireworks, was particularly noticeable at the turn of the year 2010–2011. This was also confirmed for most of the metals analyzed. Only the metals considered characteristic of fireworks (Al, Ba, Cu, K, Mg, Sr, Ti) showed elevated concentrations (Figure S2). Neither dispersion conditions prevailing on this day, wind with low velocities from south-west, nor precipitation offered a plausible explanation for this finding. Precipitation was observed only at the beginning and the end of the 14 days period. Only individual concentration peaks were found around the turn of the year 2012–2013 (Figure S5a). These occurred in each case at night during low WS and high RH as already described for 2011. The $PM_{2.5}$ peak concentration on New Year's Day was very pronounced and associated with similar meteorological conditions as on New Year's Day 2011 (and 2019), i.e. low winds from south-west (Figure S4f and S8f). Thus, just as meteorological conditions failed to explain the missing PM peak on New Year's Day 2011, our available data also failed to explain the exceptionally high $PM_{2.5}$ concentration on January 1, 2013. The situation at the turn of 2014–2015 was very similar to that of 2012–2013. However, unlike the previously described period, phases of low WS and high RH also occurred in this study and were not associated with high PM concentrations (Figure S5 and S6). The high PM concentrations on New Year's Day are associated with WS below 1 m/s (Figure S5f and S6f).

New Year's Day 2017 occurred during a relatively long period with WS around or below 1 m/s, frequently changing WD and high RH with low T compared to the other periods (Figure S7). During this period, a gradual increase in eBC concentration was observed. However, no additional eBC peak occurred on New Year's Day. The $PM_{2.5}$ concentration, on the other hand, exhibited the significant peak in concentration at midnight as expected for New Year's Days. The period around New Year's Day 2018–2019 was very similar to the 2012–2013 period with high PM concentrations at low WS and high RH, albeit much lower PM peaks were observed on New Year's Day (Figure S8a). During the highest PM concentration, wind conditions were similar to 2013, with WS below 1 m/s from the south-west. The situation around the turn of 2020–2021 was different from all previously periods (Figure S9). The eBC concentration was comparatively low and did not show pronounced peaks, excluding the peaks on New Year's Eve and New Year's Day. The $PM_{2.5}$ concentration exhibited almost identically high peaks on the late evening of New Year's Eve and shortly after midnight on New Year's Day. However, unlike the previous New Year's Eve events, the $PM_{2.5}$ concentration did not switch fell and declined slowly and fluctuated over several days. A direct connection between the observed fluctuations and the meteorological parameters was not evident. However, it was noticeable that the RH showed pronounced diurnal fluctuations in the days before the turn of the year, with mostly lowest values around noon, while it was stable, at a relatively high level after the turn of the year.

In summary, the correlations between the meteorological parameters and the observed $PM_{2.5}$ and eBC concentrations were statistically significant and provided clear contributions to the variability of the observed concentration. However, meteorological conditions have not provided an identifiable method for explaining some of the very large differences in $PM_{2.5}$ and eBC concentrations on New Year's Day.

3.3. analysis

The data were analyzed using PMF5.0 (EPA, US Environmental Protection Agency) to assign eBC, PAHs, and metals to the most relevant sources. In this PMF analyses, PAHs, 15 elements, daily average of eBC and $PM_{2.5}$ (total variable), and the some selected organic substances were included. Due to the small number of samples and limited analyses (without inorganic ions), it was not possible to identify all sources relevant to the $PM_{2.5}$ mass. However, the analytical data were sufficient to identify the major sources of PAHs, BC, and metals and to determine their relative contribution of fireworks to these pollutants. Thus, the goal of PMF analysis was not to identify the entire contributors to $PM_{2.5}$, but to identify the contributions of the major sources to the proportions of the above pollutants. As a result, 3 factors were separated and further described in more detail below. The corresponding factor profiles can be found in the SI Figure S10.

3.3.1. Factor profiles

3.3.1.1. Factor 1 - firework emissions. Factor 1 was dominated by high concentrations of the elements: Cu (79%), Sr (79%), Ba (75%), Mg (71%), K (70%), Al (49%), and S (42%), which were strongly correlated with fireworks burning (Miranda et al., 2004; Rai et al., 2020). The chemistry of fireworks was commonly based on fuels and oxidizer, containing potassium nitrate (KNO_3), charcoal, sulfur (S). Al, Mg, strontium nitrate ($Sr(NO_3)_2$), and barium nitrate ($Ba(NO_3)_2$) were common compounds as effect charges of pyrotechnic products (Srinivasan, 2017; Keller and Schragen, 2021). When these compounds were burned, they emitted a distinctive flame color. Briefly, KNO_3 was commonly used as a propellant, while Al and Mg were used as fuels and white luminous agent in fireworks (Lorenzo et al., 2021). In addition, the firework color was also formed by metal salts such as Sr for red, Ba for green, and Cu for blue-violet. These three elements were effective markers for fireworks (Walsh et al., 2009; Vecchi et al., 2008). Therefore, factor 1 was considered as "fireworks" emissions. On average, this factor also accounted for about 18% of the chromium, 12% of the lead and 2% of the zinc. Only about 2–4% of the individual PAHs and about 5% of the eBC were associated with this factor. Thus, PAHs in this factor, which can be interpreted as the average composition of fireworks emissions, have concentrations in the $PM_{2.5}$ between 6 and 280 μg/g. These values were comparable to the range of PAH concentrations in the emission PM reported in the previous study (Betha and Balasubramanian, 2014).

3.3.1.2. Factor 2 - domestic heating emissions. Factor 2 was characterized by high contribution of 1,8-Naphthalic anhydride (95%), PAHs (75–82%), 4-H-Cyclopenta [def]phenanthren-4-one (75%), eBC (73%), and hopanes (40–68%). 1,8-Naphthalic anhydride, and 4-H-Cyclopenta [def]phenanthren-4-one were oxidized polycyclic hydrocarbons (o-PAH) found in wood combustion emissions at high concentrations (Orasche et al., 2012; Czech et al., 2018), and therefore considered as a marker for wood combustion. In this factor, the hopane pattern showed high similarity with hopane pattern from coal combustion (Křůmal et al., 2013). Therefore, in previous study in Augsburg, it was interpreted as indicator of exposure to brown coal combustion for domestic heating (Schnelle-Kreis et al., 2007). Based on these results, factor 2 was interpreted as "domestic heating" emissions.

3.3.1.3. Factor 3 - traffic emissions. Factor 3 was dominated by high

Appendix

concentrations of Ca (93%), Na (79%), Ti (66%), Zn (63%), Fe (54%), B (57%), Cr (56%), Pb (58%), Al (48%) elements, and 4 hopanes compounds (45%). Emissions from traffic were a significant source of metals to the atmosphere. These can come from the combustion of trace amounts in gasoline and diesel fuels, brake and tire wear particles, and resuspended road dust (Pant and Harrison, 2013; Sanderson et al., 2014). Therefore, the traffic emissions were divided into the following three categories: traffic exhaust, traffic abrasion, and traffic resuspension.

Ca and Zn were often added to lubricating oil to protect engine components (Liati et al., 2015). Therefore, Ca and Zn have been considered as markers for traffic exhaust sources, specifically from diesel fuel (Sanderson et al., 2014; Liati et al., 2012). In addition, metal fragments (e.g., Fe-bearing) mechanically abraded from diverse parts of the engine and/or the exhaust after-treatment systems have also been found in the engines exhausts (Sappok et al., 2012). In factor 3, the hopane pattern showed a high similarity to the vehicle exhausts pattern (Krůmal et al., 2013). The class of traffic-related abrasion includes all particles that can be attributed to brakes and tires abrasion associated with motor vehicle and traffic emissions based on marker elements (e.g., Fe, Zn, Ti, and Cr) and morphology (Habre et al., 2014; Pant and Harrison, 2013). For example, brake wear due to abrasive processes produced Fe, Ti, and Cr containing materials (Kukutschová and Filip, 2018). In addition, Zn has also been considered as a marker for tire abrasion, as it has been added to tire tread in the form of zinc oxide and organozinc compounds to facilitate the vulcanization process (Jandacka et al., 2017). Resuspended material from traffic was primarily a mixture of fine material on the road and roadside that was stirred up by tire movement and headwinds. High concentrations of Na were most likely from salt based de-icing agent applied to Augsburg roads in winter (Gu et al., 2011). Ti, Fe, and Al were considered as marker elements for mineral crustal particles such as suspended soil and road dust (Gu et al., 2011). Ca also probably originated from the resuspension of dust (Loyola et al., 2012). In addition, Fe and Al were also identified as the marker elements for asphalt, along with small proportions of Cr and Zn (Munmullage et al., 2016). Meanwhile, Cr and Pb in road dust could be derived from road paint ($PbCrO_4$) (Li et al., 2019). Thus, factor 3 can be summarized as "traffic" emissions. On average overall investigated periods, this factor contributed to about 14–21% of PAHs concentrations and 22% of eBC.

3.3.2. Factor contributions

As mentioned above, PMF explained the $PM_{2.5}$ concentrations reasonably well. However, a deeper analysis showed that some huge values (>25 μg/m^3), such as the repeatedly discussed period between Christmas and New Year's Eve 2010, but also the very high value on New Year's Day 2013, were not captured in a representative fashion (Fig. 1(a)). Fig. 2 showed that the time series of the three factors' contributions and their respective average concentrations on New Year's Day and in the reference periods were recorded. Factor 1 (fireworks emissions) showed a significant peak in concentration on all New Year's Days. Small contributions of this factor to $PM_{2.5}$ were also observed on New Year's Eve and partially on January 2. On the other days of the reference periods, factor 1 did not contribute to $PM_{2.5}$. Accordingly, the difference in concentrations between January 1 and the reference periods was highly significant (Fig. 2(b)). Factor 2 (residential heating emissions) showed comparatively low concentration variations without pronounced peaks in all periods around the turn of the year (Fig. 2(c)). However, the episode with comparatively high contribution of this source to $PM_{2.5}$ between Christmas and New Year's Day 2010 was striking. This has been already noted for $PM_{2.5}$, eBC, PAHs, and some elements. In addition, very low levels of this factor were found in the beginning of 2019. The comparison of all measured values showed no significant differences between New Year's Day and comparison periods (Fig. 2(d)). Like factor 2, factor 3 (traffic emissions) showed a little variations in concentration (Fig. 2(e)). The episode in 2010 described for factor 2 did not occur here. However, it was noticeable that in some years, very low concentrations of this factor were estimated for January 1. To our knowledge, this was an artifact of the PMF analysis, which was not able to fully separate factor 1 from factor 3. As a result, lower concentrations of these factors were found on New Year's Days than in the comparison periods.

3.3.3. Proportion of fireworks in particulate PAHs, eBC, and metals on New Year's days

Based on PMF analysis, the contributions of fireworks to air pollution with PAHs, eBCs, and metals on New Year's Day can be estimated. The

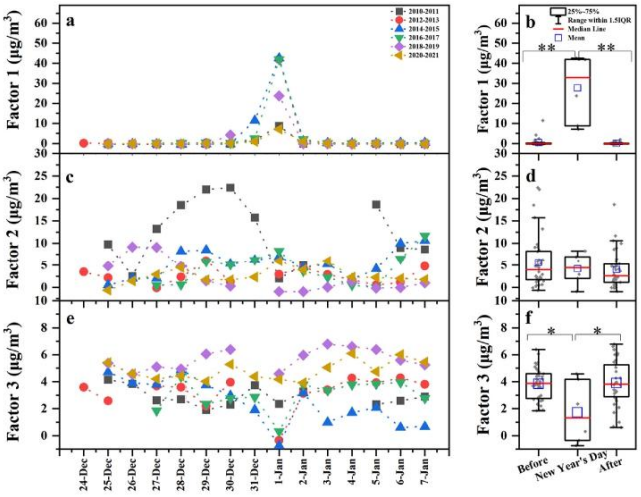


Fig. 2. Left panel, Time series of the daily contributions of the source factors to the $PM_{2.5}$ concentration*. Daily mean concentrations of factor 1 (a) factor 2 (c) and factor 3 (e) in the periods studied. Right panel, Summarized comparison of the daily means of the concentrations of factor 1 (b), 2 (d) and 3 (f) on New Year's Day with the reference periods before and after. The significance levels (**, $p < 0.01$, *, $p < 0.05$) refer to the differences between the respective means. Note: the absolute concentrations of the three factors were overestimated because many $PM_{2.5}$ sources were not considered such as, secondary organic aerosols.

Appendix

basis for the estimation were the average concentrations of the respective component and $PM_{2.5}$ estimated from PMF analysis in factor 1 (fireworks emissions) and the contribution of factor 1 to $PM_{2.5}$ on the New Year's Days.

On average overall periods investigated and all quantified PAHs, fireworks accounted for about 35% of the PAHs. Thereby, there were large differences between the individual New Year's Days. For instance, the lowest contribution from fireworks was estimated for January 1, 2021, with an average PAHs contribution of 6%. However, on New Year's Day 2019, about 84% of PAHs were associated with the fireworks emissions. On New Year's Day 2011, 2013, 2015, and 2017, fireworks contributed an average of 20%, 56%, 28%, and 24% of PAHs in $PM_{2.5}$, respectively. The ranking of fireworks contributions to eBC concentrations was analogous to that of PAHs. The lowest contribution was found about 12% on New Year's Day 2021, while the 2019 eBC (calculated) could be entirely from this source. For 2011, 2013, 2015, and 2017, the contribution of fireworks in the total eBC load was estimated as 26%, 64%, 42%, and 26%, respectively. On average overall periods studied, the contribution of fireworks to eBC was about 45%. As expected, the pattern of metals contributions from fireworks consisted of two parts. Firstly, the metals (and sulfur) present high concentrations in the pyrotechnic sets and have no very strong source on the fireworks days, i.e., Ba, Cu, K, Mg, S, and Sr were attributed to the fireworks by more than 91% on average. Al is attributed to fireworks by about 86%, which further supported by previous study (Lorenzo et al., 2021). It was also found that some firework tracer species (Cu, Ba, Sr, Al, and Pb), which exhibited the highest enrichments during the fireworks display. Only small variations in the proportions from year to year were estimated. Thus, the very high concentrations of these substances on New Year's Days were almost entirely due to fireworks. Secondly, the metals that have strong sources besides fireworks had varying proportions due to fireworks on New Year's Days. On average for all New Year's Days studied, the proportions attributable to fireworks were estimated to be 67%, 77%, 44%, 59%, 64%, 75%, and 33% for Ca, Cr, Fe, Na, Pb, Ti, and Zn, respectively. As for PAHs, the lowest contribution of these elements from fireworks was determined to be 20% on average on January 1, 2021. In other years, the contribution of fireworks to these metals was quite variable.

In summary, it was possible to estimate the contributions of fireworks to air pollution with PAHs, eBC, and metals using PMF analysis. In contrast to previous studies, comparatively high contributions to PAHs concentrations were found on New Year's Days. The study also showed that the contributions from fireworks on New Year's Day 2021 were much lower than in the other years. The measures imposed due to the COVID-19 pandemic (ban on sale of fireworks, ban on fireworks in public places, and nighttime curfew) have caused a significant reduction in the intensity and duration of fireworks on January 1, 2021, leading to the observed reduction in emissions.

3.3.4. Limitations

PMF analysis developed in this study to estimate the contributions of fireworks to $PM_{2.5}$ on New Year's Days was adopted based on number of underlying hypotheses and therefore imposing limitations on the reliability of the expected results. The key hypotheses, their limitations, and the resulting uncertainties were briefly summarized below.

A condition for conducting PMF is a sufficient relationship between observations and variables. There are no clear guidelines for this in the literature. In our case, the ratio is about 2 (78 observations, 37 variables), which gives stable results of the PMF analysis. As our analysis showed, the PMF is able to detect singular events (here the fireworks), if they show significantly different source profiles compared to the other relevant sources. However, for obtaining stable PMF results it is advisable to combine several independent measurements of the events (fireworks). These can be observations at different times, as in our case, or observations at different locations at the same time.

Our PMF analysis was performed to estimate the contributions of fireworks to PAH and eBC concentrations. This assumes that the relevant sources for these substances can be identified. From our previous studies in Augsburg, traffic emissions and residential heating are known as the most important sources of PAHs and eBC (Li et al., 2018). We believed that the misclassification of PAHs and eBC from sources other than traffic and residential heating to the fireworks was negligible. An additional essential assumption of PMF analyses was that the profiles (composition) of the sources were constant during the period considered. However, due to changes in technology and legislation in the investigated period, i.e., traffic and residential heating, have changed in quantity and quality (composition). In addition to the introduction of particulate filters and the continuous tightening of emission standards, especially for diesel vehicle, the introduction of Augsburg Environmental Zone has certainly contributed to a qualitative change in traffic emissions. With the respective regulations (1. BImSchV, 2010) revision, the building heating sector will also shift to lower-emission fireplaces and therefore may also change the emissions quality. However, in general, we estimated that the changes in the emission profiles have small error in the analysis of the distribution of PAHs and eBC.

When discussing the results of PMF analyses, it was often assumed that the factors can be fully separated from each other. However, a closer look at the results shows that these were only the case if the profiles of the factors (composition) and their time courses differ significantly. The fireworks factor, by its nature, showed a clearly discernible pattern with distinct peaks on New Year's Days and small contributions on December 31 and January 2. On the other days of the comparison periods, this factor was closely zero. On the other hand, contributions from building heating on January 1, 2019, and contributions from transportation on New Year's days in 2013, 2015, and 2017 could not be determined. This resulted in an overestimation of the contributions from the other sources on these days. The extent to which these contributions were due to fireworks on the days in question cannot be clearly assessed from the available data. Conservatively estimated, we assumed an overestimation of the fireworks on these days of a maximum of 50% of the estimated value.

3.4. Carcinogenic and mutagenic potencies of PAHs

The application of carcinogenic equivalents (BaP_{TEQ}), and mutagenic equivalents (BaP_{MEQ}) to polycyclic aromatic hydrocarbons (PAH) concentrations can provide a more accurate risk assessment from environmental exposure to PAH. Several studies have adopted this application to assess the health risk of PAH (Liu et al., 2019; Nadali et al., 2021; Callén et al., 2014).

Therefore, in this study, the BaP_{TEQ} and BaP_{MEQ} values were also calculated using the TEF and MEF lists (Table S2). The higher carcinogenic risks of total PAHs (ΣBaP_{TEQ}) were found in Augsburg New Year's days period with average values of 14.43 ± 4.67 ng/m^3 (Figure S11), which were higher than the target annual mean values of ΣBaP_{TEQ} range (0.7–1.3 ng/m^3) in European countries (Ballesta et al., 1999). In addition, the average concentrations of ΣBaP_{MEQ} (mutagenic potencies) were approximately of 18.83 ± 6.08 ng/m^3 (Figure S11), which were higher than those at the Italian residential zone (4.2 ± 2.7 ng/m^3 for $PM_{2.5}$) (Masiol et al., 2012). And the BaP_{TEQ} and BaP_{MEQ} levels were higher during New Year's Day than whole period. The results indicated that many toxic compounds were threatening human health in the New Year's Day. However, it should be noted that the average data in this study were only collected over the 15 days (Dec.24-Jan.07), thus the level of carcinogenic and mutagenic potencies of PAHs may not fully represent the whole year in some extent.

4. Conclusion

Simplified PMF analyses were successfully used to assign PAHs, eBCs, and metals to their sources. The approach adopted did not aim to identify all possible sources, but was limited to separating the main

Appendix

contributors already identified in previous studies. The emphasis was placed on clearly separating fireworks events. PMF analyses was possible to estimate how high the contribution of fireworks to air pollution with PAHs, eBC, and metals was on individual New Year's days. In contrast previous studies, that did not show the clear accusations between fireworks and PAH and eBC concentrations, our finding suggested that the PAHs and BC, although not a major source of fireworks, were still indirectly affected by biomass combustion associated with fireworks. However, the ΣBaP_{TEQ} and ΣBaP_{MEQ} levels were higher during New Year's Days period, suggesting that many toxic compounds threatened public health during New Year's Days period. Taken together, these findings call for future monitoring programs and regulations for fireworks emissions.

Credit author statement

Mohamed Khedr: Data curation, Methodology, Writing original draft. **Xiansheng Liu**: Data curation, Methodology, Software, Writing original draft. **Hadiatullah Hadiatullah**: Methodology, Software, Writing original draft. **Jürgen Orasche**: Data curation. **Xun Zhang**: Software. **Josef Cyrys**: Data curation, Writing review & editing. **Bernhard Michalke**: Data curation. **Ralf Zimmermann**: Investigation, Supervision. **Jürgen Schnelle-Kreis**: Data curation, Supervision, Writing review & editing.

Declaration of competing interest

The authors declare that they have no known competing financial interests or personal relationships that could have appeared to influence the work reported in this paper.

Acknowledgements

The work is funded by the Germany Federal Ministry of Transport and Digital Infrastructure (BMVI) as part of SmartAQnet (grant No.19F2003B), and the China Scholarship Council (CSC) under the State Scholarship Fund (File No.201706860028).

Appendix A. Supplementary data

Supplementary data to this article can be found online at https://doi.org/10.1016/j.apr.2022.101341.

References

BImSch, V., 2010. Erste Verordnung zur Durchführung des Bundes-Immissionsschutzgesetzes, BGBL 1997 Teil 1 Nr. 17. BGBL 2010, Til I Nr. 4. https://www.gesetze-im-internet.de/bimschv_1_2010/BJNR003800010.html. (Accessed 11 August 2021).

Ballesta, P.P., De Saeger, E., Kotzias, D., 1999. State of the art of the PAHs' analysis in ambient air. Ispra 22–24, 499–505. March 1999.

Betha, R., Balasubramanian, R., 2014. PM2.5 emissions from hand-held sparklers: chemical characterization and health risk assessment. AAQR 5 (14), 1477–1486.

Callén, M.S., Iturmendi, A., López, J.M., 2014. Source apportionment of atmospheric PM2.5-bound polycyclic aromatic hydrocarbons by a PMF receptor model. Assessment of potential risk for human health. Environ. Pollut. 195, 167–177.

Croteau, G., Dills, R., Beaudreau, M., Davis, M., 2010. Emission factors and exposures from ground-level pyrotechnics. Atmos. Environ. 27 (44), 3295–3303.

Czech, H., Miersch, T., Orasche, J., Abbaszade, G., Sippula, O., Tissari, J., Zimmermann, R., 2018. Chemical composition and speciation of particulate organic matter from modern residential small-scale wood combustion appliances. Sci. Total Environ. 612, 636–648.

Eu Directive, 2013. Directive of the European Parliament and of the Council of the EU 2013 on the Harmonization of the Laws of the Member States Relating to the Making Available on the Market of Pyrotechnic Articles (Recast), OJ L 178, 28.6.2013, Directive 2013/29/EU of 12 June 2013.

Federal Environment Agency, 2020. 2.050 Tonnen Feinstaub durch Feuerwerk pro Jahr Feinstaubbelastung in der Atemluft an Neujahr besonders hoch. https://www.umweltbundesamt.de/presse/pressemitteilungen/2050-tonnen-feinstaub-durch-feuerwerk-pro-jahr. (Accessed 11 August 2021).

Greven, F.E., Vonk, J.M., Fischer, P., Duijm, F., Vink, N.M., Brunekreef, B., 2019. Air pollution during New Year's fireworks and daily mortality in The Netherlands. Sci. Rep. 9 (1), 1–8.

Gu, J., Pitz, M., Schnelle-Kreis, J., Diemer, J., Reller, A., Zimmermann, R., Soentgen, J., Stoelzel, M., Wichmann, H.E., Peters, A., Cyrys, J., 2011. Source apportionment of ambient particles: comparison of positive matrix factorization analysis applied to particle size distribution and chemical composition data. Atmos. Environ. 45 (10), 1849–1857.

Gu, J., Schnelle-Kreis, J., Pitz, M., Diemer, J., Reller, A., Zimmermann, R., Cyrys, J., 2013. Spatial and temporal variability of PM10 sources in Augsburg, Germany. Atmos. Environ. 71, 131–139.

Habre, R., Coull, B., Moshier, E., Godbold, J., Grunin, A., Nath, A., Koutrakis, P., 2014. Sources of indoor air pollution in New York City residences of asthmatic children. J. Expo. Sci. Environ. Epidemiol. 3 (24), 269–278.

Hamad, S., Green, D., Heo, J., 2016. Evaluation of health risk associated with fireworks activity at Central London. Air Qual. Atmos. Health 7 (9), 735–741.

Han, Y.M., Cao, J.J., Yan, B.Z., Kenna, T.C., Jin, Z.D., Cheng, Y., et al., 2011. Comparison of elemental carbon in lake sediments measured by three different methods and 150-year pollution history in eastern China. Environ. Sci. Technol. 45 (12), 5287–5293.

Hellén, H., Kangas, L., Kousa, A., Vestenius, M., Teinilä, K., Karppinen, A., et al., 2017. Evaluation of the impact of wood combustion on benzo [a] pyrene (BaP) concentrations; ambient measurements and dispersion modeling in Helsinki, Finland. Atmos. Chem. Phys. 17 (5), 3475–3487.

Hickey, C., Gordon, C., Galdanes, K., Blaustein, M., Horton, L., Chillrud, S., Gordon, T., 2020. Toxicity of particles emitted by fireworks. Part. Fibre Toxicol 1 (17), 1–11.

Jandacka, D., Durcanska, D., Bujdos, M., 2017. The contribution of road traffic to particulate matter and metals in air pollution in the vicinity of an urban road. Transport. Res. Transport Environ. 50, 397–408.

Jia, C., Xue, Z., Fu, X., Sultana, F., Smith, L.J., Zhang, Y., Li, Y., Liu, B., 2020. Impacts of Independence Day fireworks on pollution levels of atmospheric polycyclic aromatic hydrocarbons, (PAHs) in the U.S. Sci. Total Environ. 743, 140774.

Keller, F., Schragen, C., 2021. Determination of particulate matter emission factors of common pyrotechnic articles. Propellants, Explos. Pyrotech. 5 (46), 825–842.

Krümal, K., Mikuška, P., Večeřa, Z., 2013. Polycyclic aromatic hydrocarbons and hopanes in PM1 aerosols in urban areas. Atmos. Environ. 67, 27–37.

Kukutschová, J., Filip, P., 2018. Review of brake wear emissions: a review of brake emission measurement studies: identification of gaps and future needs. NEE 123–146.

Li, F., Schnelle-Kreis, J., Cyrys, J., Karg, E., Gu, J., Abbaszade, G., et al., 2018. Organic speciation of ambient quasi-ultrafine particulate matter (PM0. 36) in Augsburg, Germany: seasonal variability and source apportionment. Sci. Total Environ. 615, 828–837.

Li, X., Liu, B., Zhang, Y., Wang, J., Ullah, H., Zhou, M., Yu, H., 2019. Spatial distributions, sources, potential risks of multi-trace metal/metalloids in street dusts from barbican downtown embracing by Xi'an ancient city wall (NW, China). Int. J. Environ. 16 (16), 2992.

Liati, A., Dimopoulos Eggenschwiler, P., Müller Gubler, E., Schreiber, D., Aguirre, M., 2012. Investigation of diesel ash particulate matter: a scanning electron microscope and transmission electron microscope study. Atmos. Environ. 49391–49402, 1994.

Liati, A., Pandurangi, S.S., Boulouchos, K., Schreiber, D., Arroyo Rojas Dasilva, Y., 2015. Metal nanoparticles in diesel exhaust derived by in-cylinder melting of detached engine fragments. Atmos. Environ. 10134–10140, 1994.

Lin, C.C., Yang, L.S., Cheng, Y.H., 2016. Ambient PM2. 5, black carbon, and particle size-resolved number concentrations and the Ångström exponent value of aerosols during the firework display at the lantern festival in southern Taiwan. AAQR 2 (16), 373–387.

Liu, X., Schnelle-Kreis, J., Schloter-Hai, B., Ma, L., Tai, P., Cao, X., et al., 2019. Analysis of PAHs associated with PM10 and PM2. 5 from different districts in Nanjing. Aerosol Air Qual. Res. 19 (10), 2294–2307.

Lorenzo, G.R., Banaga, P.A., Cambaliza, M.O., Cruz, M.T., Azadiaghdam, M., Arellano, A., Betito, G., Braun, R., Corral, A.F., Dadashazar, H., Edwards, E., Eloranta, E., Holz, R., Leung, G., Ma, L., Macdonald, A.B., Reid, J.S., Simpas, J.B., Stahl, C., Visaga, S.M., Sorooshian, A., 2021. Measurement report: firework impacts on air quality in metro Manila, Philippines, during the 2019 New year revelry. Atmos. Chem. Phys. 21 (8), 6155–6173.

Loyola, J., Arbilla, G., Quiterio, S.L., Escaleira, V., Minho, A.S., 2012. Trace metals in the urban aerosols of Rio de Janeiro city. J. Braz. Chem. Soc. 23 (4), 628–638.

Masiol, M., Hofer, A., Squizzato, S., Piazza, R., Rampazzo, G., Pavoni, B., 2012. Carcinogenic and mutagenic risk associated to airborne particle-phase polycyclic aromatic hydrocarbons: a source apportionment. Atmos. Environ. 60, 375–382.

Miranda, J., Barrera, V.A., Espinosa, A.A., Galindo, O.S., Núñez-Orosco, A., Montesinos, R.C., Leal-Castro, A., Meinguer, J., 2004. PIXE analysis of atmospheric aerosols from three sites in Mexico City. Nucl. Instrum. Methods Phys. Res. B. 219, 157–160.

Mummullage, S., Egodawatta, P., Ayoko, G.A., Goonetilleke, A., 2016. Use of physicochemical signatures to assess the sources of metals in urban road dust. Sci. Total Environ. 541, 1303–1309.

Nadali, A., Leili, M., Bahrami, A., Karami, M., Afkhami, A., 2021. Phase distribution and risk assessment of PAHs in ambient air of Hamadan, Iran. Ecotoxicol. Environ. Saf. 209, 111807.

Orasche, J., Schnelle-Kreis, J., Abbaszade, G., Zimmermann, R., 2011. In-situ derivatization thermal desorption GC-TOFMS for direct analysis of particle-bound non-polar and polar organic species. Atmos. Chem. Phys. 11 (17), 8977–8993.

Orasche, J., Seidel, T., Hartmann, H., Schnelle-Kreis, J., Chow, J.C., Ruppert, H., Zimmermann, R., 2012. Comparison of emissions from wood combustion. Part 1: emission factors and characteristics from different small-scale residential heating

Appendix

appliances considering particulate matter and polycyclic aromatic hydrocarbon (PAH)-related toxicological potential of particle-bound organic species. Energy Fuels 26 (11), 6695–6704.
Paatero, P., Tapper, U., 1994. Positive matrix factorization: a non-negative factor model with optimal utilization of error estimates of data values. Environmetrics 2 (5), 111–126.
Pant, P., Harrison, R.M., 2013. Estimation of the contribution of road traffic emissions to particulate matter concentrations from field measurements: a review. Atmos. Environ. 7778–7797, 1994.
Pongpiachan, S., Hattayanone, M., Suttinun, O., Khumsup, C., Kittikoon, I., Hirunyatrakul, P., Cao, J., 2017. Assessing human exposure to PM10-bound polycyclic aromatic hydrocarbons during fireworks displays. Atmos. Pollut. Res. 5 (8), 816–827.
Rai, P., Furger, M., Slowik, J.G., Canonaco, F., Fröhlich, R., Hüglin, C., Prévôt, A.S., 2020. Source apportionment of highly time-resolved elements during a firework episode from a rural freeway site in Switzerland. Atmos. Chem. Phys. 3 (20), 1657–1674.
Retama, A., Neria-Hernández, A., Jaimes-Palomera, M., Rivera-Hernández, O., Sánchez-Rodríguez, M., López-Medina, A., Velasco, E., 2019. Fireworks: a major source of inorganic and organic aerosols during Christmas and New Year in Mexico City. Atmos. Environ. 2, 100013.
Rindelaub, J.D., Davy, P.K., Talbot, N., Pattinson, W., Miskelly, G.M., 2021. The contribution of commercial fireworks to both local and personal air quality in Auckland, New Zealand. Environ. Sci. Pollut. Res. 28 (17), 21650–21660.
Sanderson, P., Delgado-Saborit, J.M., Harrison, R.M., 2014. A review of chemical and physical characterisation of atmospheric metallic nanoparticles. Atmos. Environ. 94, 353–365.
Sappok, A., Kamp, C., Wong, V., 2012. Sensitivity analysis of ash packing and distribution in diesel particulate filters to transient changes in exhaust conditions. SAE Int. J. Fuels Lubr. 2 (5), 733–750.
Sarkar, S., Khillare, P.S., Jyethi, D.S., Hasan, A., Parween, M., 2010. Chemical speciation of respirable suspended particulate matter during a major firework festival in India. J. Hazard Mater. 184 (1–3), 321–330.
Saucy, A., de Hoogh, K., Vienneau, D., Tangermann, L., Schäffer, B., Wunderli, J.M., et al., 2021. Mutual effects of fine particulate matter, nitrogen dioxide, and fireworks on cause-specific acute cardiovascular mortality: a case-crossover study in communities affected by aircraft noise. Environ. Pollut. 291, 118066.
Schnelle-Kreis, J., Orasche, J., Abbaszade, G., Schäfer, K., Harlos, D.P., Hansen, A.D., Zimmermann, R., 2011. Application of direct thermal desorption gas chromatography time-of-flight mass spectrometry for determination of nonpolar organics in low-volume samples from ambient particulate matter and personal samplers. Anal. Bioanal. Chem. 401 (10), 3083–3094.
Schnelle-Kreis, J., Sklorz, M., Orasche, J., Stolzel, M., Peters, A., Zimmermann, R., 2007. Semi volatile organic compounds in ambient PM2.5. Seasonal trends and daily resolved source contributions. Environ. Sci. Technol. 41 (11), 3821–3828.
Shi, G.L., Liu, G.R., Tian, Y.Z., Zhou, X.Y., Peng, X., Feng, Y.C., 2014. Chemical characteristic and toxicity assessment of particle associated PAHs for the short-term anthropogenic activity event: during the Chinese New Year's Festival in 2013. Sci. Total Environ. 482, 8–14.
Srinivasan, K., 2017. Eco-friendly fireworks for atom bomb (Local name of cracker bomb). J. Adv. Appl. Sci. Res. 7 (1), 1–16.
ten Brink, H., Otjes, R., Weijers, E., 2019. Extreme levels and chemistry of PM from the consumer fireworks in The Netherlands. Atmos. Environ. 212, 36–40.
Vecchi, R., Bernardoni, V., Cricchio, D.D., Alessandro, A., Fermo, P., Lucarelli, F., Valli, G., 2008. The impact of fireworks on airborne particles. Atmos. Environ. 6 (42), 1121–1132.
Walsh, K.J., Milligan, M., Sherwell, J., 2009. Synoptic evaluation of regional PM2.5 concentrations. Atmos. Environ. 3 (43), 594–603.

6. CURRICULUM VITAE

Name	Xiansheng Liu
Date of birth	September 25th, 1990
Place of birth	Shandong, China
Address	Aidenbachstr. 68, 81379, München

Education

2017.10-Now	PhD Student, University of Rostock and Comprehensive Molecular Analysis (CMA) group of Helmholtz Zentrum Muenchen
2014.09-2017.07	Master of Environment science, school of Environment, Nanjing Normal University
2010.09-2014.07	Bachelor of Land resources management, school of Geography and Tourism, Qufu Normal University
Until 2010	School education